Daniel Darnikowski, M.Sc. Eng.

Institute of Fluid Flow Machinery, Polish Academy of Sciences

METHODOLOGY FOR INVESTIGATING THE DEGRADATION PROCESSES OF MODERN MATERIALS USED IN ALTERNATIVE ENERGY SOURCES EXPOSED TO FIRE AND/OR MECHANICAL OVERLOADS

A dissertation submitted to the Scientific Board of Institute of Fluid Flow Machinery, Polish Academy of Sciences in partial fulfilment of the requirements for the Degree of Doctor of Philosophy

Supervisor:
Magdalena Mieloszyk, D.Sc. Ph.D. Eng., prof. IMP PAN

Poland, Gdańsk
September 2025

"The ideal engineer is a composite. He is not a scientist, he is not a mathematician, he is not a sociologist or a writer; but he may use the knowledge and techniques of any or all of these disciplines in solving engineering problems."

- N. W. Dougherty

To my late grandfather, Mieczysław – in gratitude for his unwavering support and the values he instilled in me.

ABSTRACT

Lithium-ion batteries are a cornerstone technology in the transition toward sustainable mobility and renewable energy integration, yet their safety remains a significant challenge. Chief among safety hazards is *thermal runaway* – a self-accelerating, exothermic reaction sequence that can result in fire, explosion, and toxic emissions. This dissertation investigates the degradation processes of modern materials used in Rechargeable Energy Storage Systems for electric vehicles and stationary Battery Energy Storage Systems under conditions of fire exposure and/or mechanical overloads. The work identifies critical limitations in current regulatory fire testing procedures, particularly the UNECE R100.03 open-flame external fire test, which exhibits high variability, qualitative pass/fail criteria, limited diagnostic capability, and safety hazards to personnel and the environment.

A comprehensive literature review is combined with experimental, numerical, and statistical analyses to evaluate the thermal, mechanical, and electrochemical failure mechanisms of lithium-ion batteries, the influence of cell chemistry and architecture, and the efficacy of passive and active safety measures. A detailed examination of current global standards reveals inconsistencies in sensor placement, environmental control, and acceptance criteria. Using open-flame fire resistance testing as a core study, this thesis demonstrates how uncontrolled environmental variables (e.g., wind, flame impingement patterns) lead to poor repeatability between laboratories.

To address these issues, an alternative, quantitatively grounded methodology is developed by adapting the ISO 834-1 / EN 1363-1 furnace-based fire resistance standard, widely applied in structural fire engineering – to the evaluation of lithium-ion battery enclosures. This approach offers tightly controlled and reproducible thermal exposure, improved safety, and enhanced diagnostic value through rigorous sensor instrumentation and continuous data acquisition. Comparative analyses show that furnace-based testing significantly reduces measurement uncertainty and yields rich datasets on heat transfer, structural degradation, and propagation thresholds, thus enabling better-informed safety engineering decisions.

Complementing this methodological advance, a Thermal Runaway Emissions Aftertreatment System (TREAS) is designed and validated to mitigate the release of hazardous gases during testing, aligning with emerging environmental and occupational safety requirements. The combined methodology – controlled thermal exposure with integrated emissions management-provides a robust framework for both scientific investigation and regulatory compliance.

The outcomes of this research contribute a repeatable, data-rich fire testing protocol for battery energy storage systems, offering actionable recommendations for standards development, improved enclosure design, and enhanced public safety. By bridging fire science, battery engineering, and standardisation practice, this thesis supports the safe and reliable deployment of high-energy battery systems in next-generation transport and energy infrastructures.

STRESZCZENIE

Akumulatory litowo-jonowe stanowią kluczową technologię w transformacji ku zrównoważonej mobilności oraz integracji odnawialnych źródeł energii, jednak ich bezpieczeństwo pozostaje istotnym wyzwaniem. Najpoważniejszym zagrożeniem jest zjawisko *ucieczki termicznej* (ang. "thermal runaway") - samonapędzającej się sekwencji reakcji egzotermicznych, mogącej prowadzić do pożaru, eksplozji i emisji toksycznych gazów. Niniejsza rozprawa dotyczy procesów degradacji nowoczesnych materiałów stosowanych w systemach akumulacji energii w pojazdach elektrycznych oraz stacjonarnych magazynach energii, poddanych oddziaływaniu ognia i/lub przeciążeń mechanicznych. W pracy zidentyfikowano kluczowe ograniczenia obecnych regulacyjnych procedur badań ogniowych, w szczególności testu zewnętrznego ognia UNECE R100.03, który charakteryzuje się dużą zmiennością wyników, jakościowymi kryteriami zaliczenia/niezaliczenia, ograniczoną wartością diagnostyczną oraz ryzykiem dla personelu i środowiska.

Rozległy przegląd literatury połączono z analizami eksperymentalnymi, numerycznymi i statystycznymi w celu oceny mechanizmów awarii termicznych, mechanicznych i elektrochemicznych LIB, wpływu chemii i konstrukcji ogniw oraz skuteczności biernych i aktywnych systemów bezpieczeństwa. Szczegółowa analiza aktualnych globalnych norm wykazała niespójności w rozmieszczeniu czujników, kontroli warunków środowiskowych oraz kryteriach oceny. Studium testu odporności ogniowej w warunkach otwartego płomienia wykazało, że niekontrolowane zmienne środowiskowe (np. wiatr, charakterystyka opływu płomieni) powodują niską powtarzalność wyników pomiędzy laboratoriami.

W odpowiedzi opracowano alternatywną, ilościowo ugruntowaną metodologię, adaptującą normę ISO 834-1 / EN 1363-1 – powszechnie stosowaną w inżynierii pożarowej konstrukcji – do oceny obudów akumulatorów litowo-jonowych. Metoda ta zapewnia ściśle kontrolowaną i powtarzalną ekspozycję cieplną, zwiększone bezpieczeństwo oraz wyższą wartość diagnostyczną dzięki precyzyjnej aparaturze pomiarowej i ciągłemu rejestrowaniu danych. Analizy porównawcze wykazały, że testy piecowe znacząco redukują niepewność pomiarową i dostarczają bogatych danych o transferze ciepła, degradacji strukturalnej i progach propagacji, umożliwiając lepsze decyzje inżynierskie w zakresie bezpieczeństwa.

Uzupełnieniem proponowanej metodologii jest zaprojektowany i zwalidowany system oczyszczania emisji powstających podczas ucieczki termicznej (TREAS), ograniczający emisję substancji niebezpiecznych w trakcie badań, zgodnie z nowymi wymaganiami środowiskowymi i BHP. Połączenie kontrolowanej ekspozycji cieplnej z systemem oczyszczania emisji stanowi solidne narzędzie zarówno do badań naukowych, jak i do zastosowań regulacyjnych.

Rezultaty pracy obejmują powtarzalny, bogaty w dane protokół badań odporności ogniowej systemów bateryjnych litowo-jonowych, wraz z praktycznymi rekomendacjami dla rozwoju norm, projektowania bezpieczniejszych obudów oraz poprawy bezpieczeństwa publicznego. Łącząc wiedzę z zakresu inżynierii pożarowej, technologii akumulatorów i standaryzacji, rozprawa wspiera bezpieczne i niezawodne wdrażanie systemów akumulacji energii dużej gęstości w transporcie i infrastrukturze energetycznej nowej generacji.

ACKNOWLEDGEMENTS

First and foremost, I would like to express my sincere gratitude to my supervisor, Professor Magdalena Mieloszyk, for her continuous guidance, invaluable advice, and constructive criticism throughout the course of this doctoral research. Her expertise, scientific rigour, and patient mentorship have greatly shaped both the direction of this work and my development as a researcher. I am deeply indebted to her for creating an environment that fostered intellectual curiosity, critical reflection, and perseverance in addressing complex engineering challenges.

I am also profoundly grateful to Mateusz Weryk, Director of Centrum Techniki Okrętowej S.A., whose support and encouragement were instrumental in the realization of this project. His vision and commitment to advancing research in the field provided both the practical framework and the inspiration necessary for this dissertation. I would also like to thank the entire team at CTO S.A. for their collaboration, assistance, and for providing access to experimental facilities and industrial expertise that made the empirical part of this research possible.

This research was carried out within the framework of the "Doktorat Wdrożeniowy" programme of the Polish Ministry of Science and Higher Education, whose support enabled the integration of scientific research with industrial implementation. The programme's vision of fostering cooperation between academia and industry was instrumental in shaping both the objectives and the impact of this dissertation.

This work would not have been achievable without the contribution of the industrial partners and companies who generously agreed to share their data and experience. Their openness and trust allowed me to ground my research in real-world applications and significantly enhanced the relevance and applicability of the results presented herein.

On a personal note, I wish to extend my deepest gratitude to my partner, Ola, for her constant encouragement, patience, and unwavering support during the many demanding stages of this dissertation. Her understanding and belief in my work gave me the strength and motivation to persevere, even during the most challenging moments of this academic journey.

Finally, I would like to express my sincere appreciation to Marta Walk, whose meticulous review of the manuscript greatly improved the clarity and quality of this dissertation. Her careful attention to detail and thoughtful feedback ensured the final work achieved a much higher standard.

To all those mentioned, and to many others who have supported me in various ways throughout the course of my doctoral studies, I extend my heartfelt thanks.

PUBLICATIONS

Darnikowski, D., & Mieloszyk, M. (2021). Investigation into the lithium-ion battery fire resistance testing procedure for commercial use. *Batteries*, 7(3), 44. https://doi.org/10.3390/batteries7030044

Darnikowski, D. (2021). Study of insulation criterion assessment of EN 1363-1 and EN 1634-1. In M. Mieloszyk & T. Ochrymiuk (Eds.), *Selected Problems in Mechanical Engineering 2021* (pp. 113–134). Gdańsk: Wydawnictwo IMP PAN.

Darnikowski, D. (2024). Fire resistance test methods of battery energy storage systems (BESS): Analysis, comparison and prospects. In M. Mieloszyk (Ed.), *Selected Problems in Mechanical Engineering 2022* (pp. 31-54). Gdańsk: Wydawnictwo IMP PAN.

Darnikowski, D., Mieloszyk, M., & Weryk, M. (2022). Fire resistance of construction elements. In *Proceedings of SPIE – Sensors and Smart Structures Technologies for Civil, Mechanical, and Aerospace Systems* (Vol. 12046, pp. 203–218). SPIE. https://doi.org/10.1117/12.2615611

Darnikowski, D., & Mieloszyk, M. (2023). Fire safety of rechargeable battery energy storage systems: Present and future prospects. In *Proceedings of International Conference on Fire Safety of Battery Systems*, https://doi.org/10.12783/shm2023/37004. [Conference paper].

Darnikowski, D. (2023). Development of Thermal Runaway Emissions Aftertreatment System (TREAS) of lithium-ion batteries. *Transactions of the Institute of Fluid-Flow Machinery*, 142, 47–59.

Darnikowski, D. (2024, June). Fire safety aspects of lithium-ion batteries in energy storage and transport. Paper presented at *Nordic Fire & Safety Days*, Lund, Sweden. https://doi.org/10.23699/yns7-3n56. [Abstract in proceedings].

Darnikowski, D., & Mieloszyk, M. (2025). Experimental investigations on the repeatability of the fire-resistance testing of electric vehicle post-crash safety procedures. *Sensors*, 25(3), 688. https://doi.org/10.3390/s25030688

DEFINITIONS AND ACRONYMS

BESS (Battery Energy Storage System) is a system consisting of rechargeable electrochemical cells, modules, and packs combined with associated electrical, mechanical, thermal, and protective components, intended to store and release electrical energy for later use. The term BESS is typically used for larger-scale installations, including stationary grid applications as well as vehicular safety assessments. It is often synonymous with RESS.

ESS (Energy Storage System) is a general term describing any device or group of devices capable of storing energy in various forms (electrochemical, mechanical, thermal, or other) for subsequent release as useful energy. In the context of this dissertation, ESS primarily refers to electrochemical systems based on lithium-ion technology.

RESS (Rechargeable Energy Storage System) is a rechargeable electrochemical energy storage device, consisting of one or more cells, modules, and packs, together with necessary monitoring and protection equipment. In regulatory frameworks such as UNECE R100.03, RESS refers specifically to traction batteries installed in electric road vehicles. It is often synonymous with BESS.

Stationary ESS (Stationary Energy Storage System) is a battery energy storage system intended for stationary use (e.g. grid balancing, renewable energy integration, peak shaving, backup power). Unlike RESS, which is mobile, stationary ESS is permanently installed at a fixed location and designed to provide grid services or local energy support.

ANSI American National Standards Institute

BEV Battery Electric Vehicle

BESS Battery Energy Storage Systems

BMS Battery Management System

BTMS Battery Thermal Management System

CEN European Committee for Standardisation

CENELEC European Committee for Electrotechnical Standardisation

CID Current Interrupt Device

CPCM Composite Phase Change Material

DEC Diethyl Carbonate

DMC Dimethyl Carbonate

DUT Device Under Test

EC Ethylene Carbonate

ECOSOC United Nations Economic and Social Council

EMC Ethyl Methyl Carbonate

ESS Energy Storage System

EV Electric Vehicle

FCEV Fuel Cell Electric Vehicle

GTR Global Technical Requirement (United Nations Document)

HEV Hybrid Electric Vehicle

HRR Heat Release Rate

HTR Heat–Temperature–Reaction (loop)

HTS High-Temperature Superconductor

HVAC Heating, Ventilation and Air Conditioning

ICE Internal Combustion Engine

IEC International Electrotechnical Commission

IP Ingress Protection (rating)

ISC Internal Short Circuit

ISO International Organization for Standardization

LIB Lithium-Ion Battery

LCO Lithium Cobalt Oxide

LFP Lithium Iron Phosphate

LMO Lithium Manganese Oxide

LTO Lithium Titanium Oxide

mHEV Mild Hybrid Electric Vehicle

NCM Nickel-Cobalt-Manganese (Oxide)

NMC Nickel-Manganese-Cobalt (Oxide; same as NCM)

NFPA National Fire Protection Association

OEM Original Equipment Manufacturer

PC Propylene Carbonate

PCM Phase Change Material

PCC Phase Change Composite

PE Polyethylene

PET Polyethylene Terephthalate

PEV Pure Electric Vehicle

PHEV Plug-in Hybrid Electric Vehicle

PP Polypropylene

PSD Power Spectral Density

PTC Positive Temperature Coefficient

RESS Rechargeable Energy Storage System

SAC Standardization Administration of China

SAE Society of Automotive Engineers

SEI Solid Electrolyte Interphase

SOC State of Charge

TR Thermal Runaway

UL Underwriters Laboratories

UN United Nations

UNECE United Nations Economic Commission for Europe

USABC United States Advanced Battery Consortium

Contents

1 Introduction **4**
- 1.1 Motivation and Background of the Thesis . . . 14
- 1.2 Outline of the Thesis . . . 15

2 Safety Analysis of Lithium-ion Batteries **17**
- 2.1 Operating Principles of the Lithium-ion Battery . . . 18
- 2.2 Thermal Runaway Mechanics Analysis . . . 23
- 2.3 Mechanical Abuse of Lithium-ion Batteries . . . 28
- 2.4 Electrical Abuse of Lithium-ion Batteries . . . 30
- 2.5 Thermal Abuse of Lithium-ion Battery . . . 31
- 2.6 Unwanted Chemical Reactions of Lithium-ion Batteries . . . 32

3 Thermal Safety Systems in Lithium-ion Batteries **34**
- 3.1 Passive Safety Systems for Avoiding Thermal Runaway . . . 34
  - 3.1.1 Cell Level . . . 34
  - 3.1.2 Module Level . . . 39
  - 3.1.3 Pack Level . . . 43
  - 3.1.4 Summary on Passive Systems . . . 47
- 3.2 Active Strategies for Mitigating and Suppressing Thermal Runaway . . . 47
  - 3.2.1 Active Mitigation Methods at the Cell Level . . . 48
  - 3.2.2 Active Mitigation Methods at Module Level . . . 49
  - 3.2.3 Active Mitigation Methods at Pack/System Level . . . 52
  - 3.2.4 Comparative Analysis: Electric Vehicle vs. Stationary Energy Storage System Thermal Runaway Strategies . . . 55
  - 3.2.5 Summary on Active Systems . . . 58

4 Aim of the Thesis **60**

5 Standardisation of the Battery Energy Storage Systems Testing **62**
- 5.1 Standardisation Bodies . . . 63
- 5.2 Mechanical Test . . . 66
  - 5.2.1 Mechanical Shock Tests . . . 67
  - 5.2.2 Drop Tests . . . 69
  - 5.2.3 Penetration Tests . . . 71
  - 5.2.4 Crush Tests . . . 74
  - 5.2.5 Vibration Tests . . . 78
  - 5.2.6 Summary of Mechanical Test . . . 81
- 5.3 Electrical Tests . . . 82
  - 5.3.1 External Short-Circuit Test . . . 83
  - 5.3.2 Overcharge and Overdischarge Tests . . . 85
  - 5.3.3 Other Electrical Safety Requirements . . . 86
  - 5.3.4 Summary of Electrical Tests . . . 87

5.4 Environmental Tests . . . 87
5.4.1 Thermal Stability Tests . . . 88
5.4.2 Thermal Shock Tests . . . 89
5.4.3 Fire Resistance Tests . . . 90
5.4.4 Immersion Tests . . . 94
5.4.5 Emissions-Related Environmental Tests (Toxicity and Particulates) . . . 96

6 Battery Fire Resistance Testing Methodology 100
6.1 Fire Plume Dynamics and Heat Flux in Lithium-ion Battery Fires . . . 100
6.1.1 Fire Plume Theory in Battery Fires and Fire Resistance Tests . . . 100
6.1.2 Modelling Convective and Radiative Heat Flux from Fire Plumes . . . 104
6.2 Numerical Analysis of the Conditions for Fire Resistance Testing of LIB . . . 105
6.2.1 UNECE R100.03 Fire Resistance Test . . . 106
6.2.2 UL 1973 and UL 2580 External Fire Test . . . 108
6.2.3 SAE J2464 External Fire Test . . . 110
6.2.4 Comparison and Engineering Implications . . . 111
6.3 Empirical Evaluation of Open Flame Fire Resistance Testing Procedure . . . 114
6.3.1 Object of Investigation . . . 114
6.3.2 Experimental Results . . . 115
6.3.3 Theoretical Estimation of Temperature Inside the RESS System . . . 120
6.3.4 Summary . . . 123
6.4 Statistical analysis of Open Flame Fire Resistance Testing Procedure . . . 124
6.4.1 Experimental Setup and Instrumentation . . . 124
6.4.2 Statistical Data Analysis . . . 124
6.4.3 Conclusions . . . 128
6.5 Discussion on the Open Flame Fire Resistance Testing Procedure . . . 131
6.6 Alternative Fire Resistance Testing Procedure for Lithium-ion Batteries . . . 132
6.6.1 Alternative EN and ISO Fire Resistance Testing Procedure for Lithium-ion Batteries . . . 132
6.6.2 Limitations of Furnace-Only Testing: Venting and Pressure Effects . . . 137
6.6.3 Empirical Evaluation of the Fire Resistance Testing according to EN 45545-3 and ISO 834-1 . . . 138
6.7 Discussion on the EN and ISO Fire Resistance Testing Procedures for Lithium-ion Batteries . . . 144
6.7.1 Theoretical Foundations and Performance Criteria . . . 144
6.7.2 Experimental Setup and Instrumentation . . . 145
6.8 Recommendations for Regulatory Revisions and Standards Development . . . 147

7 Development of Thermal Runaway Emissions Aftertreatment System of Lithium-ion Batteries 150
7.1 Development and test results of TREAS . . . 150
7.1.1 Air Flow Simulations and Measurements of the TREAS . . . 152
7.1.2 Thermal Runaway Tests . . . 153

8 Summary and Conclusions of the Thesis 156
8.1 Summary of Findings and Contributions . . . 156
8.2 Unique Contributions to Knowledge in Thesis . . . 157
8.3 Recommendations and Future Work . . . 159

A Overview of the Materials used in Lithium-ion Batteries **161**
A.1 Cathode Materials . . . 161
A.1.1 Lithium Cobalt Oxide (LCO) . . . 161
A.1.2 Lithium Nickel Oxide (LNO) . . . 162
A.1.3 Vanadium-based cathodes (VO and LVO) . . . 163
A.1.4 Nickel cobalt manganese oxide (NCM) . . . 164
A.1.5 Aluminum-doped lithium nickel oxide (NCA) . . . 165
A.1.6 Lithium manganese (nickel) oxide (LMO and LMNO) . . . 165
A.1.7 Lithium iron phosphate (LFP) and other phosphate-based cathodes . . . 167
A.2 Anode Materials . . . 168
A.3 Electrolyte Materials . . . 170
A.4 Separator Materials . . . 171

B Review of the Prevention Systems and Solutions to Battery Fires **172**
B.1 Battery Management Systems as Primary Prevention Layer . . . 172
B.2 Air-Cooled Thermal Management Systems . . . 173
B.3 Liquid-Based Thermal Management Systems . . . 175
B.4 PCM-Based Battery Thermal Management Systems . . . 177
B.5 Hybrid Battery Thermal Management Systems . . . 178
B.5.1 Air-Liquid Hybrid Cooling Configurations . . . 179
B.5.2 Phase Change Material Integration in Hybrid Systems . . . 180

C Additional datasets **182**
C.1 Extra data to Empirical Evaluation of Open Flame Fire Resistance Testing Procedure . . . 182
C.2 Statistical analysis of Open Flame Fire Resistance Testing Procedure . . . 183

D Background for TREAS development **190**
D.1 Thermal runaway emissions of lithium-ion batteries . . . 190
D.2 Cleaning methods of the gas emissions . . . 191

E List of Standards and Regulations Referenced in the Thesis **193**

List of Figures **196**

List of Tables **199**

Bibliography **201**

Chapter 1

Introduction

Lithium, originally named lithion or lithina, was first discovered in 1817 by Arfwedson and Berzelius through the analysis of petalite ore ($LiAlSi_4O_{10}$) [1, 2]. However, it was not until 1821 that Brande and Davy successfully isolated the element via electrolysis of lithium oxide [3]. It took another hundred years before its electrochemical properties attracted scientific attention, notably by Lewis in the early 20th century. Lithium's appeal stemmed from its exceptional physical properties, including its low density (0.534 g/cm^3), high specific capacity (3860 mAh/g), and very low redox potential (-3.04 V vs. SHE), making it an ideal candidate for battery anodes [4].

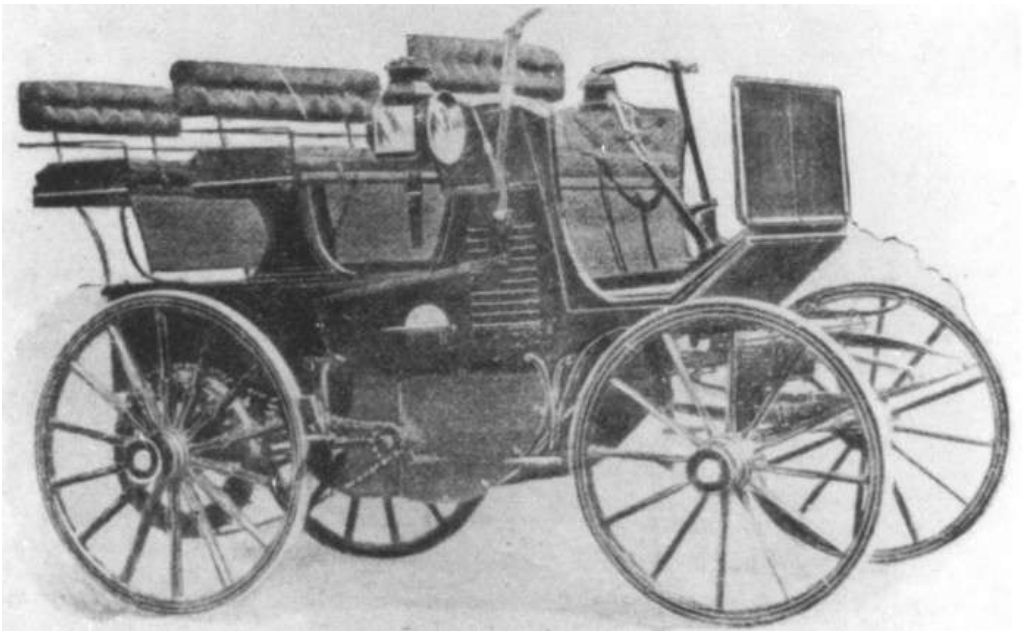

Figure 1.1: Holtzer-Cabot's 1895 model electric brake [5].

The late 19th century saw the advent of electric vehicles (EV), with innovators like Thomas Parker in England, Holtzer-Cabot and William Morrison in the United States developing early electric cars (see Figure 1.1). Batteries were to body of the vehicle and included forty-four 250 Ah chloride cells batteries adding up to about 20 kWh, the vehicle maximum speed was about 24 km/h produced by 7.5 hp motor. These vehicles gained popularity due to their quiet operation and ease of use compared to gasoline-powered cars. However, limitations in battery technology, particularly the weight and limited energy density of lead-acid batteries, since lithium has not been yet developed, hindered their widespread adoption. The subsequent rise of internal combustion engine vehicles, offering greater range and convenience, led to a decline in EV use by the 1930s [5].

The groundwork for lithium battery (non-rechargeable, not to confuse with lithium-ion) technology began in earnest in 1958, when Harris explored the solubility of lithium in a range of non-aqueous (aprotic) electrolytes such as carbonates and γ-lactones. His work revealed that lithium formed a passivation layer when in contact with certain electrolytes, a layer that could prevent unwanted chemical reactions while still allowing ions to move across it. This discovery was a key milestone, helping to stabilize lithium-based cells and sparking significant interest in the development and commercialization of primary lithium batteries [6]. Simultaneously, in 1959, Gaston Planté introduced the lead-acid battery, the first rechargeable battery, which became widely used for stationary energy storage and later in automotive applications [7].

From the late 1960s onward, the first commercial non-aqueous 3 V lithium primary batteries emerged. Notable examples include lithium-sulfur dioxide ($Li//SO_2$) batteries introduced in 1969; lithium polycarbon monofluoride ($Li//(CF_x)_n$) cells commercialized by Matsushita in 1973; and lithium manganese oxide ($Li//MnO_2$) batteries from Sanyo in 1975, originally marketed in solar-powered calculators. Other innovations included lithium copper oxide ($Li//CuO$) batteries and lithium iodine/polyvinyl-pyridine ($Li/LiI/Li_2PVP$) batteries, the latter being used in cardiac pacemakers since 1972 due to their long life and reliability [8].

Alongside these advances in primary (non-rechargeable) lithium batteries, researchers were gaining new insights into lithium intercalation - a process that led to the development of secondary (rechargeable) lithium-ion batteries (LIBs). These advances laid the foundation for the high-performance, rechargeable LIBs that have since become vital to modern technology, powering everything from mobile phones to EVs, highlighting the pioneering work in this field between 1970 and 1990 [9].

In recent years, they have become especially vital in both the transportation and energy sectors. Between 2010 and 2023, average battery costs dropped by 90%, while their performance significantly improved, with advancements such as higher energy densities and longer cycle life (see Figure 1.2) showing capacity improvements for conservative and advanced technology estimates, illustrating significant performance advancements over the period [10, 11]). These developments position batteries as a key component in the shift toward low-emission energy systems [12].

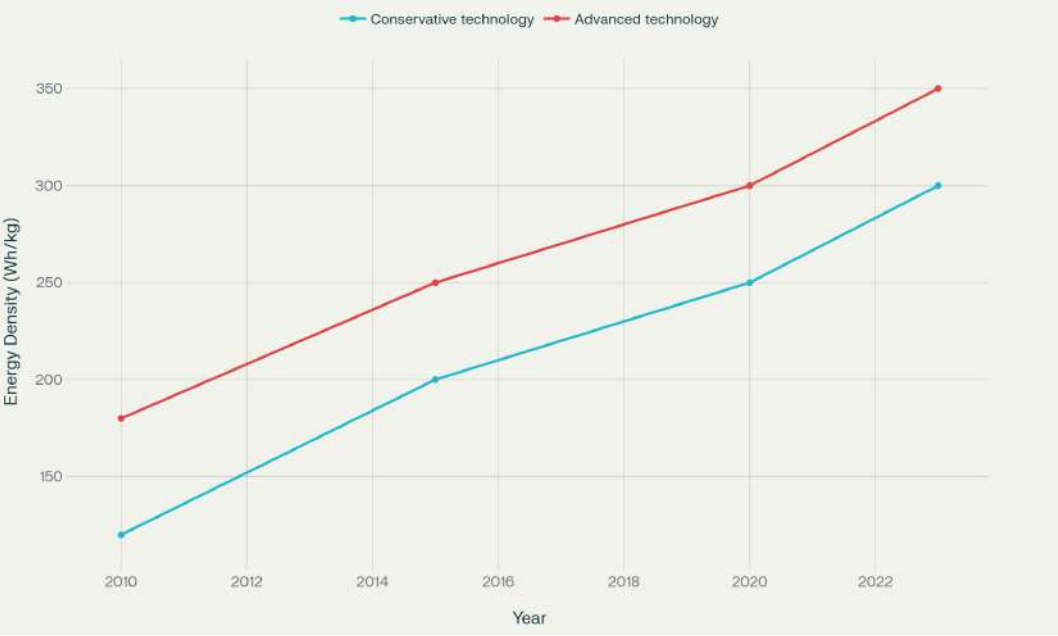

Figure 1.2: Evolution of LIB energy density (Wh/kg) from 2010 to 2023 (based on [10, 11, 12]).

In the power sector, energy storage especially battery storage plays a crucial role in maintaining electricity security. It contributes to grid stability, helps manage peak demand, and enhances

the integration of growing shares of variable renewable energy sources. A reliable electricity supply depends on keeping generation and demand balanced at all times [13]. More recently, batteries have emerged as a viable energy storage option. Falling battery costs have made them a competitive source of system flexibility, both as stand-alone solutions and when combined with solar photovoltaic or wind power [14]. In the automotive sector, the shift toward EVs is increasingly viewed by governments and manufacturers as a key strategy to cut air pollution and greenhouse gas emissions. This transition is reshaping the conventional automotive supply chain, as EVs require fewer moving parts than internal combustion engine (ICE) vehicles and rely heavily on battery systems, which is reflected in the average EV weight being 450 kg more than their ICE counter part [15]). Consequently, industries that previously operated separately are now collaborating more closely [16].

The advent of electromobility and usage of energy storage systems (ESS) in recent years has increased rapidly the number of battery applications. Rapid increment of car stock of EVs was seen in the last years with almost 14 million new electric cars registered in 2023, reaching total stock number to 40 million (shown in Figure 1.3). EVs sales in 2023 were 3.5 million higher than in 2022, which adds up to 35% year-on-year increase. Globally EVs accounted for about 18% of total cars sold in 2023 (up from 14% in 2022).

Sales of the EVs remain concentrated in just a few major markets. 60% of new electric car registrations were in People's Republic of China (hereafter "China"), 25% were in Europe and 10% in the United States, globally. In total three regions correspond to 95% of global electric sales, while other market EVs sales stay limited even in significant car markets like India and Japan.

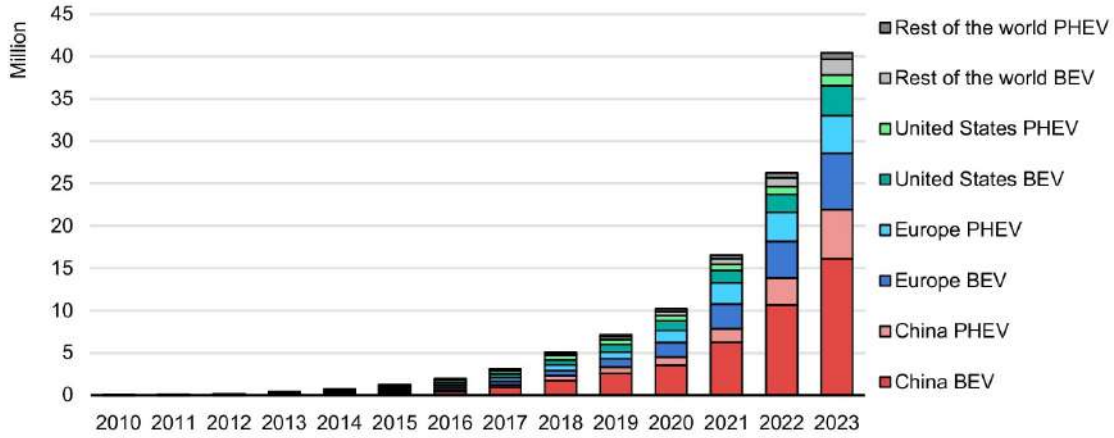

Figure 1.3: Global electric car stock trends over the years 2010 to 2023 [12].

China's electric car registrations reached 8.1 million in 2023 (see Figure 1.4), marking an increase of 35% in relation to 2022. At the same time, 1.2 million EV units were exported primarily to Europe and Asia Pacific Region. The United States new electric car registrations totalled at 1.4 million in 2023, which is a 40% year-on-year rise. In Europe, car registrations reached almost 3.2 million in 2023, marking a 20% increase from 2022. In all three regions despite, the government subsides or tax exemptions were limited or completely expired, a significant growth in car sales was recorded. While some of the individual countries in Europe recorded drop is EVs sales such as Germany and Norway (first one due to Climate and Transformation Fund ending and in second due to market being too saturated already at 95% of all cars being electric), there are still multiple markets – Sweden, France, Netherlands and the United Kingdom - which have significant room to grow [17].

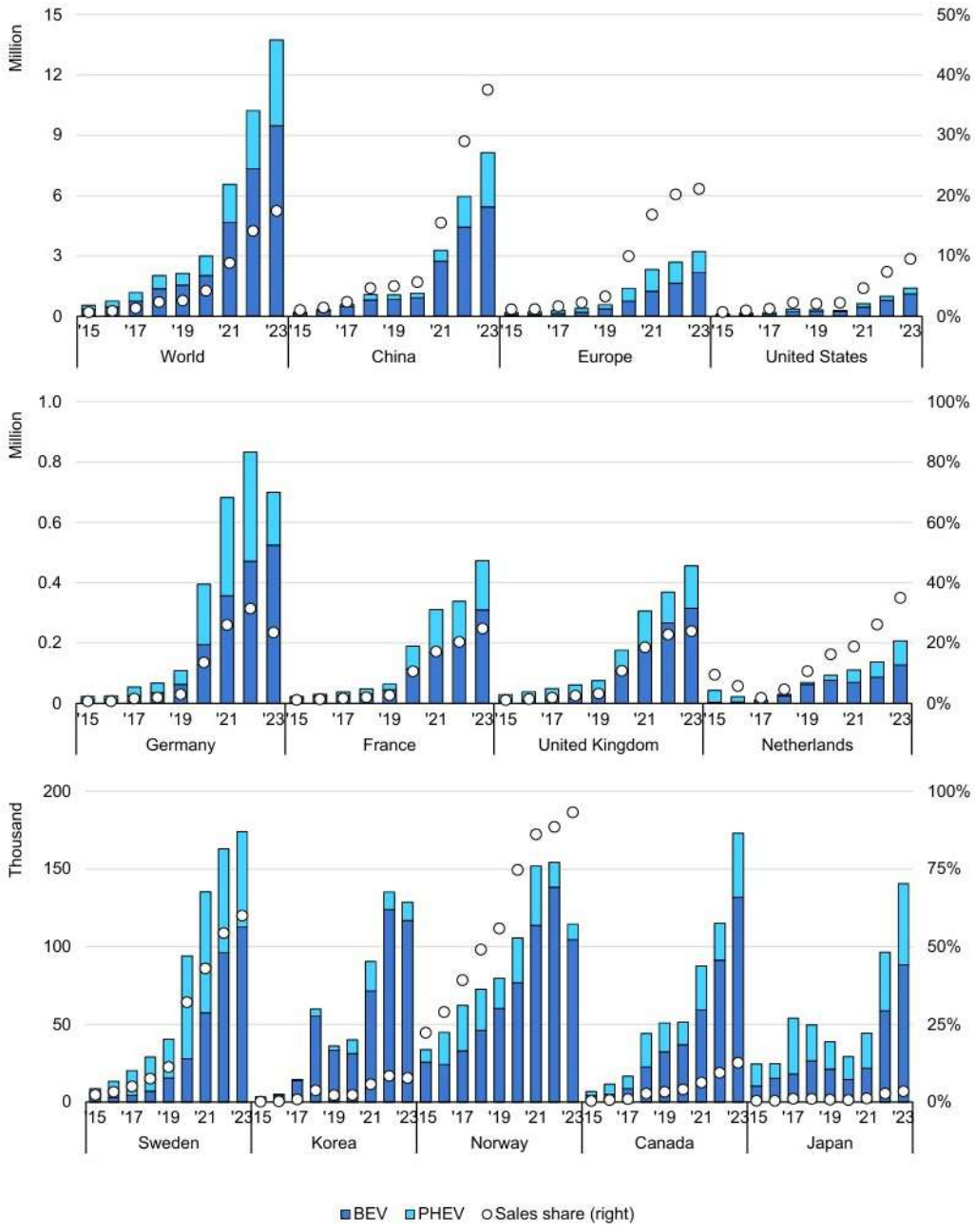

Figure 1.4: Electric car registrations and sales share percentage in selected countries and regions, 2015-2023 [12].

EVs are namely divided into three categories depending on drive section, energy sources and energy supplements [18, 19] (their share has been shown in Figure 1.5):

- **Pure electric vehicle (PEV) or battery electric vehicles (BEV)** - vehicles where a propulsion is induced only by an electric motor, energy is stored in the vehicle-mounted battery and charge is supplied from online grid.
- **Hybrid electric vehicle (HEV)** - type of cars combining the electric motor and the ICE. Power can be delivered from the ICE (both diesel or petrol) or battery. These can be further divided into:
  - **Micro hybrid electric vehicle** - operates the engine start motor with a belt-

alternator start generator.

  - **Mild hybrid electric vehicle** - start motor is replaced with integrated starter-generator located between the engine and transmission. The idea is electric generator comes alive while the petrol engine is shut down, subsequently all the working equipment relies on the electric motor. When the acceleration starts, the ICE takes over and provides propulsion (this is system is often know as "start-stop feature").
  - **Full hybrid electric vehicle** - the pivotal technology is the electric variable transmission, allowing for power splitting. It allows to launch the vehicle using the electric energy and provide initial acceleration.
  - **Plug-in hybrid electric vehicle (PHEV)** - containing battery packs and electric generator connected in series, parallel or series-parallel with the ICE. Due to the fact the 90% of urban driving range is less than 60 km, while the daily driving range greater than 100 km is less than 5%, PHEVs became quite popular choice of combining the fuel efficiency of electric motor and long range of gasoline powered units.

- **Fuel cell electric vehicle (FCEV)** - it is driven by electric motor or can be indirectly powered using hydrogen, methanol, ethanol or gasoline.

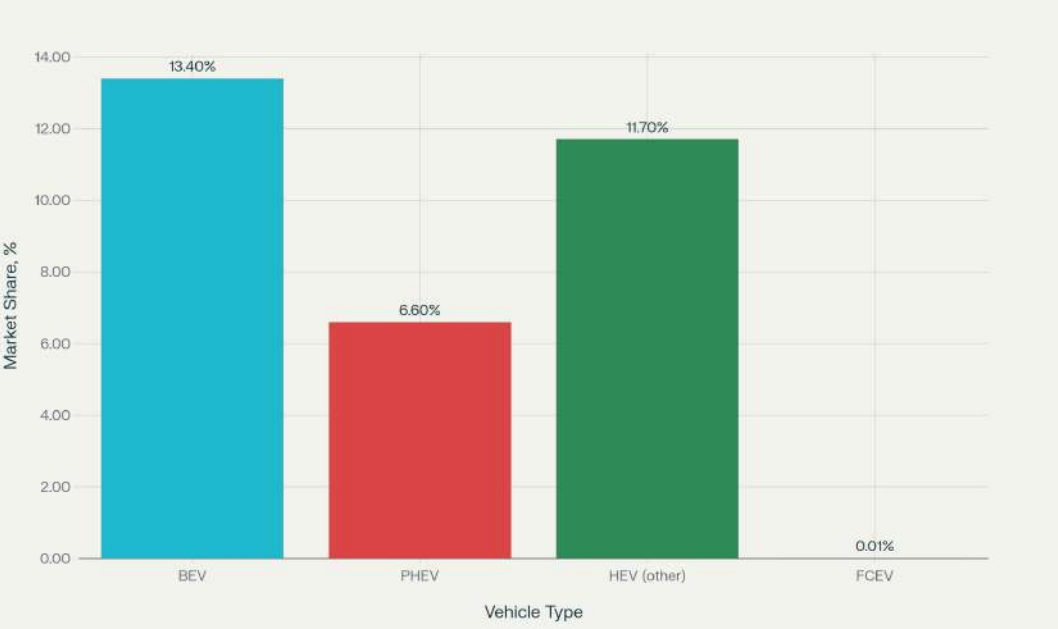

Figure 1.5: Bar chart of the market share (%) of major electric vehicle types—Battery Electric Vehicles (BEV), Plug-in Hybrid Electric Vehicles (PHEV), Hybrid Electric Vehicles (HEV, other than plug-in), and Fuel Cell Electric Vehicles (FCEV), based on [12].

In broader sense EV, according to European Union legislation, is defined as a road vehicle that is propelled solely or partially by one or more electric motors, using electric energy stored in a battery or another rechargeable energy storage system (RESS). This energy must be rechargeable from an external source of electricity, which distinguishes plug-in vehicles from conventional internal combustion engine vehicles.

The primary legal framework governing this definition is Regulation (EU) 2018/858 on the approval and market surveillance of motor vehicles. Within this regulation, EVs are categorized as either battery EVs, which are powered exclusively by electricity, or plug-in hybrid EVs, which combine an electric motor and a conventional engine but still rely on external charging. These classifications ensure that vehicles meet specific technical and environmental standards before they can be sold or used within the EU [20]. For the purpose of this thesis, when discussing

"electric vehicle" the author primarily means either BEV or PHEV, mainly due to larger batteries being installed.

Public concern regarding LIB fires has grown significantly in recent years, fuelled by high-profile incidents involving smartphones, laptops, EVs, and even e-scooters, due to significant increase in everyday use of LIBs. These events have not only drawn media attention but also raised consumer anxiety about the safety of devices powered by these batteries. For instance, the 2016 recall of Samsung's Galaxy Note 7 following spontaneous battery fires led to widespread apprehension about the reliability of consumer electronics [21, 22]. Similar concerns have been echoed in the context of EVs, where thermal runaway (TR) incidents have sparked fears over the safety of adopting EV technology on a large scale [23]. These concerns have implications for public trust and acceptance of battery-powered technologies, potentially hindering the broader transition to sustainable energy systems.

Despite EVs generally being less prone to fire than ICE vehicles per mile driven, the unique characteristics of LIB fires such as their intensity, difficulty to extinguish, and potential for TR have captured public attention [24]. High-profile incidents involving Tesla and other EV brands have received extensive media coverage, often without context regarding the relative safety of EVs compared to traditional vehicles [25, 26]. The visual spectacle of battery fires, including re-ignition risks and prolonged burn times, can contribute to a perception that EVs pose a greater safety threat, despite statistical evidence suggesting otherwise.

One of the most direct ways to compare fire risk is to look at how many vehicles of each type experience fires per a certain number of vehicles. Recent analyses of U.S. national data provide a clear comparison [27]:

- Hybrid vehicles: about 3,475 fires per 100,000 vehicles sold.
- Gasoline vehicles: about 1,530 fires per 100,000 vehicles sold.
- Electric vehicles: about 25 fires per 100,000 vehicles sold.

The growing integration of LIBs into daily life has brought safety concerns into sharper public focus, particularly as devices become more powerful and energy-dense. News coverage of battery-related fires, especially when they occur in public transportation systems or residential areas, amplifies these fears. In urban settings, the rise of electric micromobility devices - such as e-bikes and e-scooters has led to an uptick in fire-related incidents. According to the New York City Fire Department, LIB fires increased dramatically in recent years, as shown in Figure 1.6, with dozens of fires in 2022 alone resulting in fatalities and major property damage [28, 29, 30]. This has prompted local governments to consider stricter regulations, including bans on uncertified charging equipment and mandates for battery testing standards.

Moreover, consumer anxiety is often exacerbated by a lack of understanding about the underlying causes of battery fires and the relative rarity of such events compared to the total number of batteries in circulation [31]. While statistically infrequent, the severe consequences of LIB fires such as intense heat, toxic gas release, and rapid escalation contribute to a disproportionate perception of risk. Public education campaigns and manufacturer transparency about battery safety measures have been suggested as critical tools to mitigate misinformation and build confidence. Risk communication and proactive engagement with consumers are essential for aligning public perception with actual hazard levels and for fostering informed support of battery-powered technologies [32].

Global reports and articles have shown that LIB fires have largely varying characteristics from petrol-based fires [26]. An outline of the characteristic is provided below along with the recently reported events of such behaviours.

- The battery can re-fire multiple days or weeks after the accident due to slow heat transfer to adjacent modules or cells [33].

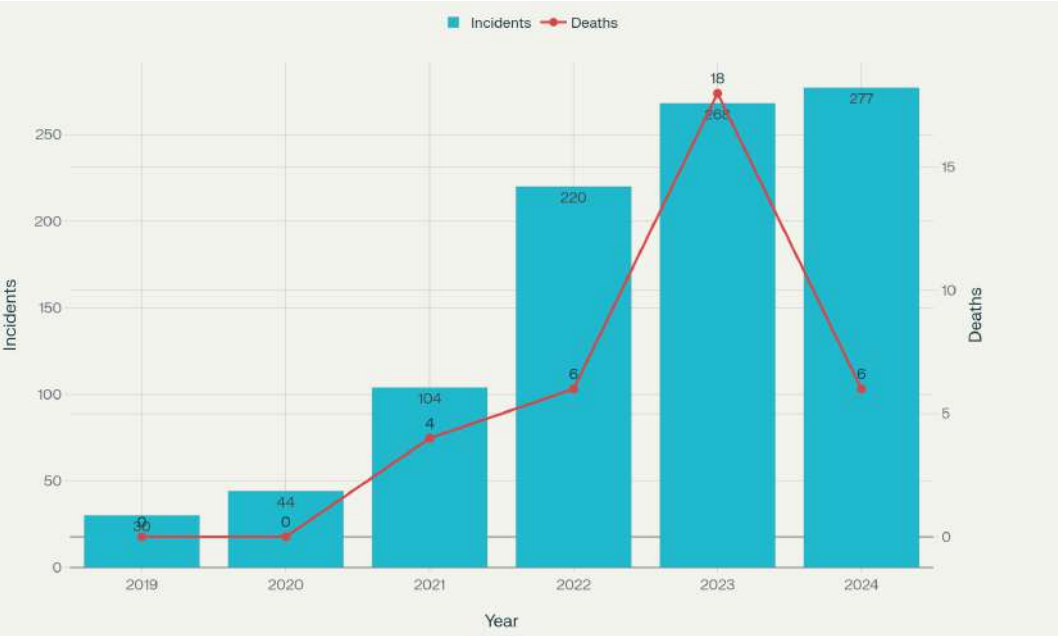

Figure 1.6: New York City Fire Department LIB fire incidents increased track (based on [28, 29]).

- LIB fires produce a range of additional toxic compounds as a result of electrolyte decomposition (e.g., lithium hexafluorophosphate), and these compounds may be released in lethal doses [34], especially in enclosed structures [35, 36].

- Battery fires require enormous amounts of water to cool-down and extinguish as the heat capacity of the cells is substantial and their accessibility is heavily impaired [37, 38].

- Battery fires are easily spread to nearby structures or vehicles due to their intensity - primarily due to jet flames, explosions, and other flaming components being projected at nearby ignitable objects [39].

As such fire resistance and mechanical integrity of EVs have become increasingly significant in the context of emerging legislation and international safety standards. With the proliferation of EVs across global markets, regulatory bodies and standardisation organisations have responded by establishing comprehensive testing frameworks aimed at addressing the unique hazards associated with high-voltage LIB systems [66]. Fire resistance evaluations focus on the behaviour of battery packs under conditions that may lead to TR, which can result from internal faults, mechanical damage, or exposure to external heat sources. Standards such as the United Nations Global Technical Regulation No. 20 (UN GTR No. 20) [67], ISO 6469-1 [68], and IEC 62660 [69] series outline procedures for assessing the ability of battery systems to withstand fire exposure without immediate propagation, thereby ensuring sufficient time for occupant evacuation and emergency response.

In parallel, mechanical testing plays a crucial role in evaluating the structural integrity and resilience of battery systems under various stress conditions, including impact, crush, vibration, and penetration. These tests simulate real-world scenarios such as vehicle collisions, rollovers, and road-induced vibrations, with the objective of preventing catastrophic battery failures. For instance, United Nations Economic Commission for Europ Regulation No. 100 mandates that batteries must maintain their electrical isolation and structural containment following a crash event [70]. In addition, national regulations such as the United States Federal Motor Vehicle Safety Standards (FMVSS) [71] and China's GB/T standards incorporate similar provisions, ensuring consistency in safety performance across jurisdictions [72, 73].

Table 1.1: List of recent incidents involving various LIBs.

Year	County	Object	Comment	Reference
2015	Canada	TTC electric bus	Caught fire; fleet grounded temporarily	[40]
2019	Norway	Electric ferry (MF Ytteroyningen)	Fire suspected from battery compartment	[41]
2021	United States	Tesla Model S Plaid	Spontaneously caught fire in Pennsylvania; driver escaped	[42]
2021	Netherlands	Volkswagen ID.3	Fire during charging at home	[43]
2022	China	Wuling Mini EV	Spontaneous combustion while parked	[44]
2022	France	Bolloré Bluebus	Two Paris buses caught fire; fleet suspended	[45]
2023	China	Li Auto L9	Caught fire while charging	[46]
2023	Netherlands	MV Fremantle Highway	Cargo ship fire; 500 EVs onboard	[47]
2023	United States	Tesla Model S	Crash into tree in Oregon; fatal	[48]
2023	United States	Tesla Model 3	Crash in South Lake Tahoe; 1 infant dead	[49]
2024	United States	Rivian R1T	Came to fire at a repair facility	[50]
2024	United Kingdom	Jaguar I-Pace	Several spontaneous fire reports; NHTSA investigation	[51]
2024	United States	Tesla Model S	Caught fire on I-65; 36,000 gallons to extinguish	[52]
2024	Germany	EV dealership	Electric car dealership burned down in Lauffen am Neckar	[53]
2024	United States	Kia EV9	Caught fire in Chattanooga, damaging vehicles and prompting evacuation	[54]
2024	United States	Tesla (unspecified model)	Caught fire in Charlotte neighborhood	[55]
2024	Canada	Tesla (unspecified model)	Crash and fire in Toronto; 4 fatalities	[56]
2024	United States	Tesla Cybertruck	Crash and fire in Las Vegas; 1 fatality	[57]
2024	United States	Rivian (unspecified model)	Fire at Rivian factory parking lot, vehicle damage	[58]
2024	China	Deepal SL03	Fire incident in mainland China	[59]
2024	China	Xiaomi SU7	Crash into guardrail in Anhui; fire and 3 fatalities	[60]
2024	China	BYD dealership	Fire at BYD dealership in Fuzhou	[61]
2024	China	Electric bicycles	Fire in residential building in Nanjing from e-bikes; 15 dead, 44 injured	[62]
2024	South Korea	Aricell battery factory	Battery explosions at factory in Hwaseong; 23 dead, 8 injured	[63]
2025	Australia	Residential (battery fire)	Lithium-ion battery fire killed 1 in Sydney	[64]
2025	United States	Tesla Cybertruck	Crash and fire in Piedmont, California; 3 fatalities	[65]

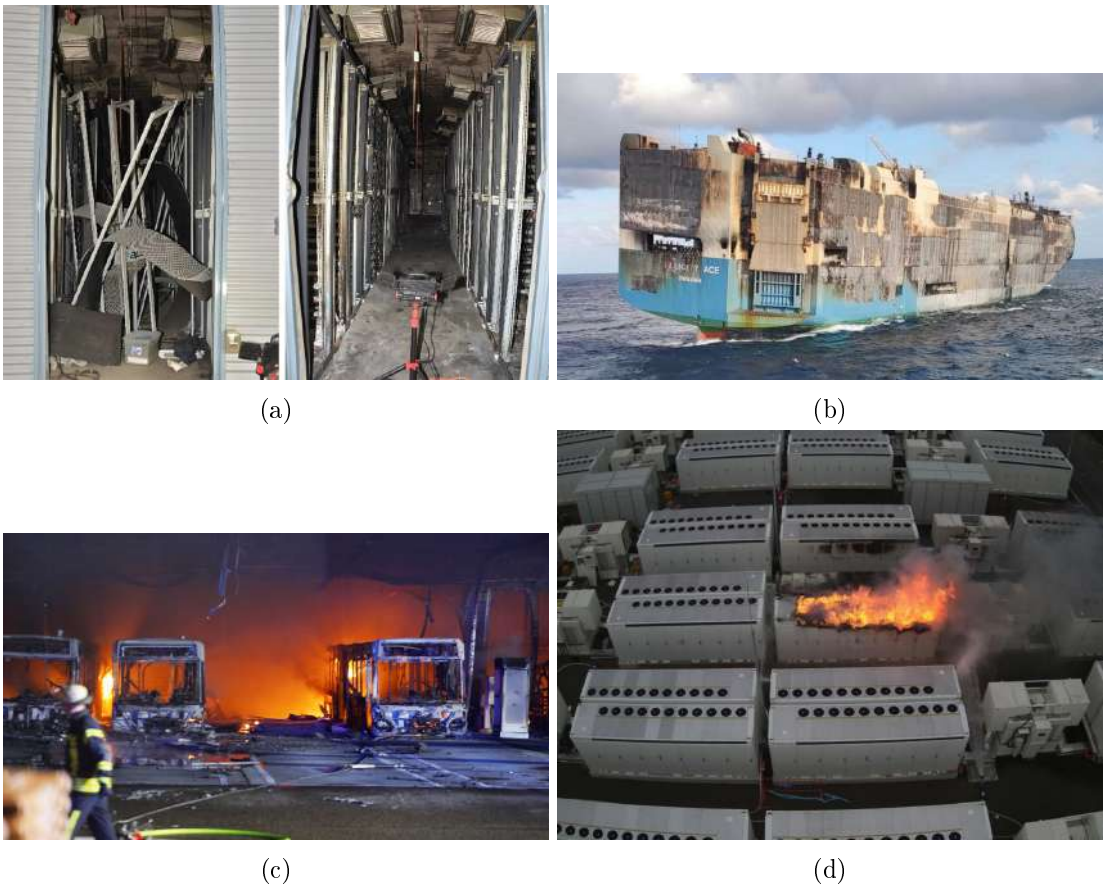

(a) (b)

(c) (d)

Figure 1.7: Selected set of fire incidents involving LIBs. (a) Aftermath inside the APS McMicken battery container; (b) car carrier Felicity Ace ablaze in the Atlantic Ocean; (c) public bus depot fire in Stuttgart, (d) Tesla Megapack unit fire.

The harmonization of these standards reflects a broader commitment to enhancing the safety and reliability of EVs, fostering public trust, and supporting the sustainable transition from internal combustion engines to electrified transport. Manufacturers are thus compelled to integrate advanced materials, thermal insulation techniques, and intelligent battery management systems to meet these stringent requirements. Ongoing research and development efforts continue to explore new methodologies and technologies for improving fire resistance and mechanical robustness, including the use of solid-state batteries, enhanced enclosure designs, and predictive diagnostic systems. As regulatory frameworks evolve, a multidisciplinary approach involving engineering, materials science, and policy will be essential to addressing the complex safety challenges posed by next-generation electric mobility. The importance of the standardisation work and the safety requirements show large losses - economic and human - during the TR of the battery - a few recent events presented in Figure 1.7 such as:

- Figure 1.7a. Aftermath inside the APS McMicken battery container following the April 2019 explosion in Arizona. The TR in one Li-ion cell cascaded through an entire rack, filling the container with flammable gases that later ignited in a deflagration when first responders opened the door. Four firefighters were injured in the blast [74]. Estimated Loss: $10–15 million USD.

- Figure 1.7b. The car carrier Felicity Ace ablaze in the Atlantic Ocean in February 2022. The ship was transporting ˜4,000 vehicles (including hundreds of EVs) when a fire broke out and spread throughout the vessel. LIBs in the EVs on board kept the fire “alight,” requiring specialized firefighting equipment. The crew was evacuated safely, but the ship

ultimately sank after burning for nearly two weeks [75]. Estimated Loss: $400–500 million USD.

- Figure 1.7c. Aftermath of a massive fire on September 30, 2021 at a public bus depot in Stuttgart, Germany. The blaze destroyed 25 buses, including two electric buses suspected of initiating the fire while charging. Over 200 firefighters responded to contain the fire. This incident, among others, prompted several German cities to temporarily suspend electric bus operations pending safety investigations. [76]. Estimated Loss: $10–25 million USD.
- Figure 1.7d. Firefighters battle a blaze in one Tesla Megapack unit at Neoen's Victorian Big Battery project in July 2021. Flames and smoke engulfed the 300 MW/450 MWh battery installation during initial testing, destroying one container and damaging another. More than 30 fire appliances responded, and the fire was contained with no injuries reported [77]. Estimated Loss: $30–40 million USD.

1.1 Motivation and Background of the Thesis

LIBs have become ubiquitous in EVs and energy storage systems (ESS), especially being part of alternative energy sources, but their safety remains a critical concern. A central issue is the risk of TR - a self-accelerating chain reaction within a battery that can lead to fires or explosions. TR is widely recognized as the primary failure mechanism in LIBs and is highly complex, being influenced by both external conditions and internal cell chemistry. Recent high-profile battery fire incidents have underscored the severity of this problem and the need for deeper understanding of TR mechanisms and following fallout in form of thermal and mechanical damage. Despite extensive research into TR triggers and behaviour at the materials level, a comprehensive understanding of whole-battery TR dynamics in context to standardisation and testing methodology remains elusive. This knowledge gap in LIB safety motivates the research performed in the project frame "Doktorat Wdrożeniowy" carried out in Laboratorium Badań Ogniowych Centrum Techniki Okrętowej S.A. in conjuction with Instytut Maszyn Przepływowych im. R. Szewalskiego Polskiej Akademii Nauk. The results of this research and cooperation is the present thesis.

Ensuring the fire safety of LIB systems requires reliable testing methods to simulate worst-case scenarios (such as vehicle crashes followed by fires) and to evaluate how batteries and protective structures behave under such stress. In practice, regulatory and industry standards mandate abuse tests to certify that battery systems are fire resistant and mechanically intact. Battery systems are put into RESS, which are primary object of this study. **In the European context, UNECE Regulation No. 100 Revision 3 (R100.03) is the definitive standard for EV battery safety testing, due to the fact it is obligatory to be followed before the RESS is introduced into market**. The intent of tests included in the standard is to ensure that in a post-crash fuel fire, the battery will not explode or endanger occupants, allowing time for escape. Due to the obligatory status of R100.03 test procedures, it is studied in present thesis in order to assess its repeatability, precision, practicality and other qualities, which good testing methodology should contain. Simultaneously, LIB testing and standardisation is a global issue, therefore such context is provided.

The standardisation shortcomings were also noted by the customers of Laboratorium Badań Ogniowych Centrum Techniki Okrętowej S.A., which prompted the multiple tripartite cooperation and allowed test data to be published in this thesis. All of the test presented in given thesis were performed on real-life samples to be later introduced into market applications and day-to-day use in EV, stationary ESS or railway auxiliary ESS.

In sum, the research undertaken in this dissertation is not limited to theoretical inquiry but is a practical knowledge oriented towards the improvement of testing practice and regulatory frameworks. By critically evaluating existing procedures and proposing a more precise and repeatable methodology, the project contributes to the development of safer and more reliable battery systems. The anticipated outcomes extend beyond the academic sphere: they provide a foundation for refining standards such as UNECE R100.03 and for informing international harmonisation efforts, thereby enhancing the credibility and reproducibility of safety assessments across laboratories. In a broader societal perspective, this work supports the secure deployment of electric vehicles and stationary energy storage systems, which are indispensable for the sustainable energy transition. Ultimately, the project outcomes - carried out by the cooperation of Institute of Fluid Flow Machinery, Polish Academy of Sciences and Laboratorium Badań Ogniowych Centrum Techniki Okrętowej S.A. - will be reflected in safer testing protocols, more robust engineering solutions, and a tangible reduction in the risks posed by LIBs, advancing both public safety and the trust in technologies that underpin a low-carbon future.

1.2 Outline of the Thesis

The thesis is organized into 8 chapters and 5 appendices. Below, each core chapter of the dissertation is mapped to its role in fulfilling the thesis objectives:

- **Definitions and Acronyms**. It contains the definitions and acronyms used in the dissertation.
- **Chapter 1: Introduction**. The thesis begins with an introduction that frames the scientific problem. This chapter establishes why the research background, surveying the safety challenges posed by TR and the inadequacies of current test methods. It sets the stage by articulating the gap in knowledge and practice that the thesis intends to fill - the need for a more quantitative and repeatable fire testing methodology for battery systems.
- **Chapter 2: Safety Analysis of Lithium-ion Batteries**. The purpose of Chapter 2 is to provide a detailed technical foundation on LIB operation and failure modes, with a focus on the conditions leading to TR and fire. Chapter 2 serves as a knowledge base - it presents the understanding of LIB failure mechanisms, and it reveals the variables that a robust test method should consider.
- **Chapter 3: Thermal Safety Systems in Lithium-ion Batteries**. Chapter 3 reviews what can be done to prevent or mitigate failures in LIBs. Its role is to survey existing safety strategies and designs used in LIB systems, thereby addressing the objective of understanding the current state-of-the-art in TR prevention. The chapter is divided into passive safety systems and active mitigation strategies. Chapter 3 contributes to the thesis by translating the battery failure mechanisms (from the previous chapter) into engineering solutions and requirements, thereby informing the design of the experimental campaign and the interpretation of results later in the thesis.
- **Chapter 4: Aim of the Thesis**. Chapter contains the aim and formal thesis of the dissertation.
- **Chapter 5: Standardization of Battery Energy Storage System Testing**. The goal is to situate the thesis within the regulatory and standardization context. It provides a comprehensive comparison of existing test standards and regulations for LIB safety globally, thereby addressing the objective of integrating with industry standards and identifying their weaknesses. Importantly, this chapter zooms in on the fire resistance test procedures in automotive standards versus analogous tests in other industries. It shows that improving test repeatability and data quality is not just academically interesting but practically urgent to improve safety standards.
- **Chapter 6: Battery Fire Resistance Testing Methodology**. This chapter is where the novel methodology is presented and validated. It is structured into several parts that together develop the new testing approach. First examines the fundamental fire dynamics and heat transfer aspects relevant to battery fires and fire-resistance tests. Here, theoretical background is given on fire plume behaviour and heat flux in large hydrocarbon fires versus controlled furnaces, and how to model the thermal exposure appropriately. This sets up the basis for fair comparison between an open-fire test and a furnace test. Then presents a numerical analysis of fire test conditions for LIB enclosures, with focusing on the UNECE R100.03 fire test parameters and discussing similar tests. Chapter closes with a discussion and recommendations, examining the implications of these findings and outlining how battery fire testing standards could evolve.
- **Chapter 7: Development of Thermal Runaway Emissions Aftertreatment System (TREAS)**. In this final content chapter, the thesis extends its scope to a related

practical challenge: managing the toxic and flammable emissions produced during TR tests. Its inclusion reflects the emerging environmental and safety regulations that restrict releasing untreated gases from battery tests into the atmosphere. The aim here is to design and validate a laboratory-grade aftertreatment system that can be used in conjunction with TR experiments to scrub harmful effluents and to improve experimental conditions.

- **Chapter 8: Summary and Conclusions of the Thesis**. The summary, conclusion, and future works required for further development of this thesis are discussed thoroughly in the given Chapter.
- **Appendix A: Overview of the Materials used in Lithium-ion Batteries.** It presents cathode families, anodes, electrolytes, and separators. Provides comparative notes on energy density versus inherent safety trade-offs and implications for external-fire performance. Serves as materials background for interpreting fire-test outcomes.
- **Appendix B: Review of the Prevention Systems and Solutions to Battery Fires.** It compiles passive and active strategies across cell, module, and pack levels: BMS functions, air/liquid/PCM and hybrid thermal management, propagation barriers, vents, fuses, and suppression.
- **Appendix C: Additional datasets**. This appendix contains additional data and graphs from the carried out experimental tests.
- **Appendix D: Background for TREAS development**. It characterizes TR emissions and their health or environmental hazards, especially in confined spaces. Reviews gas cleaning approaches - particulate filtration, alkaline scrubbing, adsorption/catalysis—and their efficiencies and limitations.
- **Appendix E: List of Standards and Regulations Referenced in the Thesis**. It contains list of standards and regulations that are subjected to analysis and evaluation in the given thesis.

Chapter 2

Safety Analysis of Lithium-ion Batteries

A lithium-ion battery is an electrochemical energy storage device composed of four essential components: the anode, the cathode, the electrolyte, and the separator. The anode, most commonly graphite, serves as the host material for lithium ions during charging, providing high reversibility and stability. The cathode is typically a transition-metal oxide, such as $LiCoO_2$, $LiFePO_4$, or Ni-rich layered oxides, which functions as the source and sink for lithium ions during cycling. Between these electrodes lies the electrolyte, usually a lithium salt (e.g., $LiPF_6$) dissolved in organic carbonate solvents, which enables ionic conduction while remaining electronically insulating. The separator, a porous polyolefin membrane (often polyethylene or polypropylene), physically isolates the anode and cathode to prevent electrical short-circuits, while allowing ionic transport through its micropores.

A critical feature of lithium-ion cells is the solid electrolyte interphase (SEI), a passivation layer that forms spontaneously on the anode surface during the first charge due to electrolyte decomposition. The SEI is electronically insulating but ionically conductive, which stabilizes the electrode–electrolyte interface by preventing continuous electrolyte breakdown while allowing lithium-ion transport. Its stability is crucial for battery longevity and safety, as degradation of the SEI can lead to increased impedance, gas evolution, or dendrite formation. Together, the coordinated roles of anode, cathode, electrolyte, separator, and SEI enable reversible lithium-ion intercalation and deintercalation, high energy density, and long cycle life, while also dictating the thermal and electrochemical safety characteristics of the cell. Schematics of the LIB are shown in Figure 2.1.

The mechanics of LIBs are inherently multi-physical: they couple electrochemical kinetics, ionic diffusion, phase transitions in electrode materials, Joule heating, and mechanical deformation arising from volume changes during lithiation and delithiation. These interdependent phenomena dictate not only the battery's performance and lifetime but also its structural and thermal stability, which are critical for safety under both nominal and abusive operating conditions. A central hazard associated with LIBs is the phenomenon of TR - a self-sustaining, exothermic cascade initiated when the rate of heat generation from internal reactions surpasses the system's ability to dissipate that heat. The process typically begins with the decomposition of the SEI layer, followed by volatile gas release, separator melting, internal short circuits (ISC), and finally the exothermic breakdown of the cathode material, often accompanied by oxygen evolution. TR dynamics are highly sensitive to factors such as state of charge (SOC), cell geometry, and the thermal characteristics of the materials involved, necessitating a mechanistic understanding for effective mitigation.

Beyond intrinsic failure modes, LIB safety is also challenged by extrinsic abuse scenarios, broadly categorized as mechanical, thermal, and electrical. Mechanical abuse - such as impact, crushing, or penetration - can compromise separator integrity and initiate internal short circuits.

Thermal abuse involves exposure to elevated ambient temperatures or flame, which can accelerate decomposition reactions. Electrical abuse includes overcharging, overdischarging, and external short-circuiting, often resulting in lithium plating or electrolyte breakdown. Each abuse type activates distinct degradation pathways and may act synergistically with others, emphasizing the need for holistic safety assessment frameworks that integrate materials science, thermal analysis, and structural mechanics.

2.1 Operating Principles of the Lithium-ion Battery

Lithium-ion cells operate on the principle of reversible electrochemical reactions involving the migration of lithium ions (Li^+) and electrons between two electrodes (anode and cathode) – separated by an electrolyte. This migration is induced by differences in electrochemical potential, which establish a cell voltage that drives electric current through an external circuit during discharge. When the cell is discharging, lithium ions deintercalate from the anode, traverse the electrolyte, and intercalate into the cathode, while the electrons follow a parallel path through the external load. Upon charging, the process is reversed, and an external energy source drives the lithium ions back to the anode. Scheme of LIB design is shown in Figure 2.1. The reversibility and efficiency of these redox reactions are the foundation of rechargeable energy storage. However, the dynamics of these reactions are not purely electrochemical; they are coupled with thermal effects that influence performance, degradation, and safety of LIB [78].

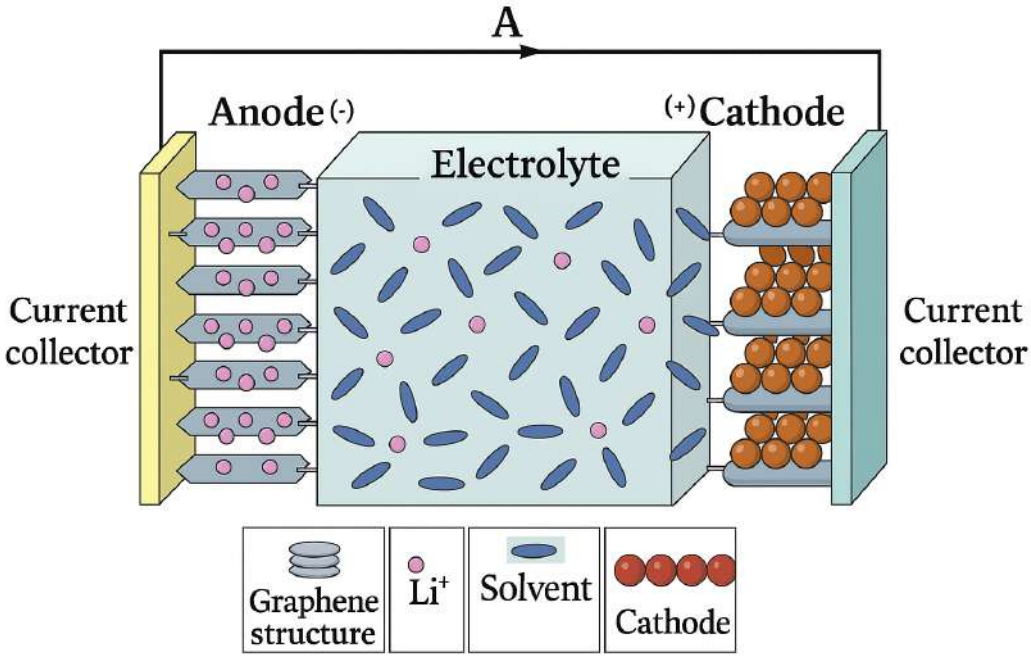

Figure 2.1: Schematic of the LIB design.

The anode in conventional lithium-ion cells is typically composed of graphite - as shown in Figure 2.1 - a layered carbon material with sufficient interlayer spacing to accommodate lithium ions during intercalation. This host-guest system is highly reversible under ideal conditions, but it experiences minor volumetric expansion during lithiation, which can lead to mechanical stress over multiple cycles. The cathode is usually a transition metal oxide with a crystalline lattice capable of reversible lithium ion uptake and release. Cathode examples include lithium cobalt oxide ($LiCoO_2$), lithium iron phosphate ($LiFePO_4$), and more recently, nickel-rich mixed metal oxides such as $LiNi_{0.8}Mn_{0.1}Co_{0.1}O_2$ (known as NMC811) [79, 80]. These cathode materials are

characterized by their structural stability, voltage profile, and thermal behaviour. Importantly, both the intercalation mechanisms and the phase transitions that occur in these materials during cycling generate or absorb heat, depending on the electrochemical state. The amount and rate of heat generated are influenced by current density, SOC, material composition, and crystallographic defects [81].

The electrolyte in a LIB is a complex solution typically composed of a lithium salt such as $LiPF_6$ dissolved in a mixture of organic carbonate solvents, including ethylene carbonate (EC) and dimethyl carbonate (DMC) [82]. The electrolyte facilitates ionic conductivity but is electrically insulating, ensuring that only lithium ions - not electrons - pass through the separator. At the same time, the separator, often made of polyolefin (e.g., polyethylene or polypropylene), acts as a mechanical barrier to prevent short circuits while allowing ionic transport [83]. Electrolytes and separators are thermally sensitive components. The organic solvents are volatile and flammable, and their decomposition at elevated temperatures can lead to the evolution of gaseous products, increasing internal pressure. If the temperature exceeds a critical threshold - typically between 120 °C and 200 °C thermal breakdown of the separator or exothermic reactions between the electrolyte and electrodes can trigger a catastrophic sequence known as TR [84].

The redox reactions during charge and discharge involve more than just electron transfer - they are coupled with entropic and enthalpic changes that influence cell temperature. For instance, the anodic reaction during discharge:

$$\mathrm{LiC_6} \longrightarrow \mathrm{C_6} + \mathrm{Li^+} + \mathrm{e^-}$$

releases heat due to the exothermic nature of lithium deintercalation. Simultaneously, the cathodic reaction:

$$\mathrm{Li_1 - xCoO_2} + x\,\mathrm{Li^+} + x\,\mathrm{e^-} \longrightarrow \mathrm{LiCoO_2}$$

also contributes to heat generation or absorption, depending on the extent of lithiation and the phase transitions occurring within the lattice. The thermal behaviour of these reactions is governed by the Peltier effect (related to entropy changes), Joule heating ($Q = I^2R$ losses, where I is current squared and R is the resistance of the conductor), and side reactions, such as SEI formation or electrolyte decomposition [85]. The SEI primarily consists of lithium ethylene dicarbonate, lithium carbonate (Li_2CO_3), and various organic lithium compounds that provide electrochemical stability under normal operating conditions. Particularly during fast charging or deep discharge, the rate of heat accumulation can surpass the rate of heat dissipation, resulting in temperature gradients within the cell and localized hot spots [86]. These thermal imbalances may lead to uneven ageing of the cell or initiate self-accelerating decomposition reactions, especially if defects or impurities are present in the electrodes. Further analysis on LIB materials used in cells are presented in Table 2.1 and Appendix A.

There are three levels LIB systems are regarded as - cell level, module or pack/system. Schematic representation is found in Figure 2.2:

- At the cell level, the unit of analysis is the individual electrochemical cell - the smallest energy-storing element in a LIB system. Each cell contains the complete electrochemical architecture required for charge and discharge: an anode, a cathode, a separator, electrolyte, current collectors, and an outer casing. Cells are manufactured in specific form factors (cylindrical, prismatic, pouch; see Figure 2.3) and are designed to operate as discrete, sealed entities. Structurally, a cell is optimized for electrochemical performance, thermal stability, and mechanical integrity at the smallest scale. In the hierarchy of battery integration, it represents the foundation upon which higher-level assemblies are built, with its performance and safety characteristics directly influencing the behaviour of larger assemblies.

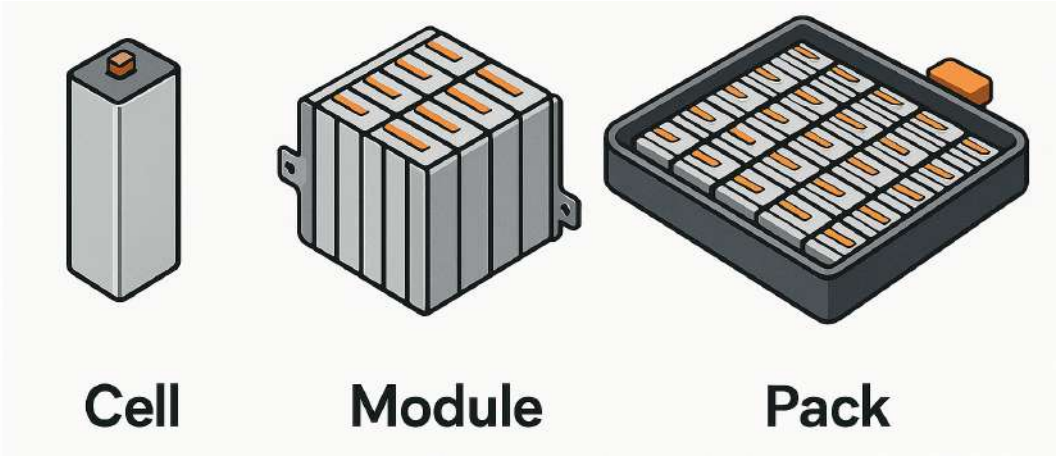

Figure 2.2: Comparison on LIB system level - cell, module or pack.

- At the module level, multiple cells are mechanically grouped and electrically connected in series, parallel, or mixed configurations to achieve desired voltage and capacity targets. Modules often incorporate structural frames, thermal interface materials, electrical busbars, and monitoring hardware (temperature and voltage sensors) to manage cell operation collectively. The design of a module must ensure uniform thermal distribution, mechanical stability under vibration or shock, and safe electrical connectivity between cells. Structurally, the module is an intermediate subsystem - it bridges the gap between the raw energy-storing cells and the complete battery system - and serves as the first structural layer where containment and thermal management of multiple cells are considered together.
- At the pack or system level, several modules are integrated into a complete energy storage unit with all necessary support systems for operational safety, performance, and integration into the target application (e.g., an EV or stationary ESS). The pack incorporates the battery management system (BMS), comprehensive thermal management systems (e.g., air, liquid, phase change material - PCM), protective housings, high-voltage connectors, fuses, contactors, and often fire suppression or venting arrangements. Structurally, the pack/system level addresses the highest-order requirements: mechanical robustness against environmental and crash loads, large-scale thermal control, electrical isolation, and compliance with regulatory standards. The primary difference from the module level is scope and integration - the pack is a fully functional, stand-alone system ready for deployment, whereas modules and cells are subcomponents within this architecture.

Lithium-ion cells are manufactured in three principal geometries: cylindrical, prismatic, and pouch - as shown in Figure 2.3. Each type presents distinctive structural, thermal, and practical characteristics:

- Cylindrical cells (e.g., 18650, 21700) use a wound "jelly roll" electrode structure housed in a rigid metal can. Their cylindrical casing provides high mechanical robustness and consistent thermal performance. They are mass-produced at relatively low cost with good reliability and safety features (venting mechanisms, current interrupt devices). However, the round shape limits packing efficiency in modules and packs, resulting in unused volume.
- Prismatic cells employ a stacked or rolled electrode assembly encased in a rectangular, often rigid aluminum housing. Their main advantage lies in efficient space utilization, enabling high volumetric energy density at the module or pack level. They are well suited for automotive and stationary applications where compact design is important. Nevertheless, their rigid design makes thermal management more challenging, and mechanical swelling during cycling can induce internal stresses.

Table 2.1: Overview of selected LIB cell configurations, detailing variations in anode and cathode materials, electrolyte compositions, separator types, and cell formats, based on [87, 88, 89, 90, 91, 92, 93].

Case	Anode	Cathode	Electrolyte	Separator	Format
1	Graphite	NCM	N/A[1]	PE-based with ceramic coating	25 Ah prismatic with two pouch cells connected in parallel
2	Graphite	$LiyNi_{frac1/3}Co_{frac1/3}Mn_{frac1/3}O_2$ (NCM) + $LiyMn_2O_4$ (LMO)	N/A	N/A	40 Ah with two parallel pouch cells
3	Graphite	NCM	N/A	PE with ceramic coating	25 Ah
4	MCMB	LFP	N/A	PP	20 Ah
5	Graphite	Single crystal NCM532 (SC-NMC532)	1-M $LiPF_6$ in EC/DMC/EMC (1:1:1 in volume)	PET /ceramic non-woven	25 Ah large-format pouch
6	Graphite	$LiNi_{0.4}Co_{0.4}Mn_{0.2}O_2$ (NCM442)	N/A	PE with ceramic coating	25 Ah commercial large format with two pouch cells in parallel
7	MCMB	LFP	N/A	PP with ceramic coating	20 Ah commercial large format with two cells in parallel
8	Synthetic graphite MAG10	NCM111 + LMO (1:1)	N/A	PE	20 Ah commercial large format with two cells in parallel
9	LTO	LCO	N/A	PE with ceramic coating	3 Ah commercial large format with two cells in parallel
10	Graphite	NCM111	1-M $LiPF_6$ in EC/DMC/EMC (1:1:1 in volume)	N/A	24 Ah
11	Graphite	NCA	1-M $LiPF_6$ in EC/DMC (1:1 by weight)	Polyolefin with ceramic coating	3.3 Ah
12	Graphite	LFP	1-M $LiPF_6$ in EC/DMC (1:1 by weight)	Polyolefin	1.1 Ah
13	LTO	NCA	1-M $LiPF_6$ in EC/DMC (1:1 by weight)	Ceramic-polymer composite	16 Ah
14	MAG10	NCM111 + LMO (1:1 by mass)	$LiPF_6$ in DMC/EMC/EC (1:1:1)	PE with ceramic coating	20 Ah pouch
15	Graphite	NCM442	$LiPF_6$ in DMC/EMC/EC (1:1:1)	PE with ceramic coating	25 Ah prismatic
16	Graphite	LCO	1-M $LiPF_6$ in EC/DEC (1:1 by weight)	N/A	950 mAh commercial soft-pack
17	MAG10	NCM111 + LMO (1:1)	1-M $LiPF_6$ in EC/DMC/DEC (1:1:1)	N/A	20 Ah pouch
18	MCMB	LFP	No info found on this	N/A	20 Ah prismatic
19	Graphite	NMC811	Concentrated Lithium bis(fluorosulfonyl)imide ($LiFSI$)/ DMC (1:1.9 by molar)	PE with ceramic coating	0.95 Ah pouch
20	Graphite	NMC532	$LiFSI$/(DMC) (1:1.9 by molar)	PE with ceramic coating	1.2 Ah pouch
21	Graphite	NMC811	$LiFSI$/trimethyl phosphate	PE with ceramic coating	0.95 Ah pouch
22	Graphite	NMC811	1-M $LiPF_6$/EC/EMC (3:7 by volume)	PE with ceramic coating	0.95 Ah pouch
23	Graphite	NMC532	1-M $LiPF_6$/ EC/EMC (3:7 by volume)	PE with ceramic coating	1.2 Ah pouch
24	Graphite	NCM111	N/A	N/A	94 Ah commercial
25	Graphite	NCM111	1-M $LiPF_6$ in EC/EMC/DMC (1:1:1 by volume)	PE-based with ceramic coating	24 Ah pouch with two cells connected in parallel
26	Graphite	NCM	N/A	PE	21 Ah
27	Graphite	NCM	1-M $LiPF_6$ in EC/PC/DEC (1:1:1 in volume)	PE-based with ceramic coating	3.3 Ah
28	Graphite	NCM811	1-M $LiPF_6$ in EC/DMC (3:7 in volume)	PE with ceramic coating	1 Ah pouch
29	Graphite	NCM523	0.6-M $LiTFSI$+ 0.4-M $LiDFOB$ in EC/PC/EMC (1:1:3 by volume)	Polyolefin	5 Ah pouch

[1] N/A - data not available.

- Pouch cells use a laminated, flexible foil package without a rigid enclosure. This format allows the thinnest and most adaptable form factors, leading to excellent volumetric and gravimetric energy density. Pouch cells can be stacked densely, maximizing energy in constrained spaces. However, their mechanical robustness is lower compared to cylindrical and prismatic cells, making them more vulnerable to external pressure, puncture, and swelling. They also require additional module-level structures for mechanical support and protection.

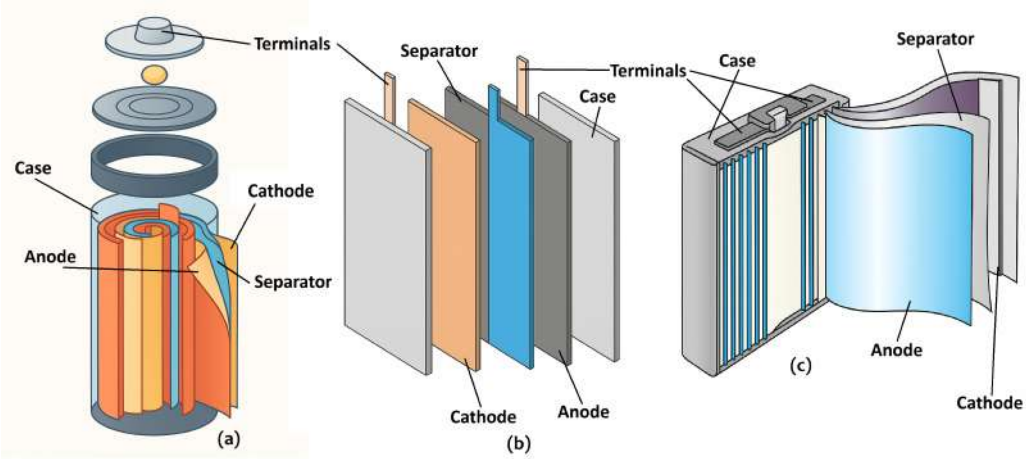

Figure 2.3: Comparison of the cell types: (a) cylindrical, (b) pouch and (c) prismatic.

Safety concerns in LIBs are inextricably linked to thermal phenomena. As the cell heats up - either from external conditions, abusive operation (e.g., overcharging), or internal defects (e.g., dendrite formation) - several degradation pathways become a possibility. The SEI layer on the anode, which initially forms as a protective film, can break down and reform continuously, consuming lithium and electrolyte in the process, leading to capacity fade and impedance growth together with heat generation. At elevated temperatures, the SEI may undergo exothermic decomposition, further increasing cell temperature. Likewise, the cathode may release oxygen when overcharged or overheated, which reacts violently with flammable electrolyte components. In parallel, the separator can shrink or melt, causing ISCs. These combined effects can culminate in TR, where the heat generated by exothermic reactions further accelerates decomposition, leading to cell venting, fire, or explosion. Once TR begins, it is self-sustaining and very difficult to interrupt, often spreading to adjacent cells in multi-cell battery packs (a phenomenon known as thermal propagation) [87, 94].

Thermal management is thus a critical design consideration in LIB systems. Passive systems include heat-dissipating materials, optimized cell geometry and thermal interface materials, while active approaches involve forced air or liquid cooling systems, PCMs, and integrated thermal sensors for real-time monitoring. BMS play a vital role in monitoring temperature, voltage, and current to prevent conditions that could lead to thermal instability. BMS involves systems that regulate battery temperature to ensure safety, maximize performance, and prolong lifespan by using active (e.g., liquid cooling, fans) or passive (e.g., heat sinks) methods to either dissipate excess heat or provide warmth in cold conditions. Research in battery safety focuses increasingly on electrolyte formulations with higher thermal stability, non-flammable solvents, ceramic or shutdown separators, and cathode materials that are less prone to oxygen release [95]. From a system-level perspective, the challenge lies in balancing energy density and safety - a higher energy density often correlates with increased reactivity and thermal sensitivity.

In conclusion, while the operation of lithium-ion cells is fundamentally electrochemical, the associated thermal effects are of paramount importance to performance, longevity, and - most

critically - safety. Heat generation accompanies every aspect of cell operation, from ionic transport and interfacial reactions to structural phase changes and material degradation. If not effectively managed, thermal effects can compromise not only the functionality of the battery, but also pose serious risks to users and the surrounding environment. Understanding and controlling these thermal processes is therefore essential in the design of next-generation lithium-ion technologies and in ensuring their safe integration into complex application.

2.2 Thermal Runaway Mechanics Analysis

TR represents one of the most critical safety concerns in LIB systems, fundamentally limiting their widespread deployment in high-energy applications. This phenomenon manifests as a cascading series of exothermic chemical reactions that lead to uncontrolled temperature escalation, ultimately resulting in fire, explosion, or toxic gas emission. The complexity of TR stems from the intricate interplay between multiple thermodynamic systems within the battery cell, each contributing heat generation through distinct pathways and temperature regimes. Understanding the step-by-step mechanisms underlying TR is essential for developing effective safety strategies and mitigation technologies in battery system design [96, 97, 98]. TR initiation cause can vary largely and most of the known causes were shown in Figure 2.4.

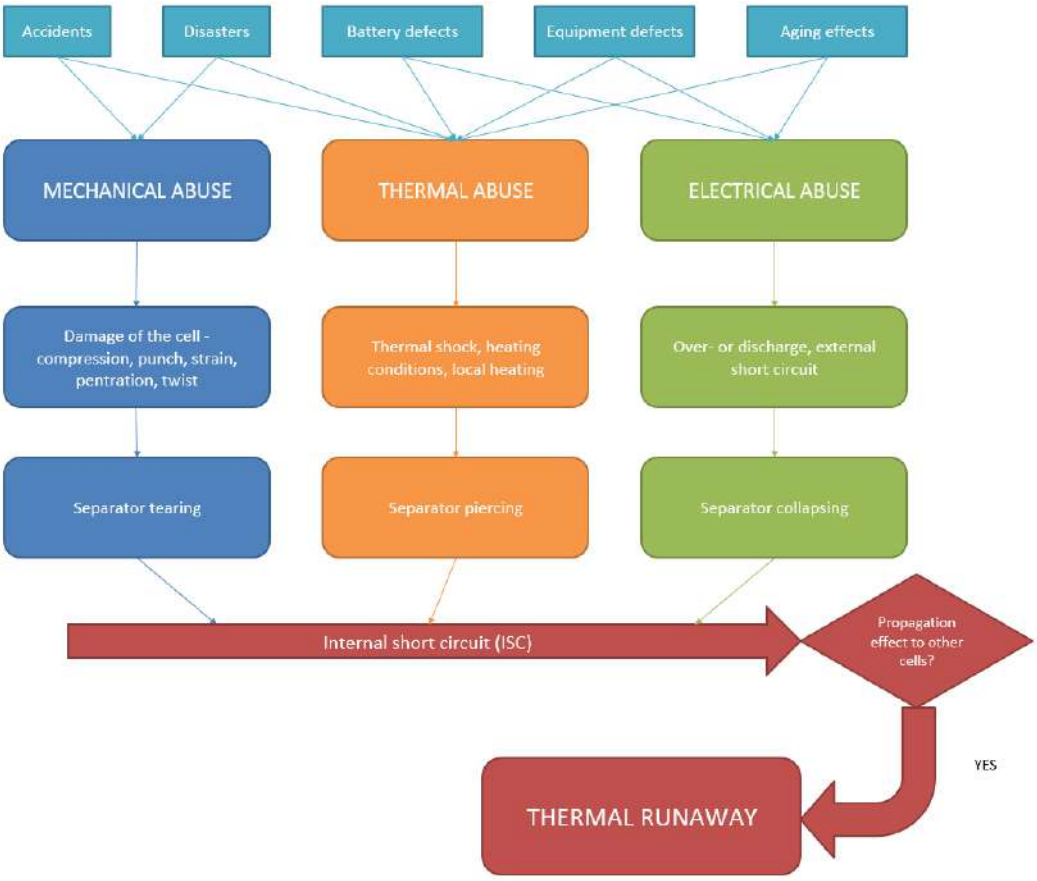

Figure 2.4: Schematic chart of TR initiation.

The essence of TR can be conceptualized through the Heat-Temperature-Reaction (HTR) loop, where exothermic reactions generate heat that elevates temperature, which in turn accelerates reaction rates, creating a positive feedback mechanism that becomes self-sustaining once critical thresholds are exceeded. This phenomenon is characterized by three distinct temperature markers: T_1 (onset of self-heating), T_2 (TR trigger temperature), and T_3 (maximum

temperature), which serve as fundamental parameters for safety assessment and thermal stability evaluation [99, 100].

- T_1 represents the onset temperature for self-heating, typically occurring when the temperature rise rate exceeds 0.004°C/s, marking the initiation of significant exothermic side reactions within the cell. This temperature commonly ranges between 78–105°C for various lithium-ion chemistries, with variations dependent on cell composition and state of charge [97].

- T_2 constitutes the TR trigger temperature, defined as the critical threshold where the temperature rise rate reaches 1°C/s, indicating that the HTR loop has become uncontrollable. This parameter varies significantly across different battery systems, ranging from approximately 130°C to 270°C depending on cell chemistry, separator design, and internal resistance characteristics. T_2 represents the point at which rapid oxidation-reduction reactions between cathode and anode materials are triggered, leading to massive heat generation [101].

- T_3 denotes the maximum temperature attained during TR, typically reaching 600–900°C in severe cases, representing the total energy release potential of the system. The temperature differential $\Delta T = T_3 - T_2$ directly correlates with the total heat generation during TR (ΔH_{TR}) according to the relationship:

$$\Delta H_{TR} = M \times C \times \Delta T \tag{2.1}$$

  where M represents cell mass, C denotes heat capacity and ΔT denotes temperature difference [97]. TR phenomenon can be divided into 5 selective stages, shown also schematically in Figure 2.5.

Stage 1: Solid Electrolyte Interphase Decomposition (80–150 °C)

The initial phase of TR involves the thermal decomposition of the solid electrolyte interphase layer, a critical component formed on the anode surface during initial battery cycling. The decomposition of this metastable SEI layer typically initiates between 80–120 °C, with the majority of reactions occurring in the 100–150 °C range [102, 103].

The thermal decomposition of lithium ethylene dicarbonate, the predominant SEI component, proceeds through a three-stage mechanism, which starts at low temperatures. In the initial stage, LEDC decomposes to evolve CO_2 and C_2H_4 gases while generating lithium propionate ($CH_3CH_2CO_2Li$) and Li_2CO_3 as solid residues:

$$\text{LEDC} \longrightarrow \text{CH}_3\text{CH}_2\text{CO}_2\text{Li} + \text{Li}_2\text{CO}_3 + \text{CO}_2 + \text{C}_2\text{H}_4 \tag{2.2}$$

The heat generated during SEI decomposition, while relatively modest compared to subsequent reactions, serves as the critical initiating factor that elevates cell temperature toward the next stage. The exothermic nature of SEI breakdown creates localized heating that compromises the structural integrity of other battery components, particularly affecting electrolyte stability and separator mechanical properties [104].

Concurrent with SEI decomposition, the anode undergoes additional exothermic reactions with the electrolyte, particularly involving lithiated graphite and organic solvents. These reactions generate additional heat while producing gaseous byproducts including hydrogen, carbon monoxide, and various hydrocarbons. The cumulative effect of Stage 1 reactions establishes the thermal foundation for subsequent escalation phases [105].

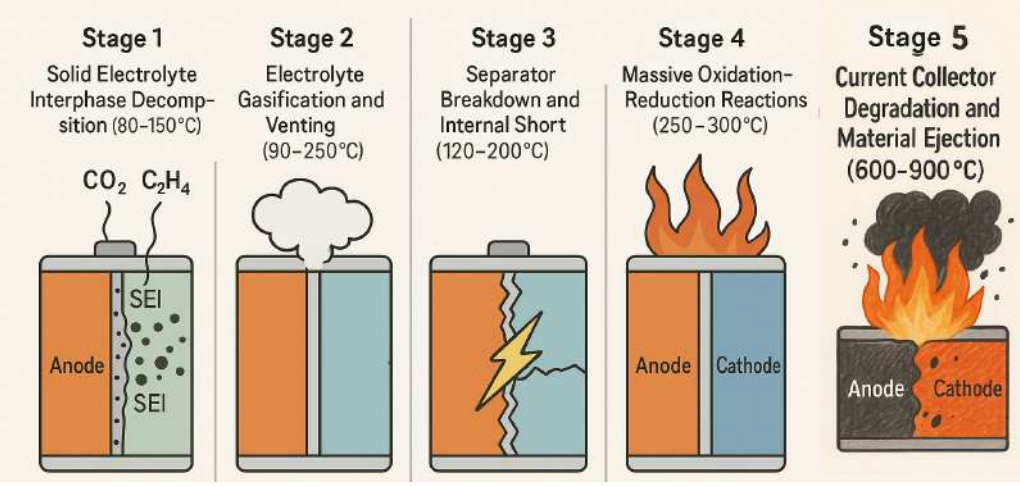

Figure 2.5: Stages of the TR.

Stage 2: Electrolyte Gasification and Venting (90–250 °C)

As cell temperature continues rising beyond 90°C, the electrolyte system undergoes systematic gasification based on the boiling points of constituent solvents. Commercial lithium-ion electrolytes typically contain ternary solvent mixtures including dimethyl carbonate (DMC, boiling point 91 °C), ethyl methyl carbonate (EMC, boiling point 110 °C), and ethylene carbonate (EC, boiling point 248°C) [106].

The gasification process occurs in distinct phases corresponding to solvent volatility. Initially, when cell temperature reaches 100–110°C, DMC and EMC vaporize rapidly, creating internal pressure buildup that leads to the first venting event characterized by white-gray smoke emission. This venting represents a critical transition point where mass transfer from the internal cell environment to the external environment begins, fundamentally altering the thermodynamic balance within the system [107].

The second gasification phase occurs around 250°C when EC vaporizes, accompanied by additional organic gases generated through side reactions with electrode materials. This stage typically coincides with more intense pressure build-up and aggressive venting behaviour, often accompanied by the release of toxic compounds including hydrogen fluoride and carbon monoxide [108].

The venting process serves a dual role in TR progression. While it provides pressure relief that can temporarily slow temperature escalation, it also removes electrolyte necessary for maintaining separator integrity and electrochemical stability. The mass loss during venting can range from 10–70% of the original electrolyte inventory, fundamentally altering the internal chemical environment and accelerating subsequent degradation mechanisms [106].

Stage 3: Separator Breakdown and Internal Short Circuit (120–200 °C)

Separator failure represents a critical transition point in TR progression, fundamentally altering the internal cell architecture and enabling direct contact between cathode and anode materials. Commercial separators typically employ polyethylene (PE) and polypropylene (PP) based materials with distinctly different melting characteristics [109].

PE-based separators exhibit melting initiation around 135°C, while PP materials melt at approximately 170°C. Modern ceramic-coated separators demonstrate improved thermal stability, maintaining structural integrity up to 200–260°C under compression conditions [110].

Separator melting initiates pore closure, initially providing a shutdown mechanism that can halt ion transport and theoretically prevent further electrochemical reactions. However, continued temperature elevation leads to separator shrinkage and eventual structural collapse, creating

direct pathways for contact between active materials.

The collapse of separator integrity enables ISCs, creating low-resistance pathways for current flow between electrodes. The heat generation rate during ISC can be estimated using:

$$Q_{ISC} = \frac{U^2 \cdot \eta}{R_{ISC}} \tag{2.3}$$

where U represents cell voltage, η denotes electrical-thermal conversion efficiency, and R_{ISC} represents the equivalent short circuit resistance. When R_{ISC} approaches very low values, instantaneous heat generation can reach extremely high rates, sufficient to melt current collectors and create localized temperature differences exceeding 1000 °C [111].

The occurrence of ISC typically coincides with rapid voltage collapse and dramatic acceleration of temperature rise rates, marking the transition from controlled thermal escalation to uncontrolled TR. However, while ISC serves as a critical trigger mechanism, it is not necessarily the primary heat source responsible for driving cells to extreme temperatures [25].

Stage 4: Massive Oxidation-Reduction Reactions (250–300 °C)

The most energetically significant phase of TR involves rapid oxidation-reduction reactions between cathode and anode materials following separator collapse. These reactions are triggered when cell temperature reaches critical thresholds, typically 250–270 °C for common lithium-ion chemistries. The onset temperature for these reactions represents the true TR trigger point (T_2), as the heat generation rate during this phase far exceeds that of all previous stages combined [99, 112]. The materials degeneration is discussed in-depth in Appendix A.

The cathode materials undergo thermal decomposition with concurrent oxygen release, creating a highly reactive environment for oxidation processes.

The released oxygen reacts vigorously with lithiated anode materials, generating massive heat release rates that drive rapid temperature escalation. For nickel-rich cathodes (NMC, NCA), the oxygen release occurs at lower temperatures due to the thermodynamic instability of high-valence nickel ions and Jahn-Teller distortion effects.

The oxidation-reduction reactions between mixed cathode and anode materials represent the dominant heat source during TR, typically accounting for the majority of the total energy release that drives cell temperatures to 800 °C and beyond. The exothermic nature of these reactions, combined with the large inventory of reactive materials, creates the characteristic explosive temperature rise that defines TR behaviour [113].

Stage 5: Current Collector Degradation and Material Ejection (600–900 °C)

At extreme temperatures exceeding 600 °C, additional exothermic processes emerge involving current collector degradation and material combustion. Recent research has identified that aluminium current collectors, previously considered thermally stable, undergo severe exothermic reactions with lithiated cathode materials at temperatures above 600 °C. These reactions occur due to the destruction of the aluminium surface passivation film by fluoride compounds, enabling direct oxidation reactions [114].

The heat release from aluminium oxidation reactions can reach −22 to −33 kJ/g (the Gibbs free energy of a substance - a negative change in Gibbs free energy $\delta G < 0$ signifies a spontaneous reaction, while a positive $\delta G > 0$ indicates a non-spontaneous one), nearly double that of electrolyte combustion (−12 to −16 kJ/g). Considering that aluminium current collectors represent approximately half the mass of the electrolyte in typical cells, the heat contribution from these reactions becomes significant during extreme TR events.

The melting of aluminium current collectors at 660 °C leads to structural collapse and the violent ejection of electrode materials mixed with combustion gases. This creates the characteristic venting event with black smoke containing metallic particles and organic combustion products.

The ejected materials often remain at extremely high temperatures, creating fire propagation risks in the external environment [114].

Heat Generation Quantification and Energy Balance

The total heat generation during TR results from the cumulative contribution of multiple reaction pathways, each with distinct temperature dependencies and kinetic characteristics. Research utilizing differential scanning calorimetry has quantified the relative contributions of major heat sources across different temperature ranges [115].

The SEI decomposition reactions typically contribute 5–10% of the total heat release, with activation energies ranging from 80–120 kJ/mol depending on electrolyte composition and cycling history. Anode-electrolyte reactions account for approximately 15–25% of total heat generation, with higher contributions observed in cells with significant lithium plating or dendrite formation.

Cathode-electrolyte reactions and oxygen release mechanisms contribute 20–35% of the total heat release, with variations dependent on cathode chemistry and state of charge. The dominant contribution (40–60%) originates from the direct oxidation-reduction reactions between cathode and anode materials following separator collapse [25].

The heat release rates during TR can reach 1 000–10 000 W/kg during peak reaction phases, far exceeding the heat dissipation capacity of typical battery thermal management systems (BTMS). This fundamental imbalance between heat generation and removal capabilities explains why TR becomes self-sustaining once critical thresholds are exceeded [97].

Kinetic Analysis and Temperature Dependencies

The kinetic behaviour of TR reactions follows Arrhenius relationships, where reaction rates increase exponentially with temperature according to:

$$k = A \cdot \exp(-E_a/RT) \tag{2.4}$$

where A represents the pre-exponential factor, E_a denotes activation energy, R is the gas constant, and T represents absolute temperature. This exponential temperature dependence explains the characteristic acceleration observed during TR progression [25].

Different reaction pathways exhibit distinct activation energies that determine their relative contributions across the temperature spectrum. SEI decomposition reactions typically exhibit activation energies of 80–120 kJ/mol, while cathode oxygen release reactions demonstrate higher activation energies of 150–200 kJ/mol. The oxidation-reduction reactions between mixed materials show complex kinetic behaviour with apparent activation energies varying between 100–180 kJ/mol depending on the specific material combinations involved.

The competition between different reaction pathways creates the characteristic multi-stage progression observed in TR events. Lower activation energy reactions dominate at moderate temperatures, while high activation energy reactions become predominant only at elevated temperatures where exponential kinetics overcome the energy barriers [25].

Gas Generation and Toxic Emissions

TR events generate substantial quantities of toxic gases that represent significant safety hazards beyond the thermal and fire risks. The gas generation occurs through multiple pathways including electrolyte decomposition, electrode material degradation, and combustion processes [108].

Carbon dioxide represents the most abundant gas species, primarily originating from SEI decomposition and carbonate electrolyte breakdown. Concentrations can reach dangerous levels rapidly, with carbon dioxide detection serving as an early warning indicator for TR initiation. Carbon monoxide generation occurs through incomplete combustion processes and represents a particularly toxic component of the gas mixture [34].

Hydrogen fluoride emission results from $LiPF_6$ salt decomposition at elevated temperatures, creating extremely toxic and corrosive conditions. Other hazardous species include hydrogen, methane, and various hydrocarbons that contribute to explosion risks when mixed with air in confined spaces [108].

The total gas generation rates can reach 0.1–0.2 mol/Ah of cell capacity, with higher rates observed in high-energy-density cells and elevated temperature conditions. The rapid gas evolution contributes to pressure build-up and violent venting behaviour characteristic of severe TR events [106].

Further analysis of gases is presented in the Appendix D.

2.3 Mechanical Abuse of Lithium-ion Batteries

Mechanical abuse of LIB cells - such as crushing, penetration, bending, or impact - poses significant safety risks, often leading to catastrophic failure modes. Full spectrum of abuses are presented in Figure 2.6. Understanding the sequence of physical and chemical events within the cell under such conditions is essential for advancing battery safety and informing improved design and testing standards [116, 96, 114].

When a LIB cell is subjected to mechanical abuse, the initial response is mechanical deformation of its structural components, including the casing, electrodes, and separator. The type and extent of deformation depend on the nature of the applied force (e.g., indentation, bending, or compression) and the cell geometry. During this stage, the jellyroll or electrode stack may undergo compression, buckling, or local cracking, while the casing may bend or fracture [117, 118, 119].

As mechanical stress increases, the separator - a porous polymer membrane isolating the anode and cathode - can rupture or tear, particularly at points of high strain localization such as shear bands in the electrode assembly. This failure allows direct or indirect contact between the electrodes, resulting in the formation of an ISC. The ISC is typically detected by a sudden voltage drop and a localized temperature spike within the cell [120, 121, 122].

The ISC triggers rapid joule heating and localized exothermic reactions due to uncontrolled current flow between electrodes. The temperature rise accelerates decomposition of the solid electrolyte interphase and initiates further breakdown of electrolyte and electrode materials. Gas generation and pressure build-up may occur, and if heat generation exceeds dissipation, TR can be triggered, leading to fire or explosion [96, 116, 123].

Experimental studies reveal that the specific failure mode depends on the abuse type, cell design, and state of charge. For instance, indentation often causes shear cracks and separator puncture, while bending may result in delamination without immediate ISC. High-frequency acoustic emission signals and digital image correlation have been used to detect these events in real time. X-ray computed tomography has shown that ISC is often a collective result of strain localization, ductile fracture of metal foils, and separator tearing [117, 118, 120].

To predict and simulate mechanical abuse outcomes, both homogenized and detailed finite element models have been developed, incorporating the anisotropic, dynamic, and state of charge dependent properties of LIB components. Failure criteria for ISC include maximum principal stress, Mohr-Coulomb, and unified strength models, which are calibrated against experimental data. These models are essential for designing safer batteries and informing regulatory standards [114, 121, 122].

Squeezing, or compressive abuse, is a prevalent mechanical threat to LIB cells, especially in automotive collisions and pack-level failures. When a battery is subjected to squeezing, the applied force leads to progressive deformation of the cell casing and internal electrode assembly. This deformation can cause the separator to thin and, under sufficient load, tear, thereby allowing direct contact between the anode and cathode and resulting in an ISC [96, 122]. The onset of internal shorting is typically accompanied by a sudden voltage drop and localized temperature

rise, which may escalate into TR depending on the state of charge and cell chemistry [121, 122].

The mechanical response of the cell during squeezing is highly dependent on the geometry of the applied force and the battery's structural properties. Experimental studies using hemispherical and flat punches have demonstrated that sharper punches induce higher stress concentrations, leading to earlier onset of internal shorting compared to blunt punches [117, 122]. Advanced modelling approaches, such as the Ludwik isotropic hardening and Drucker-Prager models, have been employed to simulate the stress-strain behaviour and predict short circuit initiation under various squeezing conditions [121, 122]. These models, validated by in-situ measurements of voltage, force, and temperature, provide critical insight into the safety boundaries of lithium-ion cells under compressive abuse [117, 122].

Shearing represents another critical form of mechanical abuse, often occurring during bending, torsion, or localized indentation. Under shear loading, the internal electrode stack may experience slippage and misalignment, leading to the formation of shear cracks within the electrodes and separator [116, 121]. These shear-induced cracks can propagate rapidly, creating pathways for direct electrical contact between the anode and cathode, which in turn triggers ISCs and localized heating [116, 120].

The severity of damage induced by shearing depends on the magnitude and rate of applied force, as well as the mechanical properties of the separator and electrode materials [121, 117]. Recent in-situ monitoring techniques, such as acoustic emission and digital image correlation, have enabled real-time detection of shear crack formation and propagation within lithium-ion cells [116]. These studies have shown that shear cracks are often precursors to catastrophic cell failure, and that the risk can be mitigated by optimizing separator toughness and electrode adhesion [116, 118].

Experimental investigations have revealed that nail penetration can lead to a cascade of failure events, including gas generation, cell swelling, venting, and in severe cases, TR and explosion [120, 124]. The outcome of penetration abuse is highly sensitive to the state of charge and cell chemistry, with higher states of charge and certain cathode materials exhibiting a greater propensity for violent failure [120, 125]. Advanced imaging and modelling techniques have further elucidated the spatial and temporal evolution of thermal and mechanical damage during penetration, providing valuable guidance for the design of safer battery systems [121, 124].

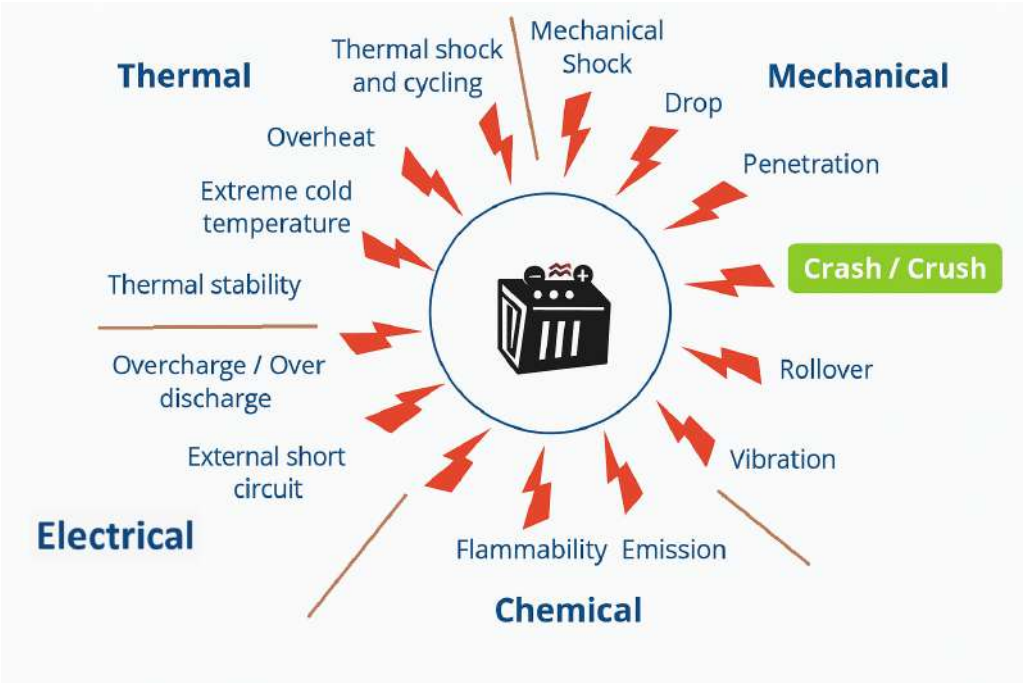

Figure 2.6: Abuse types for LIB assembly.

2.4 Electrical Abuse of Lithium-ion Batteries

Electrical abuse represents one of the most critical safety concerns in LIB systems, encompassing various forms of electrical misuse that can precipitate TR and catastrophic failure [96, 126]. The three primary categories of electrical abuse include overcharging, overdischarging, and external short circuits, each presenting distinct mechanisms of failure and safety implications [96, 127]. Understanding these electrical abuse conditions is essential for developing effective BMS and safety protocols, as they represent the most common triggers for TR events in both laboratory and real-world applications [126].

Overcharging occurs when a battery is charged beyond its maximum recommended voltage limit, leading to a cascade of detrimental electrochemical reactions [96, 128]. During overcharge conditions, the cathode becomes over-delithiated while the anode becomes over-lithiated, causing several adverse effects including electrolyte oxidation, oxygen evolution, and accelerated degradation of the solid electrolyte interphase layer [129]. Overcharge reactions depend on SOC level - with increasing SOC, the reactions become progressively more destructive, as presented in Figure 2.7. The overcharge process generates excessive heat through multiple mechanisms: increased ohmic resistance due to lithium plating, exothermic decomposition reactions, and gas evolution that increases internal pressure [130]. Overcharge-induced TR typically initiates at lower temperatures compared to thermal abuse, as the accumulated chemical energy within the battery facilitates reactions at reduced thermal thresholds [131].

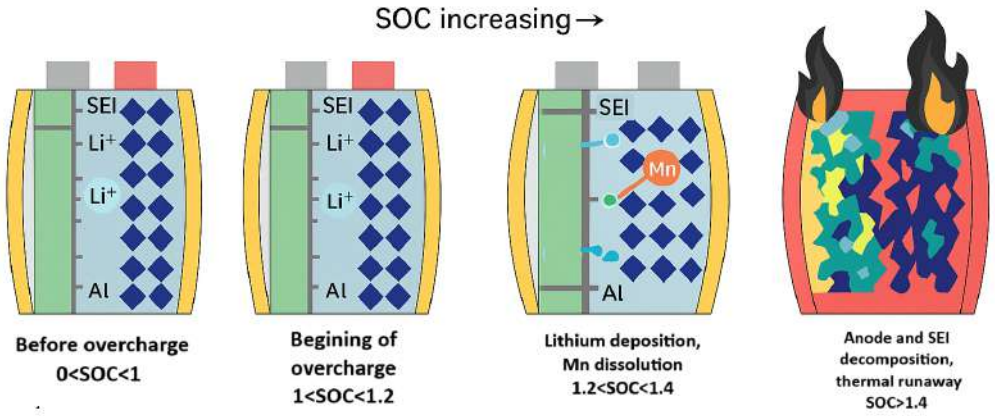

Figure 2.7: Visual representation of the overcharge process with increasing SOC.

The formation of metallic lithium dendrites on the anode surface during overcharge represents a particularly dangerous phenomenon, as these structures can penetrate the separator and create ISCs [132, 133]. At high current densities during overcharging, lithium ions transfer rapidly and deposit on the electrodes, creating lithium-ion depletion zones that lead to space charge formation and dendrite growth [132]. Additionally, the decomposition of electrolyte components during overcharge releases significant amounts of heat and produces flammable gases, including hydrogen, carbon monoxide, and various organic vapours [34, 134]. The progression of overcharge-induced TR typically follows a multi-stage process characterized by gradual temperature rise, rapid voltage increase, and eventual TR propagation [126]. From the plethora of batteries, three are mostly used in EVs and stationary ESS applications.

In **lithium-ion cells**, overcharge currents above approximately 4 C (as in C-rate - the charge or discharge current of a battery expressed relative to its nominal capacity; 1 C corresponds to a current that fully charges or discharges the cell in one hour, e.g., for a 3.2 Ah cell, 1 C equals 3.2 A) have been shown to induce separator failure and ISCs, leading to TR. In 18650 graphite $LiNi_{0.6}Co_{0.2}Mn_{0.2}O_2$ pouch cells tested at 3 C (9.6 A) and 1 C (3.2 A), safety devices prevented runaway; however, when currents exceeded ~4 C, the stored energy release outpaced protective

cut-offs, and runaway was observed at internal temperatures near 150 °C [135].

In **nickel-metal hydride cells**, overcharge currents as low as 0.1 C can initiate exothermic hydrogen evolution, separator deformation, and eventual TR if voltage - regulated charging is maintained. Accelerating rate calorimetry on sub-C NiMH cells demonstrated that micro-overcharge beyond 4.4 V cut-off precipitates runaway-like events at significantly lower temperatures (∼60 °C) compared to nominal abuse tests [136].

In **lead-acid batteries**, float charging at currents exceeding ∼0.3 C (the typical recommended maximum for valve-regulated lead-acid cells) causes rapid gassing and internal heating. Sustained overcharge currents ≥0.5 C lead to uncontrolled heat build-up and TR characterized by runaway gassing and case bulging once the heat generation surpasses the cell's dissipation capacity [137].

Overdischarge abuse occurs when a battery is discharged below its minimum safe voltage threshold, typically resulting in copper dissolution from the current collector and subsequent deposition on the electrodes [138, 139]. This phenomenon creates ISCs that manifest as a significant resistance decrease and accelerated heat generation [127]. The complete overdischarge process has revealed that copper dissolution begins at approximately -12% SOC, with ISC formation becoming detectable shortly thereafter [138]. The copper dissolution mechanism represents a well-controlled method for inducing ISCs without mechanical deformation or external intervention [138]. The consequences of overdischarge extend beyond immediate safety concerns to include permanent capacity loss and accelerated ageing effects [139]. It was shown that overdischarge-induced degradation follows distinct patterns depending on the depth of discharge, with severe overdischarge conditions leading to irreversible structural changes in both electrode materials [139].

External short circuits represent acute electrical abuse conditions characterized by extremely high current discharge rates and rapid heat generation [96, 127]. When an external short circuit occurs, the battery experiences a sudden drop in terminal resistance, leading to current levels that can exceed normal operating conditions by several orders of magnitude. The resulting Joule heating effect generates substantial thermal energy within the cell, with heat generation rates proportional to the square of the current and the internal resistance. The progression of external short circuit abuse follows a characteristic pattern involving rapid current rise, voltage collapse, and accelerated temperature increase [127]. The thermal response during external short circuit conditions depends significantly on the battery's state of charge, internal resistance, and thermal management capabilities [131].

The fundamental electrochemical mechanisms underlying electrical abuse involve complex interactions between electrode materials, electrolyte components, and separator systems [96, 139]. During electrical abuse conditions, the normal electrochemical equilibrium is disrupted, leading to side reactions that generate heat, consume active materials, and produce gaseous by-products [130]. These reactions include SEI decomposition, oxidation, electrode material breakdown, and gas evolution, all of which contribute to the thermal instability observed during abuse conditions [134, 140]. The kinetics of these reactions are strongly temperature-dependent, creating positive feedback loops that accelerate the progression toward TR [131]. The degradation mechanisms associated with electrical abuse exhibit distinct characteristics depending on the specific abuse type and severity [139]. Capacity fade, impedance increase, and voltage degradation represent common indicators of electrical abuse-induced damage, with these parameters serving as diagnostic tools for assessing battery health and safety status [96, 126].

2.5 Thermal Abuse of Lithium-ion Battery

In thermal abuse situations, a LIB experiences thermal shock or localized overheating that compromises the normal thermal balance within the cell [141]. This condition occurs when the battery's local temperature exceeds safe operating thresholds, typically initiated by external

heating sources, environmental extremes, or internal heat generation from electrical faults [141]. The thermal stability of LIBs is fundamentally governed by the thermal decomposition characteristics of their constituent materials, including electrode materials, electrolytes, separators, and other cell components. When subjected to thermal abuse, these materials undergo progressive degradation through a series of temperature-dependent reactions that can escalate into catastrophic failure modes [126].

The onset of thermal abuse is characterized by the disruption of the solid electrolyte interphase layer on the anode surface. As the temperature continues to rise, the battery enters a regime where exothermic side reactions between the electrode materials and electrolyte become increasingly prominent - following mechanism was described in Section 2.2.

The severity of thermal abuse incidents is significantly influenced by the battery's SOC, with higher levels corresponding to increased chemical energy availability and more severe TR events [114]. Battery chemistry also plays a crucial role, with lithium iron phosphate cathodes demonstrating superior thermal stability compared to nickel-manganese-cobalt. Also, lithium cobalt oxide cathodes release oxygen at lower temperatures [141]. The age and degradation history of the battery affect thermal stability, as aged batteries often exhibit compromised SEI layers and lithium plating that reduce the temperature threshold for TR initiation [142]. Additionally, the effectiveness of thermal management systems, including cooling efficiency and thermal isolation between cells, significantly influences how localized heating events propagate throughout a battery pack [143].

Prevention and mitigation of thermal abuse require comprehensive approaches encompassing materials engineering, system design, and active safety measures. At the material level, the development of thermally stable cathode materials, flame-retardant electrolytes, and ceramic-coated separators with higher melting points can significantly increase the temperature threshold for TR initiation [144]. BMS play a critical role by continuously monitoring cell temperatures and voltages, implementing algorithms to detect early signs of thermal abnormalities, and activating preventive measures such as reduced charging currents or enhanced cooling [143]. Physical design strategies include incorporating thermal barriers between cells to limit heat propagation, implementing effective heat dissipation systems, and designing controlled venting mechanisms to safely release pressure and gases during thermal events [145]. Advanced battery packs may incorporate dedicated fire suppression systems and TR propagation barriers to contain incidents and prevent cascade failures throughout the pack [146].

2.6 Unwanted Chemical Reactions of Lithium-ion Batteries

LIBs are susceptible to a series of unwanted chemical reactions that can culminate in TR, a hazardous event characterized by rapid temperature escalation and potential cell rupture or fire. Examples of unwanted reactions are shown in Figure 2.8. Exposure to temperature changes triggers highly exothermic reactions between intercalated lithium and the organic carbonate solvents (such as ethylene carbonate), resulting in the evolution of heat and flammable gases such as carbon monoxide and methane [25, 147, 148]. The heat generated from these reactions can further accelerate the decomposition of the SEI and propagate the onset of TR.

As the temperature continues to rise, cathode materials, particularly those based on layered oxides like $LiCoO_2$ and $LiNi_xCo_yMn_{1-x-y}O_2$ (NMC), undergo structural decomposition at temperatures exceeding 150 °C. This decomposition is accompanied by the release of oxygen from the cathode lattice, which reacts violently with the flammable electrolyte [25, 142] - see Section 2.2 and Appendix A for in-depth mechanisms. The released oxygen not only intensifies the combustion of electrolyte solvents but also propagates further exothermic reactions, significantly increasing the risk of cell venting or explosion. Recent studies have shown that even advanced electrolytes, such as those based on lithium bis(fluorosulfonyl)imide ($LiFSI$), are susceptible to similar exothermic reactions at high temperatures, indicating that cathode decomposition

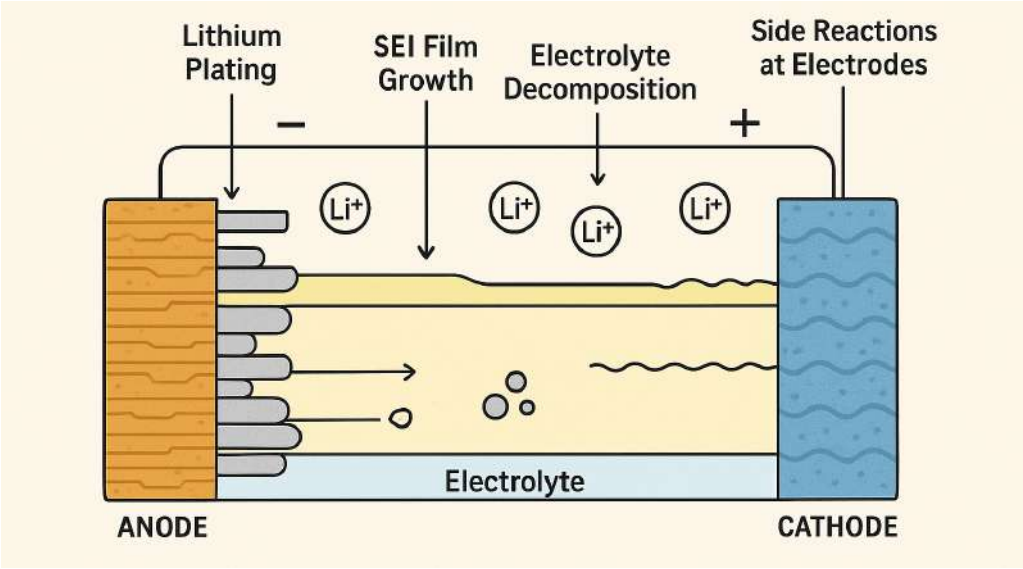

Figure 2.8: Unwanted reactions of the LIB.

remains a critical concern for LIB safety [142].

In addition to SEI and cathode decomposition, lithium-ion catalysed breakdown of electrolyte components plays a pivotal role in the thermal instability of LIBs. Quantum chemical studies have demonstrated that the presence of Li^+ ions lowers the activation energy required for the decomposition of common electrolyte solvents, such as ethylene carbonate, thereby accelerating the formation of gaseous by-products and heat under abusive conditions [149]. Furthermore, the presence of transition metal ions dissolved from the cathode can catalyse additional decomposition pathways, exacerbating TR [25]. Collectively, these unwanted chemical reactions underscore the complex interplay of electrochemical and thermal phenomena that govern LIB safety, highlighting the urgent need for robust SEI layers, thermally stable electrolytes, and cathode materials with improved oxygen retention.

Chapter 3

Thermal Safety Systems in Lithium-ion Batteries

TR in LIBs is a critical safety concern for both electric vehicles and stationary battery energy storage systems [96]. TR refers to a self-accelerating thermal failure that can lead to fires or explosions, triggered by abuse conditions such as overheating, overcharging, internal short circuits, or mechanical damage [150]. In multi-cell battery assemblies, a single cell's TR can propagate to neighbouring cells, greatly escalating the hazard [151, 152].

This chapter provides a comprehensive review of passive and active mitigation and suppression methods at three scales of battery integration: cell-level, module-level, and pack-level (see Figure 2.2 for reference) [150, 153]. Passive safety strategies are those inherent design and material measures that do not require active intervention (no external power) to mitigate the onset of TR or to suppress its propagation [153, 152]. These passive approaches act as a first line of defence - preventing thermal and mechanical abuses from initiating TR, and containing or delaying any TR that does occur so that catastrophic outcomes are avoided or minimized [96]. Active mitigation and suppression strategies involve real-time intervention - by sensors, control systems, or engineered suppression mechanisms - to prevent a detected thermal anomaly from escalating or to minimize the impact of a TR event in progress.

At the cell level, it is considered built-in safety devices and controls that detect abnormal conditions and intervene within single cells. At the module level, strategies that limit propagation from one cell to others (e.g. through cooling, isolation, or suppression within a module) are discussed in this chapter. At the pack or system level, the chapter contains comprehensive approaches for a whole battery pack or an installation, including cooling systems, fire suppression systems, and ventilation/exhaust mechanisms [21]. For each level, both experimental results (from recent safety tests and demonstrations) and theoretical or modelling studies are integrated [96, 151, 152].

A summary of TR prevention strategies in LIBs is shown in Table 3.1, categorized by cooling medium, battery shape, and study type. The table highlights key advancements in air, liquid, PCM, and hybrid thermal management approaches, with references to primary literature supporting each methodology and outcome. In-depth presentation of prevention systems and solutions to avoid battery fires is compiled in the Appendix B.

3.1 Passive Safety Systems for Avoiding Thermal Runaway

3.1.1 Cell Level

At the cell level, the priority is to enhance the intrinsic safety of the battery cell's materials and components so that the cell is more resistant to TR initiation. Even if a cell does enter TR, cell-level safeguards aim to limit the severity of the event (e.g. by slowing heat release or

Table 3.1: Summary of major findings on TR prevention strategies in LIBs (based on [87, 94, 154, 155, 156, 157, 158, 159]).

Cooling Medium	**Battery Shape**	**Type of Study**	**Major Findings**
Air	Cylindrical	Numerical	Aligned structure arrangement provides better thermal performance than staggered structure.
Air	Cylindrical	Numerical Experimental	Cubic structure of cells offers optimum cooling.
Air	Cylindrical	Numerical	~4 °C temperature uniformity achieved using reciprocating airflow.
Air	Cylindrical	Numerical Experimental	Highest cooling achieved with inlet at top and exhaust at bottom.
Air	Cylindrical	Numerical Experimental	Temperature field uniformity <5 °C achieved by adding vortex generators and jet inlets in unidirectional airflow.
Air	Cylindrical	Numerical Experimental	Temperature field uniformity of 3 °C achieved by adding air tubes around every battery cell.
Liquid	Cylindrical	Numerical	Temperature uniformity <5 °C achieved using variable aluminium block with 3 mm gradient.
Liquid	Cylindrical	Numerical	Temperature uniformity of 0.7 °C achieved by increasing contact surface area of batteries.
Liquid	Prismatic	Numerical	"Fork" type cold plate developed; 48 mL/s flow rate required for 5 °C uniformity.
Liquid	Prismatic	Numerical	Mixing liquid using Tesla valves improves cooling and temperature uniformity.
Liquid	Cylindrical	Numerical	For nano-fluids: avoid clustering, protect wires, consider boiling point of nano-fluid.
PCM	Cylindrical	Experimental	7% EG in paraffin-based composite PCM is optimum.
PCM	Cylindrical	Experimental	Novel PCM (graphene coated nickel foam with paraffin) has 23 times higher thermal conductivity than pure paraffin.
PCM	Cylindrical / Prismatic	Numerical	Novel strategy using liquid PCM (propane, ammonia, R134a, hydrogen); various combinations needed for optimum operation.
PCM	Cylindrical	Numerical	For refrigerants, avoid superheated state during cooling.
Hybrid (Mist Cooling)	Cylindrical	Numerical	3% mist and 5 g/s mass flow rate required to maintain temperature <40 °C.
Hybrid (Air / Liquid)	Cylindrical	Experimental	Water evaporation, convective, and conductive effects combined for novel cooling strategy.
Hybrid (Air / Liquid)	Cylindrical	Numerical	Liquid jackets and passive air cooling achieve 1.3°C temperature uniformity.
Hybrid (Liquid PCM)	Prismatic	Experimental	1 °C uniformity achieved with 54 mL/min liquid flow rate and 0.65 mm PCM thickness.

preventing fire) and prevent escalation to neighbouring cells or modules, as the heat dissipates to other neighbouring cells (see Figure 3.1). Cell-level strategies can be grouped into several categories:

- **Safer electrochemical materials:** Choosing or designing electrode and electrolyte materials that are less prone to violent exothermic reactions or fire in abuse conditions (e.g. thermally stable cathodes like $LiFePO_4$, non-flammable electrolytes) [160].
- **Separator and internal design features:** Using shutdown separators or other internal design elements that passively impede ion flow or heat generation when temperatures rise, thereby halting the TR process [161].
- **Built-in safety devices:** Incorporating devices such as positive temperature coefficient (PTC) thermistors, current interrupt devices (CIDs), rupture vents, and thermal fuses in the cell, which activate under high temperature or pressure to disconnect or relieve the cell [162].
- **Thermal additives and coatings:** Introducing flame-retardant additives in the electrolyte or special coatings in electrodes/current collectors that either quench combustion reactions or shut down the cell electrically when overheating occurs [163].
- **Mechanical resilience:** Designing the cell casing and components to better withstand mechanical abuse without catastrophic internal shorting - for instance, stronger casings and more robust separators to resist puncture [164].

The choice of cathode material has a profound influence on a cell's TR behaviour. Lithium iron phosphate (LFP) is a prime example of a safer cathode chemistry due to its structural and thermal stability. Unlike conventional nickel-manganese-cobalt (NMC) oxide cathodes which release oxygen and heat during decomposition, LFP does not undergo exothermic oxygen-releasing reactions within normal operating temperatures. As a result, LFP cells tend to have higher onset temperatures for TR and less severe heat release [160, 165, 166].

Integrating small fractions of safer anode materials or stabilizing the SEI can mitigate heat release. For example, pre-lithiated silicon-graphite anodes with robust SEI coatings may generate less heat under abuse because the SEI is more heat-resistant and consumes fewer exothermic reactions (the SEI breakdown is a major contributor to early heat in TR).

The liquid electrolyte in LIBs is highly flammable and a key driver of fire in TR. A crucial passive strategy is to modify the electrolyte to be less flammable or even nonflammable. One approach is adding flame-retardant additives that either suppress ignition or quench combustion radicals [167]. For instance, organophosphates or phosphazene compounds can be added to electrolytes; these additives release phosphorus-containing species upon heating that scavenge free radicals and form a protective char, thereby suppressing electrolyte flammability efficiently by isolating oxygen or capturing free radicals and acids generated in the combustion process. Recent research demonstrated a thermal-responsive phosphazene-based additive that dramatically inhibited TR - when the cell overheated, the additive decomposed endothermically and released flame-retardant products, significantly reducing combustion intensity [168].

Such additives can reduce the chance that vented gases ignite, effectively providing a built-in fire extinguisher. Another tactic is using non-flammable solvents or high-boiling-point solvents in the electrolyte. Replacing volatile carbonate solvents with, for example, ionic liquids or fluorinated ethers can raise the ignition point. Even aqueous electrolytes (water-based lithium-ion chemistries) have been proposed for stationary applications; while aqueous LIBs have lower voltage and require careful design to avoid water electrolysis, they offer - inherent safety - by eliminating flammable organics [169].

However, aqueous or ionic-liquid electrolytes are still emerging technologies and may not yet meet performance requirements for EVs. Nonetheless, ongoing progress in design strategies

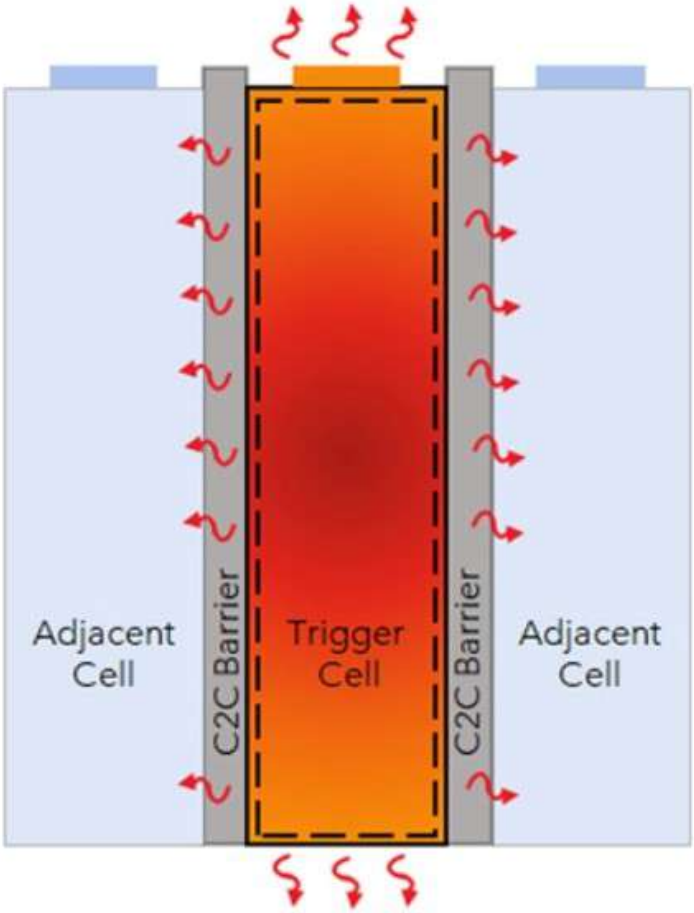

Figure 3.1: Heat propagation from cell to cell (denoted as C2C) example.

of safe electrolytes for preventing TR - continues to broaden the horizon of intrinsically safer electrolyte formulations.

The battery separator plays a pivotal safety role. A well-known passive safeguard is the shutdown separator concept: multi-layer polyolefin separators (often a trilayer of PP/PE/PP) that melt and close their pores at a threshold temperature (∼130 °C for PE). When a cell overheats, the PE layer softens and prevents ion transport while the PP layers remain intact, offering mechanical support and improving thermal stability. By blocking ionic conduction, the shutdown separator can effectively terminate the electrochemical reactions and current flow in an abused cell, potentially halting further temperature rise. However, shutdown separators have limitations: the melting that closes pores can also lead to shrinkage of the separator film. If the overheating is very rapid or localized (as in ISC), the separator may shrink and pull back, possibly causing direct contact between electrodes. To address this, manufacturers carefully design multi-layer separators so that the higher-melting-point layers (e.g. outer PP) hold structural integrity even when the PE middle layer melts. In effect, the separator self-seals, but does not mechanically collapse [170].

Additional analysis on the use on cell's materials (cathode, anode, separator and electrolyte) is described in Appendix A.

Besides shutdown behaviour, thermal stability and mechanical toughness of separators are crucial in a mechanical abuse scenario. Standard microporous polyolefin separators can start to deform at relatively low temperatures (∼100 °C) and are not strictly puncture-resistant. Therefore, improved separators often use ceramic or aramid fibre coatings, or entirely different materials like non-woven mats. A non-woven separator (e.g. made of heat-resistant fibres) will

not melt at all; while it may lack a shutdown function, it can survive much higher temperatures without degrading. For instance, separators with inorganic ceramic coatings (alumina or silica) on the surfaces can withstand temperatures above 150–200 °C, delaying or preventing TR onset. Moreover, these coatings enhance puncture strength - an important factor if cells are crushed or penetrated in a crash. If a nail penetrates a cell, a tougher separator may stay intact longer around the nail, limiting the short-circuit area and heat release, which can be the difference between a minor venting and a full TR. Most cylindrical and prismatic cells include a pressure-relief vent or score line on the can that ruptures in a controlled manner if internal pressure rises. This prevents the cell from exploding like a sealed bomb. For example, one design improvement in cylindrical cells was adding an annular groove on the can lid as a predetermined break line to ensure the vent opens quickly at a set pressure, avoiding uncontrolled case rupture [171].

An example of cell vent is presented in Figure 3.2 - cross-sectional diagram of a cylindrical cell's built-in safety vent (burst disk). Even individual cells have pressure relief features. Typical 18650/21700 Li-ion cell vent in the positive terminal cap is shown. The vent mechanism consists of a thin metal disk with a scored groove that acts as a burst diaphragm, supported by a plastic insulating ring. When the cell's internal pressure rises beyond a threshold (due to gas generation at over ∼70 bar inside the cell), the vent disk ruptures along the groove (blue arrows). This allows gas to escape through designated openings rather than blowing the whole cell apart [172].

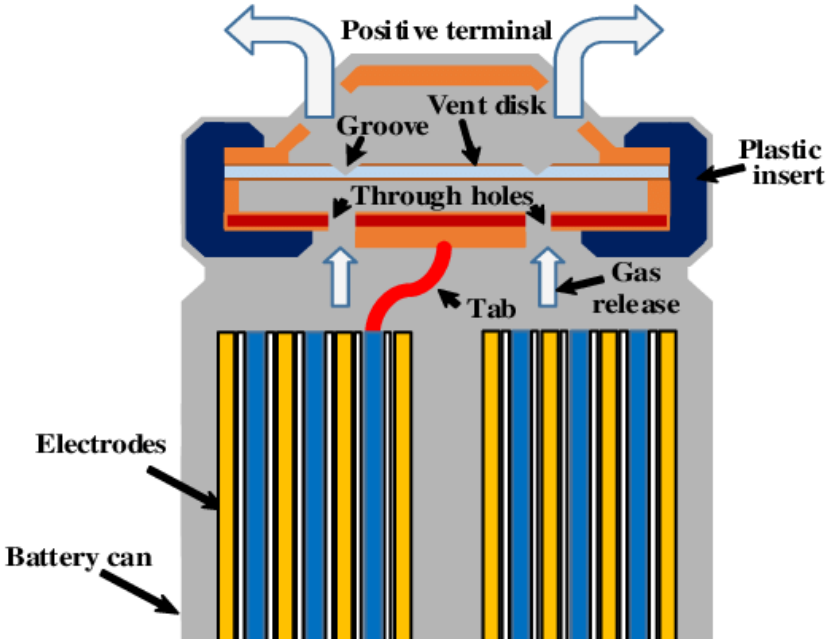

Figure 3.2: Cross-sectional diagram of a cylindrical cell's built-in safety vent (burst disk).

Thus, cell-level devices must be complemented by system-level protections for maximum effectiveness. Beyond these, researchers are developing thermally switchable components like the thermally sensitive current collector. A thermally sensitive current collector is a specially engineered devices (for example, an aluminium foil with a polymer or solder layer) that disconnects when a certain temperature is exceeded. One design uses a low-melting solder in the current collector: if the cell gets too hot, the solder melts and the current collector breaks, electrically isolating that electrode. Such mechanisms are still in development but offer another passive fail-safe to stop a runaway chain reaction inside a cell [173, 174].

To summarize cell-level measures: manufacturers combine multiple passive safeguards in modern cells. For instance, a high-capacity EV cell may use a shutdown separator and flame-retardant electrolyte additives and also vent - each kicking in at different stages of abuse. Experimental abuse tests (like nail penetration or overcharge) demonstrate that these features can delay or prevent full TR. However, no single solution is foolproof. If abuse conditions are severe (e.g. a

high-velocity penetration directly causing massive internal shorts), a cell can still go into TR despite all internal protections [169].

3.1.2 Module Level

A battery module consists of multiple cells arranged in close proximity, usually in series/parallel groupings with common structural supports and sometimes enclosed in a sub-housing. At this level, the key safety challenge is TR propagation – if one cell experiences TR, the heat and fire may spread to adjacent cells, causing a chain reaction. Modules in EVs often contain dozens of cells (e.g. a brick of 30–100 cells), and in BESS a module might contain large prismatic cells or many smaller pouch cells. Passive strategies at module level aim to prevent a single-cell failure from cascading through the entire module, or at least significantly slow the propagation to give time for detection or intervention. This typically involves thermal insulation, heat absorption, and strategic layout within the module. Key passive approaches at module scale include:

1. inserting thermal barriers or insulating materials between cells to limit heat transfer,
2. incorporating PCMs or other heat absorption media to soak up heat surges (see examples in Figure 3.3),
3. optimizing cell and module geometry to reduce thermal coupling,
4. using module enclosures or partitions that can contain flames and debris.

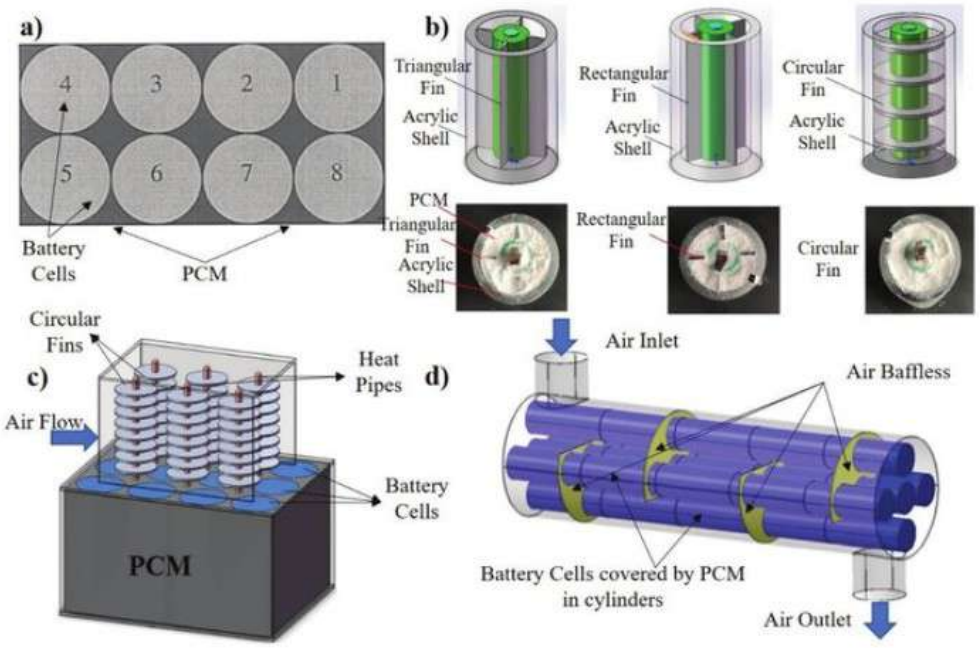

Figure 3.3: (a) The PCM-based cooling EV module. (b) Three different fin cases and corresponding experimental images [148]. (c) PCM/finned-HP integrated thermal management module. (d) the PCM integrated shell and tube battery pack [175].

Thermal Insulation Barriers Between Cells

One straightforward way to impede TR propagation is to physically separate cells with materials that block heat transfer and flame. By containing the intense heat of a runaway cell, the adjacent

cells may avoid reaching their ignition temperature. Numerous insulating materials were explored for this purpose, including ceramic fibre mats, glass fibre sheets, mica, polymer foams, aerogels, and even intumescent materials (see Figure 3.4 for comparison). The ideal barrier material has low thermal conductivity, high heat capacity, and high thermal stability [25]. It may also need mechanical strength to maintain separation between cells even if one cell casing ruptures or pressure builds - otherwise the failing cell could press directly against its neighbour. Recent experimental studies have systematically compared different barrier materials - a phase change material matrix, a ceramic fibre blanket, and a glass fibre sheet, each placed between cells in a small module. Glass fibre sheet provided the best protection, delaying propagation to the next cell by ∼900 s and even preventing the third cell in line from undergoing TR [176]. In the same tests, the total mass lost to fire/gas was reduced with the glass fibre barrier by about 6% compared to no barrier, indicating less material was burned or ejected. The glass fibre's excellent performance was attributed to its excellent thermal insulation and mechanical properties that kept heat and fire contained. By contrast, the PCM-based barrier in that study absorbed heat but did not insulate as effectively once fully melted, and the ceramic fibre, while also insulating, was slightly less effective than glass fibre in that setup.

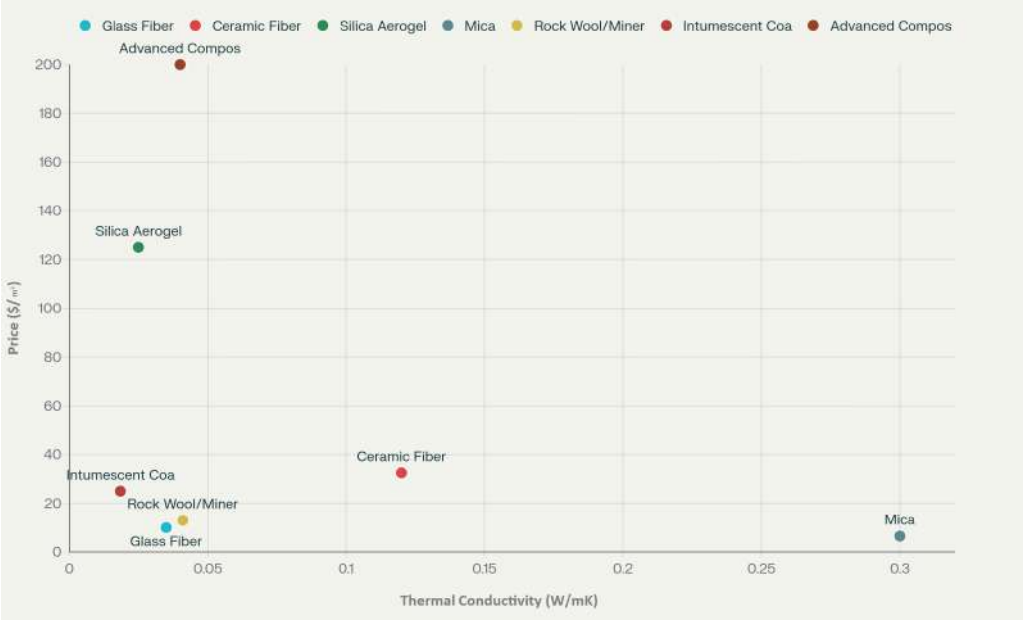

Figure 3.4: Comparison on the insulation materials - price vs. thermal conductivity (based on [158, 176, 177]).

Another study examined silica aerogel sheets as cell-to-cell barriers (aerogel is an ultralight porous silica with extremely low thermal conductivity). Varying the aerogel content and thickness, they found that thicker aerogel sheets markedly improved TR propagation resistance [178]. Aerogels are attractive because they combine low conductivity with high thermal stability (non-combustible). However, pure aerogel blankets can be brittle. Composite aerogel-fibre mats are sometimes used to add toughness. It was investigated three different thermal insulation materials (including an aerogel-based felt) in a large-format pouch cell module [179]. It was observed that all the tested materials delayed propagation compared to no barrier, though none completely stopped it in every case. By analysing each material's properties, it was identified that a low thermal diffusion coefficient (slow heat spread) and a high maximum service temperature were critical parameters for an effective barrier. In other words, the material must not only insulate well but also remain intact at the extreme temperatures of a runaway (which can exceed 600 °C in worst cases for high-energy cells).

Materials like fibreglass, ceramic fibre boards, mica sheets, and rock wool (mineral fibre)

all serve this role and have been studied for battery modules. For instance, rock wool boards (commonly used as fire insulation in buildings) can tolerate high heat and have low conductivity, making them viable to isolate battery sections though their weight and thickness might restrict EV use to some extent (more feasible in stationary BESS where weight is less critical). In addition to traditional insulators, intumescent coatings and blankets offer a dynamic form of insulation. Intumescent materials (often polymer-based with special additives) expand many times their original thickness when exposed to heat, forming a char foam that is highly insulative. An intumescent paint can swell up to 100 times in thickness under fire, creating a thick, porous char layer that thermally protects the underlying surface [158]. When applied to or placed between battery cells, an intumescent layer would automatically react to a burning cell by expanding and shielding its neighbours. These coatings block 60–90% of incident heat flux once expanded, as reported in fire protection literature. They essentially starve the propagation process of the heat needed to ignite the next cell.

One challenge is ensuring the intumescent material remains adherent and effective in the confined space of a battery module, but ongoing development is tackling these issues (for example, new formulations that expand uniformly even in constrained gaps). A complementary passive tool is the use of fire-resistant fabrics or blankets wrapping groups of cells. High-temperature fabrics (fibreglass cloth, aramid fibre like Kevlar, silica cloth, etc.) can act as fire curtains that contain flames and hot ejecta from a runaway cell [158].

These have been used in aerospace battery enclosures and are being explored for EV modules. A fire-resistant blanket does not necessarily stop heat conduction (unless combined with an insulative layer), but it can prevent direct flame impingement on adjacent cells and confine the hot gases [158].

Table 3.2: Comparative overview of common insulation materials for high-temperature applications, including their thermal conductivity, approximate cost, and qualitative assessment of mechanical strength properties (based on [146, 179, 180, 181, 182]).

Material Type	**Description of Mechanical Properties**
Glass Fiber	Good tensile strength (90-100MPa); flexible, easily handled and cut; maintains shape under moderate stress.
Ceramic Fiber	Low tensile strength (0.08-0.1MPa); excellent dimensional stability at high temperature; brittle, may fracture if sharply bent.
Silica Aerogel	Brittle, low compressive strength; prone to cracking under mechanical stress, though composite forms offer some reinforcement.
Mica	Good compression and shear properties; strong for stamping or forming; holds structural integrity under load.
Rock Wool/Mineral Fiber	Moderate tensile and compressive strength; dimensionally stable; resists deformation, suitable for non-structural insulation.
Intumescent Coatings	Flexible prior to heat exposure; upon heating, expands into rigid, protective, char-like structure, reinforcing the barrier.
Advanced Composite	Enhanced mechanical strength via composite matrix (glass fiber, polymer); retains shape, resists fracture, improved over pure aerogel.

Phase Change Materials for Thermal Absorption

PCMs operate on the principle of storing and releasing thermal energy through reversible phase transitions, most commonly between solid and liquid states. When a PCM absorbs heat during the phase transition (melting), its temperature remains nearly constant while it stores a significant amount of latent heat. Conversely, as the material solidifies, the stored energy is released in the form of heat, again at an almost constant temperature.

PCMs are substances that absorb a large amount of heat upon phase change and are thus used to moderate temperature spikes. In battery modules, PCMs (such as paraffin waxes, fatty acids, hydrated salts, etc.) can be placed around cells so that if a cell starts to overheat, the PCM melts and absorbs energy, limiting the temperature rise. PCMs by themselves do not prevent fire or block flames, but by heat absorption they can delay or possibly prevent TR initiation in nearby cells. Experimental evidence shows PCMs can be very effective in passive cooling of batteries. In lithium-ion cells with different PCM encapsulations, it was found that PCM cooling significantly decreased the cell surface temperature compared to natural convective cooling [183]. In a trigger-cell TR scenario, modules with PCM layers had the neighbouring cells stay cooler than in identical modules without PCM [184]. Integrating a aerogel-felt plus PCM composite was found to mitigate TR behaviour and heat by about $\sim$45% (temperature wise). The aerogel provided insulation while the PCM absorbed heat, a dual action that prevented the propagation of runaway.

The combination of an insulating material (to slow heat flow) and a PCM (to absorb heat) can stop propagation entirely [185]. It was demonstrated that a module with both a thermal barrier and a PCM layer showed no propagation, whereas using a cooling plate alone did not sufficiently delay propagation. The PCM's latent heat absorption effectively buys time during which the affected cell's energy is absorbed rather than passed on to its neighbours. Common PCMs for battery safety include paraffin waxes (melting around 40–80 °C, with latent heat $\sim$150–200 J/g) and salt hydrates (with higher thermal storage but can be corrosive). Paraffins are popular due to chemical stability and ease of encapsulation, but they are flammable, which is problematic if the PCM itself gets hot enough to combust. To address this, researchers use flame-retardant PCMs or add flame suppressants to PCM formulations [183, 186].

Another approach is to gel or encapsulate the PCM in a polymer matrix, so that when the PCM melts it does not leak extensively and is less exposed to air. It found embedding PCMs in porous matrices (like metal foams or graphite sheets) can improve thermal conductivity and contain the liquid phase. High thermal conductivity helps spread the heat into the PCM faster, preventing local hotspots. PCMs can be deployed in different ways at module level. One design is a PCM sheet or pad between cells (for cylindrical cells, this might be a wrapping or an inter-cell spacer filled with PCM). It was demonstrated that a phase change composite placed in a battery pack prevented propagation in their setup, TR in one cell did not spread to others when the pack was integrated with a PCC layer [186, 187].

Module Layout and Structural Design

Beyond materials inserted between or around cells, the geometric arrangement and structural design of the module itself can influence TR propagation outcomes. Several passive design strategies are noteworthy:

- **Cell Spacing and Arrangement:** A general rule states "greater distance between cells provides more thermal isolation". If cells are packed too tightly, heat transfers very quickly by conduction, convection and radiation. By increasing the inter-cell gap (even by a few millimetres) and possibly filling that gap with air or an insulator, modules can achieve a measurable reduction in propagation risk. It was showed that cell arrangement affects propagation under air cooling certain layouts allowed cooling air to reach all cells more evenly, thus avoiding any cell reaching runaway conditions [188, 189].

In thermal propagation context, a cell that is surrounded by fewer immediate neighbours (e.g. on the module periphery, or in a hexagonal spacing pattern) might transfer less heat to others. Increasing the spacing around the hottest cell in a module was shown to reduce the peak temperature and thermal gradients [190].

- **Module Enclosures and Dividers:** Many battery modules are built into a rigid casing or frame (often aluminium or polymer). By using thermally resistant materials for the casing or internal dividers, one can passively contain thermal events. For example, some modules have partitions separating sections of cells, these partitions can be made of metal (which acts as a heat sink and barrier) or polymer composites. Aluminium partition walls have high thermal conductivity, so they absorb heat quickly and distribute it (which can protect one side for a time by diluting heat, but also could transfer heat to far cells). Thick aluminium plates in modules have been tested as heat spreaders that also block direct flame, and it was found that they can prevent propagation if properly designed [191, 192].

  The downside was weight - the metal adds significant mass. Alternatively, ceramic partition boards (like insulated concrete boards or fibre-reinforced ceramic) provide strong fire barriers without as much heat conduction, though they are brittle [158].

- **Cell Mounting and Potting:** How cells are mounted can affect propagation. If cells are tightly clamped together for structural reasons, they share heat more readily. If they are mounted with small gaps or a compliant spacer, there is less direct conduction. Some module designs use potting compounds or thermal interface materials around cells for thermal management. Potting (encapsulating cells in resin or gel) can either help or hurt safety: a potting material with high thermal conductivity might spread heat, whereas a potting with low thermal conductivity could act as an insulator. However, potting compounds can be flammable; thus recent efforts are toward flame-retardant potting materials (incorporating fillers like aluminium hydroxide that release water when hot). If designed right, a potting compound can serve as both a heat sink and a fire suppressor through endothermic filler reactions [193].

- **Venting Considerations in Module:** While venting is more of a pack-level issue, at module level it is relevant how the module handles the gas and flame from a venting cell. Some designs include a rupture disk or chimney for each cell - a passive vent that routes hot gas safely out of the module [114]. Additionally, flame arrestors (screens or meshes) can be placed in vent outlets to quench flames.

As EV and BESS modules increasingly aim to pass rigorous safety tests (like not propagating beyond a certain number of cells), these passive design elements are becoming standard. It is not uncommon now for manufacturers to claim a module is TR propagation proof via internal barriers and cooling elements. Real-world validation of such claims is growing, with many citing that their modules can sustain a single cell failure without igniting the whole module. This is achieved through the combination of techniques discussed above.

3.1.3 Pack Level

At the pack level, the entire battery system in an EV or a stationary storage unit is considered, comprising multiple modules along with the pack enclosure and any ancillary protective elements. Pack-level passive strategies aim to contain a TR event within the smallest possible portion of the system and to protect the surroundings (vehicle cabin, equipment, building, etc.) from fire or explosion. The pack level is also where differences between EV batteries and stationary BESS are most pronounced, due to differences in scale, environment, and safety requirements. Key passive strategies at pack level include:

1. dividing the pack into sections or modules with fire-resistant barriers (to stop propagation beyond a module),
2. using a strong, thermally insulating pack housing that can contain fires for a duration,
3. providing passive pressure relief paths for hot gases to vent out safely, avoiding pressure build-up and explosion,
4. leveraging the vehicle or facility design (placement of the pack, separation from occupants or critical equipment) as a passive safety measure.

It was also considered how EV and BESS implementations differ in these aspects.

Segmentation and Firebreaks in Pack Architecture

By increasing the inter-cell gap and possibly filling that gap with air or an insulator, modules can achieve a measurable reduction in propagation risk [158]. It was found that arranging cylindrical cells in a staggered (diagonal) pattern rather than directly aligned improved air cooling and could reduce hot spots in a pack [194]. Similarly, it was showed that cell arrangement affects propagation under air cooling - certain layouts allowed cooling air to reach all cells more evenly, thus avoiding any cell reaching runaway conditions [188]. In propagation context, a cell that is surrounded by fewer immediate neighbours (e.g. on the module periphery, or in a hexagonal spacing pattern) might transfer less heat to others. Increasing the spacing around the hottest cell in a module was shown to reduce the peak temperature and thermal gradients [195]. In EV modules there is pressure to minimize spacing for energy density reasons. A practical compromise is to have slightly larger gaps or insulating inserts around every N-th cell or around the module edges where heat can escape. Increasing spacing around the area of a pack that experiences the highest temperature can reduce the temperature difference in the pack by $\sim$29% [191]. Thus, designers sometimes leave a larger air gap at the centre or ends of a pack row to act as a heat sink. In stationary BESS modules, energy density is less critical, so designers can afford more generous spacing or even put each cell in its own mini-compartment. There have been studies on optimal spacing between modules: increasing the gap by a few centimetres can drastically reduce radiative heat transfer between module surfaces, which is a primary mode of propagation in a pack fire [189].

Figure 3.5 contains examples of fire segmentation. Figure 3.5a presents Tesla's structural battery pack (Model Y with 4680 cells) is divided into four internal modules separated by robust structural ribs ("firewalls") and filled with a special pink foam for support and fire mitigation. In this image, one section of foam has been removed (to the left of the photograph) to reveal the cells and busbars, while the remaining modules stay encased in the foam. These internal partitions act as mechanical firebreaks that localize TR to one module. Figure 3.5b is a close-up of the Tesla structural pack's internal connections, showing rows of cylindrical cells (under residual pink foam) connected by small welded connector plates. These plates and wires form electrical segmentation: they act as built-in fuses, isolating failed cells. In a severe overcurrent or short, the thin connectors melt ("fuse blow"), preventing the fault from cascading.

In stationary BESS, segmentation can be more aggressive. Often each module (or rack) is enclosed in its own sub-cabinet. In large containerized BESS, it is common to have multiple racks, each rack can be treated as a compartment. Some BESS manufacturers install vertical fire barrier panels between racks of batteries in a container, so that if one rack is on fire, the adjacent rack is shielded for a certain period. These barriers might be made of steel or calcium-silicate board with fire retardant insulation, capable of withstanding, 1 800 s of fire exposure. The idea is to prevent a domino effect through the entire container. Evidence of the importance of such segmentation came from real incidents: a 2019 BESS fire and explosion in Arizona revealed that lack of internal barriers allowed the entire container to fill with flammable gases, leading to a

(a)

(b)

Figure 3.5: Examples of segmentation and firebreak features to prevent a single cell failure in battery packs in electric vehicles (EVs): (a) Tesla's structural battery pack (Model Y with 4680 cells) [196]; (b) close-up of the Tesla structural pack's internal connections [197].

massive event. In response, new standards (NFPA 855, UL 9540A) encourage designs where a single module burning will not take out the whole container, which practically requires passive fire partitions or very effective active suppression. In practice, passive partitions are often used since they require no activation and are fail-safe in a power outage [198, 199].

An example of segmentation on stationary unit is presented in Figure 3.6. Cross-sectional schematic of an EVLO stationary ESS enclosure is presented in Figure 3.6a. Stacks of battery modules (purple units) are arranged with intentional air gaps between each tray (module group). Red arrows indicate the "chimney effect" – in case of a TR in one module (flame icon), hot gas rises in the vertical gap and is vented out the top, bypassing other modules. Figure 3.6b is example of layout of a containerized stationary ESS. The system includes six independent battery racks, physically and electrically segmented, enclosed within a shared container. Fire mitigation is addressed via a fire water spray pipe integrated above the racks. Thermal control is maintained by an AC air outlet duct, while power electronics are separated into the power conversion system and direct current centralized control panel compartments. The architecture demonstrates both mechanical segmentation (individual battery racks) and firebreak strategies (overhead spray and airflow channeling), aiming to confine TR events to localized zones.

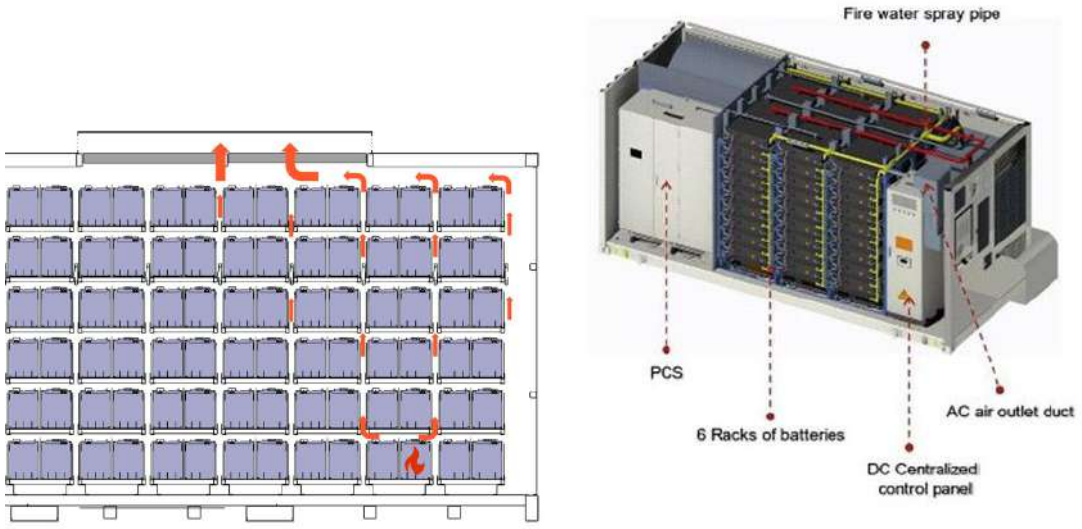

(a) (b)

Figure 3.6: Examples of segmentation and firebreak features to prevent a single cell failure in battery packs in BESS: (a) cross-sectional schematic of an EVLO stationary energy storage system enclosure (side view) [200]; (b) segmentation layout of a containerized stationary energy storage system (BESS) [201].

Pressure Relief and Venting Systems

While containing a fire is important, preventing a dangerous pressure build-up is equally critical. When batteries go into TR, they eject a substantial volume of gas (from electrolyte vapour, decomposition products, etc.). If these gases accumulate in an enclosed space, they create an explosive atmosphere and high pressure [202, 203]. A small spark can then cause a deflagration or even detonation. This risk is higher in a confined pack or, in sealed BESS containers. Therefore, passive venting mechanisms are essential to safely disperse these gases. In EV packs, manufacturers incorporate pressure relief vents or panels in the pack casing. For example, many pack designs have blow-out ports sections of the enclosure that are weaker (scored or use a bursting disk) which will pop open when internal pressure rises. Eaton and other suppliers market dedicated that normally are closed to keep water out, but will open under a slight overpressure to let gases escape [204].

These valves often also prevent backfire (some contain a membrane or tortuous path that acts as a flame arrestor, so that if the gases inside ignite, the flame will not shoot out as a jet). The venting direction is usually designed to route hazards away from occupants e.g., vents directed downward or away from the passenger compartment in EVs. As a passive device, a vent just reacts to pressure with no electronics needed. The importance of venting is reflected by safety testing standards. In the UL 9540A tests for BESS, for instance, large-scale fire testing measures how the container vents gases. If the container can vent sufficiently, the likelihood of an explosion is much reduced. Many stationary battery systems now include blow-off panels or louvres on the container or cabinet that will open at low pressure (some are held closed by magnets or low-strength bolts that give way when a certain pressure is exceeded). When a battery failure occurs, these panels pop open and direct flame and smoke out the top or sides of the container, rather than letting pressure rise inside. This is exactly what passive venting aims for: controlled release of energy rather than an uncontrolled rupture. Without venting, following scenario is possible: a flammable gas mixture builds up and later ignites, causing a devastating explosion [158].

One challenge with venting is that once opened, the vents also allow fresh air (oxygen) to

enter, which can actually feed the fire. That is why in some cases venting is coupled with active systems (like water mist). But purely passively, one can mitigate this by placing flame arrestors or one-way valves on vents. Flame arrestors (mesh screens or sintered metal filters) let gas out but cool any flame front trying to flash back in. Passive one-way valves can let pressure out, but then close to limit ingress of air. Eaton's vent valves, for instance, are designed to close again after relieving pressure, to prevent air exchange once the immediate overpressure is gone [205].

3.1.4 Summary on Passive Systems

Passive mitigation strategies are indispensable for LIB safety, forming a robust baseline of protection that does not depend on active controls or external intervention. At the cell level, manufacturers employ safer materials (like non-flammable electrolytes and stable cathodes) and built-in shutdown devices (vents etc.) to prevent abuse conditions from triggering TR and to limit a cell's energy release if it does fail. At the module level, thoughtful design incorporating thermal barriers (ceramics, fibres, intumescents) and heat-spreading/absorbing elements (PCM inserts, heat sinks) can effectively prevent or resist the TR propagation within a module. These measures, validated by both experiments and simulations, have been shown to delay propagation by many minutes or even halt it entirely in some cases.

Finally, at the pack or system level, strong enclosures, strategic segmentation, and passive venting systems work in tandem to contain fires and protect the surroundings, whether in an electric vehicle or a stationary storage facility. Real-world incidents and rigorous testing have proven that features like pressure relief vents and fire-resistant housings can be the difference between a controlled burn and an explosive disaster. It is important to emphasize that passive strategies often complement each other and are most effective as a multi-layered defence. No single passive feature can guarantee absolute safety given the energy densities involved; however, each layer (from cell-intrinsic safety to module insulation to pack venting) adds additional time and reduces severity, thus enabling active measures or emergency responses to intervene.

3.2 Active Strategies for Mitigating and Suppressing Thermal Runaway

Unlike passive safety measures (which rely on intrinsic material properties or device design to resist failure), active mitigation and suppression strategies involve real-time intervention by sensors, control systems, or engineered suppression mechanisms to prevent a detected thermal anomaly from escalating or to minimize the impact of a TR event in progress [144]. This section focuses on such active approaches to TR mitigation at the cell, module, and pack/system levels, comparing their implementation in EV versus BESS contexts (including indoor and outdoor installations), based on the latest peer-reviewed findings.

Active suppression of TR is inherently complex because of the speed and multi-faceted nature of battery failures. Once a cell enters TR, it undergoes a sequence of internal reactions releasing heat, flammable electrolyte vapour, and other gases; if the cell case or vent opens, hot gases and potentially fire are emitted externally [25].

An effective mitigation strategy must therefore either prevent the initial trigger (e.g. by early detection and shutdown), arrest the progression (e.g. by cooling or electrically isolating the failing cell before it cascades), or suppress the consequences (e.g. by extinguishing flames and controlling gas emissions). These actions may occur before, during, or after the onset of TR. Active techniques often rely on a deep understanding of TR mechanisms to target specific failure stages. For instance, the timing of intervention is critical thermal management systems must remove heat faster than it is generated to halt thermal escalation, and fire suppression systems must deploy in the narrow window after venting but before an explosion can occur in confined spaces [136].

While EV battery packs and stationary BESS share underlying LIB technology and TR mechanisms, there are crucial differences in their operating environments and safety approaches. EV batteries are constrained by weight and space, integrated in vehicles where collisions are a concern, and rely primarily on onboard passive protections and the vehicle's BMS to handle faults. In contrast, BESS installations (especially large containerized systems) can incorporate heavier dedicated safety systems (fire suppression, cooling, and ventilation) and must adhere to building and fire codes for stationary systems.

Indoor BESS pose concerns of toxic and flammable gas build-up, requiring robust ventilation or explosion relief, whereas outdoor BESS and EVs in open environments may allow easier heat dissipation but face weather and first-responder access issues [206]. The aim is to elucidate how strategies are implemented or prioritized differently (for instance, an automatic sprinkler or clean-agent flood system is feasible in a stationary facility, but an EV relies more on built-in isolation and letting a fire burn out in a controlled way under guidance of first responders [114]). By examining these nuances, the section provides a comprehensive understanding of active TR mitigation across applications, forming a basis for improved safety design in future energy storage systems.

3.2.1 Active Mitigation Methods at the Cell Level

Active mitigation at the cell level involves safety mechanisms and controls that operate on individual cells to either prevent TR initiation or mitigate its impact at the source. A single LIB cell typically includes several built-in safety devices often regarded as last line defences as well as being monitored by external circuits (part of the BMS) for signs of abnormal behaviour. While these measures are sometimes categorized as passive (since they activate autonomously when certain thresholds are exceeded), they represent targeted interventions at the cell level that can be considered "active" in the sense of producing a deliberate change in the cell's state (e.g. disconnecting it electrically or shutting down electrochemical activity) to avoid catastrophe [84, 162].

Internal Fuses and Current Interrupt Devices

One critical strategy to halt a developing TR within a cell is to break the electrical circuit before excessive heat or internal short-circuit current can build up. Lithium-ion cells commonly include internal CIDs or thermal fuses integrated into the cell's cap or electrode tab. A CID is typically a thin metal disk or diaphragm that reversibly flexes or ruptures when the internal cell pressure rises beyond a set point, thereby disconnecting the cell from the external terminals by opening the circuit. In cylindrical cells (e.g. 18650 or 21700 formats), the CID is often combined with the vent in the cell lid. Under abuse conditions such as overcharge or overheating, gas generation inside the cell increases pressure; a pressure-activated CID will snap open between about 1 MPa and 2 MPa internal pressure, stopping charge/discharge current flow and ideally preventing further heating [117, 207]. For example, two 18650 cell models with CIDs activated at about 100 °C when internal pressure reached ∼1.8 MPa successfully disconnected the cells from the circuit. This kind of rapid electrical isolation can mitigate TR by removing one source of heating (ohmic/chemical heat from continued current flow). However, CIDs have limitations - in overcharge scenarios with high pack voltages, the sudden opening of the circuit can generate an electrical arc at the CID gap, igniting flammable gases around the disconnect and potentially triggering TR despite the CIDs activation. Moreover, once a CID opens, the cell is permanently disabled, which, while safe, reduces pack capacity and requires module-level designs to manage such failed-open cells. In addition to pressure-triggered CIDs, temperature-triggered fuses (thermal fuses) and resettable PTC fuses operate based on cell temperature. A thermal fuse within the cell can be a low-melting-point metallic link that melts open if the local temperature exceeds a threshold (often above 130 °C). By blowing at elevated temperature, it interrupts current before the cell reaches the more dangerous self-heating regime above ∼150 °C [208].

Preliminary laboratory tests of such an HTS limiter integrated in a cell circuit showed improved stability under short-circuit conditions, effectively clamping the current below the internal damage threshold and then automatically resetting once temperatures normalized. This is an example of leveraging advanced materials for self-adaptive current limiting as an active TR prevention at the cell level. PTC Devices and Shutdown Mechanisms thermistors are another widely applied cell-level safeguard [209]. These are resistive elements (often polymer-based composites) that exhibit a sharp increase in resistance beyond a certain Curie temperature, thereby limiting current flow as temperature rises.

Sensing and Monitoring for Early Intervention

Active mitigation at cell level is not limited to internal passive devices; it also encompasses external sensing and control targeting individual cells. Each cell in a battery pack is usually monitored for voltage and often temperature (via surface-mounted thermistors). The BMS continuously analyses this data. When abnormal readings occur e.g. a cell's voltage drops suddenly (possible internal short) or its temperature spikes, the BMS can take active steps such as cutting off charging/discharging current to that cell or the entire pack. This is an active response aiming to remove stress from a failing cell. For instance, in overcharge conditions, an active BMS control will terminate charging as soon as an over-voltage is detected, preventing the overcharge-induced exothermic reactions; this is much faster and more controlled than waiting for a CID to mechanically break at dangerous pressure levels [25].

Advanced sensing methods have emerged recently, such as acoustic or ultrasonic sensing and fibre-optic sensing for cells. Ultrasonic monitoring can detect subtle changes in a cell's internal structure (through time-of-flight of sound waves) that precede TR, such as gas generation or expansion in a cell [210, 211]. If these early warning signs are caught, the BMS could actively reconfigure the pack (e.g. isolate the suspect cell via bypass circuits if available, or at least flag it for replacement).

Fibre-optic sensors embedded near cells can directly measure internal temperature distribution or strain with high resolution and electrical isolation They have demonstrated the ability to catch localized heating inside a cell earlier than traditional surface sensors [147]. While such sensors are still largely experimental, they represent the next generation of active cell-level monitoring that could trigger mitigation actions. The combination of early warning and rapid response is critical.

At cell level, this means detecting a cell that is entering TR (for example, by sensing its safety vent opening acoustically or a sudden pressure rise) and then activating countermeasures. Experimental systems have been built where the detection of a vent acoustic signal triggers a localized cooling spray onto that cell, successfully preventing fire spread [212]. Such a system blurs the line between cell-level and module-level, but it underscores a concept: tightly coupling sensors to actuators at the smallest scale improves reaction time. If each cell (or small group of cells) had a mini suppression module ready to douse it or isolate it upon a trigger, propagation could be aggressively mitigated [213].

3.2.2 Active Mitigation Methods at Module Level

A battery module typically consists of multiple cells grouped together (in series and/or parallel) with physical proximity, held in a frame or enclosure, often sharing cooling and monitoring infrastructure. When a cell in a module goes into TR, the heat and fire can quickly threaten adjacent cells. Module-level mitigation strategies focus on preventing propagation from the initial failing cell to its neighbours and managing the event within the module so it does not escalate to the pack. Active approaches at this level include thermal barriers coupled with cooling, module-integrated fire suppression (such as aerosol or liquid agents that deploy within the module), electrical isolation of a failing cell or group, and venting mechanisms to relieve and direct hot

gases out of the module. Many of these strategies operate together with the module's design features (passive barriers, etc.), but introduce an active element - such as a trigger that releases a suppressant or turns on enhanced cooling flow when a problem is detected. Following topics are discussed:

1. thermal management and cooling systems employed at module level for TR mitigation
2. active suppression agents inside modules (sprays, aerosol generators, etc.),
3. module segmentation and electrical disconnection approaches.

Enhanced Cooling and Heat Dissipation

One straightforward way to prevent a single cell's TR from igniting its neighbours is to rapidly remove heat from the vicinity of the failing cell, keeping adjacent cells below their ignition temperature. Modules often include cooling infrastructure (e.g. cooling plates, fins, or liquid coolant channels) as part of the BTMS for normal operation. Leveraging this for safety, an active BTMS response can flood a module with maximum cooling when a hotspot is detected. For example, in EV modules with liquid cooling plates, if a cell's temperature sensor triggers high, the cooling system could ramp up flow rate in that module or direct coolant preferentially to that area. Experimental studies indicate that active liquid cooling can significantly slow thermal propagation. Under a forced liquid cooling flow, the propagation from a triggered cell to its neighbour could be delayed long enough that the neighbour did not reach its TR threshold at all, effectively confining the event to one cell [214]. An example of such cooling plates and channelling is shown in Figure 3.7.

Industry has begun to integrate heat sensors and even pipe networks in modules, designed such that if one cell vents hot gas, the heat triggers a sprinkler-like release of coolant in that module [216]. One active method along these lines is the spraying until TR is finished: modules equipped with sprays that activate to douse cells upon overheat have been shown to effectively prevent TR propagation at the module level. The spray can be of a coolant or fire retardant liquid. The timing is crucial - it must activate right when the first cell goes into TR (detected via temperature, smoke, or pressure sensor) to soak the neighbouring cells and absorb heat. Such active spraying delayed or entirely avoided the ignition of adjacent cells in test modules, as the cooling and flame suppression took effect almost immediately [217]. Although the integration of additional subsystems - such as fluid reservoirs, pumps or pressurized canisters, and sensor arrays - introduces design complexity, such active strategies may constitute a transformative solution for modules containing densely packed, high-energy cells. An alternative concept involves incorporating dedicated TR "stopper" elements. These components do not operate as conventional cooling systems, but rather they are engineered to actively extract or redirect heat, thereby interrupting or mitigating the propagation of thermal events.

Immersion cooling could act as a thermal management method and as an ultimate TR suppressant, because any vented flames or sparks are immediately surrounded by liquid. A recent modelling study proposed an immersion system where, upon detecting a failing cell, the fluid is vigorously circulated to enhance convective cooling and even boil (carrying heat away via latent heat) [218]. Such a system could theoretically keep all cells below critical temperature, albeit with the complexity of keeping the battery in a bath of coolant. Nevertheless, some stationary BESS have started exploring coolant immersion as a safety feature rather than just a performance feature, because a non-flammable coolant can act as a TR firewall around each cell.

Module-Integrated Fire Suppression

Beyond cooling, modules can be equipped with fire suppression agents that deploy in the event of TR. One example is the use of condensed aerosol generators inside battery modules or enclosures. Aerosol fire suppression units are small canisters containing solid compounds that, when

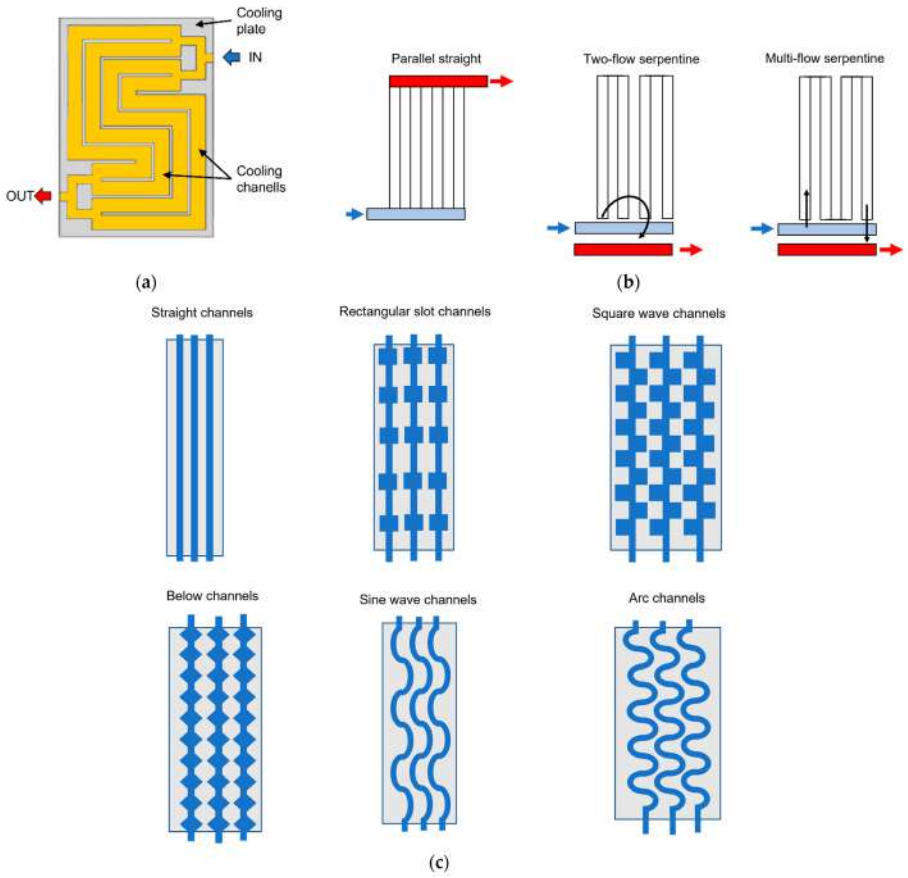

Figure 3.7: (a) Optimization of cooling plate serpentine flow channels with splitter blades; (b) schematic of channel connections; (c) mini-channel cold plate designs [215].

electrically triggered or ignited by heat, release a flood of fine particulate aerosols (typically potassium carbonate and related particles) that fill the volume and chemically inert the flames. In the context of a battery module, an aerosol unit could be set to discharge if a temperature spike or smoke is detected [219, 220].

There have been tests of aerosol suppression on lithium battery fires: an aerosol concentration of about 60 g/m^3 inside a container could successfully extinguish a battery fire and prevent reignition for at least 1,800 s [221]. Det Norske Veritas (DNV) carried out large-scale testing where aerosol units extinguished a lithium-ion rack fire in a confined space, showing the agent can be effective in knocking down flames quickly [222]. The advantage of aerosol is that it is stored in compact form and can be deployed rapidly, and it leaves no water residue. However, there are caveats: aerosol does not cool the cells significantly, so while it may extinguish flames, the cells may still be hot and can reignite if oxygen becomes available again. The solid particles can be corrosive or cause short circuits if they penetrate battery electronics, and the loss of visibility inside an enclosure can hinder manual firefighting. Because of these issues, it is advised aerosol agents alone should not always be a comprehensive solution for battery modules, especially in scenarios where ventilation will eventually bring fresh air (leading to possible flashover) [222, 114]

Another approach is incorporating liquid fire suppressants within modules. A small quantity of suppressant (water, foam, or a special chemical store) in the module can be stored that gets released when needed. There are patented systems (e.g. by DAFO Vehicle in 2020 [223]) describing a tube or bladder that runs through the module which will rupture and dispense a fire suppressant when a certain high temperature is reached. This is a passive activation but results in an active suppression action. The suppressant could be a coolant like 3M Novec or an encapsulated water mist. Tests with water mist have shown that fine mist can cool and inert

flames effectively in battery fires, although water alone might not permanently prevent re-ignition unless applied in large volume or with additives.

So module-level systems often consider additive-enhanced water or foam. Foam extinguishing agents (such as those used for fuel fires) can also be applied to battery modules. Foam has the benefit of forming a blanket that both cools (mostly water-based) and smothers by excluding oxygen. A recent study evaluated injecting firefighting foam into an EV battery pack and found it did suppress the fire; however, the thermal energy inside the pack was not removed as quickly as with water, leading to the pack still being hot (around 50 °C) after extinguishment [224, 225].

Electrical Isolation and Module Segmentation

Active mitigation at module level is not only about controlling thermal and fire effects, but also about electrical interventions to minimize cascading failures. In a series-connected string of cells (typical in modules), if one cell goes into TR and internally short-circuits, it can suddenly draw energy from neighbouring cells (those in parallel) or cause large current surges through itself from the rest of the string. This can accelerate heating and also damage other cells electrically. Therefore, an active strategy is to electrically isolate a failing cell or subgroup once a failure is detected. While CIDs and fuses discussed at the cell level achieve disconnection at the cell itself, module-level isolation might involve contactor or pyrotechnic disconnects at the module's terminals. Some advanced battery packs include pyrotechnic switches that can isolate entire modules from the pack within milliseconds when a severe fault is detected. For example, if a module's voltage collapses rapidly (indicating an internal short), the BMS could fire a pyro-fuse to sever that module's connection, preventing other modules from dumping charge into it and feeding the fire. This strategy has been used in EVs mainly to protect against crash-induced internal shorts; it is an active measure as part of a vehicle's safety system (like airbags). By segmenting the pack, each module is limited in the energy it can release. On a finer scale, there has been conceptual research on cell-level disconnects within modules. One idea is using solid-state relays or addressable fuses on every cell, so that if a cell is suspected to fail, the BMS can disconnect it [226, 227].

However, implementing dozens or hundreds of such switches is complicated and cost-prohibitive with current technology. Instead, the focus is on module level: ensure that a failing module does not drag others with it. EV manufacturers now design packs to meet regulations that require thermal propagation to be limited. Active module isolation is one means to meet this requirement. In practical terms, this could mean if one module starts venting and burning, the car's systems disconnect that module electrically and perhaps even activate cooling just for that module (if coolant loops can be zoned), attempting to confine the event [67].

3.2.3 Active Mitigation Methods at Pack/System Level

Pack or system level mitigation encompasses all the higher-level strategies employed to control TR impacts in the context of an entire battery pack or an entire stationary energy storage system. At this level, the approach becomes more holistic: the system may include fire suppression systems (sprinklers, gas flooding, etc.), ventilation and exhaust management, thermal management coordination across modules, and integration with facility or vehicle safety infrastructure. In an EV, pack-level safety might involve the design of the pack enclosure to contain or direct fires, the vehicle's computing system taking action (e.g. limiting vehicle motion, alerting occupants), and coordination with first responder procedures. In a stationary BESS, system-level mitigation includes dedicated detection (smoke, gas sensors), automatic fire suppression installations, and emergency response protocols tied into the installation [225, 228]. Key active strategies at this level are discussed:

1. fire suppression systems using gaseous, liquid, or solid agents on the pack or enclosure scale,

2. ventilation and explosion prevention measures for confined battery spaces,
3. pack thermal management and segmenting as an active containment strategy,
4. the differences in implementation between EV packs and stationary systems.

Fire Suppression Systems (Gas, Liquid, Solid Agents)

Large battery systems often rely on fire suppression systems akin to those used in buildings or engine compartments, but tailored for battery hazards. The choice of suppression agent is crucial, as evidenced by extensive research since 2020 into what agents most effectively control LIB fires. Broadly, suppression agents are categorized as gaseous (clean agents and inert gases), liquid (water, foams, special solutions), or solid (powders, aerosols). Each has advantages and drawbacks in LIB scenarios, and often a combination (or sequential use) is recommended for best results [228].

Gaseous Suppression: Common clean agents include CO_2, Halon replacements like HFC-227ea (FM-200) [229] and FK-5-1-12 (Novec 1230) [230], and emerging agents like 2-BTP (2-bromo-3,3,3-trifluoropropene) [231]. These are stored as liquefied gas and released to flood the battery enclosure with an inert or chemically active gas that extinguishes flames primarily by oxygen displacement and heat absorption. Novec 1230, a fluoroketone, has been tested in battery fire scenarios: it requires a certain concentration (design concentration often 5-6% volume per volume) to inert the environment, and it can suppress flames effectively, with one study noting it had much higher efficiency than CO_2 in both open and closed space battery fire tests [232]. However, a critical limitation of purely gaseous agents is cooling - these agents do not remove heat as effectively as water. A battery that has undergone TR will remain very hot internally even after the flames are out. If oxygen is reintroduced (e.g. by opening the enclosure or if the gas concentration drops), the materials can reignite because the core heat was not reduced sufficiently [222, 233].

This was demonstrated in incidents like the Arizona BESS explosion in 2019. A clean agent (Novec 1230) was deployed and likely snuffed the initial fire, but did not cool the batteries; when firefighters opened the container, air rushed in and a delayed deflagration occurred injuring four firefighters [233].

Recognizing this, the latest strategies often combine gas agents with others. For example, Novec 1230 and water mist have been proposed as a two-stage suppression: Novec is discharged first to knock down flames, immediately followed by a water mist to cool the batteries. It was showed that this combined approach drastically reduced peak battery temperatures and prevented re-ignition, achieving better outcomes than either agent alone. Essentially, the gas handles instant fire suppression and the water provides sustained cooling [146, 234].

Water and Water-Based Agents: Water remains one of the most effective suppressants for battery fires in terms of heat removal. Its high heat capacity and latent heat of vaporisation mean it can absorb enormous amounts of energy. Firefighters commonly use water deluge or mist to control EV and BESS fires. On the order of 0.6 m^3 of water per kWh of battery capacity might be needed to fully extinguish and cool an EV battery fire [235], which translates to tens of thousands of litres for a typical car pack. This large quantity originated from the need of continuous cooling until all cells are below TR self-heating temperature.

In a stationary system, fixed sprinkler systems or deluge systems can be installed. Experiments with full-scale container fires showed that sprinklers could prevent a single-module fire from propagating to the entire container by cooling surrounding equipment and quenching flames on emitted gases [236]. Water mist systems (which produce fine droplets) are particularly attractive because they use water more efficiently: the fine droplets evaporate quickly, displacing oxygen locally and cooling surfaces. One those installations is presented in Figure 3.8 - the system is designed to rapidly cool surfaces, displace oxygen, and suppress combustion in confined LIB installations such as BESS containers or EV charging enclosures. High-pressure nozzles

produce microdroplets (<200 μm) that evaporate efficiently, absorbing heat and reducing the risk of TR propagation [237].

Figure 3.8: Industrial water mist fire suppression system with overhead nozzles actively discharging a fine mist over a battery module area [237].

Numerical analysis of a 20-ft BESS container fire indicated that a water mist system significantly reduced flame temperatures and delayed pressure rise, thereby mitigating explosion risk [238]. The drawback of water is the potential to generate toxic run-off (water will dissolve HF, Li salts, etc., creating contaminated coolant) and it can also react with certain battery materials (e.g. residual metallic lithium or hot $LiPF_6$ salt can hydrolyse to HF). Nonetheless, the consensus in safety research is that water is indispensable for cooling, and the goal is to use it in a smart way: for instance, adding additives to water to improve its performance.

One class of additives are surfactants and encapsulators like F-500 (a proprietary firefighting additive). These additives can improve water's wetting of surfaces (better penetration into battery pack crevices) and also encapsulate hydrocarbon molecules or absorb toxic gases [239]. Tests by the German DEKRA institute compared F-500 solution to plain water and dry powder on LIB fires; F-500 was found to reduce the release of flammable gases and help water soak into the battery modules more effectively, leading to faster knockdown of fire and less risk of reignition [240]. F-500 is essentially a micelle-forming agent that can capture certain volatile organic compounds and also reduce water's surface tension.

Ventilation, Exhaust Management, and Explosion Prevention

When LIBs go into TR, they release a mix of flammable gases (CO, H_2, light hydrocarbons, etc.) and toxic by-products (HF, HCl, etc.) [130]. In a confined space, these gases can accumulate to explosive concentrations. Therefore, an active mitigation strategy at system level - especially for stationary BESS installed in buildings or containers - is proper ventilation and exhaust management. This includes both venting mechanisms that activate during an event and pre-emptive ventilation triggered by gas detection. For BESS enclosures (like walk-in containers full of battery racks), design guidelines (such as NFPA 855 and UL 9540A test data) emphasize

having explosion relief panels or vents sized to release pressure safely in case of a deflagration.

Active ventilation systems (powered fans) are often installed to purge flammable gases. A typical system might have gas detectors that, when reaching a low-level limit, turn on exhaust fans to dilute the atmosphere [241]. If high levels are detected, the system might also trigger an alarm or suppression. The enclosure's ventilation is able to be shut off during the initial stages (to starve the fire of oxygen), but this allows flammable concentration to build [233]. Developing a safer approach presents a challenge, as it requires minimizing the risk of exacerbating combustion through oxygen introduction while also preventing hazardous gas accumulation. The current best practice is to use ventilation after suppression: first, extinguish the flames with a clean agent, then vent out the gases before opening the enclosure. This requires coordination in the control system. For example, an active controller could, upon TR detection, isolate the electrical system, release a clean agent, wait a prescribed time, then activate roof exhaust fans to slowly clear the atmosphere. Such systems are integrated into their battery management units. For indoor installations (e.g. batteries in a dedicated room of a building), building codes require smoke exhaust systems. These can be repurposed or enhanced for battery gas exhaust. One active approach is the installation of blow-out panels or flame ducts: if pressure or flame is detected, a duct opens to route the hot gases and flames through a safe path (like a chimney) to the outside. This is essentially an active vent that saves the facility from uncontrolled explosions. Explosion prevention is closely tied to early gas detection. Pressure rise inside an enclosure can be an earlier indicator of TR than temperature [213].

Examples of passive elements are shown in Figure 3.9. An example valve is shown in Figure 3.9a - Eaton's 3-in-1 battery pack vent valve for EVs. This engineered vent device integrates three functions – a one-way check valve for passive venting, an active venting actuation, and a leak-check mechanism. Under normal conditions it stays sealed to maintain pack integrity, but if internal pressure rises (e.g. due to cell TR generating gas), the spring-loaded valve pops open at a low set pressure to rapidly relieve overpressure [242]. Cells are also designed to provide proper venting paths such as shown in Figure 3.9b. These routing of the fumes allows to expel them in controlled manner. Example of a roof-mounted explosion vent panel (product image by REMBE) is shown in Figure 3.9c. This is a lightweight rectangular vent panel designed for installation on a BESS container roof (model BESS.IKLI-EGV). It features a scored outline and central weak section that will tear open at a defined breaking point when internal pressure from a deflagration pushes against it. Such vents are one-time use: the panel will permanently deform and must be replaced after activation [243]. Figure 3.9d shows deflagration vent panels on a BESS container, deploying during a TR gas explosion test. This render shows a cargo-style battery container with roof-mounted explosion vents popping open and directing flames upward during an internal battery fire (panels shown in open position with flames venting). BESS units often incorporate large thin metal blow-out panels on their roofs or walls that act as weak sections to relieve pressure in case of a gas deflagration. In an event, these panels burst at a low pressure (e.g. $\sim$0.05 bar) and vent the hot gases and flames to the outside, preventing the container from violently exploding like a pressure vessel [244].

3.2.4 Comparative Analysis: Electric Vehicle vs. Stationary Energy Storage System Thermal Runaway Strategies

Both EV and stationary ESS seek to mitigate TR, but the context and constraints lead to different emphases in strategy. EV are on the move and the space and weight in a vehicle is limited. ESS, in contrast, are stationary and batteries are often housed in dedicated containers or battery rooms. It is compared how EV and stationary ESS approaches diverge or converge across the various levels of protection, highlighting key differences in design philosophy, regulatory requirements, and practical implementation.

Both electric vehicles and stationary battery energy storage systems seek to mitigate TR, but the context and constraints lead to different emphases in strategy. It is compared how EV

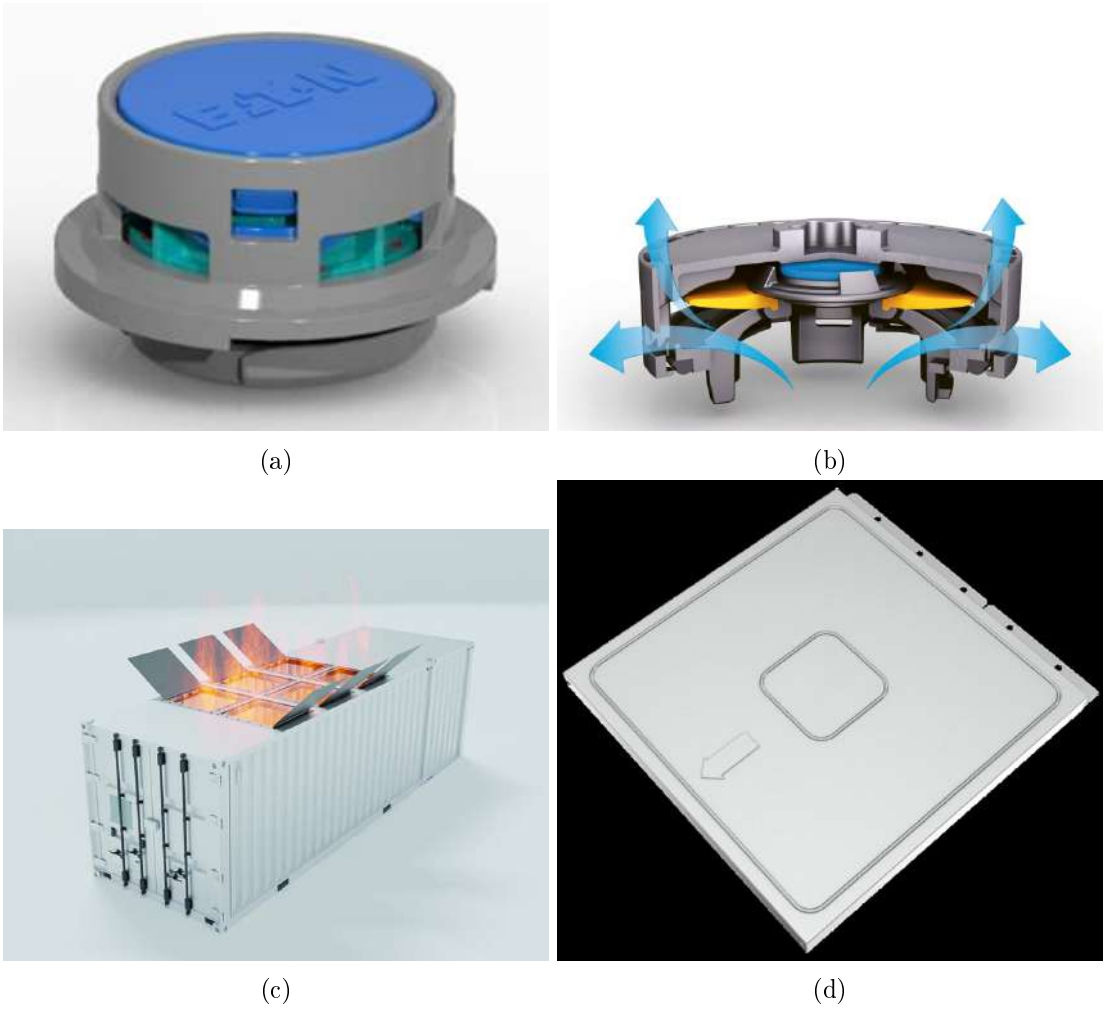

(a) (b)

(c) (d)

Figure 3.9: Examples of segmentation and firebreak features. (a) Eaton's 3-in-1 battery pack vent valve for EVs [242]; (b) Example of vent path for the cylinder battery cell; (c) Deflagration vent panels on a BESS container [244]; (d) Example of a roof-mounted explosion vent panel (product image by REMBE) [243].

.

and BESS approaches diverge or converge across the various levels of protection, highlighting key differences in design philosophy, regulatory requirements, and practical implementation.

1. **System Environment and Constraints:** EV batteries face mechanical stresses (vibrations, crashes), and the presence of passengers. BESS batteries have closer proximity to critical infrastructure or buildings. These conditions influence mitigation choices. EV manufacturers design pack intrinsic safety solutions (e.g. robust cell design, module barriers, BMS controls) to prevent TR, but largely rely on external emergency response (firefighters using water) for full suppression. In contrast, a stationary ESS can include active fire suppression systems (e.g. a complete sprinkler or clean agent system installed in the container).

2. **Detection and Monitoring:** Both EVs and ESS employ extensive monitoring, but ESS installations might have additional layers like video thermal cameras or multi-point gas detection across a facility. An EV's BMS typically monitors each cell's temperature (or a representative cell per group), voltage, and pack current. It can trigger warnings on the dashboard and even instruct the vehicle to slow down or shut off if a battery issue is detected. ESS, especially large ones, often tie into building management systems. ESS are

more likely to incorporate redundant sensors (for example, both a smoke detector and a heat detector in the battery room). EVs, due to cost and complexity, usually have only the necessary sensors for BMS function - rarely smoke sensors inside packs. For instance, EV packs now include vented enclosures with pressure sensors; a sudden pressure rise in the pack can be sensed and trigger pack isolation. ESS containers commonly have gas and smoke sensors connected to automatically cut off HVAC and initiate suppression. EVs do not have on-board gas sensors for battery vent gas, although one could envision future designs where the cabin air sensor might detect a sweet solvent smell of electrolyte as a warning.

3. **Fire Suppression and Cooling Implementation**: on-board suppression in EVs is limited. Exceptions are made in public transport buses and specialized vehicles, which have fire suppression similar to engine fire systems (typically a cylinder of aerosol or Novec that can discharge into the battery compartment). EV packs are designed with features like thermal barriers between cells or modules, and directional venting to manage a TR event. EV makers also use lower flammability chemistries [177, 245]. ESS, on the other hand, often store much larger total energy and are usually maintenance-free, so they incorporate robust active suppression: sprinkler systems in battery rooms, or clean agent flooding systems in containers. Indoor ESS are usually covered by building sprinklers per code. ESS designs opt for a strategy to allow to burn through and heavily vent the container, and then rely on firefighters, to reduce system cost (no suppression installed). This approach has largely fallen out of favour after incidents showed the risk of explosions; now the trend, supported by insurers and codes, is towards including at least some automatic suppression in ESS. EVs effectively default to a let-burn strategy once passengers are safe - firefighters often let an EV fire burn under controlled conditions or drown it in water.

4. **Ventilation and Explosion Relief:** An EV battery is relatively small and in open air, thus an explosion from gas build-up is not a typical concern (the gases will dissipate around the vehicle, unless it happens in a garage or tunnel). For ESS, deflagration prevention is critical. ESS containers have features like pressure relief panels that will blow out at low overpressure to direct an explosion upwards, and forced ventilation. EV pack enclosures are typically not airtight - they will vent to the environment if cells rupture. Automotive packs usually vent outside or under the vehicle for this reason. ESS are explicitly engineered now with NFPA guidelines: e.g., a certain vent area per volume and/or mechanical exhaust fans.

5. **Scale and Redundancy:** A single EV might have on the order of 5–100 kWh of batteries. A grid storage ESS can have 1–100 MWh of batteries in one site - orders of magnitude more cells. This scale means that propagation in ESS can involve thousands of cells, releasing far more energy and potentially a much larger fire than an EV. ESS strategies put strong emphasis on propagation prevention at early stages. Many BESS now use modular isolation. Each rack or module is physically separated by fire-resistant walls from the next, and the system is laid out to satisfy that a fire in one unit will not immediately propagate to the next. EV packs, by contrast, pack cells tightly to maximize energy density and rely on internal mitigation, but cannot use heavy firewalls between cells due to weight. Design strategy related to used materials differ: EVs may incorporate innovative lightweight materials (aerosol foams, etc.) as fire barriers, whereas ESS can use concrete walls or steel partitions between battery stacks.

6. **Regulatory Landscape:** In automotive, standards and regulations (UNECE R100, ISO 6469-1, etc.) focus on passenger safety and electrical safety. They require tests like nail penetration, crush, overcharge, etc., and usually the criteria is no fire or explosion in a specified time frame. If a certain battery type shows in tests that a single module fire

does not propagate and self-extinguishes, authorities might allow omission of sprinklers. EV makers, try to ensure one module burning will not make the whole vehicle explode instantly.

7. **Post-event and Recovery**: In EV, the typical mitigation is to extinguish if possible and then monitor. Often EVs are quarantined after a fire (some are submerged in a water tank for days to ensure no re-ignition). This is external to the vehicle's own systems. Stationary ESS operators must also plan for post-event cooling - many now have procedures to keep affected battery racks under water spray for hours after suppression. From a design viewpoint, some ESS include thermal imaging cameras that remain on to watch for any reheating of cells after the main fire is out, and if detected, could re-trigger suppression or alarms. EVs do not have such ability - once the 12 V system is likely compromised in a fire, any cameras or sensors would be down. Both share the goal of preventing catastrophic outcomes, but their means reflect their use-cases. Interestingly, cross-pollination of ideas is happening: EV manufacturers are learning from stationary suppression research (for example, incorporating non-toxic gas cooling agents inside packs), and ESS designers are adopting EV battery innovations (like cell-level fusing, thermal barriers from automotive industry). One convergence is the use of battery chemistry as mitigation: LFP chemistry, which is inherently safer (lower heat output, no oxygen release from cathode), is being widely adopted in stationary storage and increasingly in EVs for standard-range models. By choosing a more thermally stable chemistry, both EV and ESS reduce the likelihood and severity of TR, an inherently active choice at the design stage. Finally, cost and maintenance considerations differ: a BESS might have a maintenance schedule to, say, check the pressure of the fire suppression cylinders yearly, whereas an EV is consumer product with minimal maintenance, its safety features must be mostly self-contained and reliable for the life of the car without servicing. This affects what can be practically deployed.

3.2.5 Summary on Active Systems

TR in LIBs remains a critical safety concern, but the advancements in active mitigation and suppression strategies in recent years offer a robust toolkit to manage this risk in both electric vehicles and stationary energy storage systems. Through this section, we have examined layered safety approaches from the cell level up to full battery systems, highlighting how a combination of preventative control, real-time detection, and emergency intervention can drastically reduce the probability of a minor cell fault escalating into a large-scale fire or explosion.

Modern LIB cells are being equipped with an array of internal safety devices (CIDs, PTC elements, vent mechanisms) and even novel material-based shutdown features that act in synergy to halt the onset of TR. Experimental evidence shows that these can be effective in isolating failing cells electrically and slowing thermal build-up, though they are not foolproof. The trend is towards integrating intelligent safety at the material level (e.g., thermally-triggered conductive additives that halt current) [162, 209]. Combining these intrinsic measures with external BMS oversight (voltage/temperature monitoring and active cut-off) provides two layers of cell protection - one acting automatically within the cell and one via the system's brain.

If a cell does enter TR, the module-level strategies determine whether the event stays localized or propagates. It was found that active cooling and fast suppression at the module level can contain even violent cell failures. Techniques like dedicated coolant loops that activate on overheat, or small-scale suppressant releases (water mist, aerosol) inside modules have been demonstrated to prevent fire spread to adjacent cells [208, 246]. Thermal and mechanical barriers remain important, but adding active elements (sensors and actuators that respond within the first few seconds of a TR) greatly improves outcomes. The concept of a self-extinguishing battery module - one that can detect a burning cell and autonomously put out the fire before it

leaves the module - is becoming reality through these innovations.

At the largest scale, active measures like full-system fire suppression, emergency ventilation, and pack disconnects ensure that even if a module fails, the situation can be controlled and kept from endangering occupants (in EVs) or facilities (in BESS). Gaseous agents (Novec, 2-BTP, etc.) and water-based cooling have complementary roles and are often best used in combination [220, 235]. The importance of managing flammable gas and pressure build-up in enclosed systems is underscored by past accidents; thus, active venting and exhaust systems are integral in BESS designs. EV pack designs channel hazards away from people, and vehicle-level responses (like warning drivers, immobilizing the vehicle, etc.) are an active safety aspect distinct to EVs.

A comparative analysis revealed that while the underlying problem (TR) is the same, the strategies diverge due to environment. EV mitigation focuses on built-in safety and allowing time for occupant evacuation, whereas BESS mitigation invests heavily in automatic suppression and containment on-site. Neither approach is inherently better; each is optimized for its scenario [241, 247].

Despite progress, challenges remain in making these active systems fail-proof and widely adopted. False positives in detection systems can cause unnecessary activations (for example, accidentally discharging a fire suppressant in a battery container due to a sensor error can be costly and dangerous), so reliability of sensors and algorithms is paramount. The harsh environment inside battery packs (electrical noise, electromagnetic interference, mechanical shock) can make sensor readings unreliable. Another challenge is scalability and cost, adding suppression systems and complex controls increases cost, which must be justified by the risk reduction. For EVs especially, manufacturers tread a line between safety and cost to weight ratio. Nonetheless, the increasing attention from regulators and the public to battery fires likely means safety features will become selling points, not options.

In conclusion, active mitigation and suppression strategies greatly enhance the safety envelope of LIBs, which are the linchpin of modern electrified transport and energy storage. By deploying intelligent control, fast-acting protection devices, and effective firefighting measures at multiple system levels, it is possible to prevent many TR incidents and to significantly limit the damage from those that do occur. With diligent engineering and adoption of these strategies, catastrophic battery fires can transition from a headline-grabbing rarity to an almost "managed" event that, while still serious, can be handled without widespread harm. Ongoing research and real-world validation will continue to refine these approaches, moving us closer to inherently safer high-energy battery systems.

Chapter 4

Aim of the Thesis

In light of issues presented in the previous chapters, the dissertation posits a formal thesis that:

> ***It is possible to develop a quantitatively-grounded methodology to test lithium-ion battery fire safety and mechanical integrity with greater precision, repeatability, and diagnostic value than current regulatory procedures.***

It is declared the methodology for testing energy storage systems used in alternative energy sources can be developed with their fire and mechanical resistance being tested. Specifically, it is stated that by leveraging standardized fire testing protocols and by implementing rigorous sensor instrumentation, one can create a test for LIB systems, which produces consistent, repeatable thermal exposure and rich data on the battery's response. This approach is expected to significantly reduce measurement uncertainty and overcome the variability seen in open-fire tests, thereby yielding results that are both more reliable (scientifically repeatable) and more relevant for safety engineering. The hypothesis is rooted in the observation other industry standards, which are highly standardized and reproducible, thanks to strict protocols on thermocouple placement, furnace pressure, etc. By importing these well-established fire-testing practices into the battery safety domain, the test conditions can be made far more uniform and controllable than a free-burning fuel fire. The ultimate goal is that such a methodology would not only improve testing precision, but also provide deeper insight into the degradation processes of batteries under fire and mechanical stress.

Building on the background problem and thesis, the aim of the thesis is to develop and demonstrate a scientifically rigorous methodology for evaluating the fire-induced degradation processes in modern battery systems (RESS and their protective structures). This overarching aim can be understood as two complementary objectives to be implemented into works of Laboratorium Badań Ogniowych Centrum Techniki Okrętowej S.A.:

1. to critically analyse the current landscape of battery safety (both the phenomena of TR and the standards designed to address it) in order to pinpoint exactly where and why present testing methods fall short,

2. to formulate and validate an improved testing approach that addresses those shortcomings, thereby enhancing both our scientific understanding and practical safety evaluations of LIB systems.

In pursuing this aim, the research not only seeks to answer specific scientific questions, but also to produce outcomes directly relevant to industry regulators such as recommendations for new or rewritten test standards or design guidelines for safer battery systems.

The title of this dissertation — *Methodology for Investigating the Degradation Processes of Modern Materials Used in Alternative Energy Sources Exposed to Fire and/or Mechanical Overloads* — reflects the dual nature of the phenomena investigated and the interdisciplinary character of the research.

The term *mechanical overloads* encompasses stresses that arise as a *effect of thermal exposure*. When lithium-ion batteries and their protective enclosures are subjected to fire, the resulting non-uniform temperature field induces thermal stresses within structural components. These thermally induced stresses may cause local yielding, delamination, or fracture of the construction elements, ultimately compromising the mechanical integrity of the entire system. Hence, the phenomenon of *fire-induced mechanical degradation* constitutes one of the central aspects analysed within this work.

The term *structural integration* in the context of this research refers to the material and mechanical continuity of the energy storage system. Maintaining structural integration implies the absence of cracks, ruptures, or leakage paths that could enable gas venting or flame propagation between battery modules. Conversely, the *loss of structural integration* represents the onset of critical failure – a state that, under extreme conditions, may escalate into explosion or complete mechanical disintegration of the system.

The developed methodology thus addresses these coupled degradation modes by integrating the thermal, mechanical, and diagnostic perspectives within a unified testing framework. This holistic interpretation clarifies the conceptual link between the two main components of the title – *fire* and *mechanical overloads* – and justifies their integration under one methodological framework aimed at quantifying and reproducing the degradation processes in modern energy storage materials and structures.

This work also involves data collected through testing multiple real-life samples introduced into actual use in EV, stationary ESS or railway auxiliary ESS. While this adds to the practicality value of the results presented in the thesis, simultaneously author wished to note they are limited to the scope agreed upon non-disclosure and confidential disclosure agreements signed by the customers of Centrum Techniki Okrętowej S.A.

Chapter 5

Overview and Analysis of Standardisation of the Battery Energy Storage Systems Testing

Standardisation plays a pivotal role in the development, implementation, and safety assurance of modern technological systems. In the context of engineering, standardisation refers to the establishment and application of agreed-upon norms, protocols, and procedures intended to ensure consistency, interoperability, safety, and quality of products and processes across various domains [248, 249]. These standards are typically developed by international and national bodies such as the International Organization for Standardization (ISO), International Electrotechnical Commission (IEC), and national institutes like the American National Standards Institute (ANSI) or the National Fire Protection Association (NFPA). By fostering comparability, enhancing transparency, and reducing technical barriers to trade, standardisation has become an essential mechanism for supporting technological innovation while ensuring public safety and regulatory compliance.

In the rapidly evolving field of BESS, standardisation is particularly critical due to the diverse applications, complex architectures, and safety challenges associated with energy storage technologies. BESS are utilized in a broad range of applications, from grid balancing and renewable energy integration to electric mobility and emergency power backup. These systems are composed of intricate assemblies of cells, modules, and supporting hardware governed by complex thermal, electrical, and chemical interactions. As such, the development and harmonisation of testing standards is essential not only to certify performance but also to minimize risks associated with TR, electrical faults, or mechanical abuse scenarios [25, 87, 250].

The process of standardisation in BESS testing typically involves the formulation of prescriptive or performance-based test methods to simulate real-world failure conditions. These include fire resistance (e.g., UL 9540A), mechanical shock and vibration (e.g., IEC 62660 series), and abuse testing (e.g., UN 38.3). Such standards are designed through collaborative processes involving technical experts, industry stakeholders, regulatory bodies, and academic researchers. This collaborative nature ensures the incorporation of empirical data, best engineering practices, and evolving scientific understanding into test specifications. Nevertheless, as various studies show, many existing standards may suffer from inconsistencies or ambiguities - particularly in sensor placement, acceptance criteria, or simulation fidelity - which may affect reproducibility across laboratories [250]. A Table 5.1 details the standard name, reference, issuing body, issue date, targeted purpose, scope of application, and salient comments for context in research and compliance frameworks.

Moreover, given the dynamic development of battery chemistries and system configurations, standardisation efforts must adapt rapidly to encompass new technologies. Emerging materials, such as solid-state electrolytes, novel cathode compositions, and integrated BMS, introduce new

safety and performance variables that require updated testing frameworks. In this context, the role of standardisation extends beyond regulatory compliance and enters the domain of scientific and engineering advancement. Iterative feedback between experimental testing, modelling efforts, and standard development is crucial to capture degradation mechanisms under abuse conditions and to refine the methodologies that govern them [114].

Following chapter provides an overview and critical analysis of the current standardisation landscape related to BESS testing. It aims to outline the rationale, scope, and limitations of key standards; identify inconsistencies in current methodologies; and highlight areas requiring methodological refinement. Particular attention is given to procedures governing thermal and mechanical abuse tests, as these are directly linked to the degradation pathways relevant to lithium-ion based systems. By situating the discussion within both technical and regulatory frameworks, this chapter contributes to the broader discourse on improving standardised testing for safer and more reliable energy storage technologies. List of standards and regulations referenced in the thesis (particularly in given section) has been listed in bibliography and with full titles in Appendix E.

5.1 Standardisation Bodies

United Nations Economic and Social Council (ECOSOC) established in 1945 oversees multiple subsidiary bodies composed of regional commissions, functional commissions and expert bodies, standing committees and bodies [251, 252]. In 1947, The United Nations Economic Commission for Europe (UNECE) was established by ECOSOC, which includes fifty-six member states located in Europe, North America and Asia [253].

UN and UNECE introduced two major regulations for the battery EV safety - *"Uniform provisions concerning the approval of vehicles with regard to specific requirements for the electric power train"* abbreviated often times as R100.03 and Global Technical Regulation No 20 [67, 254]. Only R100 document has the status of mandatory document to comply with before a RESS is placed on the European Economic Area [255]. Both documents show a series of abuse tests including crush test, over-current protection test, vibration test, fire resistance test and (only GTR) thermal propagation test. It is important to underline the thermal propagation test is still being developed at this point and it is not mandatory procedure to undergo by the manufacturers.

International Organisation for Standardization (ISO) is responsible for bringing standards among hundred sixty-seven national standard bodies [256]. Organisation is autonomous and non-governmental, however, their actions and standard development in deeply rooted in the global market needs and based on the global expert opinion and overall consensus among stakeholders [257]. ISO and The European Committee for Standardisation since 1991 co-operate in respect to the standardisation to avoid duplication of the efforts [258].

ISO standard on the RESS safety developed over the years was ISO 12405-3:2014 [259] (from series of ISO 12405 [260, 261, 262]), which was revised to ISO 6469-1:2019 [263] and a separate document for mopeds ISO 18243:2017 [264].

International Electrotechnical Commission (IEC) founded in the 1906 is bound on making electrical and electronic technologies safer, more efficient and reliable [265]. It is a global non-profit organisation, which unites hundred seventy countries. The international standards of IEC serve as the basis for risk and quality management and are used in testing and certification to verify that manufacturers declarations are kept [266].

For EV safety requirements, IEC has developed IEC 62660 series of standards Part 1: Performance testing [267], Part 2: Reliability and abuse testing [268] and Part 3: Safety requirements [269].

Regulation of the European Parliament and of the Council No 1025/2012 states the two bodies are responsible for standardisation in the countries of the European Union - **Committee for Standardisation (CEN) and the European Committee for Electrotechnical Stan-**

Table 5.1: Comparative overview of international standards, regulations, and test methods for LIB safety and performance in electric vehicle (EV), battery energy storage system (BESS), and cell applications.

Name	**Issue Date**	**Issuing Body**	**Purpose**	**Application (EV, BESS, Cell, etc.)**
ISO 12405-1:2011	2011	ISO	Tests for performance, reliability, and abuse (high power)	Battery pack/system (EV)
ISO 12405-2:2012	2012	ISO	Tests for performance reliability (high energy)	Battery pack/system (EV)
ISO 12405-3:2014	2014	ISO	Safety and abuse testing procedures	Battery pack/system (EV)
ISO 6469-1:2019	2019	ISO	Safety requirements for rechargeable energy storage systems (RESS)	Battery system (EV)
UNECE Regulation No. 100 Rev.3	2021	UNECE	Safety of rechargeable battery installation in EVs	EV, battery system
GTR No. 20 (2018)	2018	UNECE/WP.29	Global safety regulation for electric vehicles; electrical safety/BMS	EV, battery system
IEC 62660-1:2018	2018	IEC	Performance and life testing for secondary lithium cells	Cell (EV propulsion)
IEC 62660-2:2018	2018	IEC	Reliability and abuse testing for secondary lithium cells	Cell (EV propulsion)
IEC 62660-3:2022	2022	IEC	Safety tests for secondary lithium cells	Cell (Automotive)
IEC 62933 series	2017-onward	IEC	Safety, planning, performance for BESS	Energy storage systems, BESS
FreedomCAR Battery Test Manual	2013 (Rev. 3)	USCAR/USDOE	Standardized testing methods for HEV/PHEV battery performance/life	Cell, module, battery pack (HEV/PHEV)
SAND2017-6925	2017	Sandia Labs (USDOE)	Abuse test methodology for rechargeable energy storage systems	Cell/module/pack (BESS, EV)
SAE J2464:2009	2009	SAE International	Rechargeable Energy Storage System (RESS) Safety and Abuse Testing Guide	Battery system (EV/HEV)
SAE J2929:2013	2013	SAE International	Minimum safety criteria for lithium battery systems in vehicles	Battery system (EV/HEV)
UL 9540	2025 (Ed. 3)	UL Standards	Safety for energy storage systems and equipment (system-level)	BESS, ESS (stationary)
UL 9540A	2025 (Ed. 5)	UL Standards	Test method for evaluating thermal runaway fire propagation in BESS	BESS, modules, cells
UL 2580	2022 (Ed. 3)	UL Standards	Safety tests for batteries in electric vehicles	Battery (EV, heavy robotics)
UL 1642	2020 (Ed. 6)	UL Standards	Safety evaluation of lithium cells	Cell (consumer, EV, industrial)
UL 1973	2022 (Ed. 3)	UL Standards	Batteries for use in stationary, motive auxiliary power applications	BESS, stationary/motive batteries
UN 38.3	2025 (Rev. 8)	United Nations	Safety testing for transportation of lithium batteries/cells	Cell/module/pack
NFPA 855	2023 (Ed. 2)	NFPA	Installations of stationary energy storage systems (fire safety)	BESS (stationary, ESS)
GB 38031-2020	2020	SAC	Safety requirements for power battery systems in electric vehicles	Battery systems (EV, NEV)

dardisation (CENELEC). The European standardisation goal is to boost the competitiveness of the European industry, in particular when the documents are established in coordination with the global standardisation bodies i.e. ISO and IEC. It plays an increasingly important role in the international trade and the opening-up reach of the product [270].

The European Committee for Standardization is one of three European Standardization Organizations (together with CENELEC and European Telecommunications Standards Institute) that have been officially recognized by the European Union and by the European Free Trade Association as being responsible for developing and defining voluntary standards at European level. CEN unites National Standardisation Bodies of thirty-four countries [271] and focuses on areas such as chemical, construction, consumer products, machinery, materials and other. CEN also co-operates with ISO on the basis of Vienna agreement [258].

The European Electrotechnical Committee for Standardization prepares voluntary standards in the electrotechnical field, which help facilitate trade between countries, create new markets, cut compliance costs and support the development of a Single European Market [272]. Similarly to CEN, it includes National Standardisation Bodies of thirty-four countries [271]. IEC and CENELEC also developed an agreement to work united to avoid duplication of work ("Frankfurt agreement") [273].

Since there are multiple international organisations developing standards and regulations, only the largest EV market members do create procedures on their own, such as the United States and China.

National Highway Traffic Safety Administration (NHTSA) legalizes the equipment of EVs and their batteries in the United States. It regulates the marked through Federal Motor Vehicle Safety Standards (FMVSS) to implement laws from the government [70, 274]. Another regulatory body in America is **Department of Energy (DOE)**, which as released in cooperation with Sandia National Laboratories document for recommended practices in abuse testing of RESS [275, 276]. The FreedomCAR Battery Test Manual and SAND2017-6925 define standardized testing procedures and performance benchmarks for batteries used in power-assist hybrid electric vehicles. It focuses on evaluating battery life, power capability, safety, and reliability through a series of controlled laboratory tests to support automotive development and industry consistency.

Society of Automotive Engineers (SAE) is a USA-based organisation, which globally joins together over two-hundred thousand engineers, technical experts and volunteers in the fields of automotive and aerospace [277, 278]. It develops a number of abuse tests documents, which are implemented to identify behaviour of EVs outside their standard operating range.

One of such documents regarding RESS safety tests is SAE J2464:2009 [279], containing series of mechanical, electrical and thermal tests that main goal is to investigate scale of safety hazard of given product in abusive conditions. SAE J2929:2013 [280] specifies safety requirements and test procedures for lithium-based rechargeable battery systems used in electric and hybrid vehicle propulsion. The standard addresses aspects such as electrical, mechanical, thermal, and functional safety to ensure reliable operation and minimize hazards throughout the battery system's lifecycle.

Underwriters Laboratories (UL) is a global safety science organization renowned for developing standards and conducting rigorous testing to ensure the safety and reliability of products, systems, and services. Their work spans a wide range of industries, with a significant impact on electrical, battery, and energy storage technologies. UL's standards, such as those for LIBs and energy storage systems, are widely adopted in the US and internationally, shaping regulatory compliance and industry best practices. Through its commitment to research, certification, and education, UL plays a crucial role in advancing public safety and fostering innovation in emerging technologies.

UL developed various standards for batteries used in EVs as well as BESS, such as UL 9540 (2023) [281] on energy storage systems, UL 9540A (2025) [282] on TR tests of energy

storage systems, UL 2580 (2020) [283] for batteries used in electric vehicles and other auxiliary standards as UL 1642 [284] and UL 1973 [285].

UN 38.3 establishes rigorous safety requirements and test protocols for the transport of lithium cells and batteries to ensure their safe handling during air, sea, and land shipment. The standard details procedures such as altitude simulation, thermal testing, vibration, shock, external short circuit, impact, overcharge, and forced discharge to verify battery safety before transportation [286].

National Fire Protection Association (NFPA) is a U.S.-based non-profit organization dedicated to reducing fire hazards and promoting public safety through codes and standards. In the context of LIBs and BESS, the NFPA has developed comprehensive fire protection guidelines that are widely recognized by industry and regulatory bodies. Notably, NFPA 855 (2023) [198] establishes installation requirements for stationary energy storage systems, including parameters for spacing, ventilation, fire suppression, and emergency response. The standard incorporates findings from battery fire research and real-world incident analysis, promoting risk-informed design and operational practices.

Moreover, NFPA 68 [287] and NFPA 69 [288] provide criteria for explosion protection systems, which are critical for mitigating TR events in confined spaces. These standards work in conjunction with fire test protocols and detection methodologies, offering a framework that balances safety with innovation in energy storage technology. Through its consensus-driven approach, the NFPA contributes to the safe integration of BESS into buildings and infrastructure, supporting the broader transition to renewable energy systems.

The Standardization Administration of China (SAC) makes documents regulating EV manufacturing and its components. The documents are recognized in countries such as Canada, Japan, Korea and Germany. SAC is a member of ISO and IEC and is responsible for Chinese National Committee in these organisations [289].

Due to large market of electrically propelled vehicles in China [17], SAC has advanced significantly in the RESS standards development. The newest document consolidates the EV test procedures GB 38031-2020 [73] and it introduces as a first country requirement to conduct thermal propagation tests. Abusive tests has been largely described in previous edition of the standard GB/T 31467.3-2015 [72].

5.2 Mechanical Test

Mechanical tests are critical in ensuring the safety and integrity of RESS in electric vehicles under physical stress. Regulatory frameworks in major automotive markets - notably the European Union, United States, China, and international standards - prescribe a series of mechanical abuse tests for vehicle battery systems. These tests simulate conditions ranging from vehicle crashes and vibrations to accidental drops or intrusions, aiming to verify that a battery pack can withstand such events without causing hazardous outcomes [254, 263, 275, 73, 276, 286].

The primary mechanical tests mandated in various regulations include: mechanical shock (simulating sudden acceleration or deceleration forces as in a collision), drop tests (accidental battery drop during handling), penetration tests (impaling by sharp objects leading to internal short circuits), immersion tests (flooding or submergence scenarios), crush tests (compression forces as in a severe crash or structural collapse), and vibration tests (prolonged exposure to road-induced vibrations). Subchapter provides a comprehensive review of these mechanical test procedures as specified in automotive battery safety standards, comparing key parameters and acceptance criteria across different regulatory regimes.

Each section below addresses one category of mechanical test, summarizing the test's purpose, procedural description, equipment setup (including any sensor placement or instrumentation), and key test parameters as defined by various standards. Where applicable, differences in test levels (cell, module, pack, or vehicle level testing) are highlighted. Detailed comparative tables

are provided for each test type, listing parameters such as accelerations, forces, drop heights, velocities, durations, orientations, and other conditions specified by different standards.

In addition, the pass/fail acceptance criteria generally focused on preventing catastrophic outcomes like fire, explosion, leakage, or electric shock are discussed for each test. It should be noted that virtually all regulatory standards require that during and after these mechanical tests the battery does not exhibit dangerous behaviour: for example, UNECE R100.03 stipulates that the battery system must not catch fire, explode, leak electrolyte, or rupture its enclosure under any of the prescribed tests [254]. Similarly, many standards (e.g. ISO 6469-1, ISO 12405-3, UL 2580) explicitly set - no fire, no explosion, no rupture, and no leakage - as the criteria for passing mechanical abuse tests [259, 263, 283]. High-voltage batteries are also typically required to maintain electrical isolation above a minimum threshold after testing. These stringent criteria ensure that even if a battery is severely damaged, it will not endanger vehicle occupants or first responders.

5.2.1 Mechanical Shock Tests

Mechanical shock tests evaluate a battery system's robustness against sudden acceleration or deceleration, analogous to the inertial forces experienced during impacts or crashes. In essence, a battery pack (or cell or module) is subjected to one or more high-g deceleration pulses on a test platform (often a sled or shock table) to simulate the shock from a collision [290, 291].

Accelerometers are typically mounted on the battery and/or test fixture to verify that the required peak acceleration and pulse duration are achieved. The test is usually performed in multiple orientations to stress the battery in different axes (longitudinal, lateral, and vertical). Table 5.2 summarizes key parameters for mechanical shock tests as specified by major standards. These include the pulse shape (almost always a half-sine shock), peak acceleration (in g), pulse duration, number of shocks and axes (directions), SOC of the battery, and the test levels (cell, module, pack, or vehicle level) addressed by each standard [73, 286, 254, 263, 279, 283, 276].

Half-sine pulses are specified by all listed standards for mechanical shock, though some (e.g. FreedomCAR) allow alternative pulse shapes if more representative of real crashes. The UN 38.3 transport regulation is included as it heavily influenced EV battery shock requirements (e.g. SAE standards align with UN 38.3 conditions). Mechanical shock test requirements show considerable variation across frameworks.

The peak accelerations range from single-digit g levels in some vehicle-level tests (e.g. $\sim$7 g in China's GB 38031 for packs) up to extremely high g's (50–150 g) for small-scale testing (as in UN 38.3 and SAE methods for cells). The intended scenario also differs: UNECE R100.03's shock pulses are tied to crash pulses for different vehicle categories (simulating $\sim$56 km/h crashes), whereas SAE J2464/2929 historically imposed very severe shocks on cells to envelope worst-case shipping and crash conditions. Notably, newer revisions have converged toward moderate levels - e.g. SAE J2464-2021 requires $\sim$25 g, 15 ms shocks on packs, more in line with actual crash decelerations.

Research indicates most real-world collisions produce deceleration peaks of 20–30 g for frontal or side impacts (duration $<$100 ms), and rear impacts often $<$12 g. Only in extreme crash tests (e.g. a 56 km/h rigid barrier crash) do peak decelerations approach $\sim$50–55 g [292, 293, 294]. Therefore, standards specifying 50 g shocks at pack level (ISO 12405 and 6469, UL 2580) come close to worst-case crash severity, whereas those requiring just 7–20 g (GB 38031, some UN R100 orientations) represent milder shocks.

The pulse durations also vary: European and US standards for vehicle-crash simulation often use longer pulses (80–100 ms) to mimic crash deceleration profiles, imposing a more sustained energy input on the battery. In contrast, many component-level tests (ISO, older SAE, etc.) use very short pulses $\sim$6 ms as a conservative shock that may reflect hitting a curb or small object. FreedomCAR/USABC explicitly explored two levels: a low-level shock meant to cause no damage, and a mid-level shock that might disable the battery but should not create safety

Table 5.2: Comparison of Mechanical Shock Test Requirements Across Global EV Battery Safety Standards [73, 286, 254, 263, 279, 283, 276].

Standard	*Pulse Shape*	*Peak Acceleration*	*Duration*	*Directions / Repetitions*	*Battery SOC*	*Acceptance Criteria*
UNECE R100.03	Half-sine	M1-N1[1]: 20-28 g (X), 4.5-15 g (Y) M2-N2: 10-17 g (X), 2.5-10 g (Y) M3-N3: 6.6-12 g (X), 2.5-10 g (Y)	80-120 ms	Longitudinal transverse	Max operational SOC	No fire/explosion, no electrolyte leakage into passenger compartment, isolation resistance requirements
ISO 6469-1:2019	Half-sine	70 (m/s^2)2 (Z), 50 (m/s^2) (X), 30 (m/s^2) (Y)	6 ms	3 axes × 1 directions × 6 reps	Max operational SOC	No fire/explosion, no rupture, electrical safety (isolation resistance)
SAE J2464:2021	Half-sine	See UN38.3 for 12-48 kg, 25 g (>48 kg)	6 ms (12-48 kg), 15 ms (>48kg)	3 axes × 2 directions × 3 reps)	≥95% SOC	No fire/explosion, no rupture, voltage retention, isolation resistance
SAE J2929:2013	Half-sine	Refer to SAE J2464	Refer to SAE J2464	Refer to SAE J2464	Refer to SAE J2464	Refer to SAE J2464
UL 2580:2025 (personal vehicle)	Half-sine	25 g	15 ms	3 axes × 2 directions × 3 reps	Max operational SOC	No fire/explosion, no rupture, isolation resistance, limited electrolyte leakage
UL 2580:2025 (off-road vehicle)	Half-sine	50g (≤ 12 kg) 2 5g (≤ 100 kg) 10 g (> 100 kg or system)[2]	11ms (≤ 12 kg) 15 ms (≤ 100 kg) 20 ms (> 100kg or system)	3 axes × 2 directions × 3 reps	Max operational SOC	No fire/explosion, no rupture, isolation resistance, limited electrolyte leakage
GB 38031-2020	Half-sine	7 g (Z)	6 ms	1 axes × 2 directions × 6 reps	Not specified	No fire/explosion, no rupture, isolation resistance, limited electrolyte leakage
USABC FreedomCAR	Half-sine or alternative	2 0g (low)[3], 30 g (Mid-1), 20 g (Mid-2)	11-55 ms (Low), 16-65 ms (Mid-1), 22-110 ms (Mid-2)	3 axes × 2 directions × 3 reps	Max operational SOC	No fire/explosion, no rupture, isolation resistance, voltage retention
UN 38.3:2023	Half-sine	150 g (battery [4]), 50g (large battery >12 kg)	6 ms (small), 11 ms (large)	3 axes × 2 directions × 3 reps	Max operational SOC	No fire/explosion, no rupture, no leakage, voltage retention

[1] M vehicles designed for carriage of passengers (M1 passengers vehicle, M2 buses less than 5 tonnes, M3 buses more than 5 tonnes); N vehicles designed for carriage of goods (N1 up to 3.5 tonnes, N2 up to 12 tonnes, N3 more than 12 tonnes)

[2] Pack with separate modules previously tested individually to the appropriate higher shock level.

[3] Level (intensity) of shock: low, Mid-1 or Mid-2.

[4] UN 38.3 defines:

- small cell: a cell with a gross mass <5 kg,
- large cell: a cell with a gross mass >12 kg,
- small battery: a lithium metal battery or Li-ion battery with a gross mass <12 kg,
- large battery: a lithium metal battery or Li-ion battery with a gross mass >12 kg

hazards. They also allow the manufacturer to extend pulse duration (lowering peak g) as long as the shock energy input is equivalent, acknowledging that a longer, lower-g pulse can be equally or more abusive in some cases.

All standards agree that mechanical shock must not lead to dangerous failures. The battery system should suffer no fire or explosion during or after the shocks. Most also forbid any rupture of the battery enclosure or electrolyte leakage beyond allowable traces. For instance, UNECE R100.03 requires that after the shock test (or a valid vehicle crash test in lieu of it), the battery shows no evidence of leaking fluid, no case breakage, and no fire or explosion, and it must maintain at least 100 Ω/V isolation resistance in its high-voltage circuitry. Similarly, ISO and UL standards mandate no fire, no explosion, no venting of toxic gases, and no electrolyte spillage as passing criteria.

In practice, manufacturers often instrument the battery during shock testing with voltage sensors and thermal sensors in addition to accelerometers, to detect any sudden drops in voltage (indicating an internal disconnect or short) or unexpected heating. After testing, the battery is observed (typically for 1 hour) to monitor any delayed reactions such as TR. If the battery remains intact and electrically safe (even if it ceases function), it is deemed to have passed. Notably, standards like UNECE R100 and SAE J2929 permit vehicle-level crash tests as an alternative demonstration of shock performance. For example, a pack installed in a vehicle that has successfully undergone frontal and side crash tests (per FMVSS 305 or ECE R94/R95) can be exempted from separate shock bench tests, since the crash provides equivalent or more realistic validation [71, 295, 296]. This provision underscores an important point: mechanical shock tests at component level are a proxy for crashworthiness, and alignment between shock bench-tests and actual crash pulses is an area of ongoing evaluation.

In summary, mechanical shock testing is a cornerstone of battery safety standards, designed to ensure that a battery can endure collision-level forces without precipitating a TR or other hazardous failure.

5.2.2 Drop Tests

The drop test simulates an accidental drop of a battery pack or module, for instance during maintenance, handling, or replacement. While not directly related to vehicle crashes, this test addresses the scenario of a high-weight battery being dropped from a certain height, which could damage its enclosure or internal structure. The drop test is generally conducted by lifting the battery (or cell/module) to a specified height and releasing it to free-fall onto a hard surface. Instrumentation may include accelerometers to record impact shock and high-speed cameras to observe the impact, but often the outcome is assessed by visual inspection and post-drop monitoring rather than measured data. Table 5.3 compares drop test procedures across various standards, including the drop height, orientation or surface impacted, number of drops, and test sample state-of-charge [73, 254, 263, 286, 276, 279, 280, 283]. Table summarizes key parameters such as drop height, impact surface and orientation, number of repetitions, battery level tested, initial SOC, and acceptance criteria for standards

UNECE R100.03 and ISO 6469-1 standards for vehicle batteries notably do not mandate a drop test, under the rationale a battery securely installed in a vehicle is unlikely to be dropped in normal operation. However, UL 2580 requires a drop test for any battery intended to be routinely removed or swapped (e.g. forklift or swappable EV batteries). The extreme 10 m drop onto a pole is a legacy from US Department of Energy guidelines (SAND2005-3123) to simulate worst-case abuse; most modern standards use more moderate heights (1–1.5 m). Drop height ranges from about 1 meter (in most contemporary standards for EV packs) up to 10 meters. The 10 m drop, specified in Sandia National Labs' report SAND2005-3123 and adopted by USABC in the 1990s, involves dropping the battery onto a steel pole to concentrate the impact, simulating, for example, a vehicle falling from a lift or a battery ejected and hitting a post. This is an extremely severe test seldom required in recent regulations [276, 297].

Table 5.3: Comparison of Drop Test Requirements in EV Battery Safety Standards [73, 254, 263, 286, 276, 279, 280, 283].

Standard	***Drop Height***	***Drop Surface / Orientation***	***Repetitions***	***Battery Level***	***Initial SOC***	***Acceptance Criteria***
SAE J2464:2021	≥1 m	Hard flat surface / Most vulnerable orientation	1	Pack level only	Fully charged	No fire, explosion, electrolyte leakage
UL 2580:2025	≥1 m	Concrete surface / At angle likely to produce most adverse effect	1	Pack level	Fully charged	No fire, explosion, electrolyte leakage. Isolation resistance test after 6-24h
China GB 38031-2020	Deleted from standard	N/A	N/A	N/A	N/A	N/A
USABC FreedomCAR	≤10 m	Hard flat surface / At angle likely to produce most adverse effect	1	Pack level	Fully charged	No fire, explosion, electrolyte leakage
UN 38.3:2023	1.2 m	Various orientations (flat 3 sides, edge, corner)	5 drops (one for each orientation)	Cell/battery level	Fully charged	No damage to cells, no release of contents, packaging integrity maintained

Regulatory standards in the European Union and ISO context have historically omitted drop tests entirely - reflecting an assumption that during vehicle use, large battery packs are bolted in place and not subject to drops. However, industry standards in the US and some national codes do include drop tests as a precaution for battery handling safety. SAE J2464 and SAE J2929 (which follow the UN 38.3 transport regulation) call for dropping a fully charged pack from 1 m onto a concrete or steel surface. At least one drop must be non-flat (e.g. on a corner or edge) to represent a worst-angle impact.

UL 2580 similarly mandates a >1 m drop onto a thick concrete slab, again ensuring at least one angled impact. These standards typically require only a single drop test unless the battery is designed to be removable: UL 2580 specifies that batteries intended for swapping be dropped three times on the same unit, recognizing the higher probability of accidents during frequent handling.

Chinese standards have evolved on drop testing. Earlier Chinese automotive battery guidelines (QC/T 743-2006 [298]) allowed up to a 10 m drop like the USABC method. More recent standards differentiate by level: GB/T 36276-2018 (which covers energy storage batteries and possibly EV batteries) requires a 1.5 m drop for single cells (dropped on their end) and 1.2 m for modules. This graded approach acknowledges that larger assemblies might not need as high a drop to impart similar impact energy to cells. The latest Chinese safety standard for EV traction batteries, GB 38031-2020, interestingly does not mandate a stand-alone drop test at pack level. This suggests Chinese regulators assume a securely installed pack is unlikely to be dropped; testing focuses on crash (shock) and other abuse scenarios.

SOC for drop tests is typically set high (near 100% in many protocols), under the rationale that a fully charged battery is in its most energetic (and potentially dangerous) state if damaged. Some standards like SAE J2464 specify 95–100% SOC for drop and other abuse tests. UL 2580 allows using the "maximum normal operating SOC" if the battery in practice is not charged to 100% during use. This nuance ensures testing reflects real-world conditions for batteries that intentionally limit top-of-charge (for longevity or safety).

The acceptance criteria for drop tests align with other mechanical abuses: the battery must not ignite or explode upon impact. Typically, the pack is observed for a period (e.g. 1 hour) after the drop for any signs of TR or fire. No hazardous electrolyte leakage or venting is allowed.

In UN transport tests (UN 38.3), the criteria are no fire and no disassembly; cells can vent or deform but must not explode. UL and SAE standards similarly demand no fire or explosion; UL also expects that no parts should break loose from the battery case during the drop. In practice, many large EV packs are so robustly built that a 1 m drop causes only cosmetic damage (dents), but the test ensures that internal connections or safety disconnects do not break in a way that could create a short-circuit or high-voltage exposure. It is worth noting that automotive manufacturers often conduct their own non-mandatory drop tests during development, especially for batteries that might be handled in after-sales service. For instance, if a battery pack is replaceable, companies will drop it from waist-height to ensure it will not become a fire hazard if a technician accidentally drops it.

The regulatory focus, however, remains on crash simulations (shock and crush) rather than drop. The rationale is that once a battery is installed in a vehicle, a drop large enough to matter is unlikely, thus, European and ISO standards channel attention elsewhere.

Nonetheless, the drop test serves as a straightforward, if brutal, assessment of pack structural integrity and internal retention of cells or components under sudden impact.

5.2.3 Penetration Tests

The penetration test (sometimes called the nail penetration or impalement test) is designed to assess a battery's response to a direct intrusion of a sharp object, which can cause an internal short-circuit. This test simulates scenarios such as road debris piercing the battery enclosure or a tool accidentally being driven through a battery module. In laboratory execution, a steel rod

or "nail" is forced into the battery at a controlled speed. The rod's intrusion can rupture cells and separators, leading to internal shorting and localized heating - a severe abuse condition that often precipitates TR in lithium-ion cells. The test apparatus usually involves a hydraulic or motor-driven ram equipped with the specified rod, aligned to puncture the test unit (cell, module, or pack) at a vulnerable location. Voltage and temperature probes are typically connected to detect immediate voltage collapse or thermal events, since the test often ends once a voltage drop or certain depth is reached. Table 3 compares key parameters for penetration tests across standards, including the rod's diameter, penetration speed, required depth of penetration, and test levels [73, 268, 286, 254, 263, 276, 279, 280, 283]. Table 5.4 summarises nail penetration tests, presenting specifications such as rod diameter, penetration speed, required penetration depth, test levels (cell, module, pack), battery SOC, and acceptance criteria across various international standards

The rod is typically steel, with a blunt tip in some cases. GB 38031:2020 eliminated the single-cell nail test in favour of a TR propagation test at pack level. In that test, a cell is made to go into TR (e.g. via nail puncture or heating) and the pack must show containment (no propagation to adjacent cells beyond a certain time). This shift reflects a focus on containment rather than individual cell penetration resilience. Penetration tests are among the most severe battery abuse scenarios. For a fully charged lithium-ion cell, driving a steel nail through it almost guarantees an internal short circuit and rapid heating. The test parameters above show a high degree of consistency in rod size and speed: 3 mm diameter nails for single cells and larger 20 mm diameter rods for modules or packs are common requirements [276].

The penetration speed is typically around 80 mm/s, which ensures the nail drives in fast enough to cause a sudden trauma (slower push might allow some pressure relief). GB/T 31485 standard allowed a range (e.g. 10–40 mm/s) for the needle speed [299], but ∼80 mm/s has been a de-facto standard since the USABC protocol. For depth, standards generally require the rod to go all the way through the test object or a representative depth. For a cell, full penetration (nail enters one end and exits or nearly exits the other side of the cell) is expected.

For modules or packs, which contain multiple cells, different approaches exist: SAE and USABC specify that the nail should pierce at least 3 cells in the module (if cells are aligned in the penetration path) or go 100 mm deep if fewer than 3 cells are in line. In essence, the rod must traverse a substantial portion of the battery's interior.

European and ISO 12405 series vehicle standards did not mandate a penetration test. This omission may be due to concerns over repeatability and relevance - a penetration test is extremely destructive and hard to control, and some argue it represents a very unlikely event in a properly designed vehicle (since packs have protective enclosures). However, UL, SAE, and Chinese standards historically did include penetration as they treat it as a proxy for "internal short circuit" abuse.

The Chinese approach evolved in 2020: GB 38031-2020 decided that instead of skewering a single cell and observing its behaviour (which is often inevitably a fire), it is more practical to perform a thermal propagation test at the pack level [300]. In that propagation test, one cell in a module is made to go into TR (by any method - it could be needling, overheating, or overcharging) and the safety metric is whether the runaway propagates to neighbouring cells. GB 38031 still allows using a nail to trigger that initial cell failure (the nail's diameter 3–8 mm, tip angle 20–60°, speed 0.1–10 mm/s), but the focus is on ensuring the entire pack does not erupt.

This is a shift from preventing a single cell fire (which may be near impossible in nail tests) to preventing a chain reaction, aligning with real accidents where one or a few cells might be damaged but the whole pack should not catastrophically ignite.

However, in many nail tests, the event is so fast that the cell either goes into TR or not by the time full penetration is done. The outcome can range from mild venting to violent flaming. Thus, the acceptance criteria in standards are essentially checking that nothing beyond the

Table 5.4: Comparison of Nail Penetration Test Requirements in EV Battery Safety Standards [73, 268, 286, 254, 263, 276, 279, 280, 283].

Standard	*Rod Diameter*	*Penetration Speed*	*Depth / Criterion*	*Test Levels*	*Battery SOC*	*Acceptance Criteria*
UNECE R100.03	Not required (used as trigger for thermal propagation)	Not required	Not required	Not required	Not required	Not required
ISO 6469-1:2019	Not required	Not required	Not required	Not required	Not required	Not required
SAE J2464:2021	3 mm (cell), 20 mm (module/pack)	80 mm/s	Through cell; through 3 cells or 100 mm (module/pack)	Cell, module, pack	$\geq$95% SOC	No fire/explosion, no rupture, voltage retention, isolation resistance
SAE J2929:2013	3 mm (cell)	80 mm/s	Through cell	Cell	$\geq$95% SOC	No fire/explosion, no rupture, voltage retention, isolation resistance
UL 2580:2025	1–3 mm (cell; TR initiation method	1 mm/s	Through cell	Cell	100% SOC	No fire or explosion
GB 38031-2020	Not required (test deleted)	Not required	Not required	Not required	Not required	Not required
USABC FreedomCAR	3 mm (cell), 20 mm (module/pack)	80 mm/s nominal	Through cell; through 3 cells or 100 mm (module/pack)	Cell, module, pack	100% SOC	No fire/explosion, no rupture, voltage retention, isolation resistance

battery occurs: no explosion is universally required (an explosion implies cell case ruptures in a rapid, uncontrolled manner sending shrapnel - this is to be avoided). No fire is also a common criterion, though some standards have been more lenient on internal fires. For instance, SAE say no fire extending outside the battery enclosure is allowed; the battery may emit smoke or even flames from a pressure-relief vent, but must not shoot flames or debris out of containment. FreedomCAR's older guidelines tolerated the cell itself burning (since nail penetration almost always causes a fire internally) as long as it did not lead to an explosion.

Post-test observation is important. Typically, after penetration, the battery is monitored for a certain time to ensure it has stabilized. If no fire or TR has occurred by then, the test is concluded. Many cells will go into TR within seconds to minutes of a nail penetration if they are going to at all, because the nail locally heats the cell (through internal short-circuit currents) to a point where the separator melts and the cell's chemical energy is released as heat. The test basically checks the efficacy of any internal safety features (some cells have shutdown separators or tear-away tabs that mitigate shorting effects) and the pack's ability to manage a cell failure (via venting direction, fire-resistant materials, etc.).

The trend in recent standards (like GB 38031 and also draft UN GTR proposals) is moving away from requiring every cell to survive a nail, and toward making sure that even if one cell violently fails, the whole pack does not go up in flames. This is reflected in propagation tests and requirements for thermal barriers and venting.

In summary, the penetration test is a brutal exam of a battery's internal safety under an almost unrecoverable fault. The various standards prescribe similar methods - a fast-moving steel nail of significant size - and expect the battery not to explode or endanger its surroundings. The differences lie in whether this test is required at all. Where it is required, the parameters are fairly harmonized across the international standards, thanks in part to early cooperation and data sharing in the field of battery safety research.

5.2.4 Crush Tests

The crush test (also referred to in some standards as the mechanical integrity test or compression test) assesses the battery's ability to withstand compressive forces and deformation, as would occur in a severe vehicle collision or if the battery is mechanically crushed by debris. This test essentially tries to squeeze or crush the battery pack or cell between two platens or a platen and an anvil. It is one of the most demanding mechanical tests, often resulting in significant physical damage to the battery. The test setups vary: some use a flat plate (Type A) to mimic a broad impact (like a car chassis deforming onto the battery), and others use a cylindrical or bar indenter (Type B) to simulate a concentrated impact (like a pole or edge intrusion; see Figure 5.1). Typically, the crush is applied at a slow, controlled rate (quasi-static) to a specified force or deformation limit. Instruments include load cells (to measure force), displacement sensors (to measure how much the battery is crushed), and voltage monitors (to detect sudden voltage drops indicating internal collapse).

Type A refers to a flat crushing plate (often textured to prevent slip). Type B is a round rod or bar, sometimes used for cell-level crush (e.g. 15 mm diameter rod across a cell). Some standards (SAE, IEC) specify both types: e.g. cylindrical cells are crushed between two rod halves to simulate two cells pressing, while packs use a flat plate. FMVSS 305 is the US vehicle crash safety standard which indirectly sets expectations (no battery rupture or leakage in a crash). The crush test is essentially a quasi-static crash simulation at the component level. It aims to answer the question: if the battery is pinched or squashed in a collision, will it internally short-circuit or burst into flames. Since an actual crash is dynamic, the standards have to pick either a force threshold or a deformation threshold (or both) to apply in a slow press. There are two approaches highlighted in Table 5.5:

- **Force-based approach:** Apply a specified maximum force and test if the battery with-

Table 5.5: Comparative Analysis of International Standards Governing Mechanical Crush Testing Protocols for LIB Safety Assessment based on [73, 286, 254, 276, 279, 283, 285].

Standard	Crush Force	Crush Plate Type	Crush Speed	Stop Criterion	Acceptance Criteria
UNECE R100.03	100 – 105 kN	Flat plate (longitudinal/transverse)	On-set less then 3 min (hold time of 0.1–10 s)	Reaching force limit; no fire, explosion, leakage, venting; insulation $\geq$100 Ω/V post-test	No fire/explosion; no leakage/venting; isolation $\geq$100 Ω/V post-test
ISO 6469-1:2019	See UNECE R100.03	See UNECE R100.03	See UNECE R100.03	See UNECE R100.03	See UNECE R100.03
SAE J2464:2021	Up to 1000 × battery mass	Flat plate	Recommended 5 mm/s	Height reduced to 85%, hold 5 min, then 50%; no uncontrolled venting or thermal runaway	No fire, explosion, venting; record force, intrusion, hazard severity
UL 2580:2022	Max. 100 kN	Flat plate	Recommended 5 mm/s	Height reduced to 85%, hold 5 min, then 50%; no uncontrolled venting or thermal runaway	No fire/explosion; no rupture; no toxic gases
GB 38031-2020	100 kN or 1000 × cell mass	Half-cylinder (radius 75 mm)	$\geq$2 mm/s	Voltage to 0 V or 15% deformation or 100 kN/mass × 1000; hold 10 min	No fire, explosion
USABC FreedomCAR	Less than 100 kN	semi-cylinder (ϕ75 mm)	Modules/Packs: 300 ± 60 mm/min	Height reduced to 85%, hold 5 min, then 50% or 1000 × mass; monitor for abuse	No fire/explosion; record hazard severity
UN 38.3:2023	13 kN ± 0.78 kN	Flat plate	Recommended 5 mm/min	13 kN or 100 mV drop or 50% thickness reduction; observe 6 h	No fire, explosion during test and 6 h observation
UL 1973:2022	1000 × cell mass or bar (150 mm)	Bar (ϕ150 mm) crush	Not specified	One-third OCV drop or 15% deformation or mass × 1000	No fire/explosion
IEC 62660-3:2022	less than 1000 × cell mass	Round or semi-circular bar or sphere (ϕ150 mm)	Not specified	Abrupt voltage drop to one-third of initial; or $\geq$15% deformation; or force = 1000 × cell weight	No fire, explosion, leakage; no thermal runaway after 24 h

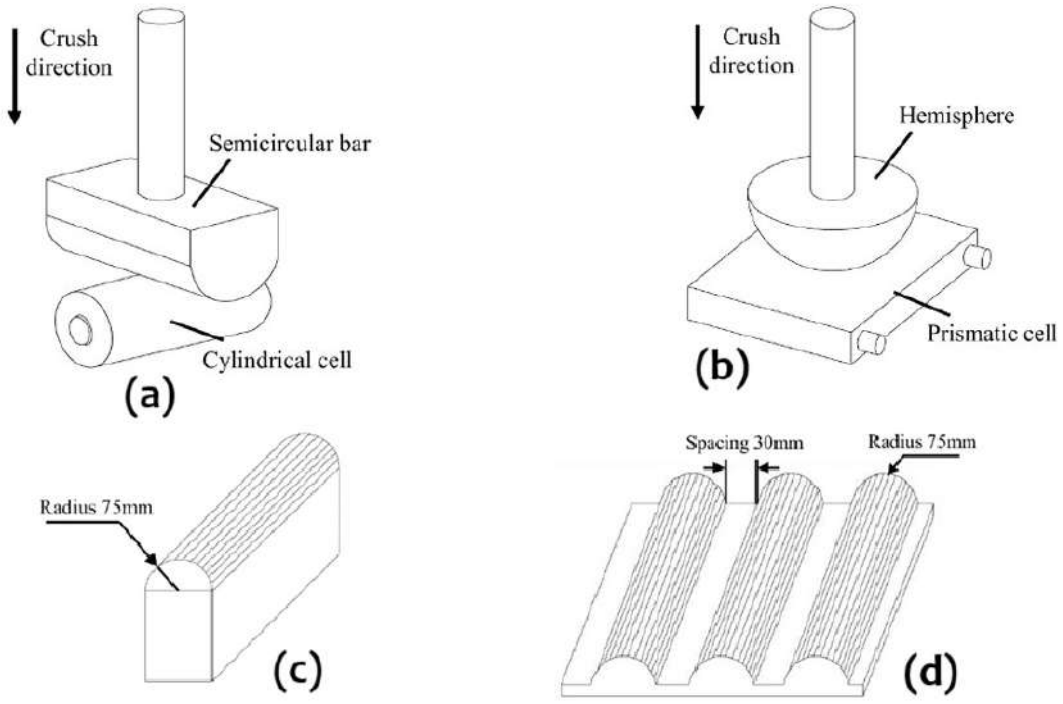

Figure 5.1: Crushing fixtures; (a) IEC 62660-3:2022 cylindrical cell crush fixture; (b) IEC 62660-3:2022 prismatic cell crush fixture; (b) IEC 62660-3:2022 prismatic cell crush fixture [269]; (c) GB 38031-2020 crushing fixture [73]; (d) SAE J2464 and UNECE R100.03 crushing plate [254, 279].

stands it without catastrophic failure. This is seen in UNECE R100.03, UL 2580, SAE J2929 for packs, etc., where 100 kN is a common target for passenger car batteries. The value of 100 kN was chosen because analyses and crash tests indicated that in a severe crash, the battery might experience on the order of 50–100 kN force distributed through its structure. For example, R100.03 required 100 kN for M1 category vehicles (cars) and allowed perhaps lower for smaller vehicles (L-category motorcycles have separate rules). A fixed force standard makes the test independent of battery size (to some degree), although obviously a very large battery might handle 100 kN easily whereas a small one might be flattened.

- **Weight-proportional (energy-based) approach:** Make the force limit proportional to the battery mass (e.g. 1000 multiplied by the weight, e.g., UN 38.3). This essentially attempts to impart roughly a constant stress or acceleration to the battery. USABC and IEC cell tests use 1000 times the weight as a maximum force, reasoning that a heavier battery will naturally experience bigger forces in a crash due to inertia. For instance, a 50 kg module would be tested up to 50 kN in this scheme. For very large packs (500 kg), this gives 500 kN, far exceeding the 100 kN used elsewhere. In reality, such forces might be overly conservative. IEC 62660-2 (cell safety) and FreedomCAR allowed using engineering judgment or crash analysis to determine a suitable force if 1000 multiplied by the weight was unrealistic in real life applications [301, 302].

The plate or indenter type significantly affects the outcome. A flat plate (Type A) distributes force evenly, often crushing the whole pack uniformly. A rounded or bar indenter (Type B) localizes the force, potentially piercing into the structure. IEC and some cell standards specify a rod for cell tests because cylindrical cells, for example, are often crushed by being pressed

between two bars across their diameter (to simulate one cell pressing into another). In pack-level tests, regulators usually choose a flat plate to simulate a wall or another flat object pressing the battery. UNECE R100.03, for instance, calls the test "mechanical integrity" and uses a rigid plate with semicircles that compresses the battery from one side (often the weakest side).

IEC 62660-2 specifies two standard plate sizes (Type A might be a plate >20 cm^2 area for cell, etc.). It was noted that guidance on where to apply the plate is often lacking, but generally the rule is to choose the location – most likely to cause damage – as per SAE J2464 or, in R100.03's case, the manufacturer and test laboratory confer to identify the worst-case orientation. This often means crushing the broad side of the pack (if that is where internal cells are closest to the wall) or at a corner (which might concentrate stress). The speed of crushing is slow – typically on the order of 1 to 10 mm per minute (i.e. quasi-static). This is done to allow any energetic events (shorts, TRs) to manifest during the compression [303] .

A fast crush might actually be less severe in some cases because it does not give time for heat to build up, but standards err on the side of conservative, slow application to maximize internal damage. For cells, extremely slow rates (0.1–0.5 mm/s) are sometimes used to simulate a gradual crush and to let the voltage drop be observed clearly.

Stop criteria vary - UL, SAE, UN and GB standards crush to a percentage of the battery's original dimension (common values: 70% or 50%, meaning a 30% or 50% compression). A stop when a target force is reached (e.g. stop at 100 kN even if the battery is not fully flattened). Some do a combination – e.g. crush to 85% thickness, hold, then continue to 50% if no failure yet, as cited in SAE J2464.

Another approach is monitoring cell voltage: IEC says if the cell voltage suddenly drops by one-third, that implies an internal short and the test can be terminated to avoid over-crushing beyond that point. This can be important for cell tests to prevent an unnecessarily extreme crush once the cell has clearly failed internally. Packs usually rely on a force or displacement limit, since monitoring every cell's voltage in a big pack is complex. Across standards, 100 kN has emerged as a de-facto crush force for a full EV pack test (for passenger cars).

The acceptance criteria for crush tests echo the now-familiar refrain: no fire, no explosion, no electrolyte leakage, and maintain electrical safety (isolation). For example, R100.03 says after the crush the battery must not leak electrolyte or vent dangerously, and it must maintain isolation resistance.

If the battery has a venting system (pressure relief), it is allowed to vent non-flammable gases, but not to spray electrolyte around. FMVSS 305 (which is a vehicle crash test standard, not a laboratory crush) specifically limits electrolyte leakage to <5 litres in the first 30 minutes after a crash and requires no dangerous voltage on the vehicle chassis. While laboratory crush standards do not quantify leakage in litres, the general rule is any visible liquid leaking out is a fail.

Rupture of the enclosure is usually not allowed either - for high voltage batteries, any crack that exposes internal components or wiring is considered a failure (since it could lead to electric shock or increase fire risk). For cell-level tests, criteria are a bit simpler: no fire or explosion. It is expected a crushed cell may open or leak (since it is small and not in its final enclosure); that is acceptable as long as it does not combust violently.

One noteworthy element: some standards allow using actual vehicle crash tests instead of a component crush. This is similar to the shock test alternative. For instance, UNECE R100.03 states that if the vehicle has passed frontal and side crash tests (per UNECE R94 and R95), then the battery is considered to have met mechanical integrity requirements if it was installed in that crash-tested vehicle [295, 296].

The rationale is that a full-scale crash imposes realistic deformation on the battery. In fact, such dynamic tests may be more strenuous than a uniform static crush. However, for certification of stand-alone batteries (e.g. for multiple vehicle use), the quasi-static crush is still needed. The difference between a dynamic crash and a static crush has been debated. Studies have pointed

out that a single-point static crush might not replicate the load distribution of a real crash.

In real crashes, the battery might be saved by crumple zones and the vehicle structure absorbing energy. A static crush test, where the battery alone takes the force against an unyielding plate, can be more severe in some aspects (no give in the system). Conversely, a static test cannot capture inertia effects where heavy components inside the pack tear loose (something a crash might do). So both have pros and cons, and the regulatory trend is to require the static component test unless a full vehicle test is available.

China's GB 38031 uses both approaches in a sense: for cell-level, they do an aggressive crush (half-cylinder indenter) until the cell voltage goes to zero or it is flattened 15%. For packs, GB 38031 requires that the pack either pass a 100 kN crush or, if a higher force is expected in its specific vehicle application, to test to that higher force. Additionally, GB 38031 ties in TR warning: if the pack is going to fail (cells crush and go into TR), the pack's monitoring system should have issued an alarm 5 minutes before a dangerous condition occurs, as part of their thermal propagation safety requirement. This essentially couples mechanical and thermal safety - ensuring the BMS can detect a crush-induced internal short and alert or mitigate before a fire develops, an advanced concept not seen in older standards.

In conclusion, the crush test is arguably the harshest test of a battery's structural design. It enforces robust mechanical packaging: cell spacing, strong casing, protective frames, and pressure relief features all play roles in passing this test. Differences among standards boil down to how extreme the conditions are (100 kN flat plate vs. weight-based, rod vs. flat, etc.), but all aim to guarantee that if a battery is damaged, it will not immediately unleash its energy as an uncontrollable fire or explosion. With the introduction of heavier vehicles and new battery form factors, these standards continue to evolve, but the fundamental safety goal remains: a crushed battery might be destroyed and non-functional, but it should remain safe – no fire, no shrapnel, no electric shock to occupants or rescuers.

5.2.5 Vibration Tests

The vibration test examines a battery's ability to endure the vibrations and oscillatory motions that occur in normal vehicle operation over its service life. Unlike the shock and crush tests (which are acute, one-time abuses), vibration testing simulates chronic mechanical stress: the repeated, cyclical loads from engine/motor operation, road irregularities, and structural resonance. While vibration is not an "abuse" in the sense of an accident, severe vibration can lead to fatigue failures of battery components (e.g. cracked welds, loosened bolts, damaged interconnects) and is therefore considered in durability and safety standards. In fact, some standards classify vibration under "reasonable foreseeable misuse" - prolonged exposure could cause internal failures that might become safety hazards (like coolant leakage or electrical shorts). The test typically involves mounting the battery on a shaking table and subjecting it to a specified vibration profile for several hours along each of 3 orthogonal axes. Instrumentation includes accelerometers to ensure the table inputs meet the required spectrum, and often instrumentation on the battery to detect resonant frequencies or structural responses.

Table 5.6 summarizes vibration test specifications across standards, including whether a sine sweep or random vibration is used, the frequency range, acceleration or Power Spectral Density (PSD) levels, axis of testing, duration, and any special conditions (like temperature) [73, 286, 254, 263, 276, 279, 280, 283, 285, 304, 305, 306]. This compilation highlights methodological discrepancies and convergence across test standards.

Vibration profiles are often derived from general vehicle vibration standards (like ISO 16750-3 or MIL-STD transport standards) [307, 308]. SAE J2380 is widely used for EV batteries. It was originally developed by Sandia and provides a realistic random vibration profile for 100,000 miles of service [306].

Many standards require repeating the vibration test at both high and low SOC to account for any dependency (cells at low SOC might loosen more due to less swelling). After vibration,

Table 5.6: Comparative overview of standardized vibration test procedures for BESS across international regulations and norms, based on [73, 286, 254, 263, 276, 279, 280, 283, 285, 304, 305, 306].

Standard	*Vibration Profile*	*Frequency Range*	*Acceleration / PSD Level*	*Duration*	*Test Axes*	*Battery SOC*	*Acceptance Criteria*
UNECE R100.03	Logarithmic sine sweep	7 – 50 Hz	2 – 10 m/s^2 (0.2 – 1 g)	12 × 15 min sweeps (3 h total per axis)	X, Y, Z	100%	No electrolyte leakage; no rupture; no venting (pack only); no fire; no explosion; post-test isolation ≥100 Ω/V (HV packs)
ISO 6469-1:2019	Random vibration	7 – 200 Hz	PSD 0.0004 – 0.5774 (m/s^2)^2/Hz	8 h (all axes)	X, Y, Z	100%	No leakage; no continuous flame > 1 s; no explosion; no rupture; maintain isolation
SAE J2929:2013	Log sweep sine vibration	7 – 200 Hz	2 – 10 m/s^2 (0.2 – 1 g)	12 × 12 × 15 min sweeps (3 h total per axis)	X, Y, Z	50%	No leakage; no rupture; no venting; no fire; no explosion; post-test OCV ≥90% pre-test
UL 2580:2022	Random vibration (SAE J2380)	10 – 2 000 Hz	PSD 0.14 – 20 (m/s^2)^2/Hz	9 min – 38 h (application-dependent)	X, Y, Z	Variable	No leakage; no fire; no explosion; pack-level only; BMS monitoring for resonance, isolation loss, abnormal volt/temp
GB 38031-2020	Random + constant-frequency	5 – 200 Hz	Random PSD per GB/T 2423.56; sine at fixed 24 Hz	Random: per GB/T 2423.56; sine: 1 h (passenger), 2 h (commercial)	Z, Y, X	≥50%	No leakage; no housing crack; no fire; no explosion; no abnormal termination; post-test insulation ≥100 Ω/V
USABC & FreedomCAR	Random vibration	10 – 190 Hz	PSD 0.4 – 11 (m/s^2)^2/Hz	8 h per axis	Z, X, Y	Max SOC	No leakage; no fire; no explosion; designed as a durability test for 100,000 miles equivalent; resonance assessment
UN 38.3:2023	Log sweep sine vibration	7 – 200 Hz	N/A	12 × 15 min sweeps (3 h total per axis)	X, Y, Z	N/A	No disassembly; no leakage; no venting; no rupture; no ignition; post-test OCV ≥90% pre-test
UL 1973:2022	Harmonic motion / IEC 61373	5 – 150 Hz	0.8 mm amplitude; Category II random per IEC 61373	Per IEC 61373 Category II protocol	X, Y, Z	N/A	No mechanical failure; no short; no fire; functional safety check; meets overvoltage and creepage/clearance requirements
IEC 62619:2022	Random + sinusoidal	5 – 2,000 Hz	PSD 0.14 – 20 (m/s^2)^2/Hz (cell/module); 0.4 – 11 (m/s^2)^2/Hz (pack)	8 h per axis	X, Y, Z	N/A	No fire; no explosion; no rupture; no leakage; no electric shock hazard; no loss of protection controls; post-test isolation per Annex B

a visual inspection and electrical check (capacity or isolation) is performed. Vibration test requirements are among the most standardized across different regulations, thanks in part to reference to common sources: many use the UN 38.3 transport test and/or SAE J2380. The UN 38.3 vibration test (which all lithium batteries must pass for shipping) involves a sinusoidal sweep from 7 Hz to 200 Hz and back, in logarithmic cycles, over 3 hours per axis. The amplitude is 0.8 mm (peak-to-peak) at low frequencies, transitioning to an acceleration of 8 g at higher frequencies. However, that 8 g is only for small cells; for large battery assemblies (>12 kg), UN 38.3 actually uses just 1 g across the board. Heavier systems get a milder requirement in UN 38.3, since the test is primarily for transport (and big packs are not resonating at high g's in packaging).

Automotive-specific standards like SAE J2380 and ISO 12405 decided that a more realistic random vibration profile is better for in-vehicle service. Road vibrations are stochastic (random) due to roughness, and contain a wide frequency range with certain intensities. J2380 provides a PSD profile typically ranging roughly 0.4 $(m/s^2)^2/Hz$ at low frequency down to 0.01 $(m/s^2)^2/Hz$ at higher frequencies, shaped to represent vehicle frame input; integrated, this yields a total acceleration on the order of 3 G-RMS. The test is run for 3 hours per axis. ISO 12405-2, ISO 12405-3 and ISO 6496-1 used similar random profiles and even required sweeps or multi-axis if applicable. The frequency range for random tests is often up to 200 Hz for pack-level (since vehicle vibration from road usually has most energy <200 Hz).

IEC 62660-2 for cells goes further to 2000 Hz to account for high-frequency vibration that small cells might see in handheld tools. Duration is usually several hours per axis.

UN 38.3 and most others choose 3 hours per axis (9 hours total). Some automotive standards extend it to 8 hours per axis to simulate longer life (for instance, heavy-duty vehicle standards or some OEM requirements go to 12 or 24 hours total). At least one standard - AIS-048 (India) - required testing at different temperatures as well (-40, +75 °C) to combine vibration and thermal stress [309].

Most standards, however, do vibrations at ambient room temperature unless otherwise specified. The axes of testing are the three orthogonal axes of the battery's mounting orientation: typically vertical (Z), longitudinal (X), and lateral (Y). Some standards refer to testing in "three mutually perpendicular mounting positions" for cells, meaning you mount a cylindrical cell in 3 different orientations to vibrate it along different internal axes. For packs, it is bolted to the table as it would in a car (with its mounting points), and then vibrated in each direction.

SOC is another consideration. Vibrations themselves do not directly depend on SOC, but SOC might influence the mechanical stiffness or mass distribution slightly (full cells vs empty cells can have different internal stresses). More importantly, after vibration, one may do an electrical check (like capacity or resistance measurement).

SAE and IEC standards require doing vibration at both high and low SOC. For example, IEC 62660-2 and the UL procedure do vibration at 100% and at 20% SOC (two separate test runs on two samples). J2380 also lists doing tests at two SOC levels on the same profile. The rationale is to ensure that no matter the state of charge (which might affect clamping force in modules or cell swelling), the battery does not suffer damage.

Acceptance criteria for vibration tests are more diverse: no fire, no explosion, no electrolyte leakage are expected (vibration should never be severe enough to cause immediate fire). So essentially it is a pass if the battery does not self-destruct dangerously. But beyond safety, vibration also addresses reliability: after the test, the battery should still function.

For instance, a standard may require that the battery retains a certain percentage of its capacity or that there is no structural damage like broken mounts or loose connectors. ISO 6469-1 required that insulation resistance still be okay and there be no loss of mechanical integrity (no cracked housing or loose parts). Some standards require an internal inspection to check for things like cell misalignment or connector damage. However, regulatory frameworks like R100.03 focus only on safety (so they do not mandate any performance retention, just no hazards). In that

sense, the pass/fail is principally safety-oriented: the pack should not leak or show open circuits that could cause safety issues. A functional check (charge/discharge) is often done to ensure the battery can still be operated or at least safely shut down.

It is pointed out that there is a wide dispersion in test conditions, but many traced to UN 38.3 or SAE J2380 as base references. UN 38.3 is considered somewhat insufficient for true automotive durability, as it was meant for transport safety (one-time shipping). SAE J2380 is more representative of the cumulative damage over a vehicle's life. For example, an EV battery in a stiff suspension vehicle might experience vibrational accelerations around 1–3 G-RMS for thousands of hours.

The test compresses a lifetime into hours by applying a higher level of vibration than average. Combined vibration and environmental stress: Some advanced standards and OEM tests run vibration at high and low temperatures to see if cold embrittlement or hot softening exacerbates vibration damage, e.g., MIL-STD tests for military vehicles do this and AIS-048 (Indian standard) [307, 309].

During vibration testing, sensor placement is important. An accelerometer is usually mounted on the vibrating table (on the fixture near the battery) to ensure the input matches the prescribed profile (closed-loop control). Sometimes extra accelerometers are put on the battery itself to measure its response (for informational purposes; not necessarily pass/fail criteria but to identify resonances). Large battery packs can have resonant frequencies in the test range. If a resonance is found (often indicated by amplification of acceleration on the pack vs table), some standards like GB 38031 require an additional test: dwell at that resonant frequency for a period (like 30 minutes) to simulate prolonged resonant vibration. This is because resonance can cause much higher stress and potential damage. US and European standards generally assume the random profile covers that, but the Chinese standard explicitly calls for resonance dwell testing, which is a thorough approach.

After the test, besides checking for safety (no fire, etc.), typically the battery is opened (if it is a sample for test) to inspect for physical damage: e.g. cracked welds, insulation wear, or cell displacement. For regulatory certification, they might not require opening (since that could damage evidence), but they require a functional test and isolation check. For example, R100.03 says after vibration, isolation resistance must still be $>100\ \Omega/V$, meaning the dielectric integrity is intact (no chafed wires causing short to chassis). If isolation fails, it is a fail because that could mean in a real vehicle the vibration wore through insulation and could shock someone or cause a short.

In summary, the vibration test ensures that the battery design is robust against the everyday "background" mechanical stress of driving. The differences among regions are minor – mainly whether a sine sweep or random vibration is used, and the intensity/duration. The trend is toward using random vibration profiles tailored to vehicle environments, as these are more realistic than simple sine sweeps. With EV batteries often lasting 8–10 years, vibration testing has become not just a safety check but a durability requirement. Nonetheless, from a regulatory viewpoint, the emphasis remains on verifying that no safety hazards (loose fragments, internal shorts leading to fires, etc.) will result from vibration. Indeed, standards treat the vibration test as an abuse test by requiring no fire or explosion (some even call vibration "abusive" since in normal conditions it should not cause immediate failure). The inclusion of vibration in essentially all battery regulations highlights recognition that mechanical stresses over time can degrade a battery's safety if not accounted for in design.

5.2.6 Summary of Mechanical Test

Mechanical testing is a cornerstone of battery safety qualification in the automotive industry's regulatory frameworks. Through shock, drop, penetration, immersion, crush, and vibration tests - each targeting a different facet of mechanical stress - standards ensure that electric vehicle batteries can withstand both ordinary and extraordinary mechanical challenges without jeop-

ardizing safety. A unifying theme in all regulations is the stringent pass criteria: regardless of test specifics, a battery system must not ignite or explode, must contain its electrolyte, and must maintain electrical isolation when subjected to mechanical abuse. These outcomes are non-negotiable prerequisites for regulatory approval of a RESS.

The comparison reveals that while European (UNECE R100.03) and international standards lean towards incorporating vehicle-crash equivalence (using crash test evidence or moderate component tests), American and Chinese standards often prescribe more direct and sometimes more aggressive component-level tests. For instance, the EU's approach historically omitted drop and nail penetration tests, focusing instead on crash shock and crush aligned with vehicle crash norms, whereas US and China developed stand-alone drop and penetration protocols (UL , SAE, China's GB) to cover handling and abuse scenarios beyond crashes.

China's recent standards like GB 38031 have introduced innovative requirements such as thermal propagation mitigation (in lieu of single-cell nail tests) and combined vibration-immersion sequences, reflecting a proactive safety philosophy. The US framework, lacking a single national regulation for batteries, relies on a patchwork: federal crash standards (FMVSS 305) ensure post-crash electrical safety, while industry standards (SAE, UL , USABC) fill in with abuse tests that many manufacturers follow. ISO, aiming for global consensus, often mirrors UNECE rules (for regulatory acceptance) but also provides optional tests for comprehensive evaluation (e.g. ISO 6469-1 includes water immersion and shock, acknowledging newer concerns).

In practice, auto-makers seeking worldwide market access tend to design to the most demanding criteria among these standards. A pack that passes UL 2580's drop and crush, China's nail penetration (propagation) test, and R100's crash pulse and isolation checks will essentially meet all regulatory requirements. Thus, there is a convergence towards best practices. Research by organizations and safety bodies continuously feeds into revisions of standards (for example, adjusting shock levels to real-world crash data or refining crush force values to avoid unrealistic excess).

The ultimate goal is a robust yet realistic battery safety test regime that assures public safety without stifling innovation with undue conservatism. By comparing the procedures and criteria, this chapter has identified how each test contributes to understanding a battery's degradation and failure modes under mechanical stress. Mechanical shocks primarily test cell retention and electrical connection integrity during a sudden jolt; vibrations test long-term mechanical fatigue; crush and penetration directly probe the cell's vulnerability to internal shorts and the pack's ability to contain such events; drops check the robustness of enclosures and mounts. All these tests, while originally devised as safety qualifiers, also inform engineers about degradation - e.g., a battery that barely passes vibration might have loosened connections that could impair performance over time. Thus, from a degradation processes perspective, the mechanical tests in regulatory standards serve as accelerated indicators of how a battery might wear or fail mechanically in the field.

In conclusion, the mechanical test procedures enshrined in regulations provide a comprehensive safety net against mechanical abuse. The comparative tables and analysis herein serve as a reference for researchers and engineers to understand the current state-of-the-art in regulatory mechanical testing for EV batteries. Ensuring compliance with these rigorous tests is not just about meeting legal requirements, but fundamentally about safeguarding users and rescuers from the unique hazards of high-energy battery systems under mechanical duress.

5.3 Electrical Tests

Electric vehicle battery packs must undergo rigorous electrical abuse tests as part of industry standards to ensure safety and reliability. These tests simulate electrical fault conditions - such as short circuits and overcharging - to evaluate whether a battery can withstand them without causing hazardous events (fire, explosion, etc.). Currently, a variety of international and

national standards specify such tests, including global regulations (e.g. UNECE R100.03 and UN GTR 20), industry standards (ISO, IEC, SAE, UL), and country-specific standards in the United States and China. However, differences in testing procedures and criteria exist across these standards, which complicates direct comparisons and has prompted calls for harmonization.

5.3.1 External Short-Circuit Test

One of the most critical electrical abuse tests is the external short-circuit test, which evaluates a battery's response when its terminals are directly shorted. The purpose is to assess the battery's ability to withstand a high current surge and to verify that protection devices (fuses, circuit breakers, etc.) function properly to prevent a dangerous situation. During this test, the battery (cell, module, or pack) is connected across a very low-resistance load, creating a near-direct short. This causes a rapid, large current flow until the battery's protective devices activate or the battery's internal impedance limits the current [310]. The main safety risks are intense ohmic heating, which can induce TR in cells, and arcing at connection points, potentially leading to fire or insulation damage. The Table 5.7 summarizes key test parameters and conditions specified in major normative documents, illustrating the variation in methodologies and safety thresholds adopted across different regulatory frameworks. This information is essential for evaluating compliance pathways and benchmarking degradation behaviour under abuse conditions relevant to RESS applications.

Test conditions for the short-circuit simulation vary across standards. Most standards specify using an external resistor in the order of just a few milliohms to maximize the fault current. For example, UNECE R100.03 and related standards use an external load of about 5 mΩ to simulate a hard short circuit [254].

In contrast, UL 2580 use around 20 mΩ for the short [283]. The duration of the short is typically maintained for several minutes or until the battery stabilizes. For instance, China's current EV battery safety standard GB 38031-2020 mandates that an external short be applied for 10 minutes with a conductor of $< 5\text{m}\Omega$ [73], similar in stringency to UNECE R100.03's requirements. U.S. and international standards likewise generally require $\sim$10 minutes of shorting unless a safety interruption occurs. Another key parameter is the SOC of the test sample. Since a fully charged battery represents the worst-case scenario (maximum stored energy), many standards require testing at 100% SOC.

Pass/fail criteria in all these standards focus on preventing catastrophic outcomes. The battery must not ignite, explode, or vent toxic gases extensively during or after the short. Activation of safety devices (e.g. fuse blow, circuit breaker trip) is expected. In practice, many EV batteries include protective circuitry that cuts off the short current within milliseconds. The test therefore verifies that such protection operates correctly and that cells can survive the initial surge until protection kicks in.

If a battery lacks external current interruption, the cells themselves must endure the short without TR. Notably, UNECE R100.03 require that after a short-circuit test, the battery exhibit no evidence of fire or explosion. Chinese standard GB 38031-2020 likewise requires no fire or explosion and also that post-test the battery's electrolyte leakage is within specified limits. In essence, despite slight differences in execution, all standards have the common safety goal of ensuring an external short does not lead to a battery fire.

In summary, the external short-circuit test is universally mandated across EV battery standards, but specific protocols differ. International regulations (like R100.03 or GTR 20) and Chinese standards demand a very low resistance ($< 5\text{m}\Omega$), often at full charge. US standards (SAE, UL) mirror these conditions closely, though UL 2580 allowed a slightly higher short resistance (20mΩ) in its procedure. These nuances can influence test outcomes, which is why a battery might pass one standard's short-circuit test but potentially fail another's if the conditions are more severe. Overall, however, all standards agree on the outcome: an EV battery must withstand a direct short without causing fire or harm.

Table 5.7: Comparison of selected international safety testing standards for LIBs with respect to overcharge, overdischarge, and short-circuit scenarios, based on [69, 73, 260, 261, 279, 297, 285, 283, 304].

Safety Test	***ISO 12405-1:2012 ISO 12405-2:2012***	ISO 6469-1:2019	***IEC 62660-3:2022***	***SAE J2464:2021***	***SAND2005-3123***	***UL 2580:2022***	***GB 38031-2020***	***IEC 62619:2022***	***UL 1973:2022***
Overcharge (rate; cut-off SOC or cut-off voltage)	5 C; 130% SOC (ISO 12405-1) 2 C; 130% SOC (ISO 12405-2)	I_{max}; as per manufacturer guidelines	1 C or 1/3 C; (BEV) 5 C or 1 C; (HEV)	120% V or 130% SOC	I_{max}; 150% V or 200% SOC	32 A; 200% SOC	I_{max}; 110% SOC	I_{max}; 110% V	≤1 C; 150% V
Overdischarge (rate; cut-off voltage or over time)	1 C; 25% V or 30 min (ISO 12405-1) 1/3 C; 25% V or 30 min (ISO 12405-2)	I_{max}; as per manufacturer guidelines	1 C; 25% V or 30 min	I_{max}; N[5]	1 C; 30 min	I_{max}; 30 min	N; 25% V (system)	1 C; 90 min	I_{max}; 30 min
External short circuit (resistance)	100 mΩ (ISO 12405-1) 20 mΩ (ISO 12405-2)	5 mΩ	≤5 mΩ	≤5 mΩ	≤5 mΩ	≤20 mΩ (cell) ≤20 mΩ (system)	≤5 mΩ	20 mΩ	≤5 mΩ
Internal short circuit	N/A	N/A	Battery-embedded nickel particles	Battery-embedded nickel particles	N/A	N/A	N/A	Battery-embedded nickel particles	N/A

[5] N represents not specified or no specific parameter indicators; I_{max} represents the maximum current that can be charged and discharged; V represents the maximum upper or lower voltage specified by the manufacturer.

5.3.2 Overcharge and Overdischarge Tests

Beyond short circuit, another category of electrical abuse tests involves forcing the battery beyond its normal voltage limits – namely overcharge (charging past 100% SOC) and overdischarge (discharging past 0% SOC, potentially into cell reversal). These tests verify that the battery's control systems (e.g. BMS) can prevent or withstand such events, and they assess what happens if those protections fail. Virtually all EV battery safety standards include an overcharge test (and usually an overdischarge test as well), since charger or BMS malfunctions could lead to these scenarios [311]. Overcharge testing are split into two types: charging the battery beyond full capacity and inducing TR to assess the potential damage or to test the overcharge protection systems, whether the cell will not reach past threshold SOC (usually above 100%). The safety risk is significant: overcharging can lead to excessive lithium plating on the anode, heat generation from side reactions, electrolyte decomposition, and ultimately cell rupture or TR if unchecked [312]. Therefore, standards require that the battery, if overcharged, does not ignite or explode.

Many EV batteries have overcharge protection circuits (voltage limits, disconnect relays) - the test ensures these work or that the cell's inherent safety mechanisms (like current interrupt device) activate in time. Standards differ in how they define the overcharge amount and method. Some specify charging to a certain multiple of the battery's rated capacity or a percentage beyond full charge. For example, SAE J2464 required up to 200% of the battery's nominal capacity in an overcharge test [254, 279]. This is an aggressive test essentially attempting to double-charge the battery (usually at a moderate current like C/3). In contrast, Underwriters Laboratories UL 2580 standard set a lower limit, it required charging a fully discharged battery at maximum specified current until the pack's protection tripped or until reaching 110% SOC [283]. Some ISO standards chose an intermediate level, such as 130% of nominal capacity [259]. These differences are quite large (110% vs 200% SOC), and indeed it has been pointed out that test parameters for overcharge vary widely between standards. Such variation can lead to different outcomes, making it hard to compare results directly - a battery might safely survive a 110% overcharge but not a 200% overcharge. For this reason, experts have called for aligning these test conditions across standards.

Chinese standards have defined their own overcharge procedures. According to GB 38031-2020, a single cell is overcharged at a constant current until the cell reaches 100% SOC or until the temperature of the cell rises above 10 °C standard operating temperature of the cell [73]. For testing at the battery pack level, the Chinese standard interestingly specifies starting from a partial charge: the pack should begin in the middle of its normal SOC range, and then it is charged using the fastest charging method allowed by the manufacturer until the pack's voltage exceeds its limit. This approach simulates a scenario where a fast charger fails to terminate correctly - starting at mid-range SOC ensures the charger stays on for a while and really pushes the pack into overcharge. Other standards, like R100.03, typically start the overcharge test from 100% SOC (i.e. continue charging an already full battery).

Regardless of method, the pass criteria are the same: no fire, no explosion, and usually no violent rupture. Batteries often vent gases or leak electrolyte in an overcharge test; this is usually acceptable as long as there is no fireball or fragmentation. Ideally, the battery's BMS should stop the charging (open a relay) once an over-voltage is detected, terminating the test safely.

Overdischarge testing, on the other hand, checks the battery's response when drained past zero charge. The risk with overdischarge is that cell voltages can reverse and cause copper from current collectors to dissolve into the electrolyte; upon subsequent recharge, copper dendrites may form and cause internal shorts, or the SEI can break down leading to heat and gas. Overdischarge tends to be less immediately dramatic than overcharge - often the cell just goes to 0 V and then degrades internally. Indeed, experimental studies show that an overdischarged battery does not heat up as much as an overcharged one in the moment [313]. Still, standards include it to ensure that BMS low-voltage cut-offs work and that no immediate safety hazard arises from a deep

discharge. The typical procedure is to connect a resistive load and let the battery discharge well beyond the point the BMS would normally cut off, sometimes even forcing reversal of a cell, for a set duration.

For example, IEC standard might require discharging at a small current for 1 hour after reaching 0% SOC or until the battery reaches some low negative voltage. As with overcharge, no fire or explosion is allowed. It is also required to check that the battery remains safe to recharge afterward, though its capacity may be permanently reduced. Practically, modern EV packs have protective circuitry that should prevent severe overdischarge by disconnecting the pack when cells get too low. The overdischarge test is thus often about verifying this protection. If a pack has no such protection, which is unlikely in EVs, the test examines the physical failure mode of cells when driven into reversal. Generally, overdischarge tests are not as stress-inducing as overcharge tests in LIBs - overcharge is far more likely to cause an immediate TR event. This is reflected in standards: while all require overcharge testing, a few earlier standards optionalised overdischarge. Nonetheless, Chinese, US, and UN standards today all include it as a necessary part of the safety test matrix

In summary, overcharge and overdischarge tests are widely implemented across EV battery standards to ensure the battery can handle abnormal voltage excursions. Differences lie in how much overcharge is applied and under what conditions.

5.3.3 Other Electrical Safety Requirements

In addition to the major abuse tests above, EV standards cover a range of other electrical safety checks. While not "abuse tests" per se, these are crucial for a comprehensive safety evaluation and are worth noting:

- **Isolation Resistance and Dielectric Withstand:** High-voltage EV battery packs must have sufficient electrical isolation from the vehicle chassis to prevent shock hazards. International EV safety standards (ISO 6469-1, and regulations like FreedomCAR in the US or UNECE R100.03) specify minimum isolation resistance (e.g. at least 100 Ω/V of the pack voltage) to ensure no dangerous leakage current [71, 263]. UL 2580 likewise includes isolation resistance and dielectric withstand tests (applying a high voltage to the pack to ensure insulation holds up) [283]. These tests ensure the battery's enclosures, wiring, and shutdown circuits protect users from electric shock under normal and fault conditions. China's GB 38031 has similar requirements [73]. Chinese regulations for EVs (such as GB/T 18384) historically have mirrored the isolation criteria of ISO/SAE. There is broad agreement internationally on isolation test methods, so this is one area with relatively little divergence among standards.

- **Thermal Protection and Temperature Control Failure:** Batteries have specified operating temperature limits, and most packs include sensors and cooling systems. Some standards test what happens if the battery's thermal management fails. For example, UL 2580 includes a "Failure of Cooling or Thermal Stability System" test [283], in which any active cooling is disabled and the battery is put through certain usage profiles or environments to see if it remains safe. Additionally, Chinese standards and ISO may include an over-heating protection test: heating the battery slowly in an oven to see if the BMS shuts it down before a critical temperature is reached. The goal is to verify that thermal safeguards (like a thermal fuse or software cut-off at given cell temperature) actually work. While not an "electrical" abuse in terms of current or voltage, this test checks electrical control of thermal risks. It complements the purely thermal abuse tests (like external fire or thermal soak) found in standards.

- **Imbalanced Charging:** EV battery modules consist of series cells that must be balanced. UL 2580 lists an "imbalanced charging" test, likely charging a pack with cells at differing

states of charge to see if the battery management can handle imbalance without overcharging some cells. This is a nuanced test ensuring the BMS algorithms and cell balancing circuits prevent any one cell from being driven into unsafe conditions. Not all standards explicitly test this, but it reflects a practical safety concern [283].

5.3.4 Summary of Electrical Tests

Electrical safety tests for EV batteries covering short-circuits, over-voltage and under-voltage abuses are fundamental to all standardization regimes in the automotive industry. They serve to qualify that a battery design can prevent or mitigate the most dangerous electrical failure modes. The common thread is that all aim to prevent battery fires and explosions under electrical abuse, but we found notable differences in test procedures and stringency.

For instance, the acceptable extent of overcharge ranges depending on the standard, and internal short-circuit testing is handled via differing philosophies. Such disparities mean that a battery might pass one standard's criteria while failing another's, purely due to test condition variations. On the positive side, the existence of multiple standards has collectively pushed the industry towards safer battery designs.

Going forward, there is strong momentum toward global harmonization of EV battery safety tests. Aligning on the worst-case test scenarios and performance criteria would enable a unified, higher safety benchmark and reduce redundant testing efforts. Initiatives under the UN (through the Global Technical Regulations) are a step in this direction, influenced by input from U.S. and Chinese experts alike. In the meantime, battery developers must design with all these standards in mind - essentially engineering for the most rigorous elements of each. By doing so, they ensure that the resulting batteries will meet the current international, U.S. and Chinese requirements for electrical safety, instilling confidence that even under severe electrical abuse, EV batteries will behave as safely as possible.

5.4 Environmental Tests

RESS in electric vehicles must undergo rigorous safety testing under various environmental conditions to ensure they can withstand abuse without catastrophic failure [96]. Regulatory homologation standards and industry standards define a battery of environmental tests designed to simulate extreme conditions and fault scenarios. These tests, which complement mechanical and electrical abuse tests, aim to verify the integrity of battery packs under thermal extremes, fire exposure, and the release of hazardous substances. The primary goal is to protect vehicle occupants and first responders by preventing TR propagation, fire, explosion, or toxic exposure for a sufficient time to allow safe evacuation [23]. Summary of environmental and thermal stress endurance parameters used in selected battery safety standards, focusing on high-temperature and thermal shock cycling tests was presented in Table 5.8. Standards include automotive, industrial, and regulatory protocols applicable to LIB systems and their subcomponents.

Below is a comprehensive analysis of the main standardized environmental tests for EV RESS, including mandatory tests in international regulations (UNECE R100.03, GTR 20-2018, Chinese GB/T standards) and voluntary or industry-specific standards (ISO, IEC, SAE, UL , etc.). The test categories examined are:

- thermal stability,
- thermal shock,
- fire resistance,
- emissions.

For each type, the purpose is compared, procedures, key parameters, pass/fail criteria, and specific challenges across different standards. Tables 5.8 and 5.9 are provided to summarize and contrast the test profiles for each category. Reviews of battery safety standards indicate that while international efforts (like the Global Technical Regulation) are harmonizing requirements, significant discrepancies remain in how different organizations approach safety testing. For example, China's mandatory standard GB 38031-2020 (EV traction battery safety) builds on UNECE R100.03 and GTR 20 but imposes more stringent conditions for environmental tests like vibration, thermal cycling, humidity, immersion, salt spray, and altitude simulations [72, 73, 254].

Such differences reflect varying safety philosophies: some regulations emphasize demonstrating robust management of hazards (often allowing built-in protection systems to function), whereas many voluntary standards adopt worst-case abuse scenarios with safety systems defeated to test inherent resilience. It is broadly recognized that improved standardization of test protocols and closer collaboration between industry and regulators are needed to ensure reliable and comparable safety performance of RESS across jurisdictions [70]. In the following sections, each major category of environmental test is discussed in detail.

Table 5.8: Summary of environmental and thermal stress endurance parameters [73, 254, 260, 269, 279, 283, 285, 297].

Safety Test	***High-temperature endurance (temperature; time)***	***Temperature shock cycling (temperature range; cycles)***
UNECE R100.03 *ISO 6469-1*	N/A	-40∼60 °C; 5
ISO 12405-1:2011 *ISO 12405-2:2012*	N/A	-40∼85 °C; 5
IEC 62660-3:2022	130 ± 2 °C; 30 min	-40∼85 °C; 30
SAE J2464:2021	300 °C; 30 min*	-40∼70 °C; 5
SAND2005-3123	N/A	-40∼80 °C; 5
UL 2580:2022	N/A	-40∼85 °C; 5
GB 38031-2020	130 ± 2 °C; 30 min	-40∼85 °C; 5 (cell) -40∼60 °C; 5 (pack or system)
UL 1973:2022	N/A	-40∼75 °C; 10

* - 5 °C increment is applied for every 30 min of exposure until the temperature reaches 300 °C or sample disintegrates.

5.4.1 Thermal Stability Tests

Thermal stability (or high-temperature endurance) tests evaluate a battery's ability to withstand elevated temperatures without undergoing TR or significant damage. The purpose is to determine the temperature threshold at which the cell or pack becomes thermally unstable, and to ensure that batteries remain safe up to and slightly beyond their maximum specified operating temperature [314]. In regulatory contexts, this can also demonstrate that the RESS's thermal management and safety circuits will act to prevent dangerous overheating.

Early incremental-heating tests (SAE J2464 and the USABC/FreedomCAR guidelines) are designed to push cells to their thermal limits in a controlled manner. They identify the precise temperature at which self-heating accelerates uncontrollably, indicating the TR threshold. These tests typically reveal cell-level stability limits and the effectiveness of any shutdown separators or venting mechanisms [276, 279].

In contrast, newer standards like UL 2580 (referring to UL 2054 [315]) adopt a simpler high-temperature endurance approach: holding the RESS at a fixed elevated temperature for

a duration. This approach verifies that no TR or fire occurs up to that temperature, without necessarily determining the exact runaway point. It provides a safety margin beyond normal operating temperatures (commonly around 50–60 °C for automotive cells) [316] and ensures the battery can tolerate transient thermal events (e.g. due to cooling system failure) without immediate catastrophe. A key difference is whether the battery's internal protection is engaged. ISO and UL tests usually disable over-temperature cut-offs (for example, pack contactors or thermal fuses) to test the inherent stability of the cells/module. UNECE R100.03, on the other hand, regards the RESS's thermal management as part of the safety concept. R100.03 requires documentation and possibly testing to show that if a component fails or the pack overheats, the battery's controls will intervene to prevent hazardous outcomes.

This reflects a philosophy difference - regulatory tests assume the vehicle's safety systems are functional, whereas many voluntary standards assume worst-case failure of all safety devices. The pass/fail criteria across standards consistently demand no fire or explosion. Venting of steam or mild gases may be allowed in some cases (venting is typically not a failure unless it is violent or ignites). SAE and USABC protocols explicitly measure the TR onset temperature, which becomes a design input for thermal management systems

The challenge in thermal stability testing is balancing realism and stringency. An incremental test to destruction yields more information but at the cost of sacrificing samples and possibly creating extreme conditions unlikely in normal service. Fixed-temperature tests are easier to perform and less destructive, but their stringency (choice of temperature and duration) must be high enough to uncover safety weaknesses. In practice, 130 °C for 30 minutes has become a common benchmark in industry, as it significantly exceeds typical EV battery operating limits while being below the decomposition point of most electrolyte solvents.

5.4.2 Thermal Shock Tests

Thermal shock (temperature cycling) tests simulate abrupt ambient temperature changes that a vehicle might experience, for instance when driving from a cold environment into a hot garage or vice versa. Rapid thermal expansion and contraction can stress battery components (cell jellyrolls, seals, welds) and potentially cause cracks or loss of integrity. The purpose of the test is to ensure the RESS can withstand repeated extreme temperature swings without leakage, fire, or performance degradation [317]. Table 5.8 compares key parameters of thermal shock tests.

Most thermal shock tests share the same low-temperature limit (−40 °C, a common qualification temperature for automotive parts). The high-temperature limit varies: UNECE R100.03 uses 60 °C as the default upper bound (since many Li-ion batteries are not intended to operate beyond 60 °C without derating), whereas ISO and UL use 85 °C to provide a larger safety margin [254, 283, 263]. Research indicates that at low temperatures the electrolyte's ionic conductivity plummets and lithium metal can plate onto anodes, raising the risk of internal short circuits upon re-warming [318]. Hence, surviving repeated −40 °C exposure is a key indicator of robustness. The number of cycles is typically five in most standards. Some cell-level standards (e.g. IEC 62660-3 [269]) require more cycles (30 cycles in one case) to capture degradation trends, however these are specific for the cells itself, not the modules or assemblies.

In all cases, no fire, venting, or explosion is allowed during cycling or subsequent observation. Minor mass loss (due to pressure-relief valve opening) might be permissible if the standard explicitly allows venting, but generally, any leakage of electrolyte is a failure. A significant difference lies in whether the RESS's thermal management or safety circuits are engaged. R100.03 permits the BMS to remain active during the test. This means if the battery pack has self-heating or cooling functions, they could mitigate the temperature swings, although R100.03 requires the cooling system be off to truly stress the battery.

More importantly, if a battery cell exceeds safe temperature, the BMS in an R100.03 test can intervene (e.g. open a contactor). However, such intervention itself would likely be considered an "abnormal termination" of the test; R100.03 explicitly states that any activation of safety

measures beyond normal operation is not allowed as an outcome during the required cycles (i.e. the battery must survive the cycles without triggering an internal fail-safe that aborts the test).

In contrast, ISO, UL, and SAE tests typically disable any such automatic cut-offs. The battery is forced to endure the full temperature range passively, which is a harsher assessment of intrinsic resilience. In one comparison, R100.03 was the only evaluated standard that allowed over-temp protection to remain active during thermal cycling.

Another procedural difference is exposure time. R100.03 and GB 38031-2020 mandates very long dwell times (at least 6 or even 8 hours) to ensure thermal equilibrium throughout the pack. This is particularly important for large battery packs with thermal inertia; it ensures even the core of the battery reaches the chamber temperature. SAE J2464's previous version used only 30 min dwells, focusing on the shock of rapid change rather than long exposure, which was slightly less severe than international standards that combine shock with prolonged stress. The outcomes and challenges of thermal shock tests include potential enclosure cracking, seal breaches, or even cell venting if internal pressure spikes with temperature. High differentials can also cause condensation of moisture (if any ingress) which may lead to electrical shorting. However, under controlled laboratory conditions with dry air or nitrogen chambers, condensation is minimized.

The primary challenge is ensuring the transition is fast but not so abrupt as to overshoot temperatures beyond the set-points. Another approach is to move batteries between two chambers (hot to cold) to achieve a < 30 min transition, which can introduce handling risks. Others use a single chamber that can be cooled and heated rapidly.

In summary, thermal shock tests verify RESS responses the worst thermal swings it might encounter in service (for example, a car in winter driving into a heated garage repeatedly). The consensus criteria across standards are that the battery should not leak, catch fire, or explode during or after cycling. In practice, well-designed automotive batteries pass these tests by using flexible cell interconnections, robust seals, and accommodating thermal expansion in the mechanical design.

5.4.3 Fire Resistance Tests

Fire resistance testing is one of the most critical parts of RESS safety certification. The fire test evaluates a battery pack's behaviour when exposed to an external fire, such as could occur if the vehicle is in a fuel fire (from its own fuel in a hybrid, or an adjacent vehicle, or a garage fire). The primary safety concern is the risk of the battery pack itself exploding or violently rupturing, which could endanger occupants and rescuers. Thus, the core pass criterion in nearly all fire tests is that the RESS must not explode during the specified fire exposure and for some time after, thereby providing occupants the chance to evacuate. Different standards have developed distinct methods to perform the fire test. Some immerse the battery or device under test (DUT) in a direct flame (pool fire), while others use radiant heat sources or burners.

While the standards involve multiple objectives to obtain for the battery in the fields of design, performance, safety design, environmental protection, classification etc., the standards set the baseline for RESS safety [96]. When products receive positive test results and are introduced to the market, the actions on the safety design become reactive after accidents or failures happen [25]. Thus, it is of utmost importance to develop high quality testing procedures to guarantee an excellent safety threshold for the users.

The standards and regulations selected for this study are: GTR 20:2018 [67], UNECE R100.03:2021 [254], ISO 12405-3:2014 [259], ISO 6469-1:2019 [263], ISO 18243:2017 [264], SAE J2464:2009 [279], GB/T 31467.3-2015 [72], SAND2017-6925:2017 [275] and UL 2580:2020 [283]. Comparison is shown in Table 5.9.

Despite the fact that there multiple standards involved the procedures are often times duplicated with small changes. A following section will present the procedures used broadly nowadays.

Table 5.9: Comparison of the EV safety standards and regulations based on [73, 254, 259, 263, 276, 279, 283, 285].

Reference name	Procedure	Pass criteria	Purpose	Assembly level (cell, module, pack)
UNECE R100.03 - Gasoline pool fire	70 s direct exposure to positive-ignition fuel, continued for another 60 s with indirect exposure (through perforated screen)	No explosion i.e. means the sudden release of energy sufficient to cause pressure waves and/or projectiles that may cause structural and/or physical damage to the surrounding of the Tested-Device	Evacuation of the occupants from the vehicle	Module or pack
UNECE R100.03 - LPG Burner	120 s direct exposure to burner flames of averaged temperature of 800-1100 °C			Module or pack
ISO 12405-3:2014	70 s direct exposure to positive-ignition fuel, continued for another 60 s with indirect exposure (through perforated screen)			Module or pack
				Pack
ISO 6469-1:2019				Pack
				Pack
GB 38031-2020			NA	Pack
UL 2580:2022 UL 1973:2022	20 min. exposure to minimum of 590 °C with (UL 2580) imprecise fire source or (UL 1973) hydrocarbon pool fire.	No explosion i.e. a violent release of energy that produces projectiles or a pressure wave from the DUT and results in DUT contents being forcibly expelled through a rupture in the enclosure or casing. No projectiles falling outside inner perimeter area.	Ability to prevent explosion	Pack
SAND2005-3123	DUT exposed to radiating surface of 890 °C ± 5% for 1200 s Fumes from DUT checked against flammability	None - purely informative procedure	Information on behaviour of the DUT under abuse conditions	Module
SAE J2464:200				Module or pack

Open flame procedure

Open flame procedures are named after usage of free burning petrol pool and using fire plume as a heating source of the DUT. There are similar "open flame" procedures in following standards and documents: GTR 20:2018 [67], ISO 12405-3:2014 [319], ISO 6469-1:2019 [68], ISO 18243:2017 [264], UNECE R100.02:2013 [320], UNECE R100.03:2021 [254] and GB/T 31467.3-2015 [72]. The exposure is induced by the positive-ignition pool fire contained in the pan of dimensions wider and longer by 200-500 mm than the DUT. Provided DUT is not a part of a vehicle, it is set at a height of 500 mm above the surface of the fuel. The test phases are presented in Figure 5.2 and described below:

- **Phase A: Pre-heating** - at least 60 s pre-heating of the petrol pan with the DUT being at least 3 m away. After 60 s, DUT shall be exposed to fire.
- **Phase B: Direct exposure to flame** - at least 70 s of direct exposure of the DUT to flames from freely burning fuel.
- **Phase C: Indirect exposure to flame** - continuation of the DUT exposure at least for another 60 s through perforated screen made of refractory material (placed in between DUT and fire pan; see Figure 5.2 Detail 1).
- **Phase D: Post-test observation** - DUT is removed at least 3 m from the burning pan for observation. The fire is extinguished either immediately after the DUT moved away or within couple minutes. The DUT surface temperature shall reach ambient or should be decreasing for the minimum of 3 h until the end of test.

During open flame test, there are following prerequisites to be met in order to carry out the test.

- Ambient temperature must be above 0 °C, wind speed above the pan must be less than 2.5 km/h.
- SOC must be adjusted to 100%.
- The quantity of fuel must be sufficient to permit the flame, under free-burning conditions to burn for the whole test duration. Only ISO 18243:2017 defines specific value to 25 l/m^2.

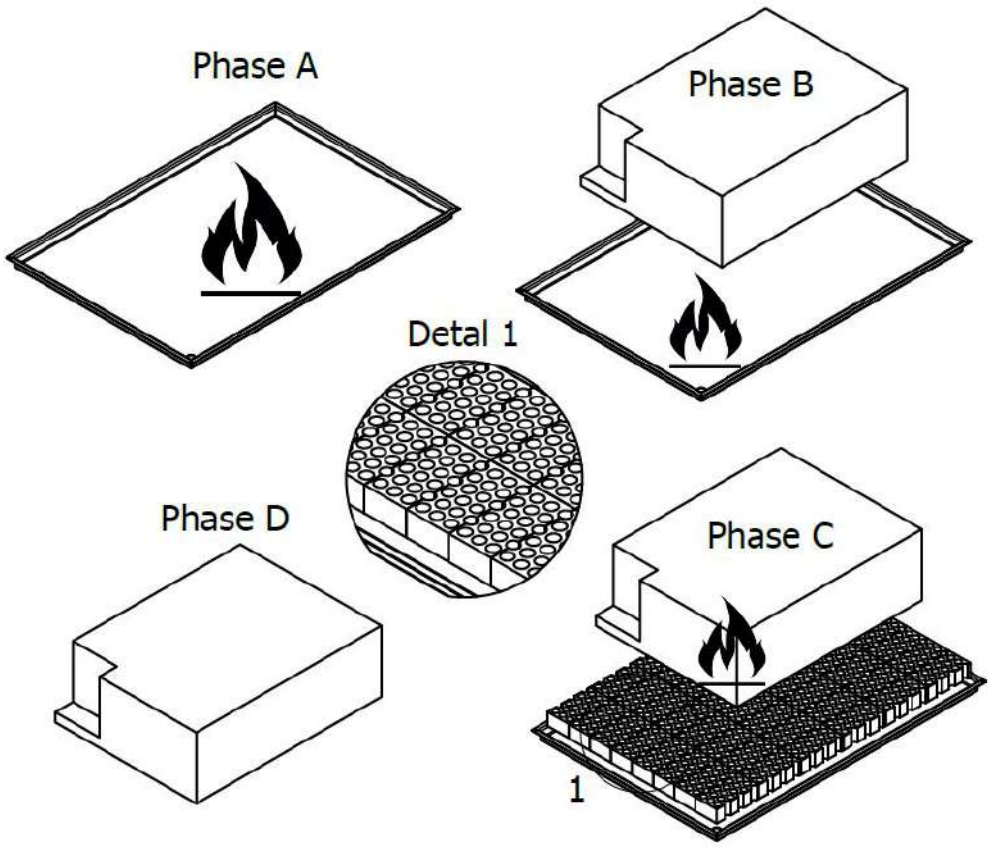

Figure 5.2: Testing set-up and procedure.

UL 2580:2020 [283] defines "External Fire Exposure Test", where a fully charged electrical energy storage assembly is subjected to a high temperature source. The source should provide uniform heating conditions at the bottom surface of the DUT, that is measured with thermocouples placed 25 mm below the DUT (shielded from the flame impingement). The test is carried out for 20 min in the temperature of 590 °C, which is required to be established within 300 s of ignition. UL 2580:2020 allows to substitute this procedure for one described in ISO 6469-1:2019, which is interesting from the total exposure time (UL 20 min vs. ISO ∼2–3 min).

LPG burner procedure

As per the newest revision of UNECE R100.03:2021 [254] and GTR 20:2018 [67], an alternative method of fire resistance testing was introduced using LPG burners instead of petrol pool burning. The procedure then consists of three stages:

- **Heating:** average temperature needs to reach 800 °C within 30 s.
- **Exposure:** average temperature after reaching 800 °C shall be maintained for 120 s within 800-1100 °C.
- **Observation:** DUT shall be observed until surface temperature reaches ambient or has been decreasing for a minimum of 3 h.

The procedure additionally requires to monitor temperature 50 mm below the DUT with the minimum quantity of five temperature sensors. Such sensors are used to establish exposure conditions within 800-1100 °C range. Testing rig constructed by Korea Apparel Testing and

Research Institute (KATRI) is shown in GTR 20:2018 [67] - see Figure 5.3. It is also required for the burner flame to be 600 mm high measuring without the tested object.

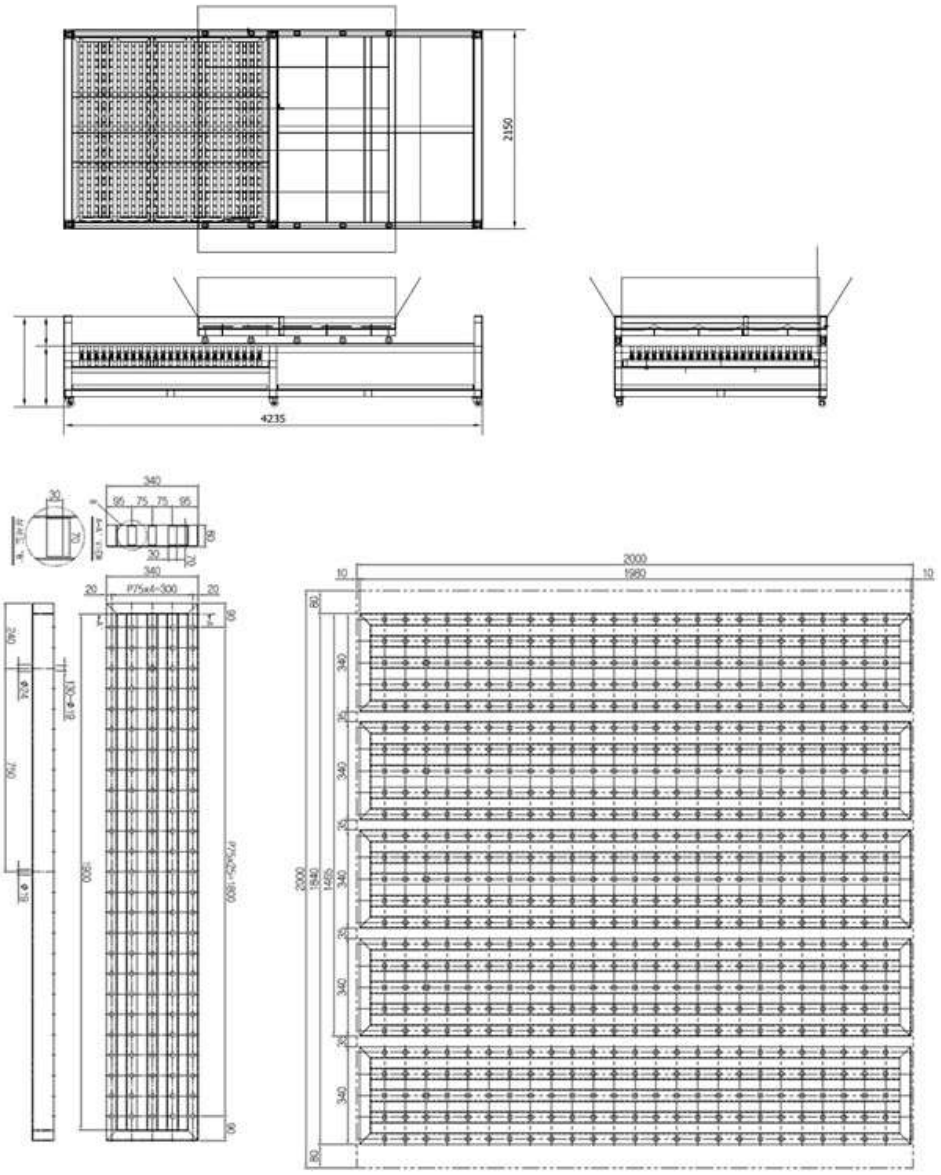
2150
4235
340
95 75 75 95
30
340
20
P75x4=300
20
2000
1980
10
10
80
80
340
340
340
340
340
2000
1840
1455
340
340
340
340
340

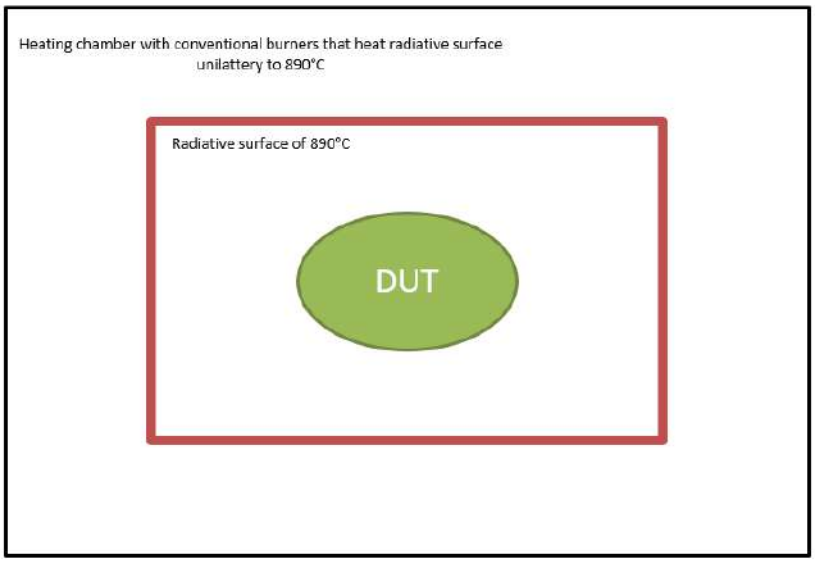

Figure 5.4: SAND2017-6925:2017 [275] and SAE J2464:2009 [279] testing set up - top view.

5.4.4 Immersion Tests

The immersion test, sometimes called the water submersion test, evaluates a battery's safety when submerged in water - particularly salt water, which is electrically conductive. This test addresses situations like an electric vehicle being flooded (e.g. in heavy rain or a flood) or a car with a battery pack ending up in water (such as a river or lake) after an accident. Water intrusion can cause electrical shorting of battery terminals or connectors and potentially lead to TR or shock hazards. The immersion test procedure typically involves fully or partially submerging the battery in a saline solution for a specified duration, and observing its behaviour during and after.

Table 5.10 provides key parameters and acceptance criteria from various international and national standards for battery immersion testing, including fluid composition, test durations, immersion conditions, and SOC requirements. The aim of each test is to ensure safety by verifying the absence of fire or explosion under simulated immersion scenarios [73, 286, 254, 263, 276, 279, 280, 285, 283, 321].

GB 38031 includes two methods: one fully submerges the pack in saltwater, the other simulates a vehicle partially submerged (pack not completely underwater). For partial submersion, GB 38031 specifies different depths depending on pack height to ensure the pack is significantly flooded.

Many standards use a high SOC (e.g. 100%) for immersion; GB 38031 requires 90–95% SOC for its sequence (it actually does immersion right after vibration, on a same sample).

Water immersion tests are a relatively newer addition to EV battery standards, introduced after incidents of EVs in floods or hurricanes raised concerns. The procedure is straightforward but can be quite dangerous, as submerging high-voltage batteries poses electrical shock risks to test personnel (proper safety measures are essential, such as using non-conductive test tanks and remote monitoring). The use of saltwater (typically around 5% NaCl by weight, approximating seawater salinity) is deliberate: saltwater is highly conductive and promotes electrolysis and corrosion, maximizing the stress on the battery's sealing and isolation. Fresh water is less aggressive in causing shorts, so a salty solution is preferred to simulate worst-case flooding (like a car in sea water or road salt brine). For example, SAE J2464 recommend ~5% NaCl solution

at room temperature (at 25 °C).

The duration of immersion is usually 2 h or until active bubbling or reaction stops. Bubbling is observed as the water may enter the pack and cause short-circuit currents leading to electrolysis of water (producing hydrogen and oxygen gas). If a battery has no breaches, there might be little to no bubbling. If there is bubbling, standards often say to wait until it subsides, but with an upper time limit. UL 2580 requires minimum 1 h soak or until bubbling stopped. The FreedomCAR procedure calls for >2 h and specifically notes to continue until bubbles stop, indicating the main reactions have ceased.

Not all automotive standards adopted immersion tests. As shown, UNECE R100.03 does not explicitly include a submersion test for the battery. Instead, R100.03 focuses on ensuring isolation resistance in the event of exposure to fluids (e.g., after a crash, the battery must maintain electrical isolation even if coolant or water ingresses, which is indirectly tested via other means). Similarly, earlier ISO standards did not have a direct immersion test (though ISO 6469-1:2019 has general requirements that likely ensure IP67-equivalent sealing) [321, 322].

However, ISO 6469-1 now references water protection, essentially requiring the battery to have an appropriate ingress protection rating (IPx7 is required) if water exposure is a concern, but it stops short of prescribing a dunk test procedure. The most robust requirements come from SAE or UL and China. GB 38031-2020 introduced an immersion test as part of a post-vibration sequence: the battery pack is vibrated, then immediately submerged to simulate a scenario like a vehicle in a flood after being rattled (perhaps mimicking earthquake or crash into water).

GB 38031 actually offers two modes: one where the pack is fully immersed in ∼3.5% salt water for 2 h, and an alternative where for very large packs (tall packs >0.85 m), where it is not needed to cover them entirely. Instead, it is ensured the pack is submerged such that either its bottom is 1 m below the surface (if pack is shorter), or if the pack is tall, at least the entire pack is under water except you leave 15 cm of water above the top. This partial submersion for 30 min is meant to simulate a realistic flooding of a vehicle's battery compartment without having to fill an enormous tank.

The criteria in GB 38031 are that the pack should not ignite or explode during the soak or after being taken out. Additionally, since GB 38031 is oriented toward safety, it likely requires the pack to not output dangerous voltages to the water (maintain isolation so that no current flows into the water accessible to passengers or rescuers). Indeed, UL 2580's criteria explicitly mention no electrical shock hazard - meaning the pack's chassis and terminals must not energize the water in a way that could harm someone. This is usually verified by measuring insulation resistance or leakage current while the pack is underwater.

During an immersion test, one often hears popping or sees bubbles as any weak points in the battery's sealing allow water to ingress. If water reaches the cells or high-voltage bus bars, it can cause short circuits. Ideally, a well-designed battery pack is sealed (IP67 or better), meaning it can be submerged at 1 m for 30 min without water ingress. Many EV packs are indeed built to IP67 standards for water and dust. Table 5.11 delineates a systematic comparison of the protection levels IPx7 and IPx8, detailing their respective water ingress resistance requirements, test methodologies, environmental parameters, and application contexts for electrical equipment in road vehicles, in accordance with the ISO 20653 standard.

The immersion test essentially verifies that - if it passes, the pack is likely well-sealed and/or shuts itself down safely when water is detected. If the pack fails, the typical result would be rapid bubbling (due to electrolysis from short-circuit currents) possibly followed by heating of cells and potentially a delayed TR or venting once the pack is removed and the water evaporates around hot components. That is why standards require observation after the test.

UL 2580 and others similarly require monitoring after removal for any signs of combustion. The acceptance criteria are straightforward: no fire, no explosion. It is generally expected that a submerged battery might short out and be permanently disabled (that is acceptable as long as it does not create an external hazard). In fact, one concern is the generation of hydrogen

gas from electrolysis - in a confined space, that could be explosive if ignited once the battery is taken out of the water. Thus, tests in laboratories are done in well-ventilated areas. The battery should not violently rupture underwater either. If a battery stays inert for the duration and after removal, it passes.

The immersion test in UL 1973 (for stationary batteries) is slightly different: instead of dunking the battery, UL 1973 calls for a moisture resistance test corresponding to the battery's enclosure IP rating (IPx7 or IPx8), often involving rain spray, humidity cycling, or shallow submersion tests depending on claimed IP code. This is more of a product certification approach, ensuring the battery can handle wet conditions in service.

In sum, immersion testing is about verifying containment and isolation. Europe does not explicitly test it in R100.03, trusting design and isolation tests, and IP tests of casing; the US addresses it via UL voluntary standards (important for safety certification in North America); and China mandates it directly due to perhaps more frequent real-world incidents (China has seen EV fires when cars were trapped in floodwaters, prompting regulators to act).

Going forward, as electrified vehicles become common in all climates, more convergence may be seen, potentially adding water exposure tests in global regulations or at least requiring a minimum IP rating for battery enclosures as part of regulatory approval. For now, the standards that do have immersion tests ensure that a battery submerged will not suddenly burst into flames or electrify the surrounding water - crucial safety outcomes for both vehicle occupants and emergency responders.

5.4.5 Emissions-Related Environmental Tests (Toxicity and Particulates)

The rapid proliferation of RESS and/or battery energy storage systems BESS, has introduced significant benefits to transportation and energy infrastructure, especially in the context of climate change mitigation and sustainable development. However, the increasing energy density, complexity, and deployment scale of lithium-ion and similar battery technologies have raised critical safety concerns - especially the risk associated with catastrophic failure events such as TR. In such scenarios, the uncontrolled heating and degradation of battery materials can result not only in fire or explosion but also in the release of toxic gases and ultra-fine particulates. These emissions pose substantial risks to human health, environmental quality, and infrastructure integrity [323].

In response to these risks, regulatory bodies and standards-developing organizations across the globe have implemented a range of emissions-related tests designed to characterize and manage the hazards associated with battery failure. Unlike traditional electrical or mechanical tests, emissions testing specifically addresses the quantity and nature of harmful substances released during fault conditions. This includes gaseous emissions such as hydrogen fluoride and carbon monoxide, as well as aerosol emissions that may include microscopic particulate matter, many of which fall in the nanoscale range and present unique toxicological properties [34, 130].

TR - the uncontrolled increase in temperature in battery cells - is the initiating event in most emissions scenarios and represents a critical failure mode across LIB technologies. When this phenomenon occurs, it leads to the decomposition of electrolyte solvents, active materials, and separator polymers, which in turn release substantial quantities of thermal energy and initiate the liberation of gases and vapours. The chemical nature of the emitted substances varies depending on cell chemistry, state of charge, battery architecture, and the surrounding environmental conditions. However, the literature agrees that certain toxicants are highly prevalent and of grave concern.

Hydrogen fluoride, for instance, is produced during the breakdown of fluorinated electrolytes and binder materials. Experimental studies have shown that HF is emitted at rates ranging from 20 to 200 mg per Wh of nominal battery capacity during catastrophic events. This implies that even for mid-sized electric vehicle packs (approx. 100 kWh), emissions can contain several kilograms of gaseous HF - a substance which is both corrosive and acutely toxic upon

inhalation [34].

Similarly, carbon monoxide is a product of incomplete combustion and organic solvent degradation. CO concentrations emitted during abuse scenarios often far exceed established occupational exposure limits. In enclosed spaces such as passenger cabins or battery housings in buildings, its presence dramatically increases the risk of toxicity or fatality. These issues are compounded by the emission of ultra-fine particulate matter (PM), often constituting combustion-generated carbonaceous nanoparticles and metal oxides, which are capable of penetrating deep into the human respiratory system to trigger long-term respiratory and cardiovascular illnesses [241, 323].

A salient feature of emissions testing is the manner in which battery failure is induced. Most protocols rely on tightly controlled abuse initiation methods, such as forced overcharge, external heating, internal short circuiting, or mechanical puncture. The selection of initiation method typically reflects the standard's scope (e.g., vehicular vs. stationary), target failure modes, and desired realism.

Once TR is initiated, emissions are collected and analysed using a range of chemical and physical detection instruments. Gaseous species are commonly monitored via Fourier-transform infrared spectroscopy, gas chromatography-mass spectrometry, or flame-ionization detectors. In parallel, advanced scanning mobility particle sizers and condensation particle counters provide real-time evaluation of particle counts and morphological characteristics in sub-micron domains [96].

The most sophisticated standards record species-specific concentrations over time, enabling not just identification of peak quantities but also dynamics of gas evolution. This data is essential for designing alarm systems, ventilation systems, and post-event recovery protocols.

Across all standards, certain emissions are consistently regarded as critical targets for measurement. These include:

- Hydrogen Fluoride, which presents both acute toxicity and corrosion risks.
- Carbon Monoxide, due to its invisible, odourless nature and high fatality risk in confined environments.
- Volatile Organic Compounds (known as VOC), such as formaldehyde, methane, ethylene, and acrolein, whose mutagenic and carcinogenic potential mandate strict supervision.
- Particulate Matter (often measured in two fractions PM2.5 and PM10), particularly <2.5 μm and nanoscale particles, characterized by high deposition efficacy within the human lungs and their ability to translocate into systemic circulation.

Yet, the degree to which each standard incorporates thresholds for these substances varies. UL standards often define acceptable upper concentration limits or acceptability thresholds based on national exposure standards (e.g., Occupational Safety and Health Administration or National Institute for Occupational Safety and Health). On the other hand, standards such as SAEs often adopt a performance-based methodology, requiring demonstration of functional mitigation (e.g., no gas impact on safety systems), rather than enforcing fixed numeric concentration thresholds.

At the vanguard of these developments is China's GB 38031 standard, whose overhaul in 2025 (planned release for 2026) reflects a paradigmatic shift from risk acceptance to risk elimination. Such regulatory stringency is likely to shape international standards harmonization in the coming years. Further convergence between automotive, transport, and stationary requirements is foreseeable, especially as unified approaches to thermal propagation containment, early fault detection, and emissions mitigation are increasingly demanded by policy, industry, and public health advocacy alike.

Ultimately, emissions testing plays a central role not only in safeguarding the end-user but also in steering battery innovation toward inherently safer chemistries, architectures, and deployment strategies.

Table 5.10: Overview of Battery Immersion Test Standards and Conditions based on [73, 263, 276, 279, 283, 321].

Standard	***Immersion Fluid***	***Fluid Temperature***	***Duration***	***Coverage / Depth***	***Battery SOC***	***Acceptance Criteria***
ISO 6469-1:2019	3.5%–5% NaCl solution	Ambient	Option 1: 2 h Option 2: 30 min.	Option 1: Full immersion	100%	No fire, explosion; alternatively IPx7 in ISO 20653 can be made
				Option 2: according to ISO 20653 IPx7: fully immerse; for test objects < 850 mm high, lowest point ≥1000 mm below liquid surface; for ≥ 850 mm high, highest point ≥150 mm below surface		
SAE J2464:2021	5% NaCl solution	Ambient	≥2 h or until visible reactions stop	Full immersion	100%	No fire or explosion
UL 2580:2022	5% NaCl solution	Ambient	1 h	Full immersion	–	No fire or explosion
GB 38031-2020	3.5% NaCl solution	Ambient	2 h immersion	Mode 1: full immersion	100%	No, fire or explosion
				Mode 2: According to GB/T 4208–2017 IPx7: fully immerse; for test objects <850 mm high, lowest point ≥1000 mm below liquid surface; for ≥850 mm high, highest point ≥150 mm below surface		
USABC FreedomCAR	3.5% NaCl solution	Ambient	≥ 2 h or until failure	Full immersion	100%	No fire or explosion; monitor ≥30 min post-test

Table 5.11: Comparison of the protection levels IPx7 and IPx8 [321, 322].

Aspect	***IPx7 (Temporary Immersion)***	***IPx8 (Continuous Immersion)***
Protection Level	Code 7	Code 8
Brief Description	Temporary immersion in water	Continuous immersion in water
Water Ingress Requirement	Water shall not penetrate in a quantity causing harmful effects or impairing performance if the enclosure is immersed in water temporarily under specified pressure and time conditions	Water shall not penetrate in a quantity causing harmful effects if the enclosure is continuously immersed in water under conditions which shall be agreed between supplier and car manufacturer, but which are more severe than code 7
Immersion Depth	1 m (minimum depth to lowest point of enclosure)	>1 m (depth agreed between supplier and manufacturer)
Exposure Time	30 min	Agreed between supplier and manufacturer (longer than 30 min)
Water Temperature	Water temperature difference from sample $\leq$5°C	Agreed between supplier and manufacturer
Test Setup - Equipment	Immersion basin/tank	Submersion basin (deeper than IPx7)
Test Conditions - Sample Positioning	Normal operating position with all covers, shrouds, and drain holes	As agreed between supplier and manufacturer
Test Conditions - Sample Size <850mm	Lowest point of enclosure 1000 mm below water surface	As agreed (typically deeper than 1000 mm below surface)
Test Conditions - Sample Size $\geq$850 mm	Highest point of enclosure 150 mm below water surface	As agreed (typically more than 150 mm below surface)
Water Pressure	Hydrostatic pressure only (atmospheric + depth)	Higher hydrostatic pressure due to greater depth
Severity Comparison	Less severe than IPx8	More severe than IPx7
Post-Test Assessment	Visual inspection for water ingress and functional testing	Visual and functional inspection as agreed
Pass Criteria	No harmful water penetration, equipment remains functional	No harmful water penetration under agreed severe conditions
Typical Applications	Outdoor electronics, automotive components exposed to temporary flooding	Submarine electronics, deep water sensors, permanently submerged equipment
Test Standard Reference	ISO 20653	ISO 20653

Chapter 6

Battery Fire Resistance Testing Methodology

6.1 Fire Plume Dynamics and Heat Flux in Lithium-ion Battery Fires

LIB fires, whether in EVs or stationary energy storage systems, pose complex fire dynamics due to the high-energy TR events and unique burning behaviour of batteries. A critical aspect of understanding these fires is fire plume theory - the behaviour of the buoyant flame and hot gas plume rising from the burning battery. The plume governs the distribution of heat and combustion products, directly affecting heat transfer to surroundings. In the context of battery fires, key plume characteristics include the centreline temperature, plume diameter (width), and centreline velocity as functions of height above the flame. These parameters inform how far and how fast heat is carried upward, which is essential for evaluating thermal effects on enclosures, barriers, and nearby equipment. Two fire plumes scenarios can be applied for fire event connected with LIB:

- Hydrocarbon pool fire - from petrol spill of the HEV or ICE vehicle with EV.
- LIB thermal runaway - for events when TR is induced within the battery cell(s).

Analysis is focused on models such as the Stefan-Boltzmann law for radiation, point-source and solid-flame radiation models, and empirical correlations (e.g. Heskestad's plume correlations and Zukoski's formulas). It is then discussed how to apply these models to practical scenarios, including the design of battery enclosures and fire barriers, and the configuration of fire safety tests. The influence of battery TR behaviour on plume development is examined, highlighting how the intermittent and energetic nature of TR can alter plume characteristics. In addition, relevant fire testing standards (UNECE R100.03, UL 2580, GTR 20) are referenced to contextualize how plume theory is considered in safety qualification, though the primary focus remains on the underlying science. Numerical examples are provided to demonstrate heat flux calculations for a given thermal plume scenario.

6.1.1 Fire Plume Theory in Battery Fires and Fire Resistance Tests

When a LIB or battery pack ignites, it often produces a buoyant fire plume similar in principle to plumes from traditional fires, but with some distinctive features due to battery chemistry and enclosure effects. Additionally, tests for fire resistance of battery packs and modules use often free burning fire pools. A fire plume can be broadly divided into two regions: the flame region (near the fuel source, where combustion is active and visible flame persists) and the plume region above the flame (dominated by hot combustion gases entrained with air). In battery fires, the

flame region may consist of jets of flame from venting cells or a diffuse flame if gases accumulate and burn above the battery, while the plume region carries hot smoke (often laden with fine particles and toxic gases) upward. Key theoretical constructs for describing plumes include the centreline temperature profile, the plume's radius or diameter as it rises, and the velocity field of the rising gases [324, 325].

In an open environment, the temperature along the centreline of a rising plume decays with height above the fire source. Classic fire plume theory provides an empirical correlation for the excess centreline temperature (temperature rise above ambient, δT) as a function of the heat release rate (HRR) of the fire and the height z. One widely used correlation, originally developed by Thomas/Zukoski and refined by Heskestad, is given by:

$$\delta T_c(z) = 9.1 \cdot (\frac{T_\infty g}{c_p \rho_\infty^2})^{1/3} \cdot Q_c^{2/3} \cdot (z - z_0)^{-5/3} \tag{6.1}$$

where T_∞ is ambient temperature, g is gravitational acceleration, c_p and ρ_∞ are the specific heat and density of ambient air, Q_c is the convective portion of the heat release rate (in kW), and z_0 is the virtual origin height of the plume [326]. This correlation is valid above the flame region (i.e. for the buoyant plume where entrainment of air has cooled the gases significantly). The virtual origin z_0 accounts for the fact that the plume behaves as if it started at a point below the actual fuel surface; for a fire of diameter D (in m) and total HRR Q (kW), Heskestad recommends:

$$z_0 \approx 0.083,\ Q^{2/5} - 1.02,\ D \tag{6.2}$$

This empirical adjustment aligns the model with observed flame heights. Notably, the $(-5/3)$ exponent in the temperature decay indicates a rapid decrease in centreline temperature with height in the far-field plume. This correlation is valid above the flame region (i.e. for the buoyant plume where entrainment of air has cooled the gases significantly) [326, 327].

In battery fires, these plume temperature correlations can be applied if the effective convective HRR is known. Convective HRR (Q_c) refers to the fraction of total heat release carried away by hot gases (as opposed to radiated heat). Many battery fires have substantial convective heat due to the hot smoke plume, though a significant fraction can also be radiated. For example, Heskestad's equation can be applied to battery fires and predicted centreline temperatures on the order of 530–1280 °C for fires in the 25–100 kW range at a height of 0.45 m. These values highlight how a larger HRR yields a much hotter plume core near the flame. In a larger-scale scenario, a full BESS module fire (propane-equivalent fire source) with a convective HRR on the order of several MW was calculated to have a centreline temperature of about 644 °C at $z = 11$ m. This indicates that even tens of meters above a large battery fire, the smoke plume can remain around 600 °C, posing a significant thermal hazard for anything caught in it or for structural elements if in an enclosure [328].

It should be noted that the above correlation assumes a statistically steady plume and might underpredict temperatures in cases where a hot layer forms (e.g. under a ceiling). In a confined or semi-confined geometry (like a battery in a vehicle or container), hot gases can accumulate, leading to higher temperatures than an open plume model would suggest. Nonetheless, the correlation provides a useful first approximation for plume temperatures in many scenarios [329].

Along with temperature, the upward velocity of plume gases is key to determining convective heat transfer and smoke dispersion. Empirical plume theory shows that centreline velocity w_c also decays with height (above the flame zone) following a power law. Zukoski [330] give the centreline velocity as:

$$w_c(z) \approx C_v \cdot (\frac{g Q_c}{\rho_\infty c_p T_\infty})^{1/3} \cdot (z - z_0)^{-1/3} \tag{6.3}$$

where C_v is an empirical constant on the order of 3.8–4.0 for free plumes. This relation indicates that the plume gases slow down as they rise (with an exponent of -1/3), due to entrainment of

ambient air which increases the cross-sectional area of the plume and reduces the buoyant driving force per unit mass. Closer to the flame (smaller z), velocities are higher; farther up, velocities decrease, eventually approaching the order of the ambient rising convection speed (and getting carried by lofting and wind). Mean velocity, u_0, follow approximately Gaussian in shape, with the centreline velocity representing the maximum value and can be derived by integrating the Gaussian velocity distribution:

$$o_0(z) \approx 0.5 w_c(z) \tag{6.4}$$

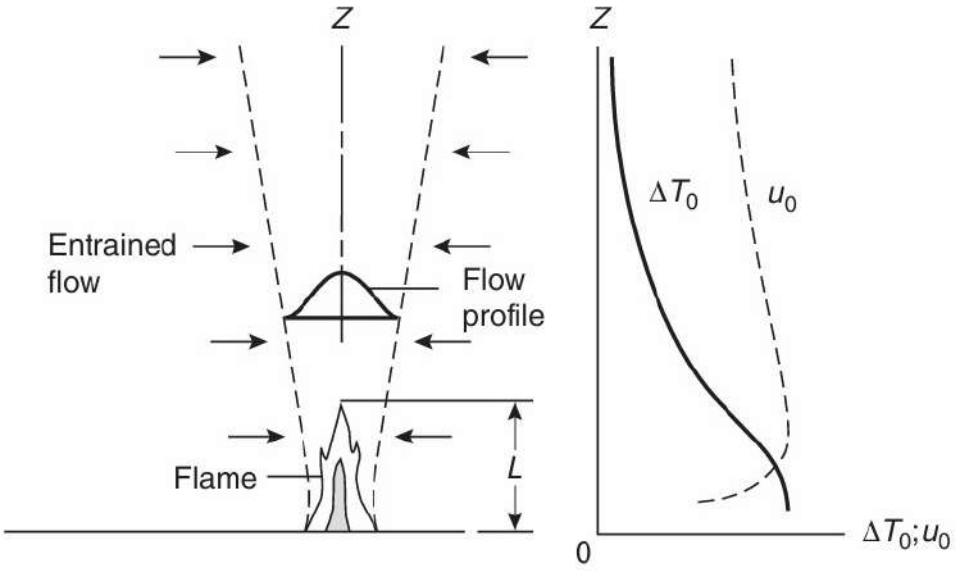

Figure 6.1: Features of a turbulent fire plume, including axial variations on the centreline of mean excess temperature, δT_0, and mean velocity, u_0.

As the plume rises and entrains cooler air, it expands in diameter. The plume radius $r_p(z)$ can be defined in various ways (for example, the radius where the excess temperature or velocity falls to some fraction of the centreline value). For many buoyant plumes, the radius increases approximately linearly with height: $r_p(z) \approx \alpha(z - z_0)$, where α is an entrainment constant. Yokoi and Zukoski suggests an average $\alpha \sim 0.10$–0.15 for a free plume. Using $\alpha \approx 0.1$, the plume diameter ($2r_p$) would be about 0.2 times the height above the fire - meaning at $z = 5$ m, the plume is roughly 1 m wide (for reference, visual observation of smoke plumes often corroborates this order of magnitude). The radial profiles of velocity and temperature in a plume approximately follow a Gaussian shape, with the highest values on the centerline and decaying towards the edges, as presented in Figure 6.1. Zukoski's analysis indicates that the velocity profile is slightly broader than the temperature profile (by about 15% in width). In practical terms, this means the plume's hot core is somewhat narrower than the full width of the plume's visible smoky column, as cooler entrained air resides toward the edges [326, 331].

Although the focus is on the plume above the flame, it is worth noting flame height correlations because they define where the flame region ends and plume-only region begins. A commonly used flame height correlation for buoyant diffusion flames (like pool fires) is Heskestad's formula:

$$L_f = 0.235 \cdot Q^{2/5} - 1.02D \tag{6.5}$$

where L_f is the average visible flame height (m). Essentially, flame height increases with the fire size (heat release rate to the power 2/5). If this formula is applied to battery fires, one must

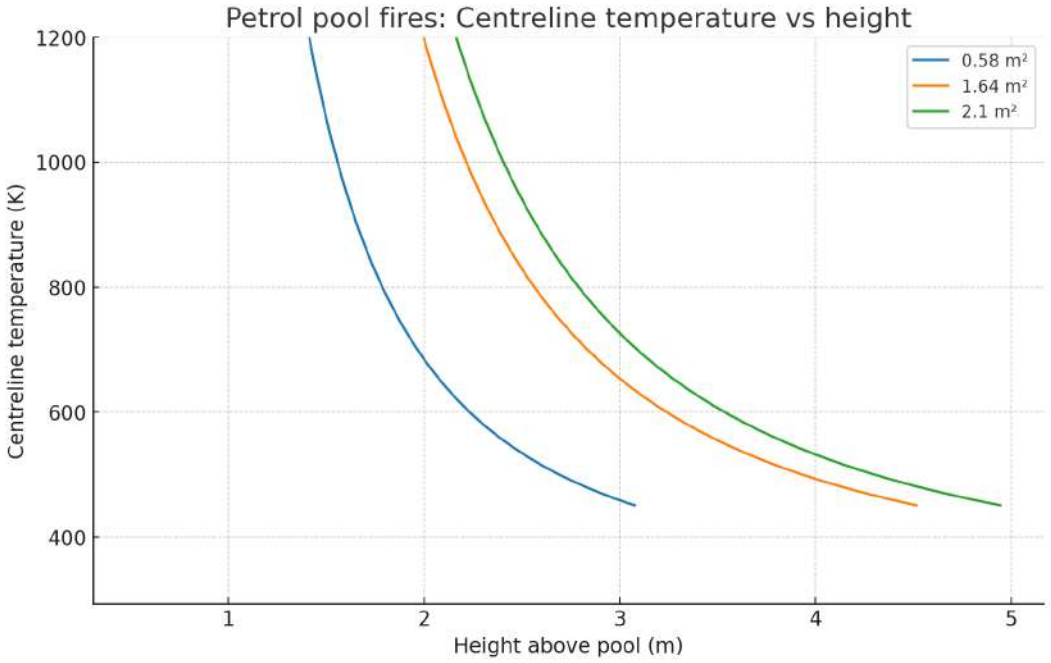

Figure 6.2: Calculation of the centreline temperature vs flame height based on Heskestad formulas' for pool values of 0.58, 1.64 and 2.10 m^2.

consider what constitutes the "flame". In an array of many cells, flames may appear at multiple locations; the flame height in such cases can refer to the highest point of continuous flaming. For example, an EV battery pack fire with $Q = 1$ MW and an effective source diameter $D = 1$ m might have an expected flame height on the order of:

$$L_f \approx 0.235 * (1000)^{2/5} - 1.02 \approx 3.7 \text{ m} \tag{6.6}$$

Flame height is important because below L_f, the plume is intermingled with flaming combustion, whereas above L_f, the plume consists of hot gases that are cooling as they mix with air. Plume models strictly apply for $z > L_f$ (above the flame tip). Within the flame zone ($z < L_f$), the centreline temperature is roughly the flame temperature (often on the order of 927–1227 °C for hydrocarbon flames) [326, 332]. For battery flames, measured flame temperatures can be lower than hydrocarbon pool fires; one study reported peak flame temperatures around 627 °C during a laptop battery TR fire [328]. This "cooler" flame is partly due to the combustion of battery electrolyte producing large amounts of aerosol (white smoke), which can dilute and radiatively cool the flame.

In empirical modelling of buoyant diffusion flames, it is recommended the use of correlations developed by McCaffrey and Zukoski to estimate the centreline temperature distribution above a fire source. These correlations describe the excess temperature rise above the ambient level, $\Delta T(z) = T(z) - T_\infty$, as an inverse power function of the vertical distance above the virtual origin z_0:

$$\Delta T(z) \propto (z - z_0)^{-n} \tag{6.7}$$

where n is an empirically determined exponent. In the continuous flame region, McCaffrey's data suggest $n \approx 1.0$, while in the far-field plume region, Zukoski's analysis yields $n \approx \frac{5}{3}$. The virtual origin z_0 represents the theoretical point from which the plume appears to emanate and is generally located below the physical fuel surface.

From a mathematical standpoint, Equation (6.7) possesses a singularity at $z = z_0$. As the distance z approaches z_0 from above, the denominator $(z - z_0)$ tends to zero, and consequently:

$$\lim_{z \to z_0^+} \Delta T(z) \to \infty. \tag{6.8}$$

This implies that, according to the raw form of the correlation, the centreline temperature at the flame base becomes unbounded. Such behaviour is clearly non-physical and is instead a direct consequence of extrapolating an empirical fit beyond its range of validity.

Physically, the region very close to the fuel surface is dominated by intense mixing-controlled combustion within the luminous flame core. Here, the gas temperature is constrained by the adiabatic flame temperature of the fuel-air mixture, which for hydrocarbon pool fires typically lies in the range $T_{max} \approx 927\,^{\circ}\mathrm{C}$ to $1927\,^{\circ}\mathrm{C}$, depending on equivalence ratio, fuel composition, and heat losses. The infinite temperatures predicted by Equation (6.8) therefore do not correspond to measurable reality, but rather to a mathematical artefact of the assumed scaling law.

The origin of this artefact lies in the derivation of the McCaffrey and Zukoski correlations, which were fitted to experimental measurements obtained in the plume region - that is, above the continuous flame and in conditions where buoyant entrainment and turbulent mixing dominate. In this far-field regime, the excess temperature decays predictably with height, following the power-law behaviour of Equation (6.7). However, in the near-field (i.e., the continuous flame zone), combustion heat release is volumetrically distributed, and the structure of the temperature field is determined by complex interactions between convection, radiation, turbulence, and finite-rate chemistry, none of which are fully captured by the simple inverse power form.

For this reason, in practical engineering analysis, it is standard practice to modify Equation (6.7) when z is close to z_0. Two common strategies are employed. First, the correlation is blended with near-field empirical regimes (e.g., McCaffrey's continuous and intermittent flame correlations) to produce a finite, physically reasonable temperature profile throughout the flame height. Second, a physical temperature cap is imposed to represent the maximum attainable flame-core temperature, often taken as $T_{cap} \approx 1873\,^{\circ}\mathrm{C}$ for hydrocarbon fuels. These modifications remove the singularity at $z = z_0$ while preserving the accuracy of the model in the plume region where the original correlation is valid. This is reflected in Figure 6.2, where areas below 1 m remain unknown for estimation. It shows three examples that has been quantified in further Sections 6.4 and 6.3, where actual data from thermocouples at 0.5 m has shown the range of temperatures between 600–900 °C, while calculations assume couple times higher temperature at or near source.

6.1.2 Modelling Convective and Radiative Heat Flux from Fire Plumes

A burning pool releases energy in two primary modes: convective heating (hot gases and flame tongues in direct contact with surfaces) and radiative heating (thermal radiation emitted by the flame, primarily from soot and hot combustion products). In a pool fire plume, a substantial fraction of the heat is carried upward by the buoyant hot gases (convective heat), which can convectively heat any object engulfed by or directly in the flame. Simultaneously, the luminous flame emits thermal radiation outward, which can heat objects at some distance or not fully immersed in the flame. The balance between these modes is characterized by the radiative fraction χ_r - the fraction of total $\dot{Q}$ that is released as thermal radiation. Sooty hydrocarbon flames typically have χ_r on the order of 0.3–0.4 (30–40%) for pool diameters up to a few meters, meaning roughly one-third of the fire's heat is radiated and the rest convected in the plume [333]. Very large fires tend to have lower radiative fractions because thick smoke can self-absorb radiation. Much of the radiation comes from the "luminous wall" of the flame - the incandescent soot in the flame envelope. The flame's interior (fuel-rich core) is cooler and emits less.

Radiation causes intense heating even if flames do not physically touch a target. A fully developed hydrocarbon flame burns at temperatures around ∼500–900 °C. The flame can be approximated as a thermal radiator at those temperatures. A blackbody at 726 °C has an emissive power $\sigma T^4 \approx 56\ \mathrm{kW/m^2}$ (with σ the Stefan-Boltzmann constant), so a large optically

thick flame can emit on the order of 10–100 kW/m^2 from its surface. In practice, measured heat fluxes incident on a sample just outside a gasoline pool fire range around 25–50 kW/m^2 during the peak burning. This encompasses both radiative and convective contributions to a temperature sensor. For instance, experiments with a 60 mL gasoline pan fire (lab scale) showed a rapid rise to ∼40 kW/m^2 heat flux in ∼30 s, a plateau of 40-52 kW/m^2 for ∼60 s while the flame was fully developed, then a decay as the fuel burned out [334]. In large-scale fires, convective heat transfer to an engulfed object can also be very high – flame convection coefficients might be on the order of 10–20 W/m^2K or more, and the flame temperature (≫ ambient) yields convective fluxes of tens of kW/m^2. In summary, an object immersed in a pool fire plume experiences total heat flux perhaps in the range of 50–100 kW/m^2 (a combination of direct flame contact and intense thermal radiation), whereas an object a short distance away (only seeing radiation) might receive on the order of a few tens of kW/m^2, depending on distance.

Several semi-empirical models are used to estimate heat flux from fire plumes. One simple approach is the point-source model, which assumes all the fire's radiant output comes from a point at some centroid of the flame. In that model, the radiative heat flux at a distance R is [333]:

$$q''_{\text{rad}} \approx \frac{\chi_r \dot{Q}}{4\pi R^2} \tag{6.9}$$

This is simple to use and conservative for distant targets, but it overestimates flux close to the fire (since a real fire is not a point). A more refined approach is the "solid flame" model, which treats the flame as an emitting cylinder or cone of finite size. In this model, one assumes the flame has an effective radiating surface area (with height and diameter determined by correlations or observations) and a uniform surface emissive power E_f. The heat flux to a target is then calculated by geometric view factors (F) between the flame surface and the target, and accounting for flame emissivity and atmospheric absorption:

$$q'' = F \cdot \tau \cdot \epsilon_f \cdot E_f \tag{6.10}$$

where F is the view factor, τ is transmittance of air (usually close to 1 for short distances), ε_f is the flame's effective emissivity ($\leq$1), and E_f is the flame surface emissive power. For large, optically thick flames (diameter > a few m), $\varepsilon_f \approx 1$ and the flame behaves like a blackbody. Then the key parameter is E_f. Pool fire data suggests flame emissive power in the range of order 100 kW/m^2 for big hydrocarbon fires [333]. Using such models, one can estimate, for example, the flux on a battery pack 0.5 m above a fire. If the flame engulfs the bottom of the pack, $F \approx 1$ for those surfaces, so flux might approach the flame emissive power (tens of kW/m^2). In contrast, at the periphery F is smaller. These models, along with correlations for flame height and tilt, are critical in interpreting standardized tests - they help translate a given test's conditions (pan size, burner output, etc.) into an equivalent heat flux or temperature exposure on the battery.

6.2 Numerical Analysis of the Conditions for Fire Resistance Testing of LIB

LIB systems are subjected to various fire exposure tests in safety standards to ensure they can withstand an external fire without catastrophic failure. The goal is typically to verify that the battery does not explode or endanger occupants in a vehicle fire, or first responders in an energy storage fire. The focus is placed on three key fire test methodologies in use: open pool-fire tests (as in UNECE Regulation R100.03 and UL 1973), a burner flame test (alternative in UNECE R100.03), and a radiative heat test (SAE J2464). Each test simulates a hydrocarbon (or other) fire in a different way. In following sections theoretical comparison on test conditions is made.

The fire plume above a hydrocarbon source is governed by buoyant convection. Modelling involves:

- Flame height correlations (e.g., Heskestad, McCaffrey);
- Convective and radiative heat flux estimation using empirical or semi-empirical models;
- View factors for radiative heat transfer;
- Use of point-source or solid flame models.

Equations shown in Section 6.1 are used to calculate heat flux and thermal dose values for 1 m^2 of pool fire (UNECE R100.03, UL 1973 - and UL 2580 if pool variant is selected) or tested element (SAE J2464). List of assumptions is shown below.

- UNECE R100.03 Pool test following assumptions are made:
  - radiative fraction $X_r \sim 0.35$,
  - heat enthalpy $\delta H = 44\,\mathrm{MJ/kg}$,
  - mass burning rate per unit area of fuel $\dot{m} = 0.055\,\mathrm{kg/(m^2 s)}$ and
  - solid flame - blackbody $T_f = 1000\,\mathrm{K}$.
- UNECE R100.03 Burner test:
  - flame emissivity $\epsilon_f = 0.85$,
  - view factor $F_{12} = 1$.
- UL 1973 Pool test see UNECE R100.03 Pool and for SAE J2464:
  - flame emissivity $\epsilon_f = 0.9$,
  - view factor $F_{12} = 1$.

Table 6.1: Heat flux and thermal dose numerical analysis theoretical results for the R100.03, UL 1973 and SAE J264 tests.

Standard	***Duration, s***	***Peak T, °C***	***Heat Flux,*** kW/m^2	***Thermal Dose,*** kJ/m^2
R100.03 Pool	130	800–900	40–50	∼500
R100.03 Burner	120	850–950	30–40	∼5,000
UL 1973 Pool	1200	800–1000	50–60	∼60,000
SAE J2464	600	890	∼90–95	∼60,000

6.2.1 UNECE R100.03 Fire Resistance Test

The UNECE Regulation No.100 (Rev.3) Annex 9E defines a fire resistance test for electric vehicle rechargeable energy storage systems - essentially a gasoline pool fire exposure beneath the battery pack. This test, derived from a fuel tank fire test (UN R34) adapted for EV batteries [335], is intended to simulate a scenario where the vehicle's battery is exposed to an external petrol fire (e.g. car fuel spill igniting under the vehicle). The test is staged in four phases:

- **Phase A: Preheating.** A pan of fuel (standard petrol) is ignited and allowed to burn freely near the test object for 60 s without the battery directly over it. In practice, the pan may be positioned beside or below at some offset during this phase. The purpose is to stabilize the fire.

- **Phase B: Direct Exposure.** The DUT is then placed directly over the burning pan - typically 50 cm above the fuel surface - and exposed to the full flames for 70 s. This is the most intense phase: the pack is engulfed in a "sheet of fire." Measured flame temperatures in this direct exposure are about on average 700 °C near the battery. The heat flux to the battery surfaces is on the order of 25–50 kW/m^2 during this phase. Physically, the pan dimensions must exceed the battery's footprint by 20–50 cm on each side to make the flame to cover it. During Phase B the battery's exterior is directly heated by flame contact and radiation, pushing it towards TR.
- **Phase C: Indirect Exposure.** After 70 s, a thermal shield (firebrick screen) is interposed between the fire and battery for an additional 60 s. The flames continue to burn, but now the battery is heated only indirectly - mainly by hot combustion gases and radiative heat through the screen's openings. This phase represents a situation where the direct flames might be somewhat separated (for instance, a brief drop in fire due to fuel depletion or some shielding). Heat flux is correspondingly lower than in Phase B.
- **Phase D: Post-test observation.** After the 130 s of fire exposure (Phases B and C), the burning fuel is extinguished. The battery is then observed for up to 3 h as it cools. This observation checks that no explosions or reignitions occur while the battery stabilizes. The safety criterion in R100 is that during the test and subsequent cooldown, the battery must not explode or disassemble in a hazardous way.

The test schematics were presented in Figure 5.2.

Table 6.2: Fire-resistance testing procedure outline [254].

Phase	***Description***	***Duration***
A	Preheating	60 s
B	Direct exposure to flame	70 s
C	Indirect exposure to flame (through perforated screen)	60 s
D	End of the test (observation)	Conditional

In addition to the prescribed test procedure described above, R100.03 require the following conditions to be satisfied during the test:

1. The test must be carried out in an ambient temperature of at least 20 °C.
2. Wind speed must be limited to 2.5 km/h measured over the fire source.
3. The flame source horizontal dimensions must be larger than the specimen by 200–500 mm.
4. Positive-ignition fuel needs to be used as a fire source.
5. The tested specimen must be set at 0.5 m height from the fire source.

The imposed wind speed limitations are predicted to be insufficient to mitigate the stochastic nature of the pool fire. Additionally, the optimal steady-state burning mode of the pool fire may not be achieved within the prescribed 60-s pre-burning period, therefore affecting overall exposure conditions.

It was demonstrated that crosswind velocities of up to 0.7 m/s can induce a flame tilt angle of 20–40°, significantly reducing the portion of the DUT covered by the fire plume (see Figure 6.3a [336]. The coverage of a tilted flame was shown to depend on the size and profile of the pool fire, as well as the type of fuel used [329]. At low or zero crosswind conditions, pool fires are prone to buoyancy-induced vortices, which generate lower-temperature regions [326]. These

fluctuations affect the exposure temperature at the sides of the DUT, as the cross-sectional area of the pool fire narrows with height—again, dependent on the pool size [332].

The R100.03 Phase A pre-burning period may be too short to stabilize exposure temperatures, as the burning model is significantly influenced by the size of the pool fire under study. For large gasoline fires (e.g., greater than 7 m^2 of horizontal pool surface), the optimal burning mode is generally achieved after 50-60 s with a stabilized burning rate ratio [337]. However, LIB applications of this scale are rare in the power train and day-to-day scenarios [338]. Conversely, Chen and Lu observed that for smaller pool fires, the burning rate ratio evolves. The steady-burning stage for small fires was found to be reached at 210 s [339], compared to the 50–60 s typical for larger fires. Furthermore, a subsequent rise in the burning rate ratio was noted after the steady-burning stage, significantly elevating temperatures, which is discussed further in Section 6.4, showing obtained test results.

An important characteristic of pool fires is their area. To quantify fire engulfment of the specimen, a pool fire extra area, A_{Extra}, is defined as the proportion of the pool fire area not covered by the tested element. It is expressed as:

$$A_{Extra} = \frac{A_{pool} - A_{DUT}}{A_{pool}} * 100\% \tag{6.11}$$

where A_{pool} is area of the pool fire, A_{DUT} is surface area of the device under test. For instance, a 40% pan excess indicates 60% of the pool fire's total area is covered by the DUT.

Fire engulfment studies were conducted with an 88.7% excess pool fire area relative to the DUT size [340]. In cases involving large pool fires and much smaller DUTs, convective and radiative heat transfer was found to be evenly distributed around the exposed DUT [341, 342]. The R100.03 standards mandate that the pool fire exceed the DUT dimensions by 200–500 mm. As illustrated in Figure 6.3b, the excess area decreases as the size of the DUT increases (see Equation 6.11. The blue line indicates the minimum excess (DUT size with an additional 200 mm), while the orange line represents the maximum excess (DUT size with an additional 500 mm). Green crosses denote the experimental data points from the study detailed in Section 6.4 and Table 6.6.

6.2.2 UL 1973 and UL 2580 External Fire Test

The UL 1973 fire test forms a foundational part of evaluating stationary ESS for resilience against external fire exposure. It stipulates that representative battery modules or systems must endure a 1200 s exposure to a standardized hydrocarbon pool fire, simulating worst-case conditions akin to those experienced in outdoor or semi-enclosed storage areas. The goal is not only to observe fire resistance but to ensure that no explosion, fragment projection, or propagation occurs post-exposure [283, 285, 343].

In both tests, the DUT - typically a fully charged battery system or module - is suspended 610 mm above a 200–500 mm larger (each horizontal dimension) pan filled with hydrocarbon fuel, most commonly heptane or gasoline surrogate, known for producing a consistent flame envelope and high radiative output. Upon ignition, the fire quickly develops into a luminous yellow plume characterized by peak centreline temperatures in the expected 890 °C level (intensifying over a 1000 °C, due to longer burn time), and average surface incident heat fluxes between 55–65 kW/m^2 (accounting for radiative and convective contributions).

To maintain burn consistency, the fuel pan may include a water layer to prevent overheating, and ignition is achieved using pilot flames or timed systems. The flame should envelop the entire DUT footprint, and wind shielding is recommended to reduce variability caused by flame tilt and flicker.

This exposure simulates real-world conditions such as a car fire, a structure fire affecting ESS units, or uncontrolled flame impingement from external fuel sources.

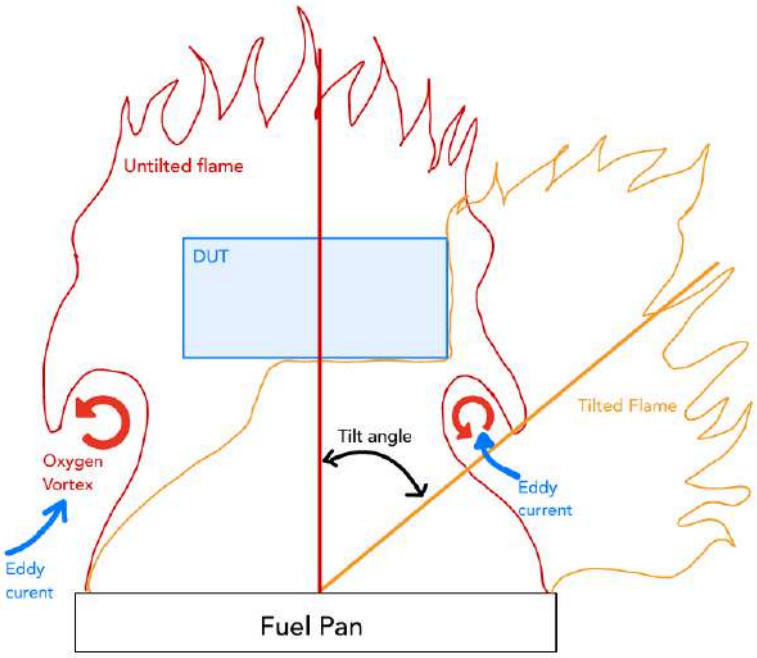

(a)

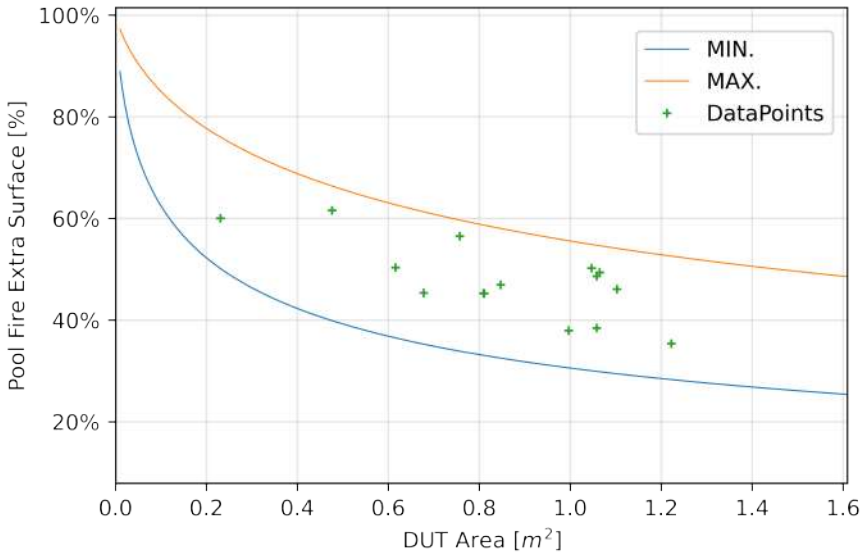

(b)

Figure 6.3: (a) Representation of non-tilted flame vortices (red), tilted flame partial engulfment of the DUT (orange), and cold air areas with eddy currents (blue). (b) DUT surface area relative to the required pool fire coverage.

The pass/fail criteria focus on explosion prevention. UL 1973 specifically requires that the ESS shall not explode during or after the fire. This is verified by inspecting for any large projectiles or sudden bursts within 1 m circle around the DUT (external edge). After the 20 min fire, UL 1973 adds a hose stream test: the battery, still hot, is blasted with a fire hose water stream (following UL 263 hose-down procedure [343]). The rationale is to simulate a firefighter's response - dousing the hot battery. The battery must not explode under the thermal shock of the water either. Any violent rupture or flying debris would constitute a failure. Essentially, even if the battery is mostly destroyed by fire, it should fail in a "safe" manner (no fragmentation that could hit personnel). UL does not forbid the battery from burning; indeed, after 1200 s in

a pool fire, complete combustion of the battery is expected. But the enclosure and cell design should preclude any detonation.

For instance, pressure-relief vents should actuate to let cells burn gradually rather than building up pressure. If the battery passes, it demonstrates a level of fire containment - it can be engulfed for a significant time without blowing apart. This is critical for stationary batteries in buildings or vehicles like railcars, where an external fire might not be escapable - the system should not worsen the fire with an explosion.

For UL 2580, which addresses automotive traction batteries, the pass/fail criteria are similarly rooted in the principle of non-catastrophic failure under thermal stress, but framed within the additional context of vehicle occupant and first responder safety. As in UL 1973, a battery exposed to the 20-min hydrocarbon pool fire is allowed to degrade, lose structural integrity, or undergo internal thermal reactions. However, it must not explode, either during or after the fire. An explosion in this context means a sudden energy release that causes fragmentation of the battery housing or propulsion of cell or module components beyond the battery enclosure.

It may be fully destroyed in the process. However, its destruction must occur in a predictable, safe, and non-violent manner. The goal is to demonstrate that, even under the worst fire conditions (such as after a collision leading to gasoline or hydraulic fluid ignition under the vehicle), the battery will not exacerbate the event by becoming an uncontrolled explosion source or by exposing rescue personnel to unacceptable levels of mechanical, thermal or electrical risk.

6.2.3 SAE J2464 External Fire Test

SAE J2464 is a recommended practice for EV battery abuse testing. It includes a method for thermal abuse by using a radiant heat source instead of open flames. Often referred to as a "radiative panel" or "hot plate" test, this approach subjects the battery to a controlled high-temperature environment meant to simulate the thermal flux of a fuel fire, without actual combustion around the battery. The typical procedure (as historically implemented at Sandia National Laboratories and other facilities) is as follows: the test sample (cell, module, or pack at 100% SOC) is placed inside a radiant heating chamber or fixture – essentially an oven or array of infrared heaters – with no direct contact between the battery and the heating elements. The heater is then rapidly ramped up to a target temperature of 890 °C (±5%) within about 90 s, and that temperature is maintained around the battery for 600 s (unless the battery's reaction forces an early stop for safety). This profile (890 °C for 600 s) is intended to reproduce the thermal conditions of a fully developed hydrocarbon fire. The temperature of 890 °C as "nominal fire temperature" comes from equivalence with large open fires (typical flames burn between 800–1000 °C). By enclosing the sample in a radiant heating apparatus, the battery is heated primarily through thermal radiation (and to some extent by hot air convection in the chamber). There is no flame impingement and no direct burning of the battery's exterior in this test - until and unless the battery itself vents flammable gases that then ignite. In many setups, multiple quartz infrared lamps or electric heating elements line the walls of a reflective chamber (sometimes called a "radiant box"), ensuring the battery sees a uniform heat flux from all sides. The battery essentially free-stands in a furnace-like environment of nearly 900 °C.

A key aspect of the radiative test is that it is highly controlled. The ramp rate (ambient to 890 °C in 90 s) is specified to be very fast - this simulates the rapid engulfment of a battery in an intense fire. The 90 s ramp roughly mimics the fire growth in a pool fire test. Once at 890 °C, holding for 10 min delivers a severe thermal load. The heat flux in such a chamber can be estimated (see Table 6.1): if the walls are ∼890 °C and behaving like a blackbody, the incident flux on the battery could be on the order of 50–70 kW/m^2 [344] (since a blackbody at 890 °C has an emissive power ∼85 kW/m^2, though in practice not all surfaces are at that temperature and not all radiation reaches every spot due to view factors [329]).

If the battery is inside a radiative enclosure or cavity, the effective view factor (see Equation 6.10) from multiple walls to the battery approaches 1.0 as the chamber becomes more

enclosed (blackbody cavity approximation).

In practical terms:

- For a large enclosure with highly emissive walls surrounding the battery, you can assume:

$$F_{panel \to battery} \approx 0.9 - 1.0 \tag{6.12}$$

- For a specimen facing one hot wall:

$$F \approx \frac{A_{battery} \cdot \cos(\theta)}{A_{panel}} \tag{6.13}$$

  where θ is the angle between the battery surface normal and the panel (0° for face-on).

The emissivity and material selection of the steel box emitter in the SAE J2464 radiative test play a critical role in determining both the instantaneous heat flux and the total thermal dose imparted to the test specimen. Emissivity governs the efficiency with which the emitter radiates thermal energy; a surface with high emissivity (e.g., oxidized or black-painted steel, $\epsilon \sim 0.9$–0.95) emits significantly more infrared radiation than a polished or reflective one ($\epsilon \sim 0.2$–0.3). Consequently, two emitters at the same temperature but with different surface finishes can yield vastly different radiative fluxes - affecting not only the rate at which the battery heats but also the cumulative thermal energy absorbed during the exposure period. A low-emissivity surface may under-deliver the intended dose, reducing test severity, while a high-emissivity surface ensures a worst-case, conservative scenario. Therefore, to maintain consistency and regulatory equivalence, the emitter's material and surface condition must be tightly controlled and characterized, as they directly influence the fidelity and reproducibility of the thermal stress imposed on the battery system. Dependency has been shown in Figure 6.4a - radiative heat flux as a function of surface emissivity for three temperatures representative of SAE J2464 radiant panel test conditions (minimum: 845.5 °C, nominal: 890 °C, maximum: 934.5 °C). The plotted values assume full view factor geometry ($F = 1.0$) and ideal blackbody orientation. The graph illustrates the linear dependence of radiative heat transfer on emissivity and the significant flux variation (approx. 30-35%) across the temperature and surface finish tolerances. In Figure 6.4b total thermal dose (in kJ/m^2) received by a battery during the SAE J2464 test is plotted against emitter surface emissivity and for a range of operating temperatures (±44.5 °C around nominal). The calculation includes a 90 s linear ramp and a 600 s steady exposure. The data highlight the sensitivity of total incident thermal energy to both emissivity and temperature variation, which directly impacts test severity and reproducibility.

The SAE J2464 criteria for passing are similar: no explosion or battery disassembly. Because SAE J2464 is a recommended practice, it often does not declare "pass/fail" in absolute terms but rather provides that the battery should not rupture or ignite explosively. In research contexts, this test yields quantitative data like time to TR ignition, max temperature reached, etc. If a battery vents and catches fire inside the chamber, that is noted. One advantage is the test can be halted by shutting off power if a dangerous condition arises (whereas a pool fire cannot be easily turned off - one must wait or attempt to smother it). The radiant test is therefore considered safer to conduct for laboratories and more repeatable. It avoids the smoke and soot of fuel fires, enabling easier post-test clean-up and analysis of the battery remnants (no added combustion debris from gasoline).

6.2.4 Comparison and Engineering Implications

Each of the above methods aims to simulate a hydrocarbon fire threat to LIB, but they do so with different approaches and test set-ups, which implicates various repeatability and practicality. Here we compare key characteristics.

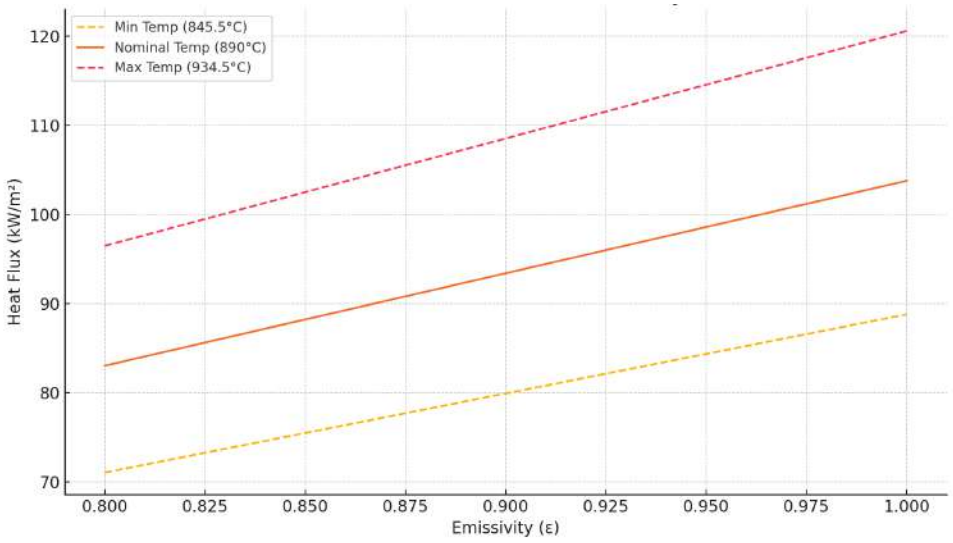

(a)

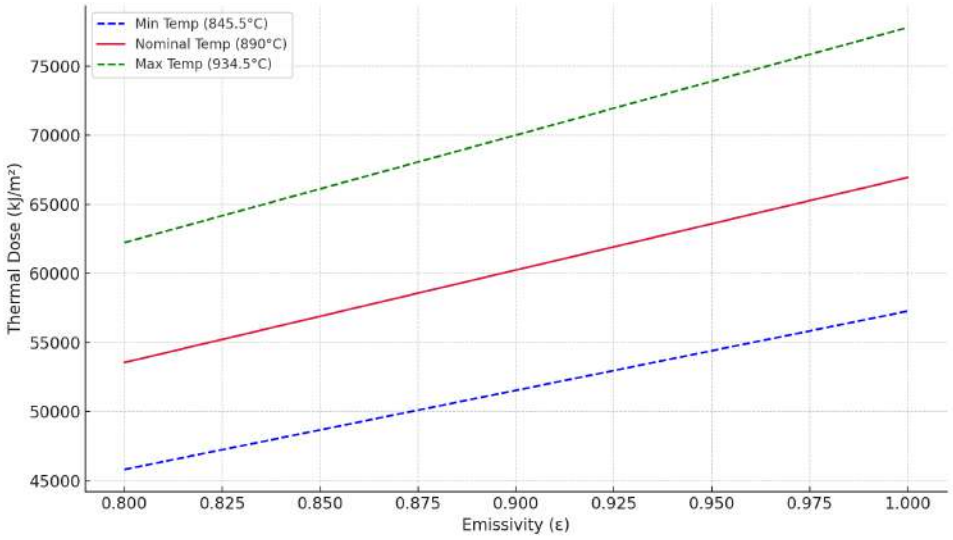

(b)

Figure 6.4: (a) Radiative heat flux as a function of surface emissivity; (b) total thermal dose of SAE J2464 radiant panel test conditions.

Heat Exposure Profile

The pool fire tests (R100 and UL 1973, and UL 2580) involve real flames and thus deliver a combination of intense radiation and direct convective heat. R100's exposure is extremely intense but short (∼2 min of flame), whereas UL's is intense and sustained (1200 s). The peak heat fluxes in both are similar (order 50 kW/m^2), but the total heat energy absorbed by the battery in UL's test is much higher due to duration. The burner test (R100 alternative) gives a similar 2 min high flux but in a controlled way - the heat flux is kept in a tighter band (30–40 kW/m^2). The radiant test (SAE J2464) provides a high but somewhat uniform heat flux (∼90 kW/m^2 theoretical and ∼70 kW/m^2 with view factor and emissivity losses) for 600 s, without flame impingement. It ramps up slightly more slowly (90 s to reach full temperature) than an instantaneous engulfment, but this is quite comparable to the growth of a gasoline fire. In essence, all methods attempt to reach flame-equivalent temperatures (800–1000 °C) around the battery. The main difference is time: short (R100), medium (SAE), long (UL). For engineers, this means R100 is mainly testing short-term flame resistance (can the battery hold together for

a couple of minutes), whereas UL 1973 is testing extended fire resistance (can the battery avoid exploding even when fully involved in fire).

Radiative vs Convective Emphasis

In a gasoline pool fire, roughly 30–40% of the heat is radiative, so an object might be heated from all sides by thermal radiation even if flames wrap primarily around the bottom. The R100 and UL tests naturally include this effect. The burner method likely has a slightly lower radiative fraction, but by having multiple burners around the item, they ensure a surround-flame condition (including radiation from flame sheets on the sides). The radiant panel test is all radiation until the battery itself ignites – which means it might slightly under-drive convective cooling effects. In real flames, convective heating is coupled with cooling: hot gases flow upward, carrying heat away as well. In a sealed radiant oven, the air is stagnant, so once the battery's surface heats, there is less removal of heat by flow. This could mean the radiant test might even be more severe in heating some internal parts than a flame would, due to reduced convective heat loss. Conversely, direct flame impingement can cause erosive burning of materials (e.g. charring of casings) that pure radiation might not until ignition occurs. Thus, each method stresses the battery in slightly different ways.

Reproducibility

The radiant heat method is by far the most reproducible. Temperature and heat flux can be calibrated and repeated with minimal variability. Results from different laboratories should agree closely if the equipment is properly calibrated. The gas burner method is also quite repeatable: fuel flow rates and burner configurations can be standardized, and they are less sensitive to environmental factors. The open pool fire is the least reproducible: small differences in fuel quality, pan geometry, or wind can lead to variations. As noted, even with standardized specs, pool fires have inherent flicker and randomness that introduce scatter in test results. There are found significant differences in exposure, due to gusts of wind temporarily deflecting flames. R100 attempts to mitigate this (e.g. wind shield fences around the setup, using the screen in Phase C to get a uniform indirect phase, etc.), but variability remains at unsatisfactory level. This has engineering consequences: to be confident of passing a pool fire test, designers often over-build safety margins (e.g. use thicker fire shields) to account for worst-case exposure.

Safety and Practicality

Conducting a full-scale pool fire test (especially 20 minutes long) is expensive, hazardous, and requires extensive preparations (fire brigades on standby, environmental permits for smoke, etc.). It is not something that can be done frequently in development. The burner test is moderately safer - it can be done indoors in a ventilated fire chamber since it is easier to scrub propane combustion gases (which are cleaner) and there is no large pool of flammable liquid, however the burner installation is complex, expensive and non-universal. The radiant test is the safest for laboratories - no open flame, and the test chamber often contains any fire that does occur (acting like a furnace). Accordingly, the SAE radiant method has been widely used in research and early prototyping, whereas regulatory compliance (which must mimic real accidents) leans toward actual fire exposure.

Evaluation of Results

From a regulatory standpoint, R100.03 is a pass/fail safety test - there is no quantitative rating, just a requirement: no explosion within given time. UL 1973 similarly is pass/fail with criteria on explosion and projectile distances. SAE J2464, being a guideline, often does not "pass/fail" a design but informs design improvements (though manufacturers can set their own criteria like

"no fire outside enclosure" etc.). The engineering interpretation of a passed R100 test is that the battery can survive a brief intense fire long enough for evacuation. A passed UL 1973 fire test suggests the battery is robust even in catastrophic fire scenarios (more relevant to property protection - e.g. an ESS might burn but not violently rupture, giving firefighters a chance to contain it).

Instrumentation and Data

In a raging pool fire, any thermocouples or heat flux gauges near the battery are likely to be destroyed or produce unreliable readings (soot deposition, etc.). Thus, R100 and UL tests are usually observed externally (e.g. infrared cameras, visual cameras) but not heavily instrumented on the battery itself (aside from internal thermocouples if it is available due to safety reasons). The burner test, being slightly more controlled, can allow a bit more instrumentation (using thermocouples on the battery and IR cameras). The radiant test in SAE readily accommodates sensors - it can embed thermocouples in the battery and run wires out since there is no massive flame to sever them (until possibly the battery itself burns). This means the radiant method is useful for mechanistic studies - for example, measuring the time it takes for internal cells to reach TR threshold under a known heat flux. Such data helps validate thermal models and fire simulations.

6.3 Empirical Evaluation of Open Flame Fire Resistance Testing Procedure

The main purpose of a fire resistance test is to evaluate the resistance against heat exposure propagated by fuel spills and ensure the driver and passengers have enough time to evacuate. The exposure of RESS to fire during the test is provided by positive-ignition engine burning under atmospheric pressure. The specimen is engulfed in flames for a given time period and then observed for any signs of explosion. This procedure (only with heat source in form of petrol) is also adopted in other standards, such as ISO 6469-1:2019 [263], ISO 18243:2019 [264] and GB 38031-2020 [73]. Additionally, provisions discussed above must be met (see Section 6.2.1).

6.3.1 Object of Investigation

The experimental analyses were performed on a complete RESS (shown schematically in Figure 6.5) with the following dimensions: 110 cm long, 80 cm wide, and 40 cm high, which was composed of lithium titanium oxide cells and a lagging system. The SOC value was set to 51% of the normal operating range prior to the test. No active protection devices were present for the test. For temperature distribution measurement, 10 thermocouples (denoted TC1–TC10) were mounted on the outer surface of the battery. The exact thermocouples locations are described in Table 6.3 and shown in Figure 6.5. All thermocouples, except for TC6, were fixed using square-shaped gypsum pads with adhesive to isolate the measuring tip from environmental influences and to measure solely the surface temperature as per EN 1363-1 guidelines [345]. Type K (NiCr-Ni) thermocouples were used in the test with class 1 accuracy according to DIN EN 60584-2, which corresponds to an error of ±3.6 °C at 900 °C. A DataTaker logger with checked deviation error of the measuring path was used as a data acquisition centre for thermocouples with a sampling interval of 3 s. Expanded uncertainty for the whole temperature measurement was established as ±4.2 °C (based guidelines in [346]).

The test rig was composed of a fuel pan, brick screen, and a cart with a grating table and specimen on top. The fire source, in the form of a steel pan filled with petrol, was fixed as a stationary element with the cart and brick screen being freely movable. The RESS was placed on the grating table constructed with steel rods with an 8 mm outer diameter with 40 mm spacing

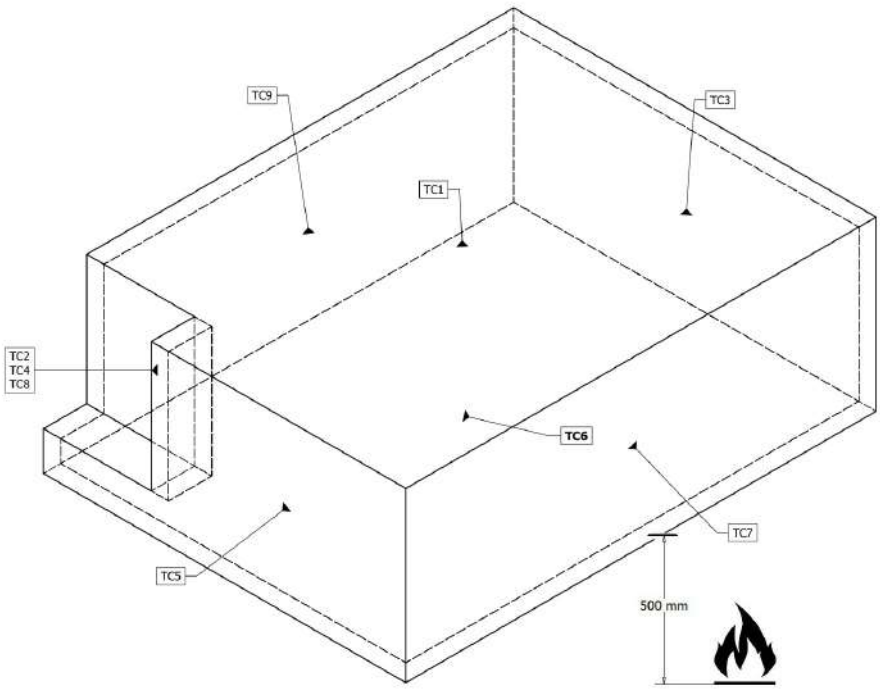

Figure 6.5: Thermocouple positioning scheme and description.

Table 6.3: Thermocouples locations on the RESS.

Thermocouple	Location
TC1, TC6	The top and bottom surface of the RESS case in the centre
TC2, TC4, TC8	The plugs
TC3, TC5, TC7, TC9	The sides of the RESS case
TC10	60 mm below the specimen in the center (in a line with TC1 and 6)

in between, additionally supported with flat steel bars. The test rig was protected from wind with panels to keep wind velocity at the pan level below 2.5 km/h.

The fuel pan exceeded the horizontal projection of the tested device by 40 cm in length and 30 cm in width (requirement is between 20 and 50 cm). One ensured that during the exposure, the RESS was positioned centrally to the pan to ensure even flame distribution. The sidewalls of the pan projected between 0 and 5 mm above the fuel level at the beginning of the test. The bottom surface of the test specimen was set at a height of 50 cm from the petrol surface.

RON 95 petrol was used in the test as a fire source. The amount of fuel for the duration of the procedure was 25 l/m^2.

Ambient conditions temperature 18.3 °C and humidity 68.1%. Average wind velocity measured at the pan level was 0.97 km/h and for the whole duration of the test, it did not exceed 2.5 km/h (TESTO thermal anemometer, calibrated, error of 0.05 m/s at 1 m/s wind speed). Fuel average temperature was 18.9 °C.

6.3.2 Experimental Results

The test lasted in total 1 h 34 min 39 s starting from the ignition of fuel up to reaching ambient temperature at thermocouples TC1–TC10 (see arrangement in Figure 6.5). Analysis presented in this section is presented for the first 10 min of the test. The results past the 10 min mark show a constant decrease in temperature until levelling with ambient conditions. The thermocouple

arrangement allowed the determination of the temperature T_{TC} distribution in space for a chosen time. A photograph from the test is shown in Figure 6.6 - the DUT is inside the flames (Phase B); the right photograph shows from bottom angle (partly showing the concrete foundation of the screen protectors).

Figure 6.6: Photograph with sample and test rig during the UNECE R100.03 test (Phase B).

For each thermocouple, the maximum recorded temperature was determined using:

$$T^P_{TCi}(x,y,z) = \max(T^P_{TCi}(x,y,x)) \text{ for } i = 1,...,10 \tag{6.14}$$

where subscript TC is related to he thermocouple, and index 1–10 denotes its location; superscript P indicates the phase of the test according to Table 6.2. Table 6.4 shows the maximum recorded temperature at every thermocouple in each phase. Analogously, the average temperature and standard deviation during each phase was determined using the following equations:

$$\overline{T}^P = \frac{1}{n}\sum_{j=1}^{n} T_{TCi}(t) \text{ for } i = 1,...,10 \tag{6.15}$$

$$\sigma^P_T = \sqrt{\frac{\sum_{j=1}^{n}(T^P_{TCi} - \overline{T}^P)}{n-1}} \text{ for } i = 1,...,10 \tag{6.16}$$

During phase A, temperatures slowly increased during the first 60 s (see Phases description for reference in Table 6.2). Next, immediate temperature spike was observed in phase B, where the specimen was directly subjected to the flame. In the course of indirect exposure to flame (phase C), the temperatures on the surface of the battery case reached their maximal values. In phase D, the test specimen was removed from the fire source and the temperatures generally dropped steadily until equalizing with the ambient temperature.

During phase A, TC9 recorded highest value. The side of the battery with TC9 faced toward the flame; thus, one assumed wind might have directed some hot air toward the battery. The highest temperatures in phase B were recorded for TC7, TC6, and TC5. The flame centre line was observed to lean toward the side with TC7; therefore, TC6 was expected to record lower temperature, despite being closer to the fire source. Next, in phase C, the highest recorded temperatures were at TC7, TC5, and TC10. Additionally, the remaining TC temperatures increased in comparison to the previous phase, suggesting that conditions started levelling around the battery, and the brick screen may notably reduce exposure. Phase D highest temperatures coincided with the transition from phase C, except for TC9, where ignition of the paint of noted.

The average temperature values show that the testing conditions peaked in phase C with 452.0 °C despite screen-reduced flame. The standard deviations of phase B and C were 218.3 °C and 239.3 °C, respectively, which supports the premise that the temperature distribution around the battery was highly irregular. With average temperature being higher later in the test and

with considerable statistical dispersion, the results indicate that a steady burning rate may have not been reached by the end of the test.

Table 6.4: Maximal recorded temperature (°C) of thermocouples TC1–TC10 and the average temperature in a given phase. Phases A, B, C, and D according to Table 6.2 and Figure 5.2.

Thermocouple	Phase A	Phase B	Phase C	Phase D
TC1	20.6	270.7	430.5	428.8
TC2	24.1	354.9	456.6	335.4
TC3	18.7	205.6	299.3	382.2
TC4	25.4	252.9	255.9	223.1
TC5	18.6	711.2	880.6	788.1
TC6	39.6	799.8	693.5	685.0
TC7	18.2	929.6	929.9	849.0
TC8	22.7	163.7	219.3	171.9
TC9	42.2	200.3	219.2	433.6
TC10	16.0	717.5	714.6	712.6
$\overline{T}$	19.1	254.7	452.0	44.5
σ_T	3.7	218.3	239.3	54.9

In addition, for all thermocouples, the rates of temperature change (RTC) v_{TC} and their maximum values were respectively determined using the following formulas:

$$v_{TCi}(x,y,z,t) = \frac{\partial T_{TCi}(x,y,z,t)}{\partial t} \text{ for } i = 1,...,10 \tag{6.17}$$

$$v^P_{TCi}(x,y,z) = \max(|v^P_{TCi}(x,y,x)|) \text{ for } i = 1,...,10 \tag{6.18}$$

where subscript TC is related to the thermocouple, and index 1–10 denotes its location. The superscript P indicates the phase of the test according to Table 6.2. Analogously, the average RTC and standard deviation during each phase were determined using the following equations:

$$\overline{v}^P = \frac{1}{n}\sum_{j=1}^{n} v_{TCi}(t) \text{ for } i = 1,...,10 \tag{6.19}$$

$$\sigma^P_v = \sqrt{\frac{\sum_{j=1}^{n}(v^P_{TCi} - \overline{v}^P)}{n-1}} \text{ for } i = 1,...,10 \tag{6.20}$$

Table 6.5 shows the maximum RTC for every thermocouple in each phase, and the average and standard deviation of the RTC in a given phase.

The highest RTC was recorded during phase B for TC6 measuring fire temperature; since the measuring tip was uncovered, the temperature spiked immediately. In phase C, TC5 registered the highest temperature of 94.0 °C, which might be attributed to the flame leaning toward TC5 and TC7, both being directly exposed to flame (protecting gypsum pad detached). This also corresponds with the highest RTCs in phase D of TC5 and TC7, as they were cooled by air immediately after the battery was removed from the flame source. Notably, a sudden rise was recorded at TC9, corresponding to the ignition of the paint in the thermocouple area.

In phase B, the highest average RTC was 17.5 °C/s, which was expected due to the rapid accretion in temperature caused by exposure to flame. However, in the following phase C, the average RTC was only 0.7 °C/s, suggesting the testing conditions started then equalized around the battery. The standard deviation was highest in phases B and C at 38.6 °C/s and 23.2 °C/s, respectively, confirming the flame was prone to momentary changes in local conditions (i.e., wind

speed and puffing). Hence, the unsteady transitory period of burning was not eliminated by the initial phase A pre-heating. The absence of a steady burning rate may result in unreliable tests performed according to the same procedure.

Table 6.5: Maximal and average RTC v_{TC} (°C/s) for thermocouples. Phases A, B, C, and D according to Table 6.2 and Figure 5.2.

Thermocouple	Phase A	Phase B	Phase C	Phase D
TC1	0.2	18.4	15.6	−7.3
TC2	0.8	30.3	−22.1	−25.0
TC3	0.9	20.6	9.9	19.8
TC4	5.1	38.5	7.8	9.2
TC5	0.4	167.5	94.0	−132.2
TC6	9.3	298.9	92.8	−163.9
TC7	0.3	152.8	−93.7	−147.1
TC8	1.4	14.9	11.3	−2.5
TC9	8.3	17.3	2.7	54.7
TC10	0.5	103.7	17.6	−77.7
$\overline{v}$	0.4	17.5	0.7	−0.2
σ_v	1.0	38.6	23.2	3.2

For a more in-depth analysis, the thermocouples were divided into sets: top, bottom, and side surfaces, and plugs.

The temperature comparison between the top and bottom surfaces of the case is presented in Figure 6.7. The maximal temperature at the bottom surface of the RESS case (TC10) was 717.5 °C (phase B) at 120 s of the test. Afterward, it fluctuated around 700 °C until 198 s (at the beginning of phase D), after which it began to decrease. This showed that the bottom surface received a steady influx of heat and the temperature of the flame at this height was set around 700 °C. The temperature peaked only at the end of phase B, which may imply the exposure conditions stabilized then (i.e., at the end of the transitory period).

Air velocity was maintained below 2.5 km/h. However, pool fire was observed to deviate from the centreline of the pan. The maximal temperature at the top surface (TC1) was only 430.5 °C (phase C). The top surface was isolated from the direct influences of the pool fire and heat transfer. Since the temperature increase at TC1 was mainly caused by conduction through the steel case, the temperature rise was less steep, but more stable.

When the specimen was removed to its initial position at the start of phase D, the bottom surface of the battery started to dissipate the heat rapidly, as reflected in the sudden RTC drop. In comparison to TC10, the TC1 RTC was much more consistent for phases B to D. Due to the battery's geometry, the measuring point of TC1 was hidden from the source flame and as stated above, the temperature rise was assumed to be mainly caused by conductive heat transfer of the steel case.

Figure 6.8 shows the temperature and RTC results on the plugs of the RESS subsystem. TC4 and TC8 were positioned in the nook of the battery; therefore, lower temperatures compared to the other points were expected at these particular locations. TC2 was placed on the plug, substantially closer to the edge; thus, it was more likely to record higher temperatures. However, the highest temperature was achieved in phase C, while fire source was reduced by the brick screen. This phenomenon may have been caused by difference in flame temperature distribution while changing from phase B to C [325]. As the height of the pool fire varies within above-mentioned phases, it influences fire temperature zones in the continuous flame region [347].

Additionally, parts of the electrical plugs ignited during the test, contributing to the inconsistency in the temperature curves and RTC changes. In Figure 6.8, a sudden rise at 108 s of

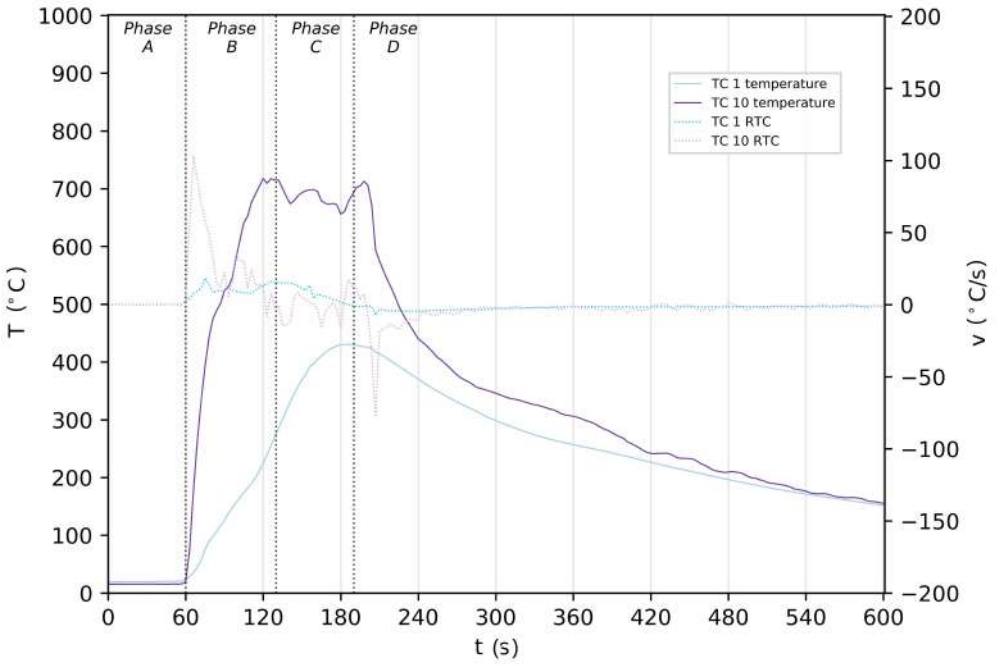

Figure 6.7: Temperature (T) and RTC (v) over time (t) of thermocouples TC1 and TC10 in the first 600 s of the test. Phases A, B, C, and D according to Table 6.3 and Figure 6.5.

the test, which corresponds with the flames curving around the nook (confirmed by the visual observations), can be noticed. This confirms the highly stochastic nature of the pool fire even under controlled environmental conditions [348].

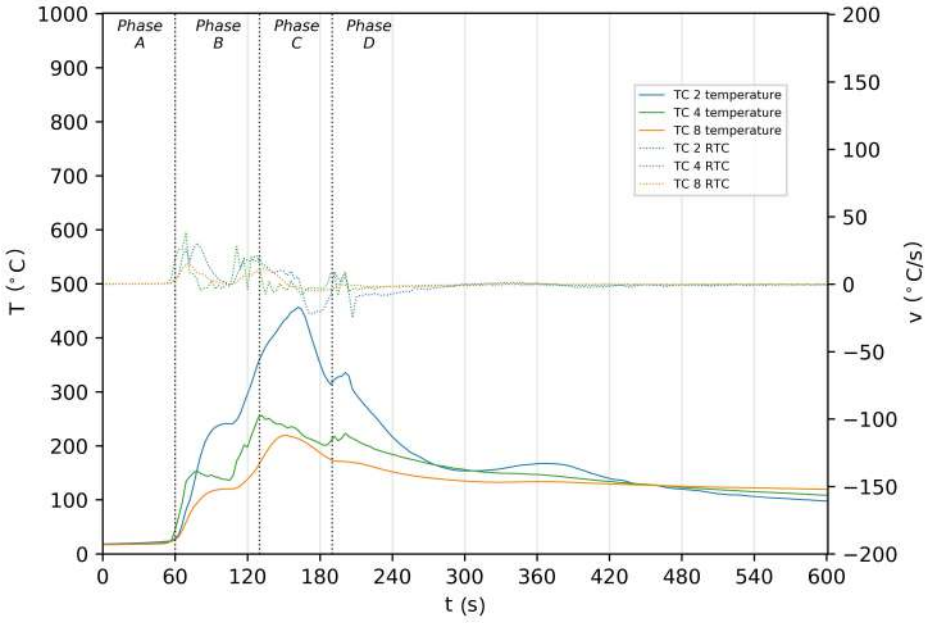

Figure 6.8: Temperature (T) and RTC (v) over time (t) of thermocouples TC2, TC4, and TC8 during the first 600 s of the test. Phases A, B, C, and D according to Table 6.2 and Figure 5.2.

The temperature measurements and RTC from the sides of the battery are presented in Figure 6.9. Firstly, a large temperature difference distribution around the battery was observed. During phase C, the highest temperatures of 929.9 °C and 880.6 °C were recorded at TC7 and

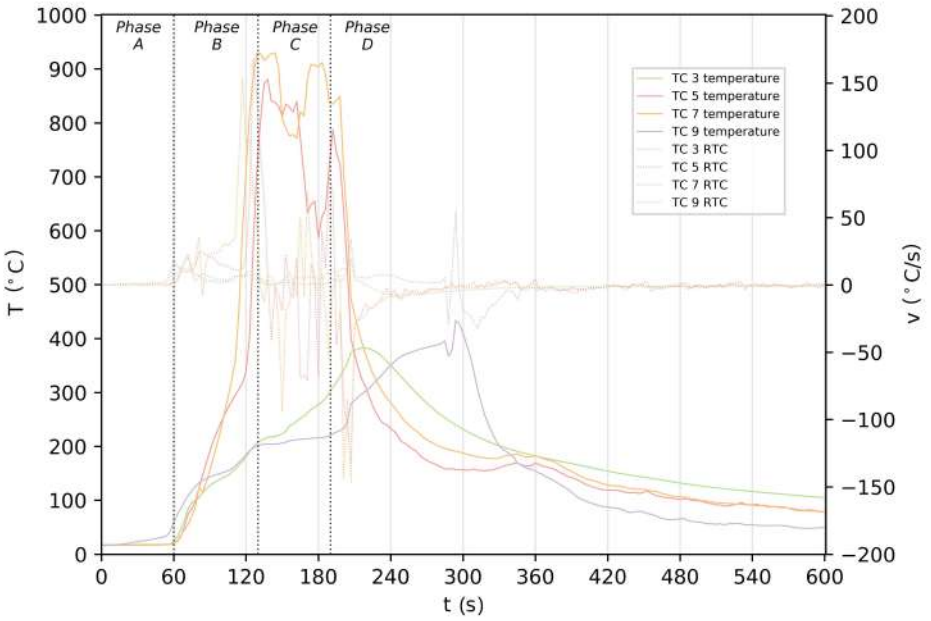

Figure 6.9: Temperature (T) and RTC (v) over time (t) of TC3, TC5, TC7, and TC9 in the first 600 s of the test. Phases A, B, C, and D according to Table 6.2 and Figure 5.2.

TC5, respectively; at TC3 and TC9, the temperature remained at max. 299.3 °C and 219.2 °C, respectively. At TC3 and TC9, the highest temperatures were registered at the moment of reverting the test specimen to the initial position during phase D. This phenomenon may be attributed to the pool fire and its unpredictable behaviour, as well as lack of a sufficiently sized fire source. The temperature readouts also indicated that the flame stabilized during phase C, similar to TC10.

It was noticed that at TC5 and TC7, a substantial fluctuation in the rate of temperature change occurred, especially during phase C. Since temperatures reached over 800 °C, the gypsum pad protecting the measuring tip detached and the thermocouples were directly subjected to the flame and its fluctuations. This event allowed to evaluate the scale of temperature changes in the battery's surroundings. In 162 s of the test, the flame stopped leaning toward the TC5 side, which can be noticed in the temperature curve, showing a rapid decline and local minimum value of 586.8 °C at 180 s. Following this, there was a temperature rise to 788.1 °C at the end of phase C, which is a difference of 201.4 °C between the values within 18 s of the test, showing that a slight change in the pool fire free-burning conditions may substantially alter the testing temperature. In contrast, the TC3 and TC9 RTCs were characterized by notably less zig-zagged curve during phases B and C, since the flame was directed to other sides. However, at the beginning of phase D and just before 300 s of the test, two spikes occurred in TC9. By visual observation, they may be attributed to the sudden ignition of the case painting, which dissipated quickly after they were noted.

Additional illustrations from the test has been shown in Appendix C.

6.3.3 Theoretical Estimation of Temperature Inside the RESS System

The temperature distribution inside the RESS system was determined theoretically. Calculations were performed using the temperature values determined experimentally during the test (see above Section 6.3.2).

The following assumptions were used to allow interior temperature calculations (specific design and simplification was chosen due to confidentiality agreement with manufacturer of the battery):

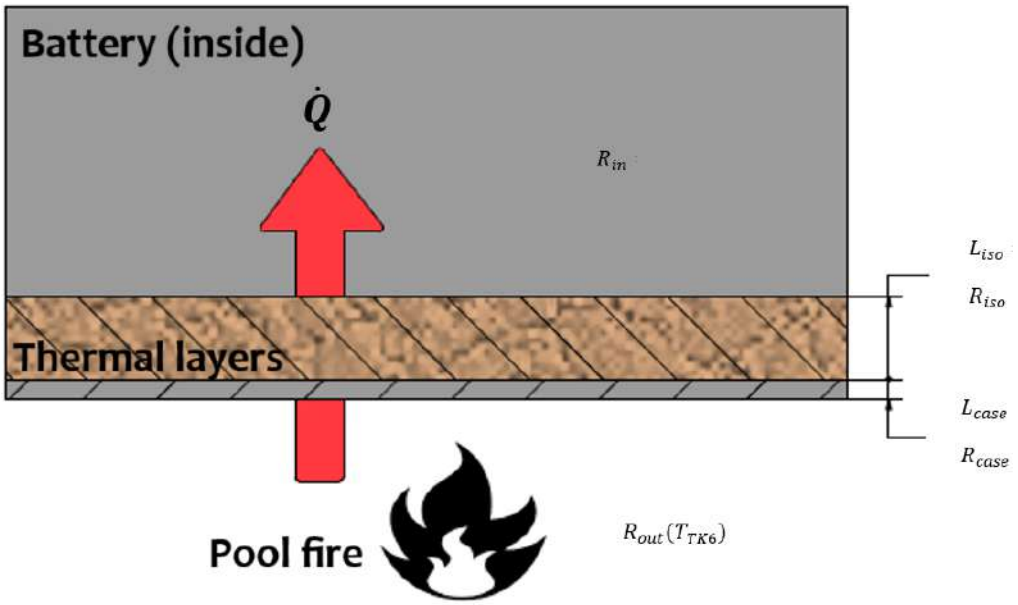

Figure 6.10: Model of the internal battery temperature calculation. See Section 6.3.3.

- Heat transfer is one-dimensional.
- R values of lagging, i.e., battery case and insulation, are taken as constant, irrespective of the temperature.
- The dominant form of heat flux generated by the fire source is presumed to be convective.
- The battery case remains airtight for the duration of the test or losses generated by the air circulating outside the battery are negligible.

A simplified one-dimensional model, see Figure 6.10, of heat transfer inside the RESS was constructed to estimate the temperature of the battery's interior and then to evaluate if the cells might have reached the critical point (T_2 in HTR loop; see Section 2.2) in comparison with known data during the fire test. For this purpose, one assumed that heat was transferred only by the bottom division and the battery was airtight with a specific amount of internal air. Heat flux was moderated with a 5 mm thick steel casing L_{case} and 20 mm thick insulation material L_{iso}. In reality, the exact material used for the RESS lagging is a trade secret of the RESS manufacturer, however, this assumptions reflect thermodynamic material properties of the used material. Parameters used for calculation are summarised below:

- Thermal insulance (R): inside $R_{in} = 0.2$ m^{2}K/W, insulation $R_{iso} = 0.5$ m^{2}K/W, case $R_{case} = 3 \cdot 10^{-4}$ m^{2}K/W, outside $R_{out}(T_{TK6})$.
- Thickness of the barrier (R): insulation $L_{iso} = 20$ mm, case $L_{case} = 5$ mm.

Pool burning heat generation consists of many variables and is dependent on the size of the pool (non-circular shapes are approximated to circular shape). Generally, according to the conservation of energy of the liquid, fire source heat flux can be expressed as [332, 326]:

$$\dot{Q} = \dot{Q}_r + \dot{Q}_c - \dot{Q}_{rr} - \dot{Q}_{misc} \tag{6.21}$$

where $\dot{Q}_r$ is radiant flux, $\dot{Q}_c$ is the heat absorbed by convective means, $\dot{Q}_{rr}$ is the re-radiant heat loss as the surface of the pool is at high temperatures, and $\dot{Q}_{misc}$ defines any other losses (i.e.,

conduction of the walls and stochastic terms). In this particular R100.03 pool fire, one assumed that the dominant heat transfer was convective.

As mentioned above, flux is estimated to be largely dependent on the convective heat transferred by the pool fire. Convective heat flux was determined using the following equation [324]:

$$\dot{Q}_r(t) = \frac{A(T_{TC6}(t) - T_{in}(t))}{R(T_{TC6}(t) - T_{TC10}(t))} \tag{6.22}$$

where A is area of the bottom surface of the RESS, T_{in} is the internal temperature, and R is total thermal insulance.

$$R = \sum_{i=k}^{n} r_k \tag{6.23}$$

where r is the thermal insulance of each division. Thermal insulance varies depending on the temperature of the medium; yet in this approximation, the R value of the case, insulation, and air inside (denoted as R_{case}, R_{iso}, and R_{in}, respectively) is taken as a constant value, since the overall results will not differ by more than 5%. The variables here were the convective heat coefficient of air outside and its thermal insulance, which were contingent upon the test temperature data of TC6 and TC10.

At the beginning of phase B, the temperature inside the battery ($T_{in}(0)$) was equal to ambient (18 °C) and it served as a starting point for iteration.

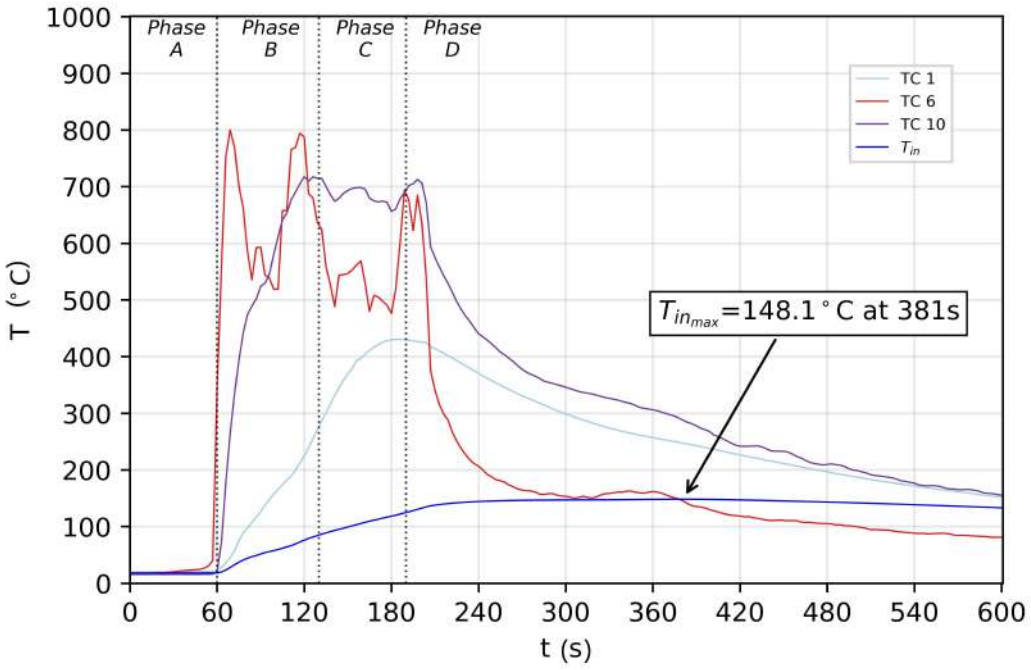

Figure 6.11: Calculated temperature inside the battery in comparison to TC1, TC6, and TC10.

Therefore, the momentary energy transferred to the inside of the battery and then the temperature increase due to such energy could be calculated as follows:

$$\Delta T_{in}(t) = \frac{1}{m(T_{TC6}(t)) \cdot C_p(T_{TC6}(t))} \cdot \frac{\delta \dot{Q}_r}{\delta t} \tag{6.24}$$

where m is the mass of air inside the battery and C_p is the specific heat at atmospheric pressure as a function of TC6 temperature. The calculation results are presented in Figure 6.11. The internal temperature was estimated to rise up to 148.1 °C at 381 s. This indicates that even

with flame source removed, the temperature is likely to rise for some additional time. Crucial to battery failure is the breaching critical point, where the TR of the battery starts, as noted in Section 2.2 T_2, ranging from about 120 to 200 °C, depending on the cell chemistry. The above results show that the reaction is more probable to happen past the flame exposure phases, where the temperatures of each insulating division, the surroundings, and the interior of the battery begin to equalise.

Considering TR phenomena stages, thermal degradation process starts between 80-150 °C with breakdown of the SEI layer and with self-sustained exothermic reactions starting at 90 °C, with the eventual melting of the separator ranging from about 120 to 200 °C, which causes an internal short circuit and rapid TR [114]. It was concluded the cell temperature was actually lower than the calculated 148.1 °C and the separator did not fail during the test (probably due to own thermal inertia). There were no signs of self-ignition or flaming from the battery, nor rupture was found on its case.

The limitations of the presented model are listed below:

- Due to the upward heat transfer direction, the above-mentioned calculations are valid only for the testing set-up with fire source below the tested device.
- The fire source dimensions may not substantially exceed the battery's horizontal projection, as the heat transfer on the sides of the battery is also expected to have a significantly higher impact on the interior temperature (the maximum range is 500 mm in each direction).
- With increasing size of the pool fire (> 10 m^2), the contribution of the radiant flux is expected to rise; therefore, the total heat flux should be either a sum of convective or radiant flux. The latter, however, is dependent on many variables due to the changing emissivity coefficient of the surface of the battery, which is attributable to random phenomena such as burning of the paint and soothing of the flame.
- The model assumes a two-layer passive heat insulation system, which is comparable to an actual system. In reality, the battery interior has more complex design and multiple barriers, and nooks that may vary the results.

6.3.4 Summary

Temperature data obtained during the fire resistance test of a RESS showed that even with the precautions required by the reference document, the flame source is highly stochastic in nature. The pool fire produced vastly diversified temperature around the casing, which was influenced by different factors such as the size of the fire pool, wind speed, and the length of the testing phases.

The variance in the temperature distribution showed that a steady burning rate may have not been reached by the end of the exposure. Lack of this state may have adverse impacts on the reliability of the procedure and therefore on failure prevention detection, which this procedure should provide.

The current restrictions and rules in the R100.03 fire testing procedure may be considered as insufficient to provide reliable conditions for a homologous testing procedure. The procedure should be revised in terms of the method of exposure.

TR of the battery is more likely to occur after fire exposure, when the temperatures begin to equalize inside and around the battery.

6.4 Statistical analysis of Open Flame Fire Resistance Testing Procedure

This study presents a statistical investigation into the repeatability of the R100.03 procedures, analysing them in terms of exposure conditions, temperature, wind effects, and the sizes of both the DUT and the pool fire. It also offers an evaluation of the reliability of these test methods as safety standards in Europe and China. The purpose of this investigation is to determine the level of repeatability in large-scale pool fire tests involving test objects engulfed in flames and to assess the provisions established in the R100 procedures.

6.4.1 Experimental Setup and Instrumentation

The experimental site consisted of stationary rectangular pans (tray) with dimensions provided in Table 6.6. The pans were filled with 20 dm^3/m^2 of 95-octane gasoline (E5, as specified in EN 16942 [349]) and 40 dm^3/m^2 of tap water. The other elements included a movable cart with the specimen, which allowed for transferring the DUT over the pool fire for Phase B, and a cart with a perforated brick screen that could also be moved above the pool fire during Phase C. The exposed surface dimensions of the DUT that were subjected to the tests are listed in Table 6.6; all samples were of rectangular horizontal projection.

The testing rig was shielded from wind by a 2.5 m-high corrugated steel fence positioned within 30 cm of the tray. At no point did the wind speed exceed the required value of 2.5 km/h. The experimental site was located outdoors, and the ambient conditions—including temperature, humidity, and average wind speed - are listed in Table 6.6.

The DUT surface areas in the study ranged from 0.23 m^2 to 1.22 m^2 while the pool fire sizes varied between 0.58 m^2 and 2.10 m^2.

During the tests, a series of type-K thermocouples were positioned around the DUT to record its surface temperatures. The schematic of the thermocouple placement is shown in Figure 6.12. The thermocouple measuring tips were mechanically fixed at specified locations on the DUT's exterior. Type K thermocouples were used, supplemented by additional thermocouples for ambient and fuel temperature measurements. Each thermocouple was connected to a data logger (Pumpa 0056/2011 with ADAM 4118 RS485 thermocouple modules) with sampling rate of 0.5 Hz. Wind velocity was measured using a Testo 480 hot-wire anemometer. The anemometer probe was positioned at the level of the pan, distanced, and shielded from the fire source to avoid interference from convective heat flows. All measuring equipment was externally calibrated in laboratories compliant with EN ISO/IEC 17025:2018 prerequisites.

The testing rig consisted of rails, two steel carts (one for DUT transport and another for the brick screen), a stationary steel rectangular tray, wind shields made of a 2.5 m high fence, and a standardised 20-feet freight container for DUT storage after the test. The movement of the carts was carried out using a pulley system, operating at a linear speed of 0.4-0.5 m/s. Additionally, a dousing system was enabled to extinguish the burning fire fool immediately after the DUT was removed from fire exposure.

6.4.2 Statistical Data Analysis

To quantify the errors and random effects during testing, each test was evaluated using statistical data analysis concepts based on the guidelines and instructions outlined in the ISO 5725 series [350, 351, 352]. This approach provides numerical insights into the repeatability and precision of the testing procedure and heat source while also contextualizing non-regulated parameters such as ambient temperature, humidity, and flame temperature. Additionally, it allows for comparisons of defined parameters within the testing procedure.

The design of the testing rig is aimed to minimize systematic errors and ensure consistent execution of each test. Random parameters influencing the test results included flame instability,

Table 6.6: Information on the dataset: test method, ambient temperature, humidity, average wind velocity, initial fuel temperature, DUT length and width, pool fire length and width, and DUT coverage.

Test No	Ambient Temp., °C	Ambient Humidity, %	Wind Velocity, km/h	Fuel Initial Temp., °C	DUT Length, mm	DUT Width, mm	DUT Surface, m^2	Pool Length, mm	Pool Width, mm	Pool Surface, m^2	Pool Extra Area %
1	18.3	68.1	1.0	18.9	1056	802	0.85	1456	1096	1.60	46.9
2	31.2	37.1	1.1	23.4	1365	808	1.10	1685	1214	2.05	46.1
3	11.2	77.5	0.7	13.3	1688	724	1.22	1950	970	1.89	35.4
4	8.4	66.1	0.4	15.1	1051	770	0.81	1480	1000	1.48	45.3
5	16.8	42.1	0.2	24.8	1323	800	1.06	1710	1205	2.06	48.6
6	17.3	28.2	0.9	16.4	1320	793	1.05	1710	1230	2.10	50.2
7	17.3	28.2	0.9	11.0	1208	825	1.00	1460	1100	1.61	37.9
8	27.6	20.8	0.9	26.4	534	433	0.23	760	760	0.58	60.0
9	31.6	25.9	0.5	27.1	830	742	0.62	1240	1000	1.24	50.3
10	3.9	90.0	0.5	3.9	953	711	0.68	1240	1000	1.24	45.4
11	4.5	94.5	0.3	4.5	1364	555	0.76	1740	1000	1.74	56.5
12	5.0	73.6	0.5	5.0	1331	800	1.06	1710	1230	2.10	49.4
13	3.2	69.4	0.8	3.2	1331	800	1.06	1710	1230	2.10	49.4
14	9.4	14.3	0.8	8.4	858	555	0.48	1240	1000	1.24	61.6
15	10.1	21.7	1.2	8.4	1054	769	0.81	1480	1000	1.48	45.2
16	22.8	46.9	0.6	25.5	1323	800	1.06	1720	1000	1.72	38.2
$\overline{X}$	14.9	50.3	0.7	14.7	1162	730	0.86	1518	1065	1.64	47.9

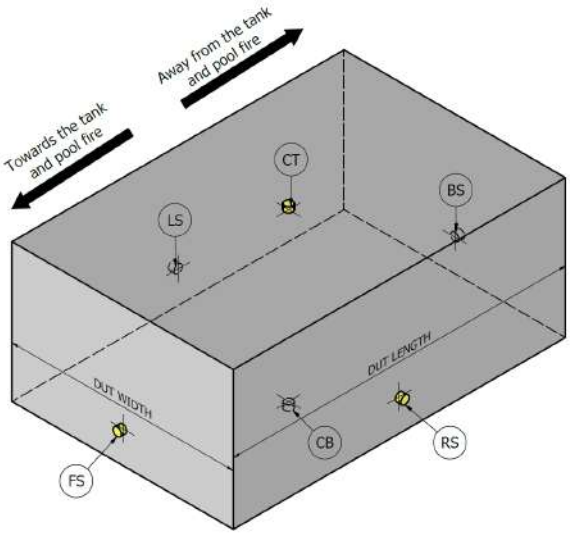

ID	Description	Location
FS	Front side	100mm from the bottom edge, mid-width
LS	Left side	100mm from the bottom edge, mid-length
RS	Right side	100mm from the bottom edge, mid-length
BS	Back side	100mm from the bottom edge, mid-width
CT	Centre top	In the geometrical centre of the top surface.
CB	Centre bottom	In the geometrical centre of the bottom surface, 150mm below.

Figure 6.12: Thermocouple positioning scheme for the dataset.

wind gusts, ambient temperature (within allowable limits), humidity, initial petrol temperature, and phase-transition times. These parameters were analysed for correlations with heating conditions, including temperature and its distribution.

The devices used in the tests were calibrated, and systematic error changes were assumed to have no impact on the system. Measured quantities were treated as random variables following a normal distribution, adhering to the simple acceptance rule [353].

For each thermocouple and test number, the time-dependent mean exposure temperature $\overline{T}$ and standard deviation σ were calculated using the following equations:

$$\overline{T}^p_{ij}(t) = \frac{1}{n^p_{ij}} \sum_{k=1}^{n^p_{ij}} T^p_{ij}(t) \tag{6.25}$$

$$\sigma^p_{ij}(t) = \sqrt{\frac{1}{n^p_{ij} - 1} \sum_{k=1}^{n^p_{ij}} (T^p_{ijk} - \overline{T}^p_{ij})^2} \tag{6.26}$$

where i denotes the thermocouples placement (CT, CB, LS, RS, FS or BS; see Figure 6.12), j is test number (1–16), i is the selected phase of the test, p represents the population and t represents time. The following data are used in the time-temperature graphs shown in Figure 6.13a.

Subsequently, the general mean and repeatability standard deviation were estimated for each thermocouple using the following equations:

$$\overline{\overline{T}^p_i} = \frac{\sum_{j=1}^{t} n^p_{ij} \overline{T}^p_{ij}}{\sum_{j=1}^{t} n^p_{ij}} \tag{6.27}$$

$$\sigma^p_{Ri} = \frac{\sum_{j=1}^{t} \sigma^p_{ij} \, (n^p_{ij} - 1)}{\sum_{j=1}^{t} (n^p_{ij} - 1)} \tag{6.28}$$

Currently, there is no available data on the repeatability standard deviation specifically for the R100.03 test. Thus, the calculated σ^p_{Ri} based on ISO 5275-4 is considered the best estimate [352]. Further checks of precision can only be performed when the repeatability standard deviation of the standard measurement method, σ^p_{Si}, is determined in accordance with ISO 5275-2.

For comparison purposes, the reference standard deviation from the time-temperature curve in ISO 834-1 [354] and the International Code for Application of Fire Test Procedures [355] is

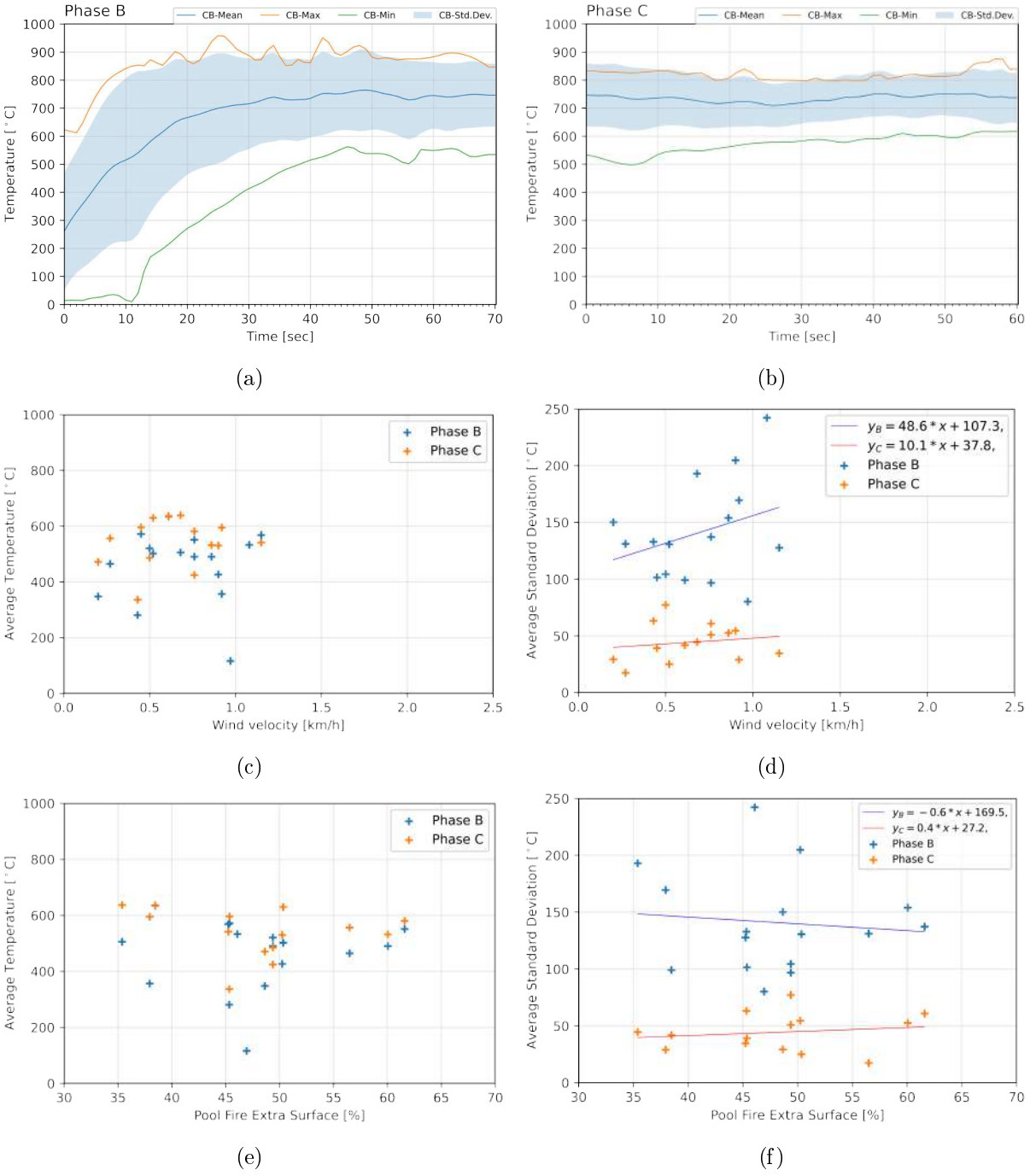

Figure 6.13: Test results charts. Temperature readings from the thermocouples located at the bottom centre of the DUT during Phase B (**a**) and C (**b**). Wind velocity in relation to average temperature (**c**) and average standard deviation (**d**) from each test (represented as points). Subsequent figures show pan coverage in relation to the average temperature (**e**) and average standard deviation (**f**).

used. This standard deviation is based on the maximum allowed tolerance in the standards of $\pm 100°C$, where σ_{Ri}^{p} equals 81.6°C. This value is then used to compute the test statistic C and the critical value C_{crit}, calculated as follows:

$$C^{p} = (\sigma_{Ri}^{p})^{2} / (\sigma_{Si}^{p})^{2} \tag{6.29}$$

$$C^p_{crit} = \frac{\chi^2_{(1-\alpha)}(v)}{v} \tag{6.30}$$

where $\chi^2_{1-\alpha}(v)$ represents the $1-\alpha$ quantile of the χ^2 distribution with $v = j-1$ degrees of freedom. For this scenario, ISO recommends $\alpha = 0.05$.

If value C^p is larger than C^p_{crit}, the test method or procedure should be investigated for discrepancies. If C^p_{crit} is larger or equal to C^p, no further investigations are necessary, and the obtained data can be used in subsequent analyses. Hence, the ratio was defined as κ factor.

$$\kappa = \frac{C^p}{C^p_{crit}} \tag{6.31}$$

κ factor is used in a summary of the test results is provided in Table 6.7 to determine the potential discrepancies.

Table 6.7: Summary of the exposure temperatures for Phases B and C - average temperature ($\overline{\overline{T^p_i}}$), repeatability standard deviation (σ^B_{Ri}) and κ factor for thermocouples CT, CB, RS, LS, FS, BS.

	CT	**CB**	**RS**	**LS**	**FS**	**BS**	$\overline{X}$
$\overline{\overline{T^B_i}}$, $°C$	325.5	667.0	463.2	476.0	342.1	506.9	463.4
σ^B_{Ri}, $°C$	123.5	138.7	127.5	158.5	84.0	164.1	132.7
κ	1.4	1.7	1.5	2.2	0.6	2.5	1.6
$\overline{\overline{T^C_j}}$, $°C$	360.6	740.2	536.2	574.1	442.5	586.5	540.0
σ^C_{Ri}, $°C$	45.7	28.4	43.7	49.9	33.1	47.0	41.3
κ	0.2	0.1	0.2	0.2	0.1	0.2	0.2

6.4.3 Conclusions

In the following chapter, it is presented and discussed the results of a series of fire-resistance tests. The aim of this analysis is to highlight the crucial aspects of the tests in terms of repeatability and accuracy. Based on the initial study made by doctoral candidate [356], fluctuations and variances were anticipated; however, multiple factors were found to influence the final results.

The analysis focused on Phase B (direct exposure of the DUT to fire) and Phase C (indirect exposure of the DUT to fire), with Phase A included only as a reference for fire stability (see Section 5.4.3 for reference on phases description). Phase D, the observation phase, was intentionally omitted as its outcomes were dependent on the DUT design, which varied significantly between samples and was confidential to the manufacturer. Each of Phases A, B, and C lasted the minimum required durations of 60, 70, and 60 s, respectively (refer to Table 6.2). Variations in the total phase lengths were attributed to the movement of the DUT and the screen.

Exposure Conditions

Fire exposure occurs during Phases B and C, where the DUT was positioned directly above the fuel tray. Due to wind variations during the test and eddy currents creating vortices around the flame, it was determined that the thermocouples along the centreline (denoted as "CB") could reliably evaluate the exposure temperature, as their measuring tips remained within the flame for the entire duration. Figure 6.13 illustrates the mean ($\overline{T^p_{ij}}(t)$), maximum, and the minimum temperature, along with the standard deviation ($\sigma^p_{ij}(t)$) during Phase B (Figure 6.13a) and C (Figure 6.13b).

At the beginning Phase B, a significant variation temperature was observed, ranging from 10.0 °C to 958.3 °C. The mean temperature increased until the 30-th second of the phase, where

it stabilized at approximately 700 °C. The maximum of standard deviation at 270.0 °C and averaged 138.7 °C throughout the phase.

Phase C exhibited relatively stable conditions, with a mean temperature of 740.2 °C and an average standard deviation reduced to 28.4 °C. The observed temperature range during Phase C was between 498.2 °C and 875.7 °C.

For thermocouples located below the DUT (denoted as "CB"), the average temperatures during Phases B and C were relatively constant, indicating that the perforated brick screen did not influence the exposure temperature along the centreline. However, temperature sensors positioned around the DUT (denoted as FS, BS, LS, and RS) showed an increase in values from Phase B to Phase C, though this change was inconsistent. Depending on the location, temperature sensors recorded increases ranging from 73.0 °C to 100.4 °C. The rising temperatures from Phase B to Phase C can be explained that the steady-state burning of the pool fire was not achieved, and the regulatory 60 s preheating period may be insufficient to establish stable temperatures. This observation aligns with findings from the results shown in previous section 6.3.

One of the reasons for the significant standard deviation observed during Phase B is that the pool fire had not yet stabilized. The R100 procedure requires a preheating period of 60 s, while it is indicated that the stabilization time may be as long as 150 s to reach the optimum burning rate under given ambient conditions [337]. To address this, either a longer preheating period should be implemented, or the heating medium should be reconsidered. Pool fires have been shown to be prone to puffing and geometry changes due to the entrainment process [330, 357]. Vortex formation and the creation of lower-temperature regions at the flame edges may explain the fluctuations observed in thermocouple readings around the tested specimen (see Table 6.7, denoted as RS, LS, RF, and BS). For both phases, the temperatures around the specimen varied, with notable standard deviations recorded. Based on the studies a recommendation can be that a proper engulfment of the sample in fire requires a substantially larger pool (above a 1:5 sample-to-pool area ratio) [340, 358]. However, this size of a pool with batteries sizing even above 2.1 m^2 is particularly unpractical. During Phase C, the temperature is almost constant along the centreline, while fluctuations of temperature were still recorded on perimeter thermocouples. The use of a perforated brick screen for pool fires between 0.58 m^2 and 2.10 m^2 did not affect the temperature readings along the flame centreline compared to Phase B. The pool sizes of 0.58-2.10 m^2 were determined by the restriction on the pool size being at minimum 200 mm and at maximum 500 mm larger than the specimen (exposed surface), see Section 6.2.1 for further reference. The range of the specimen sizes and connected pool fire sized shows Figure 6.3b.

The substantial variation in temperature at the start of Phase B can be attributed to two factors: the linear cart speed with the DUT and the DUT size. The testing method does not specify a required linear speed for the carts, which can lead to prolonged exposure of the tested device, as the Phase B timer starts only when the DUT is aligned with the tray's centreline. Without regulation of cart speed, the exposure period during Phase B can be extended by as much as 28% at an average cart speed of 0.1 m/s (see Table 6.6 and pool length). Another influencing factor is the length of the DUT, specifically the dimension parallel to the movement path. Longer specimens remain in the fire significantly longer throughout the test before reaching the centreline.

Influence of the Wind Speed and Pan-Coverage Ratio

The average wind velocities recorded during the tests ranged from 0.2 km/h to 1.1 km/h, with intermediate values remaining below the regulatory threshold of 2.5 km/h (see Section 6.2.1). Correlation graphs were generated to analyse the potential influence of wind on the flame temperature around the battery. Average temperature and standard deviation values, calculated from the thermocouples denoted as FS, BS, LS, and RS, were compared with mean wind velocity for Phases B and C, as presented in Figure 6.13.

Wind velocity was found not to influence the average temperature values on the sides of the tested specimen, as shown in Figure 6.13c. However, a correlation was observed between temperature standard deviation and wind velocity, though with a low coefficient of determination (approx. $\sim R^2 = 0.10$ and 0.03 for respectively Phase B and C). The distribution, shown in Figure 6.13d, exhibited significant homogeneity. Consequently, the dataset was deemed too sparse to produce a reliable regression model, or there is no relationship between two parameters. The average standard deviation was found lower during Phase C than Phase B.

The test results align finds from previous Section, indicating that hydrocarbon pool fires are prone to fluctuations caused by self-induced air vortices. At wind velocities below 1.1 km/h, temperature results showed no directional bias towards any side, even though the flame tilted periodically during the tests.

The pan size was determined according to the rules specified in R100.03 [254], with dimensions exceeding the specimen size by 200 mm to 500 mm. The pan-coverage ratio ranged between 38% and 65% for the samples taken for this study, as shown in Figure 6.3b. Additionally, the exact sizing of the pool fire is defined on the basis of firebrick fixed dimensions (see Figure 6.14), which due to technological issues are not cut to size.

Annex 9E - Appendix 1

Dimension and technical data of firebricks

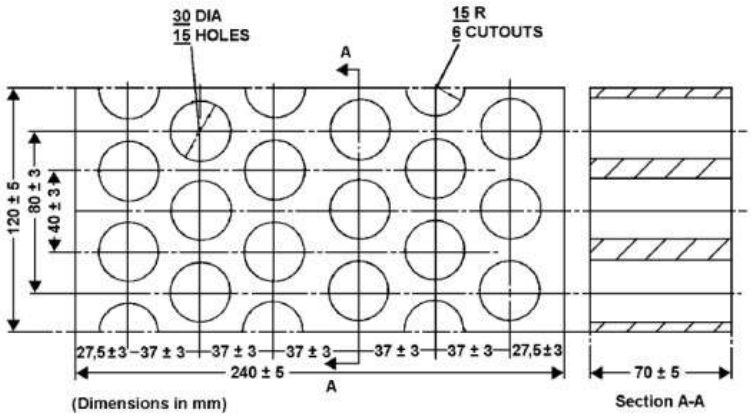

Fire resistance:	(Seger-Kegel) SK 30
Al2O3 content:	30 - 33 per cent
Open porosity (Po):	20 - 22 per cent vol.
Density:	1,900 - 2,000 kg/m3
Effective holed area:	44.18 per cent

Figure 6.14: Firebrick specification taken from UNECE R100.03 [254].

As with wind speed, correlation graphs were created to investigate the influence of the pan-coverage ratio on exposure conditions, represented by the average temperature during the test phases and the average temperature deviation. The calculations included thermocouples denoted as FS, BS, LS, and RS, which were located on all four sides of the DUT. The graphs are shown in Figure 6.13.

No correlation was found between the pan-coverage ratio and average temperature during Phases B and C, as shown in Figure 6.13e. The results demonstrate that an increase in pan-coverage ratio does not influence the temperatures around the DUT. Similarly, the average standard deviation of the temperature (Figure 6.13f) was not dependent on pan-coverage values. Phase C values for average standard deviation were consistently lower than those for Phase B, mirroring the results observed for wind speed.

Ambient Conditions and Fuel Temperature

Tests were conducted in a range of ambient temperatures above the minimum required 0 °C, with an average of 14.9 °C. Ambient temperature was measured before and during the test in the vicinity (approx. 0.5 m) from the test rig, shielded from the flame influence. Ambient humidity levels were recorded during each test, ranging from 14.3% to 94.5%. Initial fuel temperature ranged between 3.2 and 27.1 °C. These data were included in the statistical analysis to assess any correlations between humidity and the variability in temperature exposure around the device under test. However, no statistically significant correlations to exposure temperature and its distribution were found either for the initial temperature of the fuel or for ambient temperature or humidity.

To investigate correlation Pearson coefficients were determined according to following equation:

$$p = \frac{\sum_{i=1}^{n}(x_i - \bar{x})(y_i - \bar{y})}{\sqrt{\sum_{i=1}^{n}(x_i - \bar{x})^2}\,\sqrt{\sum_{i=1}^{n}(y_i - \bar{y})^2}} \tag{6.32}$$

where x_i and y_i are data points, $\bar{x}$ and $\bar{y}$ are the means and n is number of pairs. The $|p|$ values ∼0 mean no correlation, 0.0-0.2 very weak correlation, 0.2-0.4 weak correlation, 0.4-0.6 moderately stron correlation, 0.6-0.8 strong correlation, 0.8-0.9 very strong correlation, ∼1 perfect correlation [359].

The Pearson correlation coefficients in Phase B for ambient temperature, humidity, and initial fuel temperature are, respectively, −0.29 (p-value of 0.273), 0.43 (p-value of 0.093), and −0.17 (p-value of 0.532), while in Phase C are −0.17 (p-value of 0.569), 0.13 (p-value of 0.668), −0.08 (p-value of 0.793). None of the p-values indicate that the correlations are statistically significant.

6.5 Discussion on the Open Flame Fire Resistance Testing Procedure

Since the R100 fire-resistance testing procedure is used in the European Union's homologation process and sets standards for LIBs in EVs, the prescribed method should produce repeatable conditions, provided all provisions are met [360]. This testing procedure has also been adopted in other standards, such as ISO 6469-1:2019 [68], ISO 18243:2019 [264], and GB 38031-2020 [73], method is also replicated in UL 2580 and UL 1973, although with significantly longer (9 times longer) exposure time [283, 285]. Consequently, similar issues with repeatability may arise globally. Studies conducted in the course of PhD thesis have already highlighted the stochastic nature of hydrocarbon pool fires [67, 356, 361]. Although a new testing method based on LPG burners was proposed in 2020 [362], the hydrocarbon curve-based method remains in use for official homologation of battery storage systems [254, 363].

According to Table 6.7 and ISO 5275-4 [352], the Phase B κ factor exceeds 1 for all thermocouple locations except the front side, indicating that the procedure should be reviewed for inconsistencies. All provisions and requirements specified in the standard method (see Section 6.2.1) were met, and additional measures were implemented to further limit exposure condition variances. Despite these efforts, large temperature standard deviations were observed throughout Phase B (averaging 132.7 °C). Deviations resulting in the performed test may be unavoidable due to thermal characteristics of hydrocarbon pool fire and from the standardisation perspective, it is highly not recommended to use this phenomenon. Furthermore, temperature differences between the centreline and the sides (from 160.1 °C to 324.9 °C), attributable to the burning dynamics of hydrocarbon pool fires [332, 326].

Phase C exposure conditions showed positive κ value (see Section 6.4.2) in terms of repeatability assessment, as presented in Table 6.7. The influence of the perforated brick screen, which creates a nozzle effect leading to a more stable hydrocarbon pool fire, or the longer burning

time, indicate that hydrocarbon pool fires between 0.58 and 2.10 m^2 require more than 60 s to stabilize. Nevertheless, a similarity in average temperature along the centreline was observed, while the sides exhibited substantial differences, with temperatures ranging between 153.7 °C and 297.7 °C. Since the fire-resistance test for a given DUT is performed only once, a strong bias may develop toward one side. Standardized testing procedures should ensure relatively uniform testing conditions with minimal bias, as real-life pool fires can occur at random locations. The R100 fire-resistance testing procedure thus produces specific conditions that apply to only a narrow range of accident scenarios.

Wind velocity was found not to influence average temperature during Phases B or C. However, an increasing trend in standard deviation with rising wind velocity was observed, as shown in Figure 6.13d, particularly during Phase B. This indicates the vulnerability of hydrocarbon pool fires to low wind velocity changes, which aligns with observations made during the tests. No tilt bias toward any specific side was detected. Since the mean wind velocity values were relatively low (below 1.1 km/h) compared to other studied conditions [364], it can be assumed that wind velocity does not significantly contribute to the high variance observed during the tests.

For Phase C, the mean standard deviation of temperature was significantly lower than in Phase B and remained non-dependent on the pool fire extra surface. As the range of pool fire extra surface is strictly prescribed in the testing method (refer to Section 6.2.1), no data are available for DUTs significantly smaller than the pool fire. While increasing the pool fire area may reduce temperature variance around the DUT to some extent, practical challenges arise in designing a reliable testing rig with larger hydrocarbon pool fires, especially when moving parts are involved.

The insights gained from this study have valuable implications for computational modelling and simulation of fire-resistance scenarios. The variability observed in the experimental results could serve as critical input parameters for probabilistic models, such as Monte Carlo simulations, to evaluate the range of potential outcomes under similar testing conditions [365]. By incorporating the stochastic elements of hydrocarbon pool fires, such as temperature deviations and flame behaviour, these models can better predict real-world performance and inform the design of battery energy storage systems.

6.6 Alternative Fire Resistance Testing Procedure for Lithium-ion Batteries

Open-flame fire testing has become a cornerstone of safety evaluations for LIB systems, especially in EVs and ESS. Regulatory standards like the UNECE R100.03 (for EV batteries) and various national and industry standards prescribe exposing a battery pack (or ESS) to an engulfing fuel fire for a short duration to assess its resistance to fire and to ensure it does not violently rupture or explode during the exposure. This approach aims to simulate a post-crash fuel fire impinging on a battery, ensuring occupants have time to escape and that first responders are not faced with immediate battery explosions. Chapters 5 and 6 of this thesis presented such pool fire tests and highlighted significant challenges in repeatability and safety assurance. In light of those findings, this chapter explores an alternative fire-resistance testing procedure developed by PhD candidate for LIBs based on controlled furnace exposures (in line with railway fire-testing practices), and proposes a complementary pressure testing regimen to address the known shortcomings of open-flame tests.

6.6.1 Alternative EN and ISO Fire Resistance Testing Procedure for Lithium-ion Batteries

In railway applications, the fire safety paradigm differs from automotive practice: the emphasis is on fire containment and fire barrier performance within rail vehicles. EN 45545-3:2024 (recently

updated in 2024 [366]) is the European standard that specifies fire resistance requirements for fire barriers on railway vehicles. A "fire barrier" in this context could be a wall, door, partition, or enclosure that separates compartments and must resist fire and hot gases for a specified time to allow safe evacuation of passengers and crew. Notably, if LIBs are used on trains (for example, in auxiliary power units or hybrid propulsion), their housings might be treated as fire barriers between the batteries and occupied areas. The testing method mandated in EN 45545-3 is fundamentally different from the automotive open-flame test: it relies on standard furnace tests analogous to those used in building construction. Specifically, EN 45545-3 calls for fire resistance testing according to EN 1363-1:2020 (general requirements for fire resistance tests) and the appropriate part of EN 1364 (for non-loadbearing elements, e.g., walls or ceilings).

EN 45545-3 mandates that fire barrier components be tested according to EN 1363-1, which is the general standard for fire resistance tests of building elements. In practical terms, this means the battery enclosure (or a representative section of it) is mounted in a large fire furnace and exposed to a standard time-temperature fire curve while observing specific performance criteria. The standard fire curve - often called the "cellulosic" curve or ISO 834-1 curve - is defined such that furnace temperature T rises according to a logarithmic formula:

$$T(^{\circ}C) = 20 + 345 \cdot \log_{10}(8t + 1) \tag{6.33}$$

where t is time in minutes (starting from 20 °C ambient) - see Figure 6.15 for time-temperature profile. This controlled heating profile is meant to represent a realistic building fire growth - starting off moderate and becoming fully severe after some time.

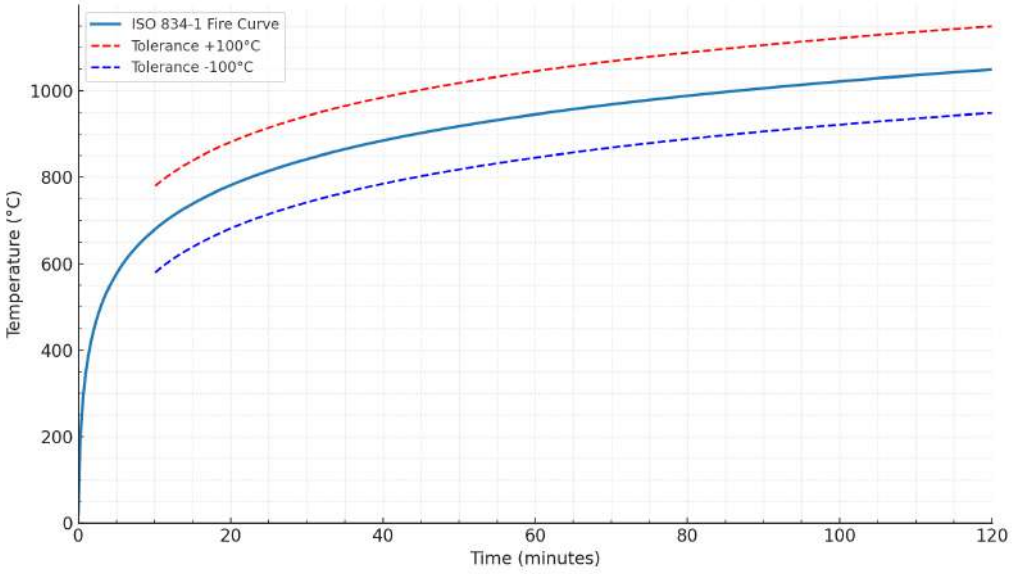

Figure 6.15: ISO 834-1 Standard Time-Temperature Fire Curve.

During the test, the battery enclosure specimen is typically installed in the furnace such that one face is exposed to the burner flames inside the furnace, while the other face is oriented to a cooler outside and can be observed. Depending on the intended scenario, the "fire side" could correspond to inside the battery enclosure (simulating an internal battery fire impinging on the walls from within) or the outside (simulating an external fire heating the battery case). In railway standards, usually the fire side is the more likely ignition side. For a battery housing, a plausible assumption is that cells inside could catch fire, so the fire side is interior and the test evaluates whether flames would breach to the exterior (passenger side). However, if a fire external to the battery (like a luggage fire) is a concern, they might test the opposite orientation. EN 45545-3 and EN 1363-1 provide flexibility in mounting, but they require that any openings or penetrations in the barrier (for cables, vents, etc.) be present or represented in the test item.

This is critical: penetrations must not reduce the fire resistance of the barrier. In practice, that means if the battery box has ventilation grills or safety vents, those are included in the sample - allowing heat and flame to enter as they naturally would - and the enclosure must still perform its duty (letter "E", "I" or "W" denotes the performance parameter). The performance parameters stand as follow:

- **E – Integrity:** The barrier must prevent the passage of flames or hot gases through to the unexposed side for the duration of the rating. Essentially, no cracks or openings should develop that let flames through, and no sustained flaming on the outside.
- **I – Insulation:** The barrier also limits the temperature rise (defined as a temperature difference between ambient temperature at the start of the test and final temperature recorded with the thermocouple) on the unexposed side to below specified levels (maximum of 140 °C average rise, 180 °C at any point, above ambient). This ensures the barrier not only stops flames but also does not get so hot on the outside that it ignites adjacent materials or harms people by radiant heat. Insulation shall not function without integrity i.e., there may not be stand-alone I10 classification, but can only be EI10 or EI10/E20 and so on.
- **W – Radiation:** The barrier limits the radiative heat flux from its unexposed surface to adjacent objects. This is a stricter criterion related to insulation – essentially controlling how much heat can be transmitted through or from the barrier. Radiation shall not function without integrity as well.

Only integrity (E) is required for barriers, especially if the other side of the barrier does not directly expose passengers. For instance, an underfloor battery box might need to maintain E15 (15 minutes of integrity) to ensure no flames penetrate into the passenger cabin above (typically such structures require between 5 to 30 minutes of integrity depending on their location). If that battery is directly below the floor, an insulation criterion (EI15) might also be needed to keep the floor temperature safe for 15 minutes (so people have time to evacuate without suffering burns or the floor catching fire). The standard provides guidance: typically ratings are expressed as combinations like E15, E30, E60 (minutes of integrity), sometimes with an I or W of the same duration, if needed. It is also important to note, the integrity performance parameter shall be fulfilled to accept results for the insulation or radiation. A stand-alone insulation or radiation performance is not accepted i.e. the battery pack cannot be classified as I15 or W15, but EI15 or EW15.

Unlike the pass/fail nature of R100 or UL, the furnace test yields a time rating for the battery enclosure. For example, a battery box might be rated E20 (integrity for 20 minutes) if it withstood 20 minutes in the furnace before flames penetrated through a gap or a glowing hole. If it also limited temperature rise appropriately, it could be EI20. Compared to R100.03 where pass/fail criteria are qualitative (if explosion is observed or not), the tested rating after EN test tells you the exact time the performance criterion is maintained. Notably, EN 45545-3 explicitly states that these measures are not aimed at saving the train or battery itself, but at aiding evacuation and preventing fire spread.

One benefit of the EN 1363-1 furnace approach is that it allows a calculation of thermal exposure (dose) in a reproducible way. In one study of railway fire tests, the incident heat flux on the specimen in an EN 1363-1 furnace was estimated to reach about 50 kW/m^2 radiative by 10 minutes, and about 67 kW/m^2 by 20 minutes (as the furnace got hotter), with a significant convective component as well [367]. For comparison, as calculated earlier, an open hydrocarbon pool fire can have ∼60 kW/m^2 incident flux on surfaces, but this value can fluctuate and is not uniform. The furnace gives a more even and steadily increasing heat load. The integrated heat absorbed by the enclosure in a 30 minute furnace test far exceeds that of the 2 minute

R100 flame test. This means a furnace-tested enclosure is being exposed to almost constant high temperature, while pool fire reaches similar temperature only momentarily.

While the heat flux calculations can be simplified to following equations:

$$Q'' = Q''_{rad} + Q''_{conv} \tag{6.34}$$

where Q''_{rad} is radiative heat flux and Q''_{conv} and convective heat flux. This can be approximated with following two calculations:

$$Q''_{rad} = \epsilon \cdot \sigma \cdot (T_f^4 - T_s^4) \tag{6.35}$$

$$Q''_{conv} = h \cdot (T_f - T_s) \tag{6.36}$$

where ϵ is effective emissivity (typically 0.7–0.95 for burner flames), σ is Stefan-Boltzmann constant, h is convective heat transfer coefficient (typically 30 W/m^{2}K in fire testing as per SFPE recommendations) and T_f is flame temperature (ambient) and T_s is a surface temperature.

The heat flux calculations are highly dependent on multiple physical and experimental factors that significantly affect the final values of Q''. One of the most critical parameters is the surface temperature of the heated specimen—when the surface temperature is low compared to the furnace or flame environment, the resulting heat flux (from both convection and radiation) becomes significantly higher. Variations in surface emissivity (ϵ) can change the radiative heat flux substantially, as this component is proportional to the fourth power of temperature. Similarly, the convective heat transfer coefficient (h) depends on the setup's geometry, the orientation of the specimen, the gas flow regime, and turbulence levels. In simplified calculations, assuming a constant h provides a useful estimate, but real conditions often vary dynamically during the test due to thermodynamic characteristic of the flame.

The design and configuration of the experimental apparatus also exert considerable influence. In actual fire test furnaces, spatial variations in radiative intensity, flame impingement, and gas flow irregularities may result in non-uniform heating of the test object. These effects are not captured in the simplified analytical model presented in the thesis. Additionally, thermal properties of the tested material—such as thermal conductivity, specific heat capacity, and density—strongly govern the rate at which the material absorbs and distributes heat. Importantly, heating can trigger phase transitions or chemical processes in certain materials. For example, intumescent coatings may expand upon heating, altering the surface geometry and thermal resistance. These material-dependent effects can both buffer and delay heat transfer, and must be accounted for when interpreting or applying theoretical heat flux results in real-world fire scenarios.

A Figure 6.16 shows heat flux scenarios, which reflect two most common design strategies. First approach assumes the use of non-insulating materials (e.g., steel), therefore the specimen surface reaches 70% of the furnace temperature. The relationship was assumed based on empirical temperature characteristic of non-protected steel under heating conditions [368]. Second example shows a specimen with cooling and insulating elements, which may have their surface maintained below the level of 180 °C (e.g., ceramic wool, gypsum boards). Calculations account for radiative and convective heat transfer with emissivity set to 0.8 and convective heat transfer coefficient to 30 W/m^{2}K. From the heat flux curve shown in Figure 6.16, it can be assumed the heat flux is much more severe for elements of lower surface temperature (see "Heat Flux Test 2" curve). Simultaneously, for the elements that rapidly rise in temperature (e.g., steel; see "Heat Flux Test 1" curve in Figure 6.16), arises a matter of mechanical integrity due to material expansion or degradation in case of lower melting point metals, such as aluminium.

Despite the variable above, which are mainly connected to the specimen properties - not the apparatus - a furnace test, by adhering to EN 1363-1, ensures the sample is exposed to the same thermal exposure profile each time with satisfactory repeatability. This is crucial for

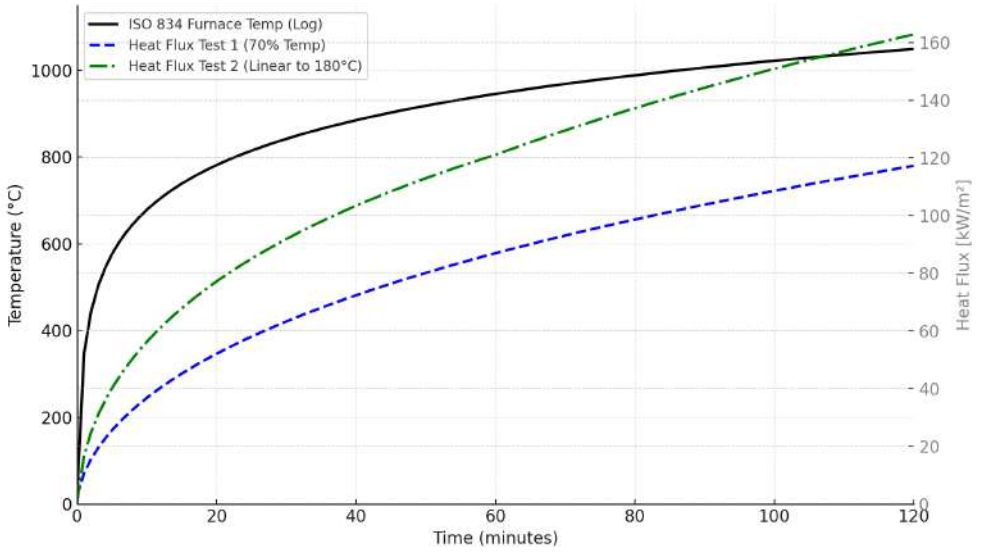

Figure 6.16: ISO 834 furnace temperature (logarithmic profile) and corresponding heat flux variants.

standardisation and certification purposes; it gives authorities and manufacturers confidence that meeting the criteria in one test will be representative to real performance conditions. In building construction and railway standards, fire resistance tests are designed with strict protocols to maximize repeatability. The regulations includes such details as thermocouple placement, furnace pressure, etc., which are all standardized. By leveraging those protocols for batteries, it may import decades of fire-testing good practices and experience into the battery field.

Another aspect of control is that the severity of the test can be tuned or varied in an appropriate way to replicate real life need (each variant shall be explicitly described in the standard). For example, if a particular application does not require a full 30-minute barrier, one could test to a shorter duration. Regardless, any deviation is documented and repeatable, due to standardised curve and tolerances. This kind of flexibility is not possible with pool fire without introducing enormous uncertainty.

From a safety and environmental standpoint, furnace tests are cleaner and easier to manage. Burning a battery generates toxic gases (see Appendix D for further review) and often requires scrubbers or special environmental permits. A furnace, being an enclosed system (often with afterburners or heat exchangers for the exhaust), can combust with cleaner products. If no actual battery electrolytes are involved (testing empty enclosures), the only emissions are from the gas burners heating the furnace, which are equivalent to a normal industrial heater, which aligns with sustainable testing practices and avoids releasing potentially harmful gases from burning Li-ion cells into the atmosphere.

Laboratory personnel are also exposed to far lower risk - the worst case in a furnace test is typically that the specimen fails by igniting on the outside or by developing cracks, but not an unpredictable explosion - then the test can be immediately stopped and preventive measures are used. By contrast, in live battery fire tests there is always a risk of a cell violently ejecting shrapnel or a flammable electrolyte eruption that can endanger people and equipment. Many laboratories do not allow tests with live LIBs, unless extensive precautions are taken; a furnace test of the enclosure circumvents this by focusing on the enclosure's capability to protect against fire rather than initiating a battery fire.

Finally, data acquisition is generally easier in a furnace scenario. Thermocouples can be placed on the specimen (unexposed side temperatures, etc.) without fear of being destroyed by open flames or severed by explosions. Continuous temperature data at dozens of points can be performed during the duration of the test. This approach is invaluable for understanding

heat distribution around the enclosure and determine the weakest areas of the object. In pool fire tests, multiple thermocouples were used and temperature data was obtained on the battery surface. However, many were damaged during the process by the flame environment and the data scatter was high. In a furnace test, data quality is high because the heating is uniform and sensor placement is standardized (for instance, EN 1363-1 prescribes plate thermometers for furnace temperature and insulated pad thermocouples for unexposed face). This wealth of data can help refine thermal models and improve designs in a way that binary outcome pool-fire tests cannot.

6.6.2 Limitations of Furnace-Only Testing: Venting and Pressure Effects

While controlled furnace tests can simulate the thermal aspect of a fire, they inherently do not capture the electrochemical and mechanical responses of a battery undergoing TR. In a real battery fire or abuse scenario, as cells overheat they will eventually vent gases and possibly ignite, leading to internal pressure spikes and even explosions if the battery enclosure is sealed. This aspect is absent in a furnace test where typically the battery enclosure is empty (or contains only passive temperature sensors). Thus, a furnace test alone may prove a battery box can keep out an external fire, but it does not reflect all the internal processes occurring inside the battery .

One specific limitation is the inability of a static furnace test to reproduce high-pressure venting and pulsating pressure loads that occur during cell failures. Lithium-ion cells, when driven into TR, generate hot flammable gases. If these gases ignite, either immediately or after mixing with air, they can create a deflagration - essentially a rapid burning that raises pressure. Even without ignition, the sudden release of ∼100–200 kPa of vapour in milliseconds can produce shock-like pressure waves inside a battery enclosure [96].

EN 45545-3 and EN 1363-1 do not involve internal pressure - they only impose a slight external pressure on the fire side (∼20 Pa) to simulate fire-driven pressure, which is negligible compared to battery vent pressures. Therefore, if one only relies on a furnace test, it might certify a battery enclosure that holds back fire but would either burst or catastrophically vent if the cells inside went into runaway. This is unacceptable from a safety standpoint. Some standards for stationary battery systems are already recognizing this: NFPA 855 (Standard for Installation of Stationary Energy Storage Systems) [198] requires either explosion prevention measures (inerting, etc., per NFPA 69 [288]) or deflagration venting per NFPA 68 for battery enclosures [287]. The principle in NFPA 68 is that any enclosure with flammable gas accumulation must have vent panels or other means to relieve pressure before it builds to a destructive level. For EV battery packs, such venting strategies are not yet standardized. The pack's casing should either be strong enough to contain the worst-case internal pressure or have intentional weak points (vents) that will open in a controlled manner to release pressure.

During TR, cell venting can generate pressures on the order of a few bar in an enclosed space if not vented in controlled. Tests conducted in closed vessels have shown that even a single Li-ion cell can raise the pressure by ∼100–200 kPa or more upon failure (depending on volume). In modules with many cells, if they go into runaway nearly simultaneously (worst-case scenario, it may be triggered by an external fire heating all cells), the pressure could rise very rapidly. If the battery enclosure is rigid and sealed, it may rupture at welded seams or weak points, potentially turning pieces of the battery enclosure into projectiles. Alternatively, if the battery enclosure has a vent aperture, hot gases and flames will jet out of that vent - which is preferable to an explosion, but then one must ensure the vent directs the gases safely (e.g. upward, away from passengers). None of these dynamics are addressed by just testing the box in a furnace with no internal pressure source. A second phenomenon is the mechanical shock from cells or module fragments. In real failures, cells have been known to burst open or even eject like small jet flames when the internal pressure blows the casing. This could impact the battery enclosure from inside. A furnace test does not account for projectiles or impact loads on the battery enclosure walls.

At the same time, one might argue a robust battery enclosure that survives a fire is likely strong, but it is not guaranteed to handle an exploding cell internally. Finally, TR is often accompanied by fast flame jets (if the gases ignite) which can locally heat parts of the battery enclosure much more severely than an external diffuse fire.

6.6.3 Empirical Evaluation of the Fire Resistance Testing according to EN 45545-3 and ISO 834-1

This section presents a detailed statistical analysis of six full-scale fire resistance tests conducted on real-life battery casing samples. The analysis is based exclusively on the prepared dataset, focusing on the experimental results and the statistical repeatability of the obtained measurements. Following dataset information (especially on the DUT) is strictly confided due to confidentiality agreements.

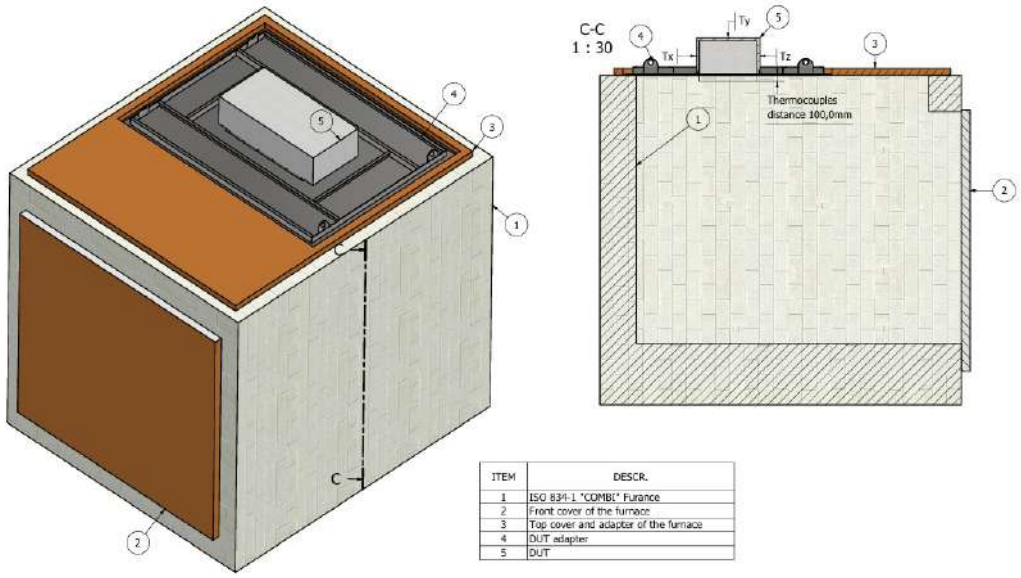

Figure 6.17: ISO 834-1 / EN 1363-1 fire resistance test set-up (fire from inside the battery).

The test involved fire resistance furnace built to fulfil EN 1363-1 and ISO 834-1 requirements. The apparatus contains large test chamber (usually 4x3x4 m^3), which allows to simulate either fire for vertical samples (e.g., walls) or horizontal (e.g., ceilings), as shown in Figure 6.17. The scheme shows furnace and adapters needed to test "fire inside" scenario. For the battery casing, usual mode of testing is horizontal set-up to simulate the lithium-ion cells TR, which produces heat upwards. Often times due to to the scale of the furnace, apart from the DUT, an adapter is required to cover rest of opening to the furnace. Test set-up is presented in Figure 6.17, where No 1 is test furnace, No 2 is front cover (the furnace can be used for vertical and horizontal samples), No 3 is partial cover (the horizontal opening has 12 m^2 of area and the samples are usually below 2 m^2), No 4 is steel adapter with DUT fixing and No 5 is DUT. DUT is also prepared in a way, that it is opened from bottom (on average at least 80% of the total bottom surface area; this is pretest assumption) to allow hot gases to come inside the enclosure. Following opening ratio of at least 80% shall be maintained for all of the compartments within the enclosure of the battery pack, simultaneously not damaging the mechanical integrity of the DUT. This requires individual approach due to the fact the battery packs are vastly different. All other elements, i.e. connectors and cables shall be placed within the enclosure walls as intended and also tested against fire (protruding each side at least 200 mm). Additional, thermocouples (Tx, Ty, Tz) may be added from the unexposed side to confirm the uniform heating, these however may not be at the same time evaluated for the insulation criteria.

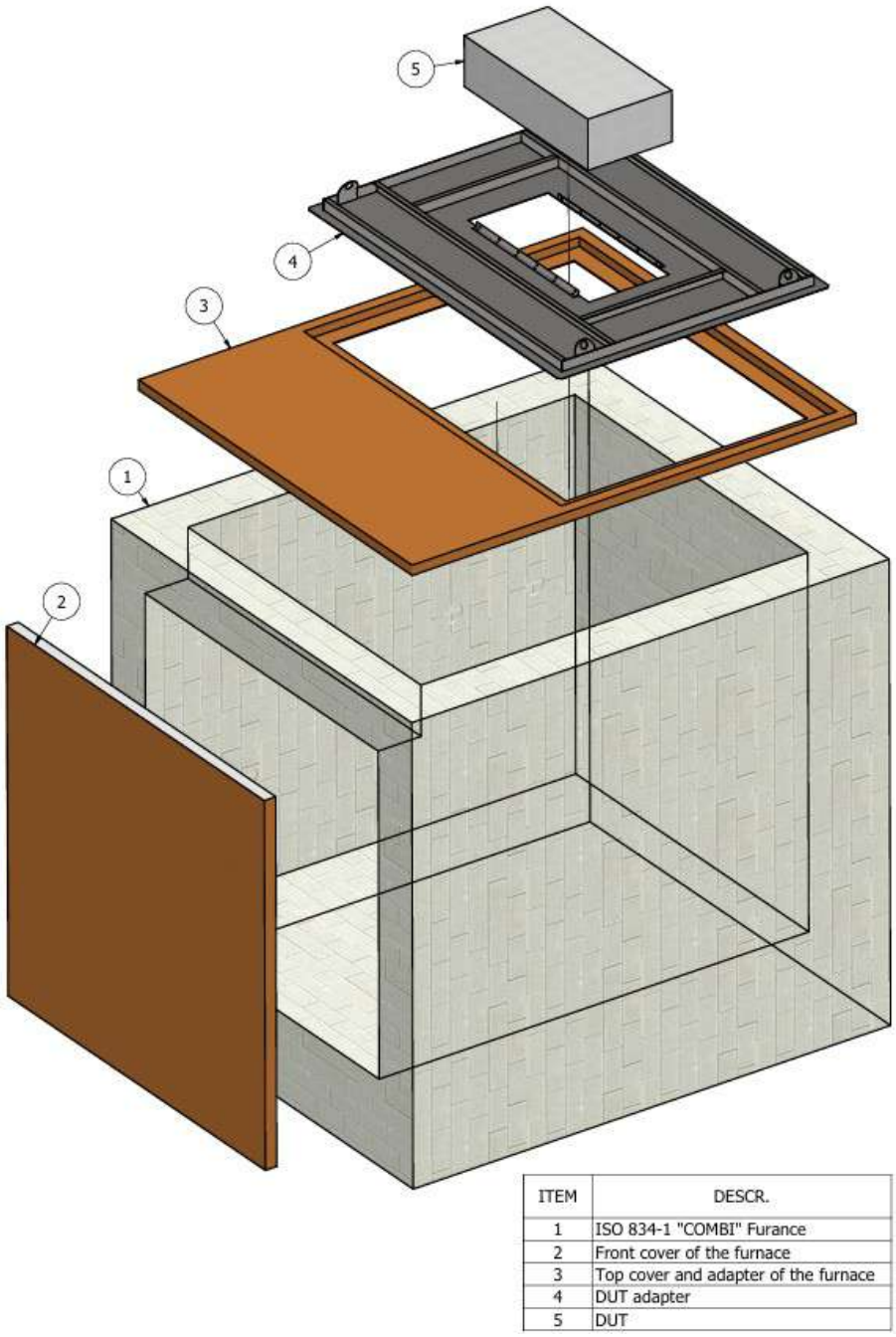

ITEM	DESCR.
1	ISO 834-1 "COMBI" Furance
2	Front cover of the furnace
3	Top cover and adapter of the furnace
4	DUT adapter
5	DUT

Figure 6.18: ISO 834-1 / EN 1363-1 fire resistance test set-up (fire from inside the battery) - exploded view.

Figure 6.18 shows exploded view of the testing set-up, as well as photographies from the tests in Figure 6.19 and 6.20.

Test were conducted on 6 samples of battery enclosures, used for real life applications. Battery enclosures were prepared to be fixed to steel adapter (No 4 in Figure 6.17 and Figure 6.18) and openings at the bottom were made to allow hot air to flow inside.

For each test, time-resolved recordings of the average temperature (T_{avg}) and the recalculated deviation parameter (D_{err}) were obtained. Deviation parameter is calculated based upon EN 1363-1 formulate i.e.:

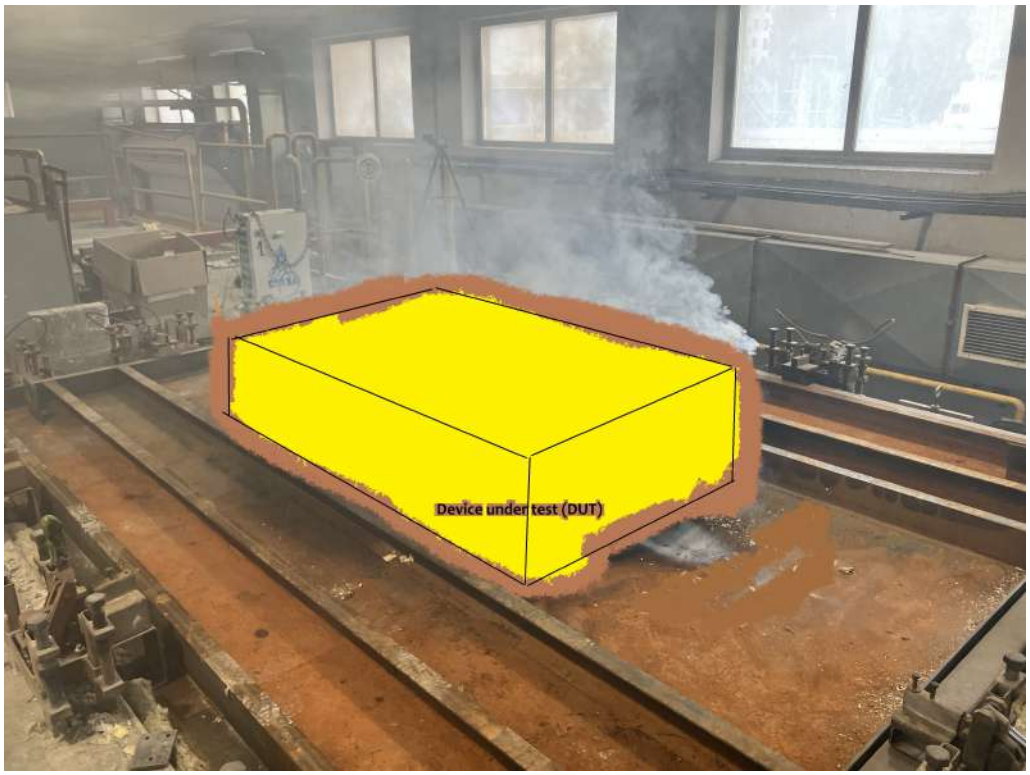

Figure 6.19: ISO 834-1 / EN 1363-1 fire resistance test - example photo from unexposed side.

$$D_{\text{err}} = \frac{A - A_s}{A_s} \cdot 100\% \tag{6.37}$$

where D_{err} is deviation, A is the area under the actual furnace temperature/time curve and A_s is the area under the standard temperature/time curve.

Cross-Test Repeatability of T_{avg}

The cross-test standard deviation of T_{avg} - calculated at each minute across the six tests-averaged approximately 5.1 °C, with a median of 4.8 °C and a 95th percentile of 9.8 °C. Minimum and maximum instantaneous deviations in this window were 2.6 °C and 12.3 °C respectively. This low spread confirms a high degree of repeatability in the applied thermal load.

Pairwise correlation is used to evaluate statistical measure and to quantify the strength and direction of the linear relationship between two T_{avg} curves. For two variables X and Y, the most widely used measure is the Pearson correlation coefficient, defined as

$$\rho_{X,Y} = \frac{\operatorname{cov}(X,Y)}{\sigma_X \, \sigma_Y}, \tag{6.38}$$

where $\operatorname{cov}(X,Y)$ denotes the covariance between X and Y, while σ_X and σ_Y represent the standard deviations of X and Y, respectively. The coefficient $\rho_{X,Y}$ takes values in the interval $[-1, 1]$, where $+1$ corresponds to a perfect positive linear relationship, -1 indicates a perfect negative linear relationship, and 0 implies the absence of a linear association.

In empirical research, the sample version of the pairwise correlation is used to estimate $\rho_{X,Y}$. Given n paired observations (x_i, y_i), the sample correlation coefficient is defined as:

$$r_{X,Y} = \frac{\sum_{i=1}^{n}(x_i - \bar{x})(y_i - \bar{y})}{\sqrt{\sum_{i=1}^{n}(x_i - \bar{x})^2 \sum_{i=1}^{n}(y_i - \bar{y})^2}}, \tag{6.39}$$

Figure 6.20: ISO 834-1 / EN 1363-1 fire resistance test - example photo from exposed side.

where $\bar{x}$ and $\bar{y}$ denote the sample means of X and Y. This coefficient provides an interpretable and normalized measure of the degree of linear dependence between the two variables.

Pairwise correlation coefficients for T_{avg} profiles in the 10–30 min window ranged from 0.83 to above 0.93, indicating strong similarity not only in temperature levels but also in heating characteristics and transient behaviour across tests.

The ISO 834-1 model curve is strictly followed by the real time temperature T_{avg}. When compared with standard deviation over time, it has minimal variance at all, as shown on Figure 6.21.

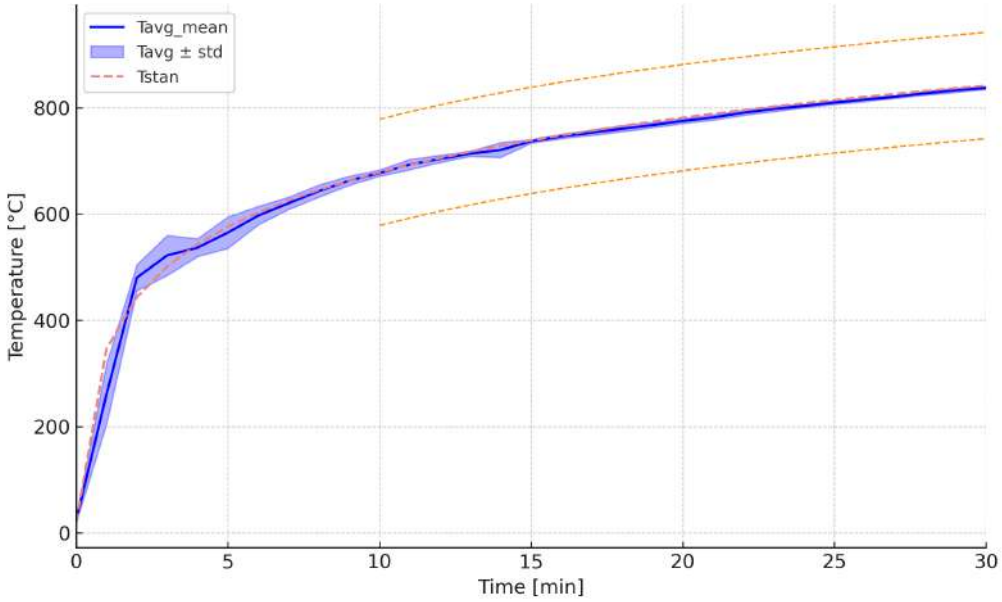

Figure 6.21: ISO 834-1 Standard Time-Temperature Fire Curve - average (blue line) from the dataset with tolerances and standard deviation.

Stability of D_{err} and κ factor

D_{err} remained extremely stable across all tests:

- All six tests had 100% of data points within ± 0.25 and ± 0.5 tolerance bands.
- Mean D_{err} values ranged from -0.00 to $+0.20$.
- Standard deviations were between 0.002 and 0.036.

Despite the initial deviation caused by heating inertia of the furnace, the deviation over time remained within tolerance with very small deviations as shown in Figure 6.22.

The C to C_{crit} ratio consistently remained below the acceptance threshold. Miniscule standard deviation from the tests has shown the precision of the test equipment is retained, especially starting from the 10-th minute of the test.

As per ISO 5725-4 guidelines, when $C \leq C_{\mathrm{crit}}$, the values may be accepted for further research over trueness and bias. As shown on Figure 6.23, C values in time are significantly lower. C_{crit} is changing over time due to the fact, the fire resistance tests concluded at different times (due to DUT failures).

Test Analysis

When considering the entire test duration, the within-test standard deviation of T_{avg} is also small ($\sim$ 3–57 °C), which reflects the natural increase in temperature over time. Global D_{err} statistics show relatively repeating heat distribution, particularly in the initial ramp-up phase. For example, one test recorded only $\sim$ 47% of points within ± 0.25 of mean over the full duration, that may be considered high. However, this discrepancy is reduced entirely when restricting to the 10–30 min window.

The analysis demonstrates that:

1. Cross-test T_{avg} variability in steady-state is low (mean $\sim$ 5 °C), meeting stringent repeatability requirements.

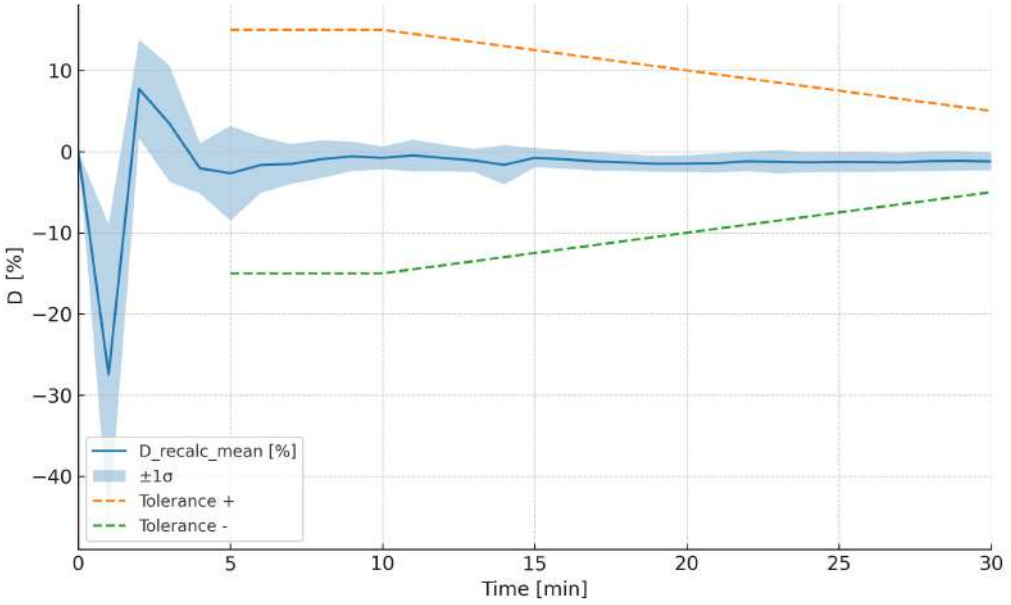

Figure 6.22: ISO 834-1 Standard Deviation of Fire Curve (from Figure 6.21) - T_{avg}, T_{avg} with standard deviation and T_{stan} standard curve.

2. Temperature profile correlations are high (0.83–0.93), supporting consistency in both thermal load and transient response.

3. The C to C_{crit} ratio remains tightly clustered around zero with minimal scatter (mean standard deviation 0.036), showing excellent precision.

4. Initial heating phase differences are the main source of whole-test variability and can be mitigated by protocol alignment.

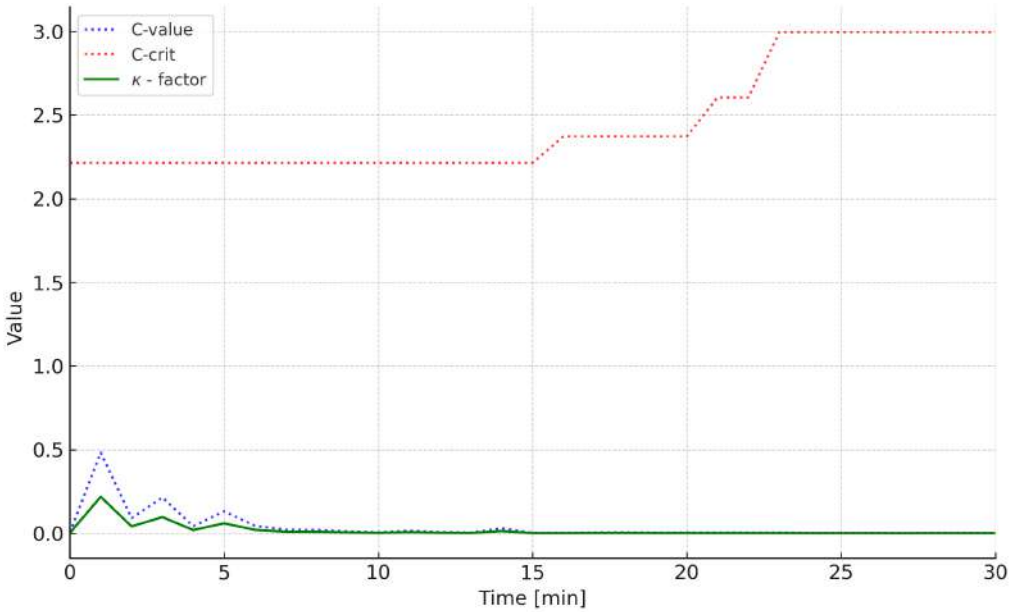

Figure 6.23: κ factor (C to C_{crit} ratio; Y-axis) over time (X-axis) during the fire resistance test.

6.7 Discussion on the EN and ISO Fire Resistance Testing Procedures for Lithium-ion Batteries

Based on the analysis and experimental data above, an integrated methodology for assessing LIB enclosure fire safety is proposed that comprises both thermal resistance testing and pressure/venting testing. This methodology is intended to provide a comprehensive evaluation of a battery enclosure's performance in fire scenarios, covering the spectrum of conditions from an external fire exposure to an internal cell failure explosion. It combines the strengths of existing standards (from building/railway and battery domains) and could serve as the basis for future regulatory procedures. The methodology can be divided into theoretical criteria: Fire Resistance (Thermal), Pressure/Venting and practical test setup as follows. This division integrates crucial hazards appearing in operation of LIBs.

6.7.1 Theoretical Foundations and Performance Criteria

Fire resistance (thermal) criteria can be adopted from the classical criteria E (Integrity) and I (Insulation) of EN 1363-1 for a specified time period relevant to vehicle safety goals. A requirement shall be set that the battery enclosure maintain either E5, E10, E15 or E30 and additionally EI10 to 30 when exposed to an external fire (insulation or radiation shall not function without integrity fulfilled, see Section 6.6.1 for detailed explanation). The exact durations can be debated - they should align with evacuation needs (e.g., passengers out of a car within 5 minutes, or first responder arrival by 10 minutes). Given that current R100.03 is ∼2 minutes and has minimal insulation requirement, aiming higher (e.g., EI10 or more) builds extra safety.

The insulation criterion (I) specifically could be related to preventing internal cell TR. This is to ensure the interior (battery side) of the enclosure does not exceed e.g., 120 °C or predefined temperature of T_2 of HTR (see Section 2.2) for at least 5 minutes (EV specific; for stationary ESS and trains the evacuation times shall be regarded as per route design). This is a functional way to combine safety: essentially require that an external fire cannot drive the battery into TR for a certain time. If that is met, likely the integrity is also maintained.

For internal fire scenarios (battery burning inside-out), the same criteria E and I can be applied in reverse: the enclosure should contain the flames for given amount of minutes (E from inside; 5 min for EV) and not overheat the outside beyond safe limits, so that if people are nearby or if the battery is under a vehicle, it does not ignite adjacent materials quickly.

For pressure/venting criteria, Pressure Relief (P) criterion was introduced. For example:

> "P criterion: The enclosure shall not rupture when subjected to an internal deflagration pressure up to P_{max}, and if equipped with a vent, it shall successfully relieve pressure at or below P_{set} without fragmenting or dislocating itself and elements of the sample."

P_{max} could be defined as the worst-case expected pressure from a full battery failure. Assuming that the maximum pressure value in a sealed EV pack during TR determined during experimental or numerical tests is 1.5 bar, the value of P_{max} should be 2 bar (to include safety margin). It was determined under estimation that the packs vary largely in design. Alternatively, it is required to perform a static test at double the normal vent opening pressure P_{set}. The success criteria in a test would be: no panels detachment, no dangerous fragmentation, and the vent area successfully opens. A fragment impact criterion may also be considered - for instance, if cells explode inside, pieces should not penetrate the enclosure walls (this is analogous to a ballistic integrity test).

Lastly, a thermal flux criterion could be indirectly included. Radiation "W" shall be measured when the battery box is right below passenger cabin. Even without direct flame, the radiated heat should not ignite upholstery above. For a battery pack under a passenger car, radiation requirement may be disregarded.

6.7.2 Experimental Setup and Instrumentation

Testing approach for battery systems shall include two-way verification, depending on where fire originates:

- **Fire from inside to outside ($i \rightarrow o$):** this is when the fire starts inside the enclosure, propagating from the lithium-ion cells throughout whole enclosure. It is expected the enclosure maintain fire resistance (integrity - E) for given duration. Additional parameters such as insulation and radiation are optional. Test set-ups were presented in Figures 6.17 and 6.18.
- **Fire from outside to inside ($o \rightarrow i$):** occurring during the fire from outside source affects the battery pack heating it from outside. Testing set-up is presented in Figure 6.24.

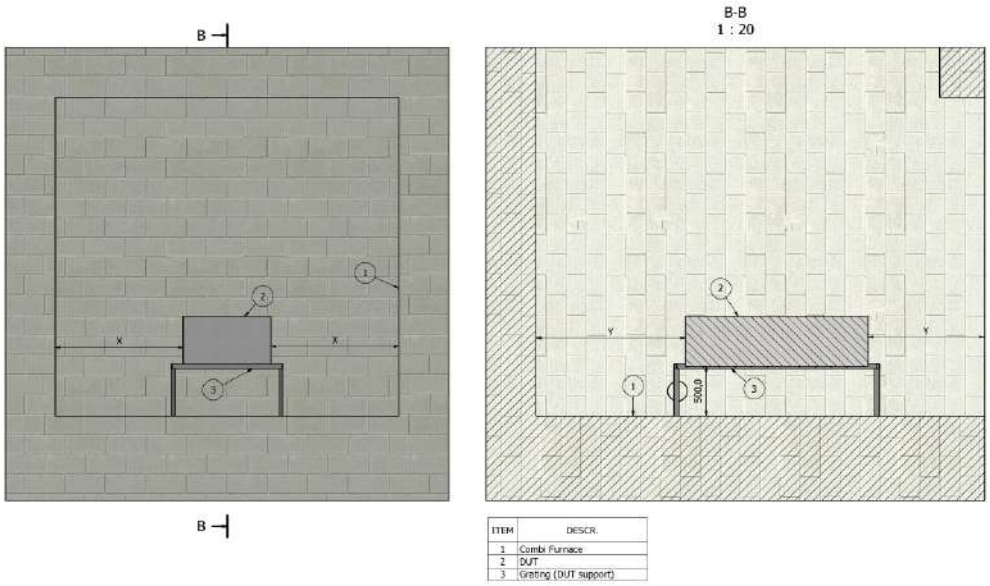

Figure 6.24: Fire inside test model representation.

With fire from inside, the battery enclosure (or its representative section) is mounted in a furnace opening or frame. If the full pack is too large for available furnaces, one strategy is to test the most vulnerable part (for instance, a wall section with a vent or a window, or a corner with a joint). Due to individual design, representative sample shall be selected by the laboratory and/or certification body. The enclosure should be in its normal orientation (if the fire exposure is assumed to come from below, then test with fire on bottom side, etc.). Thermocouples (Type K, mineral insulated as per EN 1363-1 for unexposed surface) would be attached to the face opposite the fire to record temperature rise. The furnace is run according to the time-temperature curve for the duration of interest or until failure. During the test, observers (or cameras) note any through-openings or flaming. Cotton pads can be applied if needed to check for hot gas escape igniting them (standard integrity test). The test is documented in terms of time to integrity loss (if it occurs) and temperature rise. An example of successful E20 / EI15 ($i \rightarrow o$) test is as follows: No integrity failure up to 20 minutes; at 20 minutes average unexposed side temperature rise of 140 °C, peak 180 °C (passes insulation criteria for 15 minutes).

Fire from outside is a set-up where a battery enclosure would be put inside the furnace on the grating stand, at least 500 mm above the floor (mimicking the R100.03 requirement) and engulfed by fire. Battery shall be subjected to EN 1363-1 [345] standard time-temperature fire curve or optionally, when regarding the exposure from petrol fire hydrocarbon curve from EN 1363-2 [369]. Dummy fill may be used inside the enclosure instead of LIBs to minimise the

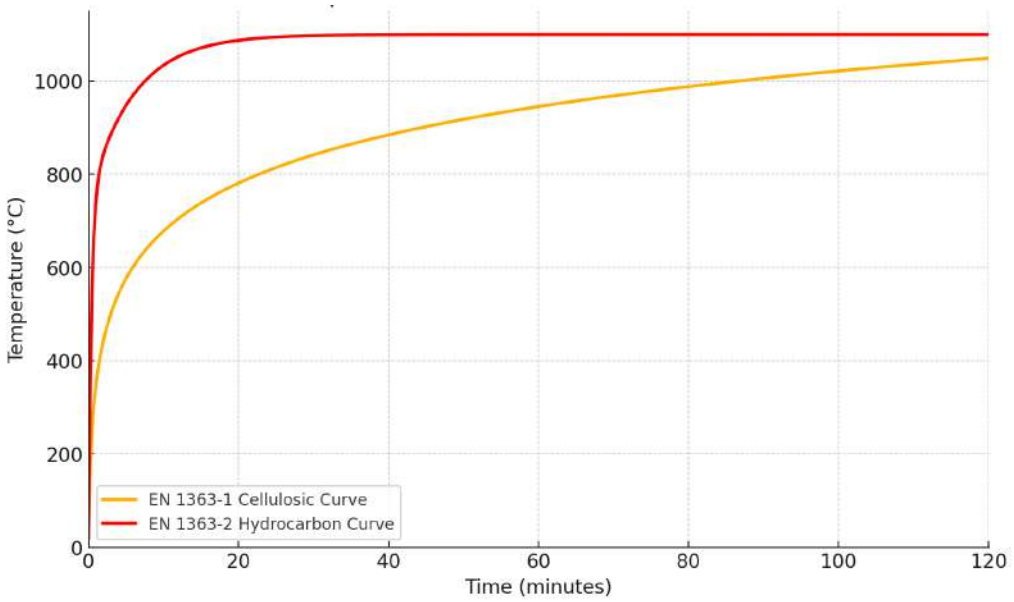

Figure 6.25: Fire resistance test - fire from outside - example of a test set-up.

environmental impact of the test as well as economic threshold. Dummy fill should have similar heat capacity of the cells to be used (as per manufacturer declaration).

This poses significant challenge, due to the fact the geometry of the cell as well as chemistry impact significantly the heat capacity [370], as summarised in Figure 6.26. It is suggested to use low-cost, moldable and reusable materials, such as steel reinforced concrete or ceramic bricks with steel or other metal profiles inside. This is to replicate differences in thermal conductivity of the various geometry cells, that are substantial due to layers wrapping. Through cell conductivity is largely impaired.

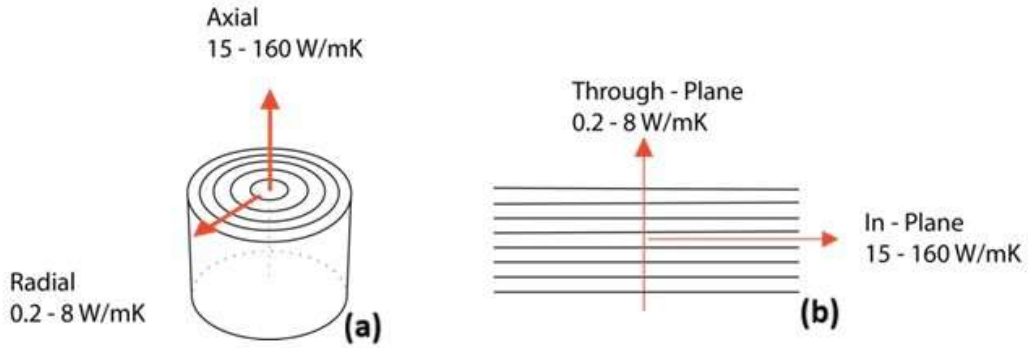

Figure 6.26: Thermal conductivity of cells depending on geometry - (a) cylindrical and (b) prismatic/pouch cell.

Temperature inside the battery shall be monitored by the type K thermocouples located on the dummy fill (outside and inside, on both material types - ceramic elements and metallic parts). It is important to set threshold temperature (with safety margin e.g., 80% of TR initiating temperature) of cell previously tested against TR in tests such as IEC 62619 or SAE J2464 [304, 279]. These temperature are usually within 80–120 °C (see Chapter 2 for in-depth analysis). When set threshold temperature is surpassed after given time of exposure, the test is deemed as failed.

For the pressure test, an identical enclosure shall be mounted it in a safe area (blast cage or open field). If the enclosure has a designated vent area, instrument that with high-speed video

or sensors to detect when it opens. Place pressure transducers inside the enclosure and outside for reference. A pressure test would involve a small propane burner inside the closed enclosure to fill it with a propane/air mix (or even battery off-gas collected from prior tests), then ignite via an electric match. Modern explosion test standards (like NFPA 68) often do something similar to certify vent panels. Alternatively, a compressed air blast could be used. The pressure trace is recorded. The outcome should be that the maximal pressure is below the rupture strength of the container and that if a vent is present, it opens and limits the pressure to a safe level (usually vents are designed so that P_{red} - the reduced pressure after venting - is under a certain value the structure can withstand). Additionally, after the test, the enclosure should remain in one piece, and the vent opening ideally is the only major opening created.

6.8 Recommendations for Regulatory Revisions and Standards Development

Given the insights from the methodology described in previous chapter, the following recommendations are put forth to update and improve battery fire safety regulations. The recommendations are created based on the PhD candidate and fire testing expert knowledge gained in process of performing tests in Laboratorium Badań Ogniowych in Centrum Techniki Okrętowej S.A., as well as making research in doctoral project.

Furnace-based fire resistance testing shall be introduced as an option or requirement. Regulatory bodies (such as the UNECE WP.29 working group for EV safety, or national bodies writing EV standards) should consider incorporating a fire resistance test based on EN 1363-1 standard heating conditions. This could initially be an alternative compliance path to the existing pool fire test. Created compliance path is a state-of-art document, aiming to provide appropriate safety level to battery systems across the industries, which is currently lacking in legislature and standardisation. For example, for a fire outside, a regulation could state:

> "The RESS shall be subject to either (a) the fuel fire test as per current procedure or (b) a fire resistance furnace test of X minutes following time-temperature curve as per EN 1363-1 and EN 1363-2 (standard or hydrocarbon curve), with no explosion occurring during the test or surpassing temperature rise inside the DUT over cell TR threshold temperature."

For the fire inside:

> "The RESS shall be subject to a fire resistance furnace test of X minutes following standard temperature curve as per EN 1363-1, with passing integrity criteria for given amount of minutes."

Providing this option would encourage manufacturers to design for and demonstrate performance in the more controlled test. Over time, if proven superior, the furnace test might replace the pool fire test. The data in this thesis supports that a furnace test of even 10 minutes at high temperature is more demanding and reliable than a 2-minute pool fire. The regulators can be assured that passing the former implies at least equal (if not better) safety than the latter.

Pressure relief or containment capabilities shall be required as well. Regulations should explicitly address the internal explosion/pressure aspect. It is recommended adding a clause such as:

> "The RESS enclosure shall incorporate pressure relief provisions or sufficient mechanical strength to withstand the maximum pressure from gas venting during TR or provide evidence the pressure relief systems mitigate pressure rises."

As a starting point, regulators could adapt from stationary ESS standards: NFPA 855 already essentially mandates that large battery enclosures either prevent ignitable concentrations or be equipped with deflagration venting sized per NFPA 68. Two solutions of an EV battery design could be be taken into consideration. In the first, the battery cells will not all fail at once (prevention of worst-case). In the second, the battery casing construction will contain venting elements that remove gases safely. A concrete regulation might say:

> "If the RESS is not open to atmosphere, it shall include a venting device that operates before the internal pressure exceeds 20 kPa (for example) above atmospheric, or the enclosure shall withstand at least 150 kPa without rupture."

The numbers can be debated, but the concept forces manufacturers to think about gas management.

No external flame emissions (integrity E), external surface temperature must remain below Y °C (to protect occupants or to avoid igniting adjacent materials), and no rupture of enclosure (containment). These would make the outcomes less ambiguous. In a furnace test, these are naturally checked (appearance of the flames, temperature rise). Regulators can specify acceptable temperature rise on surfaces - for inside-out test a standard 180 °C shall be accepted, however, outside-in test should be specific to TR temperature i.e., when it starts depending on the cell chemistry. Due to measurements being taken and obtaining time-temperature graph of the temperature inside is possible, an enclosure can be approved for the use of specific cell chemistry. Pass/Fail Criteria with fire protection principles shall be aligned. Rather than the current binary criteria (no explosion), criteria should incorporate quantitative limits.

Dedicated test standard for battery enclosures may be developed. A likely path is that organizations like ISO or IEC will develop a specific standard that covers both the thermal and pressure aspects, which can be titled "Fire Resistance and Containment Test for EV Battery Enclosures". It is recommended that standard bodies draw from EN 1363-1 together with existing BESS testing standards (e.g., UNECE R100.03, NFPA 855, UL 9540) to cover both domains. The standard can be divided into parts for the appropriate characteristic i.e.,: Part 1: fire test (EN 1364 adapted to battery box size and including internal temperature measurement) and Part 2: pressure vent test. It was noted that researchers in Korea (KATRI) [362] have already prototyped apparatus with gas burners to replace pool fires. This is a step in control, but still indicated allowable tolerance 800–1100 °C which is quite wide and the testing rig is case specific. A industry grounded EN 1363-1 and ISO 834-1 approved furnace would be far tighter controlled (usually ±100 °C tolerance in fire tests) and the infrastructure is already in place.

In the next step, if evidence continues to show the furnace method is superior, regulators could phase out the pool fire test except perhaps for cases where validating a specific scenario is needed. The pool fire test could be reserved for confirming that, the vent of a battery opens appropriately in a real fire (since a furnace test might not cause the vent to open if internal does not heat enough). Future EV regulations requiring:

> "Battery system must have a fire resistance rating of at least Exx/EIyy (i $\longleftrightarrow$ o) per ISO xyz (battery enclosure fire test), and must demonstrate no explosion when cells are induced into TR (thermal propagation test or fire outside test)."

where "xx" is integrity time and "yy" is insulation time, and "xyz" is the standard reference number.

Additionally, as the industry progresses, the direct application section (i.e. describing for what test results can be applied to, meaning approving multiple cell chemistry based on single test, changes in materials used for enclosure etc.) can be developed. Shared knowledge and testing would accelerate industry forward, while keeping the competitiveness between manufactures.

Before enshrining these changes, research should be done to correlate the results of furnace tests with real-world outcomes. One could run side-by-side tests: one vehicle with a fire-rated

enclosure vs one with a standard enclosure in a burn to see the difference. If dramatically better (which it is expected - likely the fire-rated one prevents any TR in the given time), that data would convincingly support regulation change. Academia and industry should work on such demonstration projects. This thesis contributes by outlining the concept and initial justification. Further validation will make the case ironclad.

In conclusion, by adopting an alternative fire resistance testing procedure that uses controlled furnace exposures for thermal evaluation and supplemental pressure/venting tests for internal explosion evaluation, the safety assessment of LIB systems can be significantly improved. This approach provides repeatable, rigorous metrics (like fire resistance ratings and pressure tolerances) rather than the variable and qualitative outcomes of current open flame tests. It supports regulatory innovation by bringing battery testing in line with well-established fire safety engineering practices. It is recommended the standards organizations and regulatory bodies take up this methodology, refine it, and incorporate it into the next generation of EV safety standards. The result will be a higher level of confidence in battery fire safety, safer products for the public, and a more scientifically grounded framework for engineers to design against one of the most challenging failure modes of modern electrified transportation.

Chapter 7

Development of Thermal Runaway Emissions Aftertreatment System of Lithium-ion Batteries

The Thermal Runaway Emissions Aftertreatment System (TREAS) project was conceived as a response to emerging environmental and safety regulations that increasingly restrict the uncontrolled release of gaseous emissions generated during TR events in LIBs. These events, known for their highly exothermic and toxic character, often result in the release of substantial quantities of flammable gases, metal particulates, and volatile organic compounds. In typical laboratory environments, TR testing is conducted in open or semi-ventilated conditions, where emissions are not adequately captured or treated. This regulatory and ecological gap necessitated the development of a specialized laboratory-grade after-treatment system-TREAS-capable of mitigating the impact of emissions released during TR testing procedures on LIB cells and modules. TREAS project outcomes have been implemented into Centrum Techniki Okrętowej S.A. laboratory testing rig systems to provide cleaner air, while performing LIB testing.

TREAS was developed during the course of the "Doktorat Wdrożeniowy" as an interdisciplinary extension of the core research on degradation and safety of RESS. It serves two complementary functions. First, it enables the controlled capture and treatment of gas-phase and particulate emissions under laboratory conditions. Second function is to enhance the accuracy and reproducibility of TR experiments by minimizing the influence of external environmental variability (e.g., airflow, pressure gradients, and contamination). The system incorporates a modular set of filtration, scrubbing, and neutralization units designed to handle a range of emission profiles associated with different cathode chemistries and states of charge. In doing so, TREAS contributes not only to improving laboratory safety and environmental compliance, but also provides a standardized platform for emissions quantification - critical for informing risk assessment, regulatory policy, and future design of thermal mitigation technologies in electric vehicles and stationary storage systems.

Background on the TR emissions of LIBs and cleaning methods of the gas emissions relevant to this method was presented in Appendix D.

7.1 Development and test results of TREAS

TREAS was developed in stages with the optimisation of the air flow with the use of 3D modelling (Siemens NX), CFD computations (SOLIDWORKS Flow Simulation) and measurements on prototype and testing of TR NCM cells in various configurations. The overall size of the installation was 4 m high and 0.3 mm wide bag filter chamber with supplementary accessories (silo with hopper and hood with pipes). Next sections present subsequent steps in TREAS development process.

Figure 7.1: TREAS prototype testing site. P1, P2 and P3 probing points of the air flow. T1, T2, T3 temperature measurement points.

The prototype is shown in Figure 7.1. The photograph shows the bag filter chamber in the middle, exhaust fan to the left and the hood with connecting pipes to the right. The air flow probing points were located at hood outlet - P1, bag filter inlet - P2, exhaust fan outlet - P3. Temperature measurement points were positioned on top of the burned cell - T1, bag filter inlet - T2, bag filter outlet - T3. P1 serves as a referral how much fumes are drawn from the burning cell, P2 shows the flow before the bag filtration and P3 after bag. While T1 shows the cell burning temperature (fumes), T2 indicated the temperature of air before the bag filtration and T3 after. This set of probing location delivers information about the losses of the system and capability of processing cell fumes, as well as overall temperature gradient in the system, mainly due to filtration bags being incapable of withstanding high temperatures (~60 °C).

7.1.1 Air Flow Simulations and Measurements of the TREAS

The air flow in TREAS was simulated with SOLIDWORKS Flow Simulation CFD software. TREAS 3D models were tested with various connectors (at 90° and 45° inlet and outlet angles) at 50°C and 300°C. Two products of the bag filters were tested with one being able to withstand 80 °C and other 350 °C, safety margins were added. The fan performance was 1500 m^3/h. which corresponded to the real fan output. The model presumed the bottom outlet for the sorbent waste was closed for the sake of simulation simplicity. The overall pressure drops were respectively 300.9 Pa and 171.4 Pa (from model) for 50 and 300°C. The final model was shown in Figure 7.2. The analysis has shown the air flow before the filter bag were at about 13 m/s, which were deemed optimal for the filtration purposes.

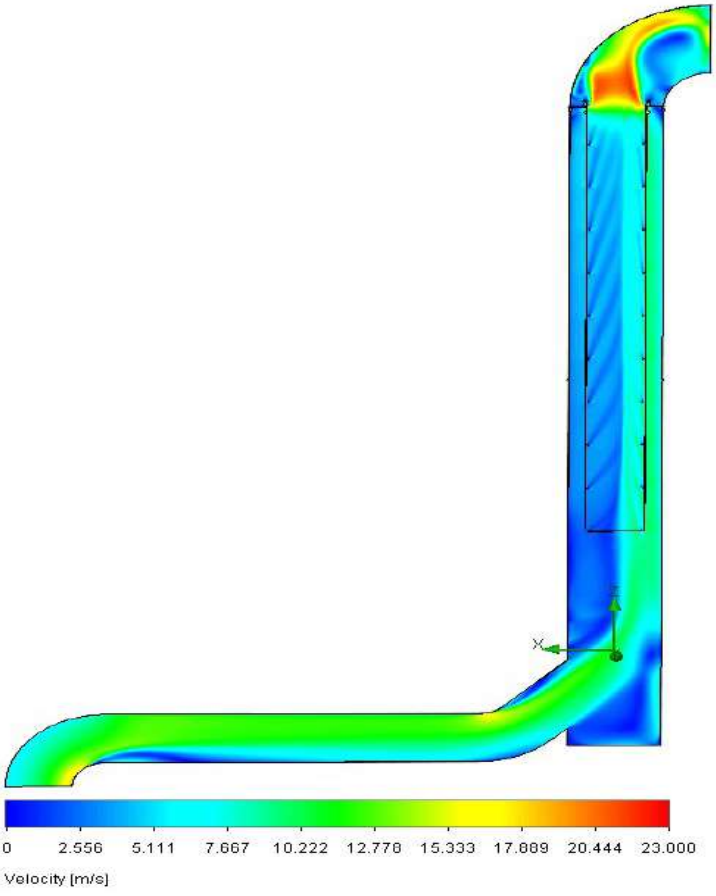

Figure 7.2: TREAS final model simulation at 50°C and 1500 m^3/h.

The measurement of the air flow was made on the TREAS prototype with the use of TESTO 480 anemometer and 0635 hot-wire probe. The probing was made in three locations shown in Figure 7.1. Two fan presets were tested at 80% and 90% for 30 min each:

The results of the flow measurement are shown in Figure 7.3. The wind speed at the extraction hood inlet (P3) and before the filter (P2) is respectively 5 and 2-times lower than the simulated. It was found this is caused attributable to air leakages of the dosing system and waste removal. Simultaneously, the air flow was deemed sufficient to provide the transport and mixing of the dry sorbent, allow for periodical waste removal (jet-pulse), as well as limit the temperature of the TR gases, which may cause the filter to disintegrate. The wind speed at the fan exhaust was found similar to the simulated results.

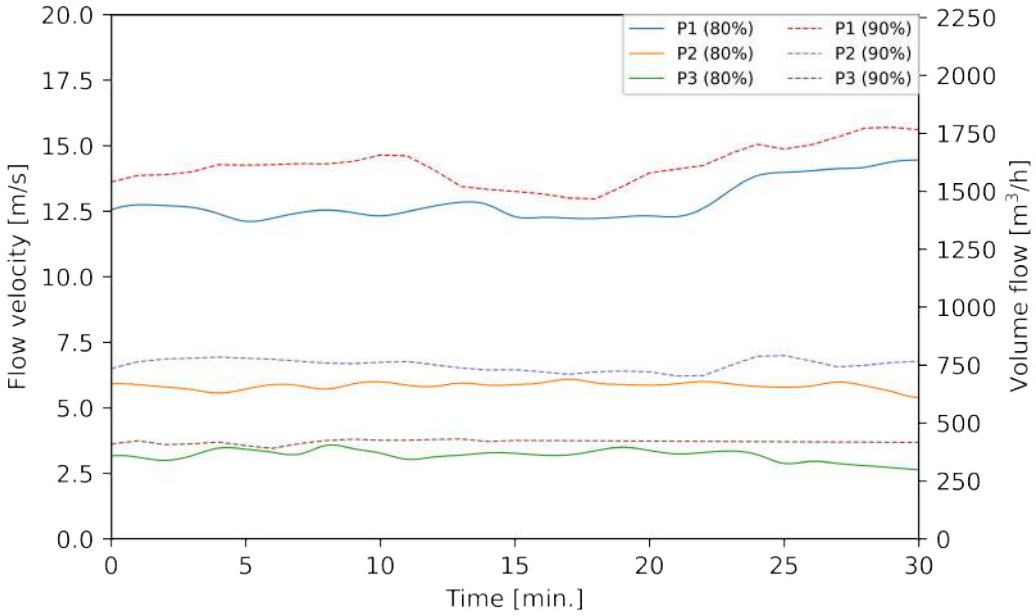

Figure 7.3: Flow measurements of the TREAS prototype at an ambient temperature and two fan performances. P1, P2 and P3 probing points of the air flow, see Figure 7.1.

7.1.2 Thermal Runaway Tests

A series of tests were prepared to test the prototype performance in terms of gaseous composition (carbon dioxide, hydrogen and hydrogen fluoride) and temperature distribution inside TREAS. For the gas analysis a IR carbon dioxide sensor (resolution 0-100% v/v) and electrochemical sensors for hydrogen (resolution 0-40000 ppm v/v) and hydrogen fluoride (resolution 0-10 ppm v/v) were used. Configurations are shown in Table 7.1. Each of the test set-ups were tested two times using NCM pouch battery cell (3.7 V, 60Ah, 220 Wh, 300x180x12 mm, 1120 g).

The mean emission values were collected in Table 7.2. For the first and last set-up with one pouch battery cell, the carbon dioxide values are consistent, together with hydrogen. In second set-up, the amount of carbon dioxide is doubled corresponding to the two pouch cells being burned. Hydrogen concentrations were at the level of 1.0-1.2% v/v, thus not exceeding lower flammability limit (4% v/v for H_2). Carbon dioxide peak value was 4.5% and for the hydrogen was approximately 1.1% ppm.

No hydrogen fluoride was recorded for all of the processes. This may be caused due to dilution with high air volume flow (160 l/s). The sole efficiency of dry sorbent injection (without dilution) could not be measured due to excessive temperature of the TR gases exceeding sensor limits (50°C). Based on theoretical production of the HF of 193.6 mg/Wh [34] and and for

Table 7.1: Testing configurations of number of cells, fan and jet pulse preset and dosage.

Test No	Cell No	Fan Preset, %	Sorbent Dosage, g/s	Pulse jet preset
1	1	80	1.8	2 s air jet pulse with 45 s break
2	2	90	1.8	2 s air jet pulse with 45 s break
3	1	80	0	Off

Table 7.2: Mean values of the emitted gases.

		CO_2, g	**H_2, g**	**HF, g**
Set-up 1	*Average*	215.2	3.0	<0.1
	Std.Dev.	3.0	0.0	—
Set-up 2	*Average*	543.8	5.4	<0.1
	Std.Dev.	90.9	1.3	—
Set-up 3	*Average*	212.7	2.1	<0.1
	Std.Dev.	4.7	0.1	—

the CO_2 of 36.6% [371], the calculated performance of dry sorbent injection and dilution is respectively 99% and 89%.

Table 7.3: Maximum temperature rises recorded in testing set-up 1-3 for thermocouple T1-3.

	T1, $°C$	**T2, $°C$**	**T3, $°C$**
Set-up 1 - Tmax	545.3	158.3	100.4
Set-up 2 - Tmax	765.3	186.2	111.3
Set-up 3 - Tmax	756.4	220.7	135.1

Temperature measurement points were positioned above the cell (T1), before the filter (T2) and behind the filter (T3), see Figure 7.1. The maximum values recorded in each testing set-up were shown in Table 7.3. The temperature recorded before the filter (158.3-220.7$°C$) exceeded the maximum temperature allowable for the bag filter (120$°C$). Due to high temperature, bag filter after each testing series was replaced. Despite high volume flow (approx. 1600 m^3/h) and supply of the ambient air, the TR gas temperature was still relatively high after the filtration (T3).

During TR, a plethora of toxic gases is produced, posing significant danger in confined space fire scenarios. LIB fire requires to be doused through cooling means, due to its self-sustaining burning processes. The risk of such fire is minimised with the mandatory testing, that often include causing TR on purpose. This, however, again is bound to produce vast amounts of toxic substances, which should be filtered or purified.

Based on the foregoing results, the following conclusions were drawn.

1. Dry sorbent injection based on calcium hydroxide dosage of 1.8 g/s and volume flow of approx. 1600 m^3/h may be used for filtration of the TR gas emissions with estimated performance of 99% for hydrogen fluoride and 89% for carbon dioxide.

2. Wind speeds of 5-7.5 m/s are sufficient to provide dry sorbent transfer and filtration of the emitted gases. Large leakage losses are caused due to sorbent hopper and waste funnel.

3. The average production per Wh for CO_2 and H_2 were 1060.3 mg and 11.8 mg respectively. The peak recorded values were 4.5% (CO_2) and 11000 ppm (H_2).

4. Pouch NMC cell of 220 Wh production of hydrogen did not exceed a lower flammability limit of 40000 ppm v/v.

5. Temperature of the TR gases with the flow level of approx. 1600 m^3/h were at minimum 100.4°C. The temperature of the gas above the burning cells were at maximum 765.3°C.

Chapter 8

Summary and Conclusions of the Thesis

8.1 Summary of Findings and Contributions

This research set out to tackle a pressing challenge in battery engineering: how to more reliably test and ensure the fire safety of LIB systems used in alternative energy sources. A comprehensive investigation was conducted, spanning fundamental analyses, experimental trials, and methodological innovations.

The key findings and contributions of this work can be summarised as follows:

- Current fire testing procedures are presented and critically analysed to be imprecise and inconsistent. Through a critical review and experimental replication of the UNECE R100.03 external fire test, the thesis conclusively demonstrated that the existing regulatory approach suffers from poor precision and limited repeatability. Multiple open-flame fire tests (simulating the R100.03 pool fire scenario) were performed on battery enclosures. The results revealed significant variability in thermal exposure and outcome, even under nominally identical conditions. Factors such as slight changes in wind or short preheating phase led to large fluctuations in measured temperatures and burn characteristics. It was found that the R100.03 test produces a stochastic environment with outcomes that are difficult to reproduce quantitatively. The repeatability standard deviation for critical temperature metrics in the pool-fire tests was high, and between-test variability was unacceptably large. It was confirmed that the current method lacks the metrological reliability. This is a scientifically significant result, as previously, no published data existed on the repeatability of the R100.03 fire test. In short, one major contribution of this work is identifying and quantifying the limitations of the prevalent battery fire test.

- It was developed and validated a new fire-resistance testing methodology for EV battery enclosures, based on controlled furnace exposure (ISO 834-1, EN 1363-1 and EN 1363-2), which proved to improve repeatability and data quality. The innovation of the research was to transplant the concept of a standard time-temperature furnace test into the field of batteries.The work addressed the core hypothesis that such an approach would yield more reliable and informative results than the traditional pool-fire test. The repeatability and precision of the furnace method were quantitatively confirmed. The analysis showed extremely low standard deviation among tests, meeting stringent criteria per ISO 5725 series for repeatability. It was demonstrated, by controlling the fire exposure through a furnace, one can obtain stable and reproducible conditions suitable for comparative analysis and material evaluation. In practical terms, this means that safety performance of different battery enclosure designs can be fairly compared using this method, and subtle improvements (e.g., use of better insulation or intumescent coatings) can be reliably detected in the temperature data - which was not feasible with the coarse pass/fail nature of R100.03 tests.

It was noted that conducting the furnace tests was logistically easier and posed lower risk. There were no uncontrolled flames outside the furnace, and all combustion by-products were contained and treated, aligning with cleaner lab practices. The success of the ISO 834-1 and EN 1363-1 based method as documented in this thesis lays the groundwork for it to be taken up in future standards or research.

- Comparison of the two approaches (pool-fire vs. furnace) yielded critical insights into fire physics and battery safety. By studying both methods side by side, the research uncovered why the pool-fire test is so variable and how the furnace overcomes those issues. It was found that in the open pool-fire, even with measures like a specified pan size and an allowed wind speed range, the flame behaviour around the DUT remains highly unpredictable. Turbulence and the heterogeneous nature of a large gasoline fire lead to uneven heating - some areas of the battery may be shielded by their own smoke or by flame lean, while others get direct flame contact, resulting in temperature non-uniformity. On the other hand, the furnace method created a controlled environment where the only significant variability observed was during the initial ramp (due to furnace thermal inertia), and even that was systematic and could be calibrated out. The thesis therefore contributes not just a method, but also an evolved framework for battery fire testing grounded in rigorous engineering principles.

Overall, the scientific and practical significance of the work can be distilled into a clear message: The work presented in the thesis has advanced the field of battery safety by demonstrating that batteries can be tested in a far more rigorous and meaningful way than we currently do. It challenges the status quo of regulatory testing (identifying its flaws through data) and offers a concrete, validated alternative approach. This approach yields a wealth of information (helping scientists understand battery failure better) and has direct practical benefits (helping engineers design safer batteries and enclosures, and regulators set more evidence-based standards). The work bridges a gap between fire science and safety, bringing techniques from one domain (fire resistance testing) to bear on another (battery engineering) in an innovative manner.

It provides an evidence-based testing methodology for regulatory bodies to acknowledge this issue and seek improvements. The experimental evidence and the following analysis strongly supports formal thesis that *it is possible to develop a quantitatively-grounded methodology to test lithium-ion battery fire safety and mechanical integrity with greater precision, repeatability, and diagnostic value than current regulatory procedures.* Thesis of the work was proven and the aim reached.

8.2 Unique Contributions to Knowledge in Thesis

The unique contributions of Daniel Darnikowski's PhD dissertation made in the course of "Doktorat Wdrożeniowy" are delineated in this section. These contributions are identified in the context of current LIB safety knowledge, recent research, and standard practices.

- **Quantitative evidence of limitations in existing fire tests:** The thesis provides the first public and rigorous statistical demonstration, through series of tests on real life ESS that the prevailing battery fire safety test (UNECE Regulation No. 100 Revision 3, external gasoline pool-fire) suffers from poor repeatability and precision. Through repeated full-scale trials under nominally identical R100.03 conditions, it was shown that small uncontrolled factors (wind, fuel distribution, etc.) cause large variability in heat exposure and outcomes. By bridging this knowledge gap, the work compels regulators to acknowledge that current fire-testing protocols for batteries lack the metrological reliability expected in safety-critical standards.

- **Furnace-based fire resistance testing adapted to LIBs:** A central achievement of this dissertation is the adaptation of the time-temperature furnace test to battery testing. The thesis adapted the ISO 834-1, EN 1363-1 standard fire curve as well as EN 1363-2 hydrocarbon curve into the battery safety testing. This methodological innovation replaces the uncontrolled open flame of UNECE R100.03 with a controlled furnace exposure, yielding dramatically improved repeatability and data quality.

- **Improved instrumentation and metrology in fire testing:** The research also made significant enhancements to how battery fire experiments are instrumented and analysed, exceeding current standard practices. In PhD dissertation, a comprehensive sensor and data acquisition setup for fire tests was developed, including thermocouple arrays on and inside the battery enclosure, airflow anemometers, and hygrometers to monitor ambient conditions.

- **Augmenting and proposing standards revisions:** The dissertation proposes concrete modifications to improve standards, essentially extending existing frameworks. Notably, it recommends a two-pronged testing regime to replace the singular R100.03 fire test. In this proposed framework, regulators would require a furnace-based external fire resistance test (as developed in the thesis) and a complementary internal hazard test such as an overpressure venting or internal ignition trial. This dual approach ensures that a battery enclosure is evaluated both for external fire exposure and for its ability to contain or safely relieve an internal thermal runaway - an aspect not addressed by R100.03.

- **Integration with industry practice and standardization networks:** the work exemplifies application-oriented research by actively involving industry stakeholders and standardization bodies in the development of its contributions. The experimental program was conducted in an accredited fire-testing institute (Centrum Techniki Okrętowej S.A.), where a custom test stand was built to implement the new procedures.

- **Development of a Thermal Runaway Emissions Aftertreatment System (TREAS):** The thesis introduces a custom-engineered system designed to capture and neutralize toxic gases and particulates released during LIB fires and/or thermal runaway tests. This is a novel technical solution addressing the emerging requirement that destructive battery tests be safe for personnel and the environment.

- **Bridging fire science and battery engineering:** A noteworthy original element of this thesis is its truly interdisciplinary approach - it bridges the gap between fire safety engineering and battery technology. The research creates a synergistic framework. It allows fire dynamics (flame spread, heat transfer) to be studied in the context of battery layouts and materials, and conversely uses battery failure data to inform fire barrier design. By explicitly "bridging fire science, battery engineering, and standardisation practice", the dissertation provides a model for integrative safety research. This systemic contribution ensures that developments in one field (e.g. improved fire test methods) are directly translated into the language of the other field (battery safety requirements), fostering a more unified approach to LIB safety challenges.

The presented doctoral research is distinguished by its strong practical orientation, conducted not only within the academic framework of the Institute of Fluid Flow Machinery of the Polish Academy of Sciences, but also in the works of the accredited Laboratorium Badań Ogniowych of Centrum Techniki Okrętowej S.A. This dual setting ensured that the work was firmly grounded in both scientific rigour and industrial relevance. Importantly, all experiments were performed on real-life battery modules and systems supplied by multiple manufacturers, which allowed the

methodology to be validated under conditions directly reflecting market applications in electromobility and stationary energy storage. As a result, the thesis not only contributes to fundamental understanding of LIB fire safety, but also delivers implementable testing procedures and technological solutions that can be directly translated into improved safety standards and certification practices worldwide.

8.3 Recommendations and Future Work

While this thesis has made substantial progress in improving LIB fire testing methodology, it also recognizes the limitations of the proposed approach and the need for further research to fully implement and generalize the findings. Several important considerations and future directions emerged from this work:

- Bridging the gap between controlled tests and real-world scenarios: A controlled furnace test, as developed here, focuses mostly on the thermal aspect of an external fire threat. By design, it does not replicate the electrochemical and mechanical abuse that occurs during an actual battery thermal runaway. In a real EV accident, for example, cells may be damaged, leading to internal short circuits, gas venting, and possibly internal ignition - phenomena which a furnace (with an empty or non-energized enclosure) does not reproduce. This is a known limitation: a furnace test can demonstrate that an enclosure resists an external fire (preventing flames from entering), but it does not prove the enclosure can contain an internal fire or explosion. Therefore, one recommendation is that any future standard testing regime should be two-pronged - exactly as proposed in this thesis's integrated methodology. Firstly, include a furnace-based thermal resistance test (outside-in fire exposure) to ensure robust fire barrier performance. Secondly, include a pressure/venting test (or an internal ignition test) to ensure that if a battery does go into runaway, the enclosure can either safely vent the pressure or withstand it without rupturing. Thus, regulatory bodies (UNECE, ISO, etc.) are advised to consider adding a venting or explosion containment test. Some nascent steps are already seen (e.g., UNECE's draft GTR on thermal propagation), and this research bolsters the case for formalizing such tests.

- Generality and scalability of the furnace method: The furnace-based approach was tested on a specific set of battery enclosure samples (six full-scale specimens, each presumably of a certain design/size). While results were excellent in terms of repeatability, additional studies are needed to ensure the method's robustness across different laboratories and battery designs. One limitation noted is that all furnace tests in the study were done in the same facility, under carefully controlled settings. To fully prove that this method is universally repeatable, a round-robin test campaign should be conducted where multiple laboratories perform the same furnace test on identical specimens and compare results. According to ISO 5725 principles, one must assess not only repeatability (same laboratory, same operator) but also reproducibility (different laboratories). The methodology may need minor adaptations (e.g., use of multiple furnace burners for very large samples to maintain uniform heating) - these details should be explored by future researchers.

- Correlation with actual battery behaviour: An important future step is to correlate the results of the furnace test with real battery fire outcomes. In this thesis, the furnace tests often used either empty enclosures or involved heating a pack without inducing internal TR (for safety and repeatability reasons). While this isolated the thermal barrier performance, it does not directly show how a given enclosure would fare with live cells inside. It is recommended that further experiments be conducted where a battery pack with cells is subjected to a controlled external fire (perhaps in a furnace or with well-controlled burners) to see if passing the furnace criteria truly ensures prevention of thermal runaway for the specified

duration. These studies would essentially tie together the thermal test performance and actual safety outcome, providing a complete picture.

- Integration into standards and industry practice: The thesis makes several recommendations for updating standards. It proposes that future regulations could incorporate the furnace-based methodology, possibly inspired by the precedent in railway standards. A short-term recommendation is for standard committees (such as the UNECE working group on electric vehicle safety, or ISO TC22/SC37 on electrified powertrain safety) to initiate technical evaluations of this method. This could start as an informative annex or alternative test in standards - for example, allowing manufacturers to perform a furnace fire test in lieu of the pool-fire test to demonstrate compliance, while data is gathered. Over time, if proven effective, it could become the primary requirement. There may be some industry resistance initially (due to the perceived difficulty or cost of furnace tests), but the thesis argues convincingly that costs could actually be lower - because furnace tests are more controlled, they may reduce the number of repeat tests and they eliminate the need for large quantities of flammable fuel and hazardous site preparations. Outreach and communication of these benefits will be important future work to ensure the research has real impact.

In conclusion, the work presented in this dissertation significantly advances public capability to test and understand LIB fire safety. It delivers a method that enhances precision, repeatability, and insight, addressing a crucial gap in current safety engineering. However, it also highlights that a single method is not a panacea - a combination of tests (thermal and pressure) is needed for holistic safety, and ongoing refinement and validation are required to integrate the method into the fabric of standards globally. The limitations identified (lack of internal pressure simulation in furnace tests, need for inter-lab studies, etc.) are not setbacks but rather clear directives for the next steps the research community and industry should take. By following these recommendations - adopting integrated test criteria, conducting further validation studies, and updating standards - stakeholders can ensure that the rapid growth of battery technologies will be matched by equally advanced safety verification techniques. The ultimate measure of success will be a future where battery fire incidents are rarer and far less severe, thanks in part to the improved testing and design practices informed by research such as this. This thesis has laid the groundwork by showing what is possible, proving the original thesis and aim of the works. As LIBs continue to power our world, ensuring their safety is both a technical and a public trust imperative. The comparative and quantitative approach championed in this dissertation represents a significant stride toward that goal, merging scientific rigour with practical solutions for one of the foremost engineering challenges of our time.

Appendix A

Overview of the Materials used in Lithium-ion Batteries

A.1 Cathode Materials

A.1.1 Lithium Cobalt Oxide (LCO)

Lithium cobalt oxide ($LiCoO_2$, LCO) cathodes constitute one of the most mature and historically dominant chemistries in lithium-ion battery (LIB) technology. At their peak, LCO-based cells accounted for more than 50% of the global LIB cathode market, driven primarily by the proliferation of portable electronic devices such as mobile phones, laptops, and cameras [372]. Although their market share has declined in recent years due to the rise of cobalt-scarce or cobalt-free chemistries like NMC ($LiNi_xMn_yCo_zO_2$) and LFP ($LiFePO_4$) in electric vehicles and stationary storage, LCO remains a key material in niche sectors where high volumetric energy density is paramount. The cathode material is typically synthesized via solid-state reaction between lithium carbonate and cobalt oxide at elevated temperatures (800–1000 °C), producing a highly ordered layered structure that facilitates reversible lithium intercalation. Continued advancements in coating strategies and dopant incorporation aim to suppress surface reactivity and enhance cycling stability [373, 374].

It has the chemical formula $LiCoO_2$, consisting of layers of CoO_2 octahedra with lithium ions occupying the interlayer sites in a layered α-$NaFeO_2$ type structure [375]. LCO was first identified as a high-energy-density cathode by Goodenough and co-workers in 1980 [376], and it became the basis for the first commercial Li-ion cells in the early 1990s. Manufacturing of LCO cathodes typically involves high-temperature solid-state synthesis: for example, mixing lithium carbonate (Li_2CO_3) with cobalt oxides (e.g., Co_3O_4) and calcining in air or oxygen at about 600–800 °C, followed by annealing near 900 °C to obtain the well-crystallized layered phase [375, 377]. This produces LCO powder with the desired $R\bar{3}m$ crystal symmetry. Alternative fabrication methods such as sol.gel processing and co-precipitation are also employed to improve homogeneity and control particle size [377]. In a typical cathode roll manufacturing process, LCO powder (often blended with a carbon conductive additive and binder) is coated onto aluminium foil to serve as the cathode electrode [378]. The result is a reliable cathode material with high volumetric energy density and good compatibility with common liquid electrolytes and graphitic anodes [379].

Compositionally, LCO is cobalt-rich, with cobalt comprising approximately 60% of the cathode's mass. This results in high production costs and significant exposure to geopolitical and ethical concerns, particularly due to cobalt's concentrated supply chain in politically unstable regions [380]. The environmental burden associated with cobalt extraction is substantial, including toxic effluents, habitat degradation, and CO_2 emissions. Although recycling of LCO-based batteries has historically been limited by inefficient separation techniques, recent developments

in hydro-metallurgical recovery processes have increased cobalt and lithium yields while reducing environmental impact [381, 382]. These advances contribute to modest improvements in the sustainability profile of LCO, albeit insufficient to counterbalance its ecological liabilities in large-scale applications. Nonetheless, LCO cells exhibit excellent calendar life under moderate cycling regimes, maintaining structural integrity and performance in low-drain environments. The market price of Lithium Cobalt Oxide (LCO) cathode active material currently stands at approximately $16.70 per kilogram [383] (as of 05.07.2025).

Electrochemically, LCO features a theoretical specific capacity of 274 $\text{mAh} \cdot \text{g}^{-1}$ [376], though practical capacities are capped at approximately 140–160 $\text{mAh} \cdot \text{g}^{-1}$ due to structural degradation risks at deep states of charge [384]. The voltage window of 3.0–4.2 V versus Li/Li_+ provides high energy density but simultaneously accelerates electrolyte decomposition and transition metal dissolution at elevated potentials. Delithiation beyond 4.2 V induces irreversible changes in the layered lattice, promoting oxygen evolution and phase collapse. Thermal stability is another limiting factor: LCO begins to exhibit exothermic reactions and oxygen release above approximately 180 °C, initiating self-heating and raising the risk of TR in abusive conditions. Therefore, tight thermal and electrochemical control strategies are imperative for LCO-containing systems, particularly when employed in multi-cell configurations [385].

From a safety perspective, LCO is inherently less stable than other cathode chemistries such as lithium iron phosphate (LFP) or lithium manganese oxide (LMO). Its relatively low onset temperature for thermal decomposition, combined with high oxygen release potential, increases the likelihood of exothermic reactions with flammable organic electrolytes [386]. Safety incidents involving LCO-based batteries have underscored the need for robust protective mechanisms, including pressure-relief valves, thermal fuses, and advanced BMS. Experimental studies have shown that TR can be initiated at temperatures as low as 180–200 °C, necessitating stringent controls to prevent overcharging and overheating [387]. Consequently, while LCO remains competitive in markets where volumetric energy density is critical, its declining market share in broader sectors reflects both economic and safety-driven transitions toward alternative chemistries. Compared to other cathode chemistries, such as $LiFePO_4$, which is thermally stable up to 250 °C, LCO is more prone to fire and explosive reactions [388]. Abuse conditions such as overcharging, crushing, or external fire can lead to internal short-circuiting, venting of flammable gases, and ignition. Nail penetration and impact tests on LCO cells often result in gas release and ignition if cells are at high state-of-charge. The vented gases are hazardous and include Co-containing particulates [389]. Safety mitigation measures include thermal shutdown separators, current interrupt devices, venting mechanisms, and battery management systems that limit charging and temperature. Material-level safety improvements include particle coatings (e.g., $AlPO_4$, ZrO_2) and doping to suppress oxygen release [390]. While no battery is immune to failure under extreme abuse, modern LCO batteries incorporate multilayer safety strategies that have proven effective in consumer electronics, where billions of units operate with few incidents [388].

A.1.2 Lithium Nickel Oxide (LNO)

Lithium nickel oxide ($LiNiO_2$, LNO) cathodes are of notable interest due to their high theoretical specific capacity of approximately 274 $\text{mAh} \cdot \text{g}^{-1}$, attributed to the full oxidation of Ni_{3+} to Ni_{4+} during delithiation processes [391]. LNO cathodes are typically synthesized via solid-state reaction or co-precipitation methods, followed by high-temperature calcination to ensure phase purity and cation ordering [392]. Their composition primarily includes lithium and nickel, often doped or surface-modified with other metals (e.g., Co, Al, Mg) to enhance electrochemical stability [393]. Although nickel is more abundant than cobalt, its use in high-energy battery cathodes contributes to moderate material costs and limited scalability due to purification demands. In terms of recyclability, LNO materials can be recovered via hydrometallurgical and pyrometallurgical processes, though nickel recovery remains less economically viable than lithium [394]. The current market price for high.purity $LiNiO_2$ (LNO) cathode active material is approximately $16

per kilogram [395]. Environmental implications are significant: nickel extraction and processing are energy-intensive and generate notable CO_2 emissions and aqueous effluents [396]. LNO's market penetration remains limited compared to NMC ($LiNi_xMn_yCo_zO_2$) chemistries due to inferior cycle life and instability under commercial conditions, yet its high capacity renders it attractive for niche applications. Thermally, LNO exhibits moderate stability but undergoes oxygen release above 200–250 °C, which contributes to TR risks [397].

Safety concerns are paramount when assessing lithium nickel oxide as a cathode material. LNO demonstrates a high degree of reactivity, particularly under overcharge or thermal abuse conditions, where oxygen evolution from lattice degradation acts as an oxidizer, accelerating exothermic reactions with the electrolyte. This results in increased propensity for TR—a critical limitation in transport and stationary energy storage applications. Structural instability during deep delithiation exacerbates the formation of resistive surface layers and crack propagation within the cathode, further impairing safety [398]. Studies have shown that LNO-based cells exhibit higher heat generation rates and lower onset temperatures for exothermic decomposition compared to other layered oxide cathodes such as NMC and LCO [397, 399]. Moreover, LNO cathodes lack inherent self-healing mechanisms or phase transitions that would mitigate thermal degradation. Consequently, the commercial adoption of LNO is restricted by stringent safety requirements, particularly in contexts involving elevated temperatures or potential mechanical abuse.

A.1.3 Vanadium-based cathodes (VO and LVO)

Vanadium-based cathodes, particularly vanadium oxide (VO) and lithium vanadium oxide (LVO), have been explored extensively for their high theoretical specific capacities and structural versatility. VO cathodes, typically in the form of V_2O_5, offer a theoretical capacity of up to 294 $\text{mAh} \cdot \text{g}^{-1}$ due to their multi-valent vanadium redox states, while LVO can achieve approximately 275 $\text{mAh} \cdot \text{g}^{-1}$ depending on composition and crystallinity. These materials are often synthesized via sol-gel, hydrothermal, or solid-state routes, allowing for tunable morphologies and particle sizes that impact electrochemical performance [400]. Despite their promising capacities, the commercial adoption of VO and LVO cathodes remains limited due to challenges in cycling stability and rate capability, often linked to structural degradation during lithiation/delithiation cycles [401]. From a cost perspective, vanadium compounds are more expensive than conventional lithium iron phosphate (LFP), but they are less costly than cobalt-based materials and exhibit lower geopolitical supply risks [402]. This reflects the recent transaction price of V_2O_5 (more than 99.5% purity) at about $13.85 per kilogram [403]. Vanadium is moderately toxic, and occupational exposure is regulated, though its overall environmental footprint during extraction and processing is less severe than cobalt [404]. Recyclability is an advantage; vanadium oxides can be recovered from spent cathodes through hydrometallurgical processes, supporting a more sustainable battery lifecycle [400]. However, the global market share of vanadium-based cathodes remains marginal compared to dominant technologies like NMC (nickel-manganese-cobalt) or LFP systems.

In terms of safety, VO and LVO cathodes exhibit moderate thermal stability, generally lower than LFP but higher than NMC materials. Vanadium oxides can release oxygen at elevated temperatures, posing risks of TR under abusive conditions [405]. However, their lower energy densities compared to NMC reduce the overall severity of potential safety incidents. Moreover, recent advancements in electrode architecture and electrolyte formulations have improved the thermal response of LVO-based systems, pushing the onset temperature for exothermic reactions to safer thresholds. Toxicological assessments indicate that vanadium exposure primarily affects the respiratory system and kidneys, which necessitates careful handling during manufacturing and end-of-life processing. Nonetheless, with proper engineering controls, the safety risks associated with vanadium-based cathodes are manageable. Emerging research is also exploring surface coatings and dopants to suppress structural collapse and thermal degradation, further enhancing

the safety profile of these materials [87].

A.1.4 Nickel cobalt manganese oxide (NCM)

Nickel cobalt manganese oxide (NCM) cathodes, also called NMC, are a family of layered $LiMO_2$ materials (M = Ni, Co, Mn) that dominate many high-performance lithium-ion batteries. They crystallize in the same layered structure as $LiCoO_2$ (LCO) but with Co partially substituted by Ni and Mn in various ratios. Common compositions include NCM111 (Ni:Co:Mn = 1:1:1), NCM523, NCM622, and Ni-rich NCM811 (80% Ni, 10% Co, 10% Mn) [406, 165]. Increasing the Ni fraction increases capacity and energy density while reducing costly Co content, so newer cathodes have trended from NCM111 toward Ni-rich NCM811 to boost EV range and lower material cost. These oxides are typically manufactured via co-precipitation: mixed Ni–Co–Mn hydroxide or carbonate precursor particles are first precipitated from solution, then calcined with lithium compounds at high temperature to form the lithiated oxide. Careful control of pH, temperature, and agitation yields spherical precursor particles with optimal size, density, and purity, which in turn lead to superior electrochemical performance in the final cathode [407].

NCM cathodes offer high voltages (3.7–3.8 V average) and high capacities, translating to excellent energy density. The theoretical specific capacity of layered $LiNi_xCo_yMn_{1-x-y}O_2$ is on the order of 270–280 $\text{mAh} \cdot \text{g}^{-1}$ [408], though practical cells utilize only about half of this to avoid structural collapse. Still, Ni-rich compositions outperform older $LiCoO_2$: for example, NCM811 can deliver over 20 $\text{mAh} \cdot \text{g}^{-1}$, significantly above LCO's 150 $\text{mAh} \cdot \text{g}^{-1}$ practical limit [399]. Higher Ni content increases initial capacity but tends to degrade faster over time. Ni-rich cathodes suffer from cation disorder, electrolyte oxidation, and particle cracking. These lead to gradual capacity fade and impedance growth. Research has shown that increasing Ni content reduces long-term capacity retention [409]. Mitigation strategies include dopants (e.g., Al, Mg), nanoscale coatings, and single-crystal particle designs [410]. With such measures, modern NCM batteries can achieve hundreds to thousands of cycles with moderate capacity loss, though generally still below the longevity of lithium iron phosphate (LFP) cells.

Cost and resource considerations are key factors in selecting NCM cathodes over alternatives like LCO, LFP, and NCA. Cobalt is the most expensive component in conventional layered oxides, so reducing Co content has been a priority. Moving from NCM111 to NCM811 dramatically lowers cathode cost per kWh [165]. Ni-rich NCM variants and NCA (e.g., $LiNi_{0.8}Co_{0.15}Al_{0.05}O_2$) were developed to maximize energy density with minimal cobalt. As of 2022, NCM-type chemistries (including NCA) accounted for about 60% of global EV battery capacity, while LFP held under 30% [177]. By 2023, LFP's share rose above 40%, reflecting cost advantages despite NCM's superior energy density [411]. The market price of Lithium Nickel Manganese Cobalt Oxide (NMC811) cathode active material currently stands at approximately $22.00 per kilogram [412]. Cobalt sourcing raises ethical and environmental issues, as 60–70% is mined in the Democratic Republic of Congo with notable human rights concerns [380]. Extraction of cobalt and nickel is energy-intensive and emissions-heavy. Though NCM batteries have high recycling value due to Ni and Co, global cobalt recovery rates are only ∼30% [381]. New hydrometallurgical methods exceed 95% metal recovery [413], and the EU has mandated 90% recovery of Ni and Co by 2028, aiming to improve sustainability.

A major drawback of NCM cathodes is limited thermal stability, particularly in Ni-rich variants. Under high temperatures or overcharge, delithiated NCM can undergo exothermic decomposition, releasing oxygen that reacts violently with electrolyte [414]. The onset temperature for TR drops with increasing Ni content—from ∼306 °C for NCM111 to ∼225 °C for NCM811 [25]. This is due to weaker metal–oxygen bonds in Ni-rich oxides. Cycling-induced microcracks in Ni-rich particles expose fresh surfaces to electrolyte, triggering additional heat and gas release. These feedback loops increase fire risk. To address this, manufacturers apply Al/Mg dopants, protective coatings, and battery management systems to suppress reactions [142]. Despite such controls, NCM-based batteries have narrower safety margins than LFP cells, highlighting the

importance of continued innovation to ensure safe, high-energy battery systems.

A.1.5 Aluminum-doped lithium nickel oxide (NCA)

NCA cathodes (typically $LiNi_{0.8}Co_{0.15}Al_{0.05}O_2$) are manufactured primarily through co-precipitation followed by high-temperature calcination, resulting in layered nickel-rich oxides stabilized by aluminum doping [415, 416]. The aluminum doping not only enhances structural integrity but also improves cycling stability. These cathodes have a high theoretical specific capacity of approximately 275–280 $\text{mAh} \cdot \text{g}^{-1}$ [378], translating practically to about 180–200 $\text{mAh} \cdot \text{g}^{-1}$ in commercial cells. NCA materials generally operate up to about 4.3 V versus Li/Li^+, providing superior energy densities ideal for electric vehicles. However, their costs remain elevated due to nickel and cobalt scarcity and extraction challenges [417]. Environmental concerns arise from the toxicity of nickel and cobalt, necessitating careful management and recycling [418, 32]. Fortunately, hydrometallurgical recycling approaches effectively recover valuable metals, although efficiency varies with technology maturity. Long-term cycling performance is robust yet susceptible to capacity fade, driven by microcracking and nickel-induced surface reactions. Globally, NCA cathodes represented approximately 8% of the EV battery cathode market in 2022, behind NMC and LFP chemistries [177, 419]. Despite cost and recyclability challenges, their energy density and Al-induced improvements solidify their market significance. The current market price for Lithium Nickel Cobalt Aluminum Oxide (NCA, $LiNiCoAlO_2$) cathode active material is approximately $17.85 per kilogram [420].

Safety concerns with NCA cathodes centre primarily around thermal stability and susceptibility to mechanical and thermal abuse. The high nickel content contributes to oxygen evolution at elevated temperatures, notably around 200 °C, resulting in TR risks [421]. While aluminium doping elevates thermal decomposition onset temperatures compared to undoped $LiNiO_2$, NCA remains less stable than cobalt- or iron-based cathodes, experiencing exothermic reactions at relatively low onset temperatures (around 165 °C for NCA compared to approximately 180 °C for $LiCoO_2$) [25]. In TR scenarios, NCA cells release significant heat and toxic gases, including hydrogen fluoride and phosphoryl fluoride, posing substantial hazards [34]. Under mechanical stress, such as crushing or penetration, NCA cathodes exhibit severe internal short circuits, rapidly escalating to violent thermal events with peak temperatures surpassing 500 °C [25]. Consequently, extensive safety measures, including robust thermal management systems and protective battery enclosures, are essential for the deployment of NCA-based battery systems in demanding environments. Ongoing research continually explores novel protective coatings, electrolyte additives, and structural reinforcements to mitigate these inherent safety risks [416].

A.1.6 Lithium manganese (nickel) oxide (LMO and LMNO)

Lithium manganese oxide (LMO, $LiMn_2O_4$) and lithium manganese nickel oxide (LMNO, typically $LiNi_{0.5}Mn_{1.5}O_4$, also known as high-voltage spinel LNMO) are both spinel-structured cathode materials with similar crystal frameworks but distinct compositions and properties. Both are commonly manufactured via solid-state calcination or co-precipitation methods, yielding polycrystalline spinel powders; in the case of LNMO, careful control of synthesis (e.g. temperature and cooling rate) is often required to manage Ni/Mn cation ordering which can affect performance [422, 423]. Compositionally, LMO is a manganese-only spinel (Mn^{3+}/Mn^{4+} redox couple), whereas LMNO substitutes half the Mn with Ni, introducing a Ni^{2+}/Ni^{4+} redox couple that raises the operating voltage to about 4.7 V (vs. 4.0 V for LMO) [424]. This higher voltage of LNMO translates to greater theoretical energy density: both LMO and LMNO have similar theoretical specific capacities around 146–148 $\text{mAh} \cdot \text{g}^{-1}$ (one Li per formula unit) [423, 378], but LMNO's higher voltage yields more energy per cycle. In terms of cost and raw materials, LMO is one of the cheapest cathodes due to the abundance of manganese and absence of cobalt, and LNMO remains relatively low-cost as well, avoiding expensive Co by using moderate amounts

of nickel [423]. Both materials are considered more environmentally benign and less toxic than cobalt-rich layered oxides; manganese and nickel pose fewer toxicity and supply-chain concerns than cobalt-based cathodes [425, 378]. Nickel is still toxic in soluble forms, but its content in LNMO is lower than the Co in NMC/LCO, and Mn is comparatively benign. The lack of cobalt also means recycling these chemistries is less lucrative - LMO especially has low economic recycling value since recovered Mn is cheap, whereas LNMO's Ni content offers somewhat higher incentive but still far less than Co-based systems [425, 381]. Electrically, both LMO and LMNO offer high power capability due to their 3D lithium diffusion pathways in the spinel lattice, making them suitable for high-discharge applications [378]. Thermal stability of the spinel cathodes is generally superior to that of layered oxides like LCO or NMC: LMO in particular has been noted for its stability and safety, with a higher decomposition onset temperature than LCO, and it has often been blended into NMC/LCO cathodes to improve thermal stability and reduce safety risks. In commercial use, LMO has been widely deployed since the mid-1990s - in early-generation lithium-ion batteries for power tools and in electric vehicles (often in combination with NMC) - owing to its low cost and acceptable performance/safety profile. The current market cost for spinel-type Lithium Manganese Oxide ($LiMn_2O4$) cathode active material is approximately starting from $7.52 per kilogram [426]. LMNO, on the other hand, is a newer material still under active research and not yet widely adopted in the market; its promise of cobalt-free high energy density has driven extensive investigation, but issues with cycle life and electrolyte compatibility have so far limited its commercial deployment to pilot projects and experimental cells [423, 427].

Safety under abuse conditions is a critical differentiator for cathode materials, and both LMO and LMNO (spinels) generally exhibit more benign behavior than the traditional layered oxides. In thermal abuse scenarios (overheating or fire exposure), LMO-based cells tend to remain stable to higher temperatures before undergoing exothermic decomposition. Fully charged LMO cathodes (approx. $Li_0Mn_2O_4$) do not release significant oxygen until reaching roughly 300–375 °C, whereas charged LNMO ($Li_0Ni_{0.5}Mn_{1.5}O_4$ with Ni^{4+} present) begins to undergo oxygen-releasing structural changes at temperatures below 300 °C [428]. This stark difference is attributed to the Ni^{4+} in LNMO, which is thermodynamically prone to reduce by liberating O_2, in contrast to the more stable Mn-only redox in LMO [429]. Consequently, LMO cells can tolerate higher abuse temperatures before triggering TR, whereas LNMO cells - especially at high state-of-charge - may enter TR more readily once the 250–300 °C threshold is crossed, as the released oxygen violently reacts with flammable electrolyte [428]. That said, both spinel cathodes are still considered safer than Co- or Ni-rich layered cathodes (e.g. LCO, NCA or high-Ni NMC), which can release oxygen at even lower temperatures and with greater heat output [430]. Under mechanical abuse (impact or crushing leading to internal short-circuit), cells with LMO or LMNO cathodes still face the risk of TR, but the severity of the event is often lower than with high-Ni or Co chemistries. Studies have shown that LMO-based cells exhibit a slower TR propagation and lower peak temperatures/pressures compared to NMC-based cells during nail penetration tests, reflecting the spinel's inherently lower exothermic oxygen release [25]. LMNO, while offering high voltage, shares some safety advantages of the spinel structure (e.g. robust framework and no cobalt) but will still release oxygen if overheated, so its safety lies between that of LMO and traditional NMC - improved over NMC due to lack of cobalt, but not as thermally inert as LFP or pure LMO. Overall, both LMO and LMNO are considered relatively safe cathodes: they have high thermal thresholds and do not undergo the rapid oxygen-driven combustion that makes LCO and high-Ni NMC chemistries so hazardous [430]. Nonetheless, LMNO's higher energy content and lower decomposition onset mean that stringent safety measures (thermal management, shutdown separators, etc.) are still required. In summary, LMO's long track record in industry demonstrates its benign failure behavior and tolerance to abuse (it was chosen in part for its safety in early EV batteries), whereas LMNO, though promising, must be carefully engineered (e.g. with stable electrolytes and protective coatings) to achieve a comparable level of safety under thermal or mechanical stress [423, 428].

A.1.7 Lithium iron phosphate (LFP) and other phosphate-based cathodes

Lithium iron phosphate ($LiFePO_4$, LFP) is an olivine-structured cathode material in the polyanion family of lithium-ion battery electrodes. Its crystal lattice consists of $FePO_4$ units with strong P–O bonds, which distinguishes it from layered transition-metal oxides [431]. LFP was first reported in 1997 as a rechargeable cathode delivering about 100–120 mAh $\cdot$ g^{-1}, with a theoretical one-electron capacity of $\sim$170 mAh $\cdot$ g^{-1}. It operates at a moderate voltage around 3.4 V vs Li/Li^+, using the Fe^{2+}/Fe^{3+} redox couple [160]. Other phosphate-based cathodes have been explored by substituting the transition metal: for example, $LiMnPO_4$ offers a higher operating voltage of $\sim$4.1 V (Mn^{2+}/Mn^{3+}) and similar theoretical capacity ($\sim$170 mAh $\cdot$ g^{-1}) but suffers from sluggish kinetics [432]. Likewise, $LiCoPO_4$ (with Co^{2+}/Co^{3+} at $\sim$4.8 V) can deliver about 167 mAh $\cdot$ g^{-1} theoretically, yet in practice it exhibits rapid capacity fading due to low conductivity and electrolyte decomposition at high voltage [433]. Among the phosphate cathodes, LFP stands out for its exceptional structural stability and has become the most widely adopted, thanks to advances that overcame its early drawbacks in electronic and ionic transport [160, 434]. Nanostructuring, carbon coating, and cation doping are now routinely employed in LFP manufacturing to improve its rate capability and utilization of active material. Industrial production of LFP powders can be achieved via solid-state reactions, hydrothermal syntheses, or sol-gel processes, often followed by a carbothermal treatment to obtain carbon-coated $LiFePO_4$ composite particles with enhanced conductivity. These manufacturing innovations (notably the conductive network formation) enabled LFP to attain near-theoretical capacity and power output in commercial cells [435, 160]. The olivine phosphate framework thus provides a high-performance, cobalt-free cathode option that has matured significantly since its inception [434].

A key advantage of LFP and related phosphate cathodes is the use of inexpensive, earth-abundant elements (iron, phosphorus, oxygen) instead of scarce metals like cobalt or nickel. This composition makes LFP comparatively low-cost and less susceptible to supply risks or price volatility in raw materials. In addition, the LFP chemistry is environmentally and biologically benign: it contains no heavy metals that pose toxicity or contamination concerns. Studies have highlighted LFP's "green" credentials, noting its low toxicity and minimal environmental impact relative to layered oxide cathodes. The elimination of cobalt in particular not only removes ethical and ecological issues associated with cobalt mining, but also improves the safety and environmental profile of the battery lifecycle [436, 434, 160]. From a lifecycle perspective, LFP cells can last so long that fewer replacements are needed, potentially offsetting the slightly higher material usage per kWh due to LFP's lower energy density. One challenge, however, is that the very factors making LFP inexpensive (its use of iron and phosphorus with no high-value metals) reduce the economic incentive for recycling these batteries [381]. Traditional hydrometallurgical or pyrometallurgical recycling relies on recovering valuable metals like Co, Ni, or Cu; in LFP the recoverable value is mainly lithium and some iron compounds, which on their own may not justify the cost of recycling operations [413]. Nonetheless, researchers stress the importance of recycling LFP cells at scale to reclaim lithium and prevent landfill disposal of the phosphate materials, since improper disposal of spent LFP batteries could still cause environmental degradation and resource waste. Recent work on direct cathode regeneration and alternative recycling methods shows promise in making LFP recycling more feasible despite the low inherent scrap value. Overall, the benign chemistry of phosphate cathodes affords advantages in cost and sustainability, even as it prompts new strategies to ensure end-of-life materials are efficiently recovered [394].

Phosphate-based cathodes are widely prized for their long-term durability and stable electrochemical performance. LFP in particular is known for its outstanding cycle life: cells can sustain thousands of charge-discharge cycles with minimal capacity loss, far exceeding the longevity of most layered oxide (e.g. NMC) cells under similar conditions. The robust olivine framework undergoes only minor volume changes ($\approx$6–7%) between the charged and discharged states, which mitigates mechanical strain and structural degradation over repeated cycling [437]. This intrinsic stability underlies the ability of LFP batteries to retain capacity over many years of use. In terms

of electrochemical parameters, LFP provides a specific capacity around 150–160 $mAh \cdot g^{-1}$ in practical cells (close to its 170 $mAh \cdot g^{-1}$ theoretical limit) and a nominal voltage plateau near 3.3 V [438]. This yields a moderately high gravimetric energy density (typically on the order of 90–150 $Wh \cdot kg^{-1}$ at the cell level, depending on cell design) - lower than Ni-rich layered oxides, but sufficient for many stationary and automotive applications where LFP's other benefits dominate. Furthermore, LFP can sustain high charge/discharge rates when engineered with nanoscopic particles or conductive coatings, enabling excellent power capability without rapid capacity fade [160]. The combination of long life, decent energy content, and high reliability has driven a dramatic rise in LFP's popularity across the battery industry. In recent years, LFP cathodes have captured a substantial share of the lithium-ion battery market, especially for applications prioritizing safety, longevity, and cost over maximum energy density. For example, lithium-iron-phosphate now accounts for roughly one-third of global EV and storage battery capacity, a share that has grown rapidly as manufacturers embrace its low-cost and stable performance profile [166]. Analysts note that LFP is often the preferred choice for battery systems where extended cycle life and tolerance to full charge are required, whereas NMC/NCA chemistries may be selected when higher energy density is paramount. Overall, the resurgence of phosphate cathodes in the 2020s underscores their well-rounded characteristics - ample performance for general-purpose use, coupled with superior lifespan, affordability, and raw material security - which make LFP an attractive cathode for large-scale deployment in diverse contexts [439].

Perhaps the most compelling advantage of LFP and related phosphate-based cathodes is their exceptional safety. The polyanionic phosphate structure is intrinsically more resistant to TR than the layered oxides, owing to the indelible strength of the P–O covalent bonds [96]. In LFP, the Fe–O bonds are stabilized by the phosphate groups, so the cathode does not release oxygen even when severely overcharged or overheated. This contrasts with $LiCoO_2$ and Ni-based oxides, which start to liberate O_2 from the lattice at elevated temperatures (typically above 180 °C for $LiCoO_2$ when overcharged), feeding combustible reactions in the cell [25]. LFP cells can tolerate substantially higher temperatures before entering TR; experimental abuse tests show onset temperatures on the order of 180–200 °C for LFP, compared to around 130–150 °C for typical NMC chemistries under the same conditions [414]. Moreover, even if an LFP battery is forced into TR, the reactions are less violent and release less heat overall than those in oxide-based cells. In inert atmosphere nail penetration and overheat tests, LFP cells exhibit a slower temperature rise, lower peak heat release, and significantly less flammable gas evolution than NMC counterpart. These results confirm that the phosphate cathode acts as a stabilizing influence during abuse, making it considerably harder to ignite a cell or cause an explosion. Additionally, the absence of cobalt in LFP removes a catalyst for toxic or exothermic reactions, further improving its safety profile. In practical terms, LFP batteries are regarded as among the safest lithium-ion chemistries - they are less prone to TR, show superior tolerance to overcharging, and are more stable under mechanical stress or high temperature operation. This inherent safety has been a major factor in the broad adoption of phosphate cathodes for large-scale applications: from home energy storage units to electric vehicles and even air transport of batteries, LFP's robust thermal behaviour and non-toxic constituents provide critical risk mitigation. In summary, the phosphate-based cathode family offers a level of safety and stability that is unmatched by most other high-energy battery materials, making it a chemistry of choice when safety is the paramount concern [141]. A summary of comparison of selected cathode types is shown in Figure A.1.

A.2 Anode Materials

Graphite and silicon are prominent lithium-ion battery anodes, and their degradation under extreme conditions such as fire and mechanical overloads remains critically important. Lithi-

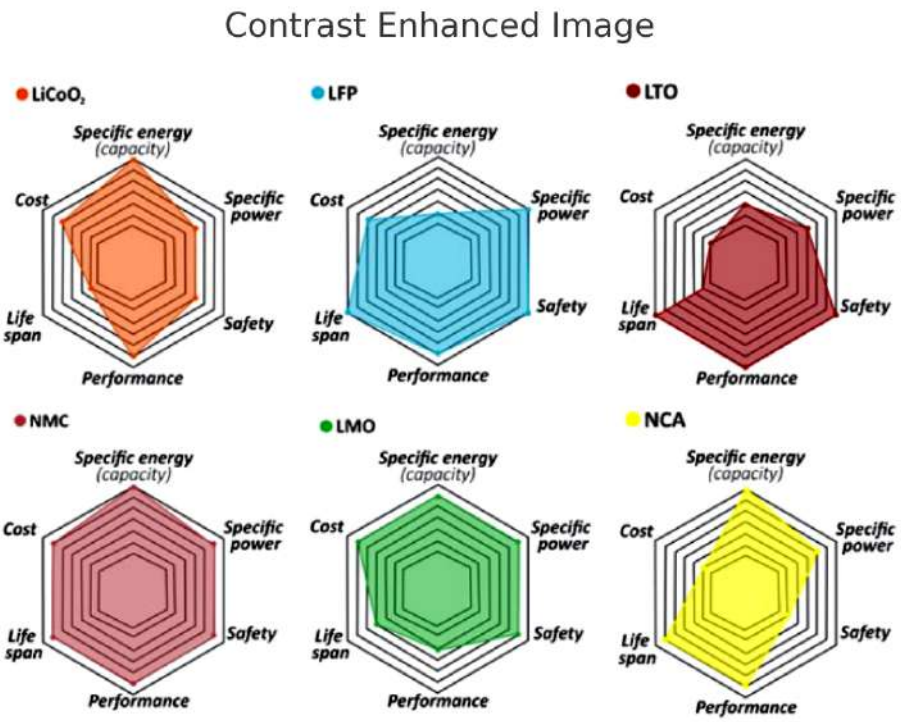

Figure A.1: Comparison of the cathode types.

ated graphite anodes exhibit exothermic decomposition of the solid-electrolyte interphase and electrolyte interactions starting at moderate temperatures (approximately 60–90 °C), generating gases like CO_2, H_2, and C_2H_4 and initiating self-heating processes [440, 136]. Recent studies employing in-situ techniques have demonstrated SEI breakdown and gas release from graphite at elevated temperatures [441]. The initial SEI decomposition destabilizes the interface, potentially leading to TR at higher temperatures (>200 °C), as lithiated graphite further reacts with electrolyte components and cathode-released oxygen [441, 129]. Mechanical abuse, including crush and penetration, similarly induces internal short-circuits, triggering rapid heat generation and decomposition [442].

Silicon-based anodes, despite their higher capacity, introduce additional thermal stability challenges due to substantial volume expansion during lithiation. This expansion causes continuous cracking and reformation of the SEI layer, making it vulnerable to rapid decomposition under thermal stress [443]. Silicon-graphite composite anodes exhibit earlier onset and more severe TR behaviour compared to pure graphite anodes, particularly at high charge states [443]. Strategies such as electrolyte additives (e.g., vinylene carbonate) have been shown to enhance SEI stability and delay TR by modifying decomposition pathways [444].

For comparative assessment, $Li_4Ti_5O_{12}$ and meso carbon microbeads are also evaluated. LTO features exceptional thermal stability due to its "zero-strain" structural characteristics, minimal SEI formation, and negligible lithium plating, significantly delaying TR even under severe abuse conditions [167]. Conversely, MCMB, while structurally stable at high temperatures, experiences accelerated SEI growth and increased impedance similar to graphite under thermal stress [445].

Overall, the developed methodology incorporates thermal and mechanical abuse tests combined with advanced characterization techniques to elucidate degradation mechanisms. This comprehensive approach enhances understanding of SEI dynamics and material decomposition under thermal stress, supporting the design of safer anode materials and thermal management strategies [446, 441].

A.3 Electrolyte Materials

The electrolyte plays a pivotal role in lithium-ion batteries, governing ion transport, interfacial chemistry, and ultimately performance and safety [447, 448, 449]. Since Sony's first commercial cell in 1991, most LIBs have relied on a liquid solution of $LiPF_6$ in organic carbonates, which provides room-temperature ionic conductivities on the order of $10^{-2}\mathrm{S}\cdot\mathrm{m}^{-1}$ and enables high power capability [450]. However, rising demand for greater energy density, longer service life, and improved environmental stewardship has spurred intense research into solid and gel electrolytes that promise superior safety and sustainability [451].

State-of-the-art liquid formulations typically dissolve 1 mol L^{-1} $LiPF_6$ in a 1:1 (v/v) ethylene carbonate / dimethyl carbonate mixture, sometimes blended with low-viscosity linear carbonates or flame-retardant co-solvents [452, 32]. Manufacturing is straightforward - high-purity salt and solvents are mixed in a dry room and injected into cells, so liquids remain the lowest-cost option and still command 95% of the LIB market [453]. Yet these electrolytes are volatile (flash point < 40°C), flammable, and prone to hydrolysis that releases HF, posing toxicity and recycling challenges [454]. Long-term durability also suffers because continuous solvent decomposition consumes lithium and thickens the solid-electrolyte interphase, reducing capacity retention over thousands of cycles.

Inorganic ceramics such as garnet type $Li_7La_3Zr_2O_{12}$ (LLZO) or sulfide glasses like $Li_{10}GeP_2S_{12}$ can reach $10^{-3}-10^{-2}\mathrm{S}\cdot\mathrm{m}^{-1}$ at room temperature, are non-volatile up to ∼800 °C, and tolerate anodic limits above 5 V [451, 455]. Solid electrolytes double as the separator, simplifying cell architecture, and, crucially, allow pairing with lithium-metal anodes whose theoretical specific capacity is 3860 $\mathrm{mAh}\cdot\mathrm{g}^{-1}$ [456]. Moisture sensitivity (especially for sulfides that emit toxic H_2S) and high sintering costs remain barriers, but recent alloying and surface-coating strategies have markedly improved air stability and interfacial resistance. Several automotive prototypes have already demonstrated solid-state pouch cells exceeding 400 $\mathrm{Wh}\cdot\mathrm{kg}^{-1}$ with stable 1000 cycle lifetimes [457].

Gel systems immobilise a conventional liquid inside a porous polymer matrix (e.g. PVDF-HFP, PAN or PEO), delivering conductivities near $10^{-3}\mathrm{S}\cdot\mathrm{m}^{-1}$ at ambient temperature while markedly reducing leakage and flame propagation [458]. Fabrication involves casting or electrospinning the polymer film, followed by solvent uptake, and is already mature for "Li-po" batteries in consumer electronics. Incorporating ceramic nanofillers such as BN nanotubes improves thermal stability to ∼250 °C and suppresses dendritic lithium growth, extending cycle life with lithium-metal anodes [459, 460]. Although polymers can oxidise at 4.5 V and add complexity to recycling streams, the lower free-solvent content eases hazardous-waste handling relative to pure liquids [458].

Most field failures trace back to exothermic SEI breakdown at ∼90–120 °C, followed by cathode oxygen release above 150 °C and combustion of the liquid electrolyte, triggering TR [448]. Gel matrices slow solvent vaporisation, delaying ignition, whereas all-solid cells largely eliminate flammable constituents and tend to fail benignly (electrolyte fracture or shorted Li dendrites without sustained fire) [461]. Nonetheless, sulfide ceramics require hermetic sealing against moisture to avoid H_2S evolution, and brittle oxides can crack under stack pressure, so comprehensive safety still demands balanced materials, cell design, and robust battery-management systems [449].

Flame-retardant additives (e.g. organophosphates), high-flash-point solvents, and "localized high-concentration" electrolytes dramatically raise ignition thresholds while preserving electrochemical performance [452, 453]. In parallel, up-scaled solid-state pilot lines have reported 100 mm-wide tapes of composite LLZO at costs approaching 100 $\mathrm{Wh}\cdot\mathrm{kg}^{-1}$, hinting at future parity with liquid systems [462]. Recycling innovations such as supercritical CO_2 extraction recover 90% of spent solvents, mitigating environmental burdens [32]. Continued progress across chemistry, processing, and policy will therefore determine which electrolyte architecture - liquid, gel,

or solid - dominates next-generation energy-storage markets.

A.4 Separator Materials

Commercial lithium-ion battery separators are thin, microporous polyolefin films - chiefly polyethylene (PE) and polypropylene (PP). Dry (melt-extrusion-stretching) and wet (solvent-extraction) processes create an interconnected pore network that balances ionic conductivity with mechanical strength [463, 464]. Popular monolayer PP or PE membranes, and especially multilayer PP/PE/PP designs, exploit the lower melting point of PE for thermal shutdown while retaining PP's higher mechanical integrity [465, 466]. Typical commercial separators are $\sim$20 μm thick with 30–50% porosity, delivering low ionic resistance yet preventing electronic contact between electrodes [464]. Thanks to these attributes, PE and PP account for the overwhelming majority of separator volume in today's Li-ion market [465].

Separator properties directly influence cell performance and lifetime. High porosity and thin thickness minimize ohmic loss, allowing electrodes to approach their theoretical capacities (e.g., 372 $\mathrm{mAh \cdot g^{-1}}$ for graphite) without significant polarization [447]. Polyolefins are chemically inert and non-toxic inside the cell, but their hydrophobicity can hamper initial electrolyte wetting [465]. Environmentally, their persistence is problematic; recent work shows that spent PE/PP separators can be cleaned and redeployed in "second-life" batteries, reducing waste and cost [467]. At scale, polyolefin separators remain the most economical option, costing only a few US cents per square meter, while advanced alternatives remain an order of magnitude higher [466].

Safety considerations dominate separator engineering. PE shuts down ionic transport by pore collapse near $\sim$130 °C, whereas PP retains mechanical integrity up to $\sim$165 °C, providing a staged defence against TR [465, 466]. If heat flux outpaces shutdown, however, further shrinkage or melting can trigger internal short circuits; therefore minimal area shrinkage and high puncture resistance are critical [468]. Modern separators exceed 150 MPa tensile strength and $< 5\%$ shrinkage at 150 °C, metrics that correlate with a markedly lower short-circuit rate in abuse testing [466].

Laboratory innovations aim to push safety margins further. Ceramic-coated polyolefin separators (Al_2O_3, SiO_2) boost thermal stability beyond 200 °C and improve electrolyte wettability, while adding only $\sim$2% to cost [469]. Electrospun non-woven mats of polyimide or cellulose introduce sub-micron fibres that raise porosity and flame retardance [470]. Flame-retardant grafts or fillers suppress ignition and can self-extinguish during nail-penetration tests [468]. Although these approaches remain pre-commercial, they outline a clear path toward separators that will enable next-generation high-energy cells without sacrificing safety [471].

Appendix B

Review of the Prevention Systems and Solutions to Battery Fires

Preventing fires in LIBs has become a critical focus as energy storage systems proliferate across portable electronics, electric vehicles, and stationary storage applications due to the high energy density and flammable nature of organic electrolytes and electrode materials [96, 25]. Effective fire prevention demands a multi-layered approach encompassing real-time electrochemical state monitoring, precise thermal regulation, robust structural containment, and rapid suppression mechanisms [472, 126]. Battery management systems (BMS) serve as the first line of defence by continuously supervising cell voltages, currents, and temperatures to detect and correct abnormal conditions before they escalate into TR [96, 228]. Meanwhile, battery thermal management systems (BTMS), including air, liquid, and phase-change material - based cooling, actively regulate cell temperatures to mitigate localized heating and maintain uniform temperature profiles under varied operating conditions [473, 472].

Early detection technologies, such as off-gas sensing and acoustic monitoring, provide critical warnings by identifying precursor signs of cell decomposition and electrolyte breakdown, enabling timely intervention before ignition occurs [126, 228]. Structural solutions incorporate thermal barriers, insulating materials, and engineered venting pathways to confine failures within individual cells and prevent propagation to adjacent cells or modules [473, 144]. In parallel, fire suppression systems deploy tailored agents - including aqueous vermiculite dispersions, aerosolized extinguishing powders, and clean agents to swiftly quench incipient flames and absorb exothermic reaction heat within battery enclosures [228, 144]. Recent advancements focus on integrated safety platforms that synergize BMS algorithms, BTMS control, and suppression activation into unified architectures capable of automated, rapid response to emergent thermal events [126, 144].

B.1 Battery Management Systems as Primary Prevention Layer

BMS represent the cornerstone of LIB safety, integrating a suite of monitoring, diagnostic, and protective functions that collectively mitigate the risk of fire and catastrophic failure. At the most fundamental level, BMS continuously monitors the voltage and current of each cell and the overall pack, ensuring that all cells operate within their manufacturer-specified safe limits. By detecting overvoltage, undervoltage, and overcurrent events in real time, the BMS can quickly intervene to curtail current flow, disconnect faulty modules, or shut down the system, thereby preventing dangerous conditions that could lead to TR [96, 474, 475]. Advanced voltage monitoring employs predictive filtering and hysteresis algorithms to distinguish between genuine faults and transient fluctuations, reducing false alarms and maintaining operational stability [96, 474, 475].

Beyond electrical supervision, cell balancing is a core BMS function that addresses the inherent variability in cell capacity and ageing rates within series-connected packs. Through either passive shunting of excess energy or active redistribution using capacitive or inductive convert-

ers, the BMS equalizes the SOC among cells, maximizing usable capacity and extending battery life [96, 476]. This balancing process is essential for preventing individual cells from exceeding critical voltage thresholds during charging or discharging, which could otherwise result in localized degradation or safety hazards [96, 476].

Thermal management is equally vital, as lithium-ion cells are highly sensitive to temperature excursions and gradients. The BMS orchestrates a network of thermistors, resistance temperature detectors (RTDs), or infrared sensors distributed throughout the pack to monitor temperature in real time [96, 477]. When hotspots or abnormal temperature rises are detected, the BMS can activate cooling systems, adjust power output, or initiate emergency shutdowns to maintain all cells within the optimal thermal window, typically 20–45 °C [96, 477]. In severe cases, the system may deploy thermal barriers or isolate overheating cells to prevent the propagation of TR [96, 477].

Modern BMS platforms increasingly incorporate early fault detection through off-gas and hydrogen sensing. As cells degrade or experience internal faults, they can emit trace gases such as CO_2, CO, HF, or H_2 before any significant voltage or temperature anomaly is apparent. By integrating MEMS-based gas sensors and electrochemical detectors, the BMS can identify these early warning signs and take pre-emptive action, such as isolating affected cells or modules, long before ignition or venting occurs [25, 96]. This gas monitoring capability significantly enhances the time window for intervention and is particularly valuable in large-scale or high-energy battery systems [25, 96].

Another advanced diagnostic function is the application of electrochemical impedance spectroscopy within the BMS. Electrochemical impedance spectroscopy provides a frequency-domain analysis of each cell's internal impedance, revealing subtle changes in charge transfer resistance, electrode degradation, or SEI growth that may precede more obvious electrical or thermal anomalies [478]. By periodically comparing measured impedance spectra to baseline models, the BMS can assess state of health in real time, schedule predictive maintenance, and avoid unexpected failures [478]. This proactive diagnostic approach extends the BMS's role from simple protection to active life-cycle management.

Finally, the BMS is responsible for implementing safety interlocks and emergency protocols. When abnormal conditions are detected, whether electrical, thermal, or chemical, the BMS triggers hardware interlocks to disconnect affected cells or modules, halt charging and discharging, and engage passive or active cooling systems [475, 474, 96]. These interlocks are typically designed to meet stringent functional safety standards (such as IEC 61508/61511), ensuring that fault containment is automatic and does not rely on operator intervention [474, 475, 96]. By isolating faults and preventing their propagation, the BMS minimizes collateral damage and facilitates safe system recovery.

In summary, the BMS provides a comprehensive, multi-layered defense against battery fire hazards by integrating voltage and current protection, cell balancing, thermal management, gas and impedance sensing, and robust interlocks. Each of these functions contributes unique insights and control mechanisms, ensuring that LIB systems operate reliably and safely across a wide range of applications [96, 25, 472, 475, 474, 478].

B.2 Air-Cooled Thermal Management Systems

Air-cooled thermal management systems remove heat from LIB cells by directing ambient or forced airflow over their surfaces, offering a lightweight and cost-effective solution for low to moderate power applications. In passive configurations, natural convection driven by vehicle motion or buoyancy can suffice, while active systems use fans or blowers to enhance heat transfer under high load or low speed conditions [479, 480, 476, 481].

The convective heat transfer coefficient, h, critically determines cooling performance, with forced convection increasing h by up to 50% compared to natural convection, thereby reducing

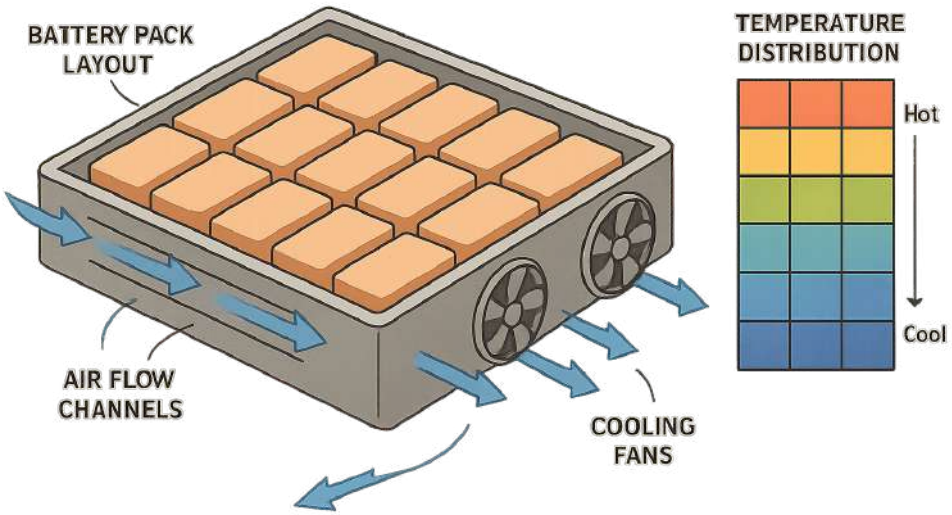

Figure B.1: Air cooled battery assembly representation.

peak cell temperatures. Computational fluid dynamics (CFD) studies demonstrate that fan placement at pack ends or top panels yields more uniform airflow through serpentine or parallel channels, keeping the maximum temperature difference across cells within 5 °C under typical duty cycles [479, 480, 482, 481].

Inlet and outlet manifold design strongly influences airflow distribution: vertical inlet-top / outlet-bottom configurations outperform side-inlet setups by lowering flow resistance and creating balanced velocity profiles. Multi-path duct networks with Z- or U-shaped channels mitigate hot spots by guiding air through high-heat zones, although they incur higher pressure drops and parasitic fan power [479, 480, 482].

Hybrid strategies that combine air cooling with PCMs or heat pipes enhance transient performance: PCMs absorb peak discharge heat spikes, while airflow removes stored energy between duty cycles, reducing cycle-to-cycle temperature rise and improving lifecycle cost efficiency. Embedding porous metal-foam spreaders between cells increases conduction to air channels, boosting effective h by 30% and lowering maximum cell temperature by approximately 4 °C [482, 480].

The choice of duct-lining and flow plate materials also affects thermal performance: high conductivity metals (aluminium or copper) paired with low friction coatings reduce pressure drop and facilitate heat transfer from cell walls to airflow. Composite plates with integrated baffles allow targeted cooling of high-heat generation cells without excessive fan power, while closed loop fan speed control based on real-time temperature feedback can save 10–15% of parasitic energy compared to fixed speed operation [479, 481, 480].

Fan and blower selection is critical: brushless direct current blowers provide rapid response and fine speed control, enabling precise thermal regulation. Variable speed control synchronized with instantaneous heat flux can lower peak temperatures by 8% over constant speed schemes, while packaging constraints and noise requirements guide fan integration within sealed housings [482, 481].

For small-to-medium format packs where thermal loads rarely exceed 2 kW, air-cooled systems strike a favourable balance between simplicity and cost: lifecycle cost analyses show up to 30% lower capital and maintenance expenses compared to liquid systems in these applications [476, 479, 480, 170]. However, high-power or large format packs often require liquid or hybrid cooling due to air's lower heat capacity and conductivity.

Recent studies employ machine learning surrogate models to optimize multidimensional design parameters cell layout, duct geometry, and fan placement under varying duty cycles, enabling

rapid exploration of novel configurations that meet temperature uniformity targets with minimal prototyping. Experimental validations corroborate simulation results, demonstrating that advanced air-cooled architectures can support next generation battery packs [482, 170, 480].

B.3 Liquid-Based Thermal Management Systems

Liquid-cooled battery thermal management systems represent the most effective approach for maintaining optimal operating temperatures in high-energy density LIB packs under demanding conditions such as fast charging and high discharge rates [481]. The superior thermal conductivity and specific heat capacity of liquid coolants, compared to air-based systems, enable significantly enhanced heat transfer coefficients ranging from 1000 to 5000 W/m^2K, thereby providing more efficient thermal regulation [483]. Liquid cooling systems utilize the principle of forced convection heat transfer, where coolant circulates through dedicated channels or plates in direct thermal contact with battery cells, facilitating rapid heat removal and maintaining temperature uniformity across the battery pack [481]. The implementation of liquid cooling has become increasingly critical as battery energy densities continue to rise, with contemporary high-performance electric vehicles requiring thermal management systems capable of dissipating heat loads exceeding 2 kW during fast charging operations [483]. Example of such system is shown in Figure B.2.

Advanced computational fluid dynamics modelling has significantly enhanced the understanding of complex thermal-hydraulic phenomena within liquid cooling systems, enabling precise optimization of channel geometries, flow distributions, and coolant properties to maximize thermal performance while minimizing parasitic energy consumption [484]. The fundamental heat transfer mechanisms in liquid-cooled systems involve conduction through cell materials and thermal interface layers, followed by convective heat transfer to the circulating coolant, which together enable effective temperature control even under extreme operating conditions [477]. These principles form the basis for increasingly efficient and compact liquid cooling solutions suitable for electric vehicles, grid storage, and other high-power applications [484].

The selection of appropriate coolant fluid is critical for optimal system performance, with ethylene glycol-water mixtures being the most widely adopted solution due to their balanced thermal properties and freeze protection capabilities [483]. Water-glycol mixtures, typically containing 50% ethylene glycol, provide enhanced thermal conductivity compared to pure glycol while maintaining acceptable viscosity and pumping power requirements [483]. Advanced coolant formulations, including nanofluids enhanced with nanoparticles such as Al_2O_3, CuO, and graphene oxide, demonstrate superior thermal performance by increasing thermal conductivity by up to 40% compared to conventional base fluids [484]. Coolant properties must balance thermal conductivity, specific heat capacity, viscosity, electrical conductivity, chemical stability, and environmental impact to achieve optimal performance across varying temperature ranges [485].

Thermophysical properties exhibit significant temperature dependence, necessitating careful consideration of operating ranges when designing liquid-cooled systems [483]. For instance, the viscosity of water-glycol mixtures decreases exponentially with increasing temperature, reducing pumping power requirements at elevated temperatures but potentially compromising heat transfer performance at low temperatures [477]. Recent research on phase-change nanofluids exploits latent heat effects to provide superior thermal regulation during transient high-power events [483]. Additionally, dielectric coolants such as fluorinated hydrocarbons enable direct immersion cooling configurations that eliminate thermal interface resistances, although at higher cost and with more complex system requirements [95].

Cooling plate design is a key aspect of liquid-cooled thermal management, where heat transfer efficiency is directly influenced by channel geometry, flow distribution, and interface contact area [484]. Mini-channel and micro-channel cooling plates with hydraulic diameters ranging from 0.1 to 3 mm provide enhanced performance through increased surface-area-to-volume ratios and improved convective heat transfer coefficients [484]. Serpentine, parallel, and spiral channel con-

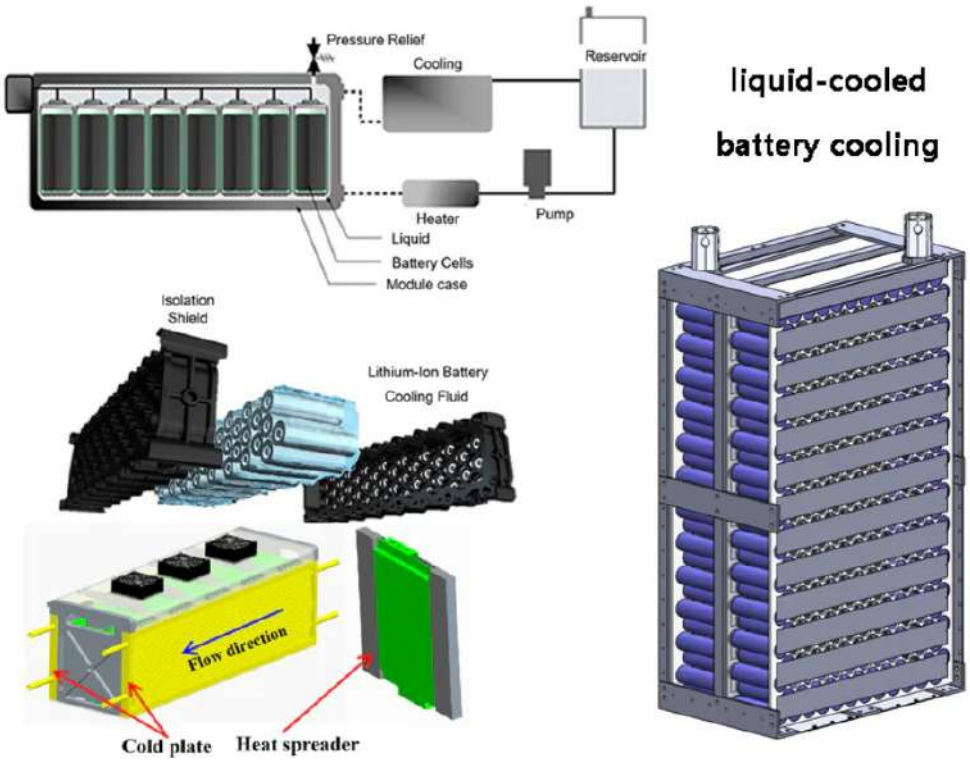

Figure B.2: Liquid cooling of the battery module representation.

figurations have been studied, with optimized geometries demonstrating temperature reductions of 3–5 °C compared to conventional rectangular channels [483]. Advances in additive manufacturing and precision machining have enabled complex channel geometries that maximize heat transfer while minimizing pressure drop and material usage [484].

Topology optimization approaches employing computational algorithms have yielded novel designs such as bionic-inspired structures and fractal-based networks that outperform conventional plates in both thermal performance and pressure drop characteristics [477]. Topology-optimized plates have demonstrated pressure drop reductions up to 40% while improving temperature uniformity [484]. Integrating multiple inlet-outlet configurations and manifolds enhances flow distribution, with optimized designs achieving temperature variations below 2°C across large battery modules under high-power conditions [483].

Heat transfer enhancement in liquid-cooled systems is achieved through passive and active techniques including surface modifications, flow optimization, and advanced coolants [483]. Two-phase cooling systems utilizing dielectric fluids such as $SF33$ exploit latent heat of vaporization to achieve heat transfer coefficients exceeding 10,000 W/m^{2}K during nucleate boiling [95]. Flow strategies such as reciprocating and pulsed flows enhance thermal uniformity by reducing stagnation zones and promoting turbulence within channels [484]. These enhancement mechanisms allow systems to maintain battery temperatures within optimal ranges under extreme fast-charging conditions exceeding 6 C [483].

Innovative approaches including micro-pin fins, dimpled surfaces, and vortex generators within channels promote boundary layer disruption and increase convective heat transfer by 30–80% compared to smooth channels [477]. Hybrid systems combining nanofluids, microchannels, and phase-change materials have exhibited synergistic improvements, with one study reporting a 3.44 °C reduction in maximum battery temperature for only a 5% increase in pumping power [484]. These strategies advance the development of efficient thermal management solutions for next-generation high-power battery systems [483].

Thermal interface materials (TIMs) minimize contact resistance between cells and cooling

plates, with interface resistance contributing 10–30% of total thermal resistance in liquid-cooled systems [477]. High-conductivity materials, such as thermally conductive adhesives, gap fillers, and phase-change TIMs bridge microscopic air gaps and surface irregularities [95]. Advanced solutions, including direct contact and immersion cooling configurations, eliminate interface resistance by providing direct coolant cell contact [484]. TIM selection must balance thermal conductivity, compliance, electrical isolation, chemical stability, and long-term reliability [483].

Recent developments include graphene-enhanced TIMs with conductivities exceeding 35 W/mK, a vast improvement over conventional silicone-based formulations limited to 1–3 W/mK [484]. In-situ polymerization and nanoparticle functionalization have yielded TIMs with improved wetting characteristics and reduced interfacial resistance [477]. Integration of conductive structural adhesives enables combined thermal management and mechanical fastening, reducing assembly complexity and cost while enhancing performance [95].

Design optimization balances thermal performance, pressure drop, and pumping power through multi-objective methods such as genetic algorithms and entropy weight-TOPSIS [483]. Flow distribution strategies, including parallel, series, and hybrid configurations significantly influence temperature uniformity and efficiency, with optimized designs achieving temperature differences below 5°C across modules [484]. High-fidelity computational models integrated with optimization algorithms have led to efficient systems that maximize heat removal while minimizing energy consumption [477].

Pressure drop analysis is essential, as excessive losses increase pumping power requirements and reduce overall efficiency [484]. Channel geometries must balance heat transfer enhancements with acceptable pressure drop penalties, typically below 10 kPa for automotive applications to minimize parasitic consumption [483]. Pumping power optimization studies reveal optimal flow rates where thermal gains outweigh energy costs, with velocities ranging from 0.1 to 0.4 m/s depending on configuration [484].

Liquid-cooled systems offer superior TR prevention compared to air cooling, containing events within individual cells and preventing propagation [95]. Dielectric coolants eliminate electrical short-circuit risks while providing high thermal conductivity for effective heat removal during emergencies [484]. Standards such as UL 9540A and IEC 62619 establish rigorous testing requirements for liquid-cooled systems, with certified designs demonstrating controlled thermal behaviour and minimal fire risk under abuse conditions [477].

Innovations such as manifold-based designs, variable cross-section channels, and scanning flow methods have achieved temperature uniformity improvements of 62.5% and reductions in average temperature differences by 92% compared to steady-flow approaches [477]. Synergistic integration of nano-fluid coolants with microchannels has demonstrated additional temperature reductions of 3–5 °C in identical geometries [95]. Advances in precision machining, chemical etching, and additive manufacturing continue to enable complex microchannel geometries that maximize thermal performance while minimizing energy consumption and system complexity [484].

B.4 PCM-Based Battery Thermal Management Systems

PCM based battery thermal management systems (BTMS) leverage the latent heat of fusion to absorb and store heat generated by Li-ion cells during operation, thus maintaining cell temperatures within optimal limits [155].

Organic paraffin-based PCMs are favoured for their high latent heat density (about 190 kJ/kg) and chemical stability, whereas inorganic salt hydrates and eutectic mixtures offer tunable melting points to match battery thermal requirements [155, 486]. Key selection criteria include melting temperature (20 – 45 °C), minimal sub-cooling, high latent heat, and compatibility with cell materials [486]. Low PCM thermal conductivity (0.2 W/mK) is typically enhanced by conductive fillers such as expanded graphite or metal foams to improve heat transfer within the PCM matrix [487].

PCMs can be integrated at both cell and pack levels. At the cell level, cylindrical cells may be encapsulated individually in PCM blocks moulded to cell geometry for uniform heat absorption. At the pack level, PCM occupies interstitial spaces between cells inside a sealed enclosure, forming a contiguous thermal buffer. Hybrid configurations combine PCM with secondary media (e.g., forced air or liquid cooling channels) to extract stored heat post-PCM melting, extending effective thermal regulation without excessive volume or pump power [155, 486].

Experimental and numerical studies report that pure PCM cooling can reduce peak cell temperatures by 4–10 °C versus uncooled packs under high-rate discharge and achieve temperature uniformity within 1 – 2 °C [488]. Composite PCMs enhanced with 2% wt. silver nanoparticles cut surface temperature rise by up to 60% over pure paraffin under constant heat flux [486]. In PCM-liquid hybrid systems, peak temperatures as low as 31.5 °C and non-uniformity of 1.75 °C have been demonstrated at moderate C-rates with modest pump power [155].

Pure PCM solutions face finite latent capacity and leakage risks once melted. Micro-encapsulation and containment enclosures address leakage and maintain long-term stability [488]. Embedding metallic fins or porous foams can boost effective PCM thermal conductivity by up to fivefold, reducing thermal resistance and local hot spots [487]. Design guidelines recommend matching PCM melting point and latent heat to battery geometry and load profiles to balance thermal regulation and added mass [155].

B.5 Hybrid Battery Thermal Management Systems

The escalating adoption of EVs necessitates advanced BTMS that can effectively maintain optimal operating conditions while addressing the inherent limitations of conventional single-mode cooling approaches. Hybrid battery thermal management systems represent a paradigm shift in thermal control strategies, combining multiple cooling methodologies to achieve superior performance characteristics. These systems integrate the advantages of different thermal management approaches, such as air cooling, liquid cooling, PCMs, and heat pipes, to create synergistic solutions that address the complex thermal challenges posed by modern LIB packs. This comprehensive review examines the current state-of-the-art in hybrid BTMS technologies, with particular emphasis on air-liquid cooling combinations that leverage the complementary benefits of both cooling mediums.

The fundamental premise underlying hybrid thermal management systems stems from the recognition that individual cooling methods possess inherent limitations that can be mitigated through strategic integration [154]. Air cooling systems, while simple and cost-effective, suffer from limited heat transfer coefficients and inadequate performance under high discharge rates. Conversely, liquid cooling systems demonstrate superior heat removal capabilities but introduce complexity, weight penalties, and potential reliability concerns related to coolant leakage. Hybrid systems seek to optimize the trade-offs between performance, complexity, cost, and reliability by intelligently combining these approaches to maximize cooling effectiveness while minimizing system drawbacks [489].

The theoretical foundation of hybrid BTMS design is predicated on the principle of thermal load distribution, wherein different cooling mechanisms operate synergistically to manage heat generation across varying operational conditions [490]. During low-power operations, passive or low-energy cooling methods may provide adequate thermal control, while high-power scenarios can activate additional cooling mechanisms to maintain battery temperatures within optimal ranges. This adaptive approach not only enhances thermal performance but also contributes to overall energy efficiency by reducing unnecessary cooling energy consumption during periods of reduced thermal demand [491].

Contemporary research in hybrid BTMS has demonstrated significant improvements in key performance metrics, including maximum temperature reduction, temperature uniformity enhancement, and energy consumption optimization [154]. Advanced hybrid configurations have

achieved temperature reductions of up to 72.5% compared to single-mode cooling systems while maintaining temperature differences below 5 °C across battery modules [492]. These performance improvements are particularly pronounced under extreme operating conditions, where single-mode systems typically fail to maintain adequate thermal control [493].

The integration of advanced materials and innovative design configurations has further expanded the capabilities of hybrid thermal management systems. The incorporation of PCMs with enhanced thermal conductivity, micro-channel heat exchangers, and smart control algorithms has enabled the development of compact, efficient, and responsive thermal management solutions [157]. These technological advancements have positioned hybrid BTMS as the preferred solution for next-generation electric vehicle applications, where thermal performance requirements continue to escalate in response to increasing battery energy densities and fast-charging capabilities [494].

B.5.1 Air-Liquid Hybrid Cooling Configurations

Air-liquid hybrid cooling represents one of the most promising approaches in contemporary battery thermal management, offering a sophisticated balance between thermal performance and system practicality. These configurations strategically combine the simplicity and reliability of air cooling with the superior heat transfer capabilities of liquid cooling to create versatile thermal management solutions that can adapt to varying operational demands. The fundamental design philosophy centers on utilizing air cooling for baseline thermal management while employing liquid cooling for enhanced heat removal during high-power operations or extreme environmental conditions [495].

The architectural design of air-liquid hybrid systems typically incorporates dual cooling pathways that can operate independently or synergistically depending on thermal load requirements [491]. Primary configurations include series arrangements where air cooling provides initial heat removal followed by liquid cooling for additional thermal control, parallel configurations where both cooling methods operate simultaneously, and adaptive systems that dynamically switch between cooling modes based on real-time thermal conditions [154]. Each configuration offers distinct advantages in terms of thermal performance, energy efficiency, and system complexity, requiring careful optimization based on specific application requirements and operational constraints.

Recent experimental investigations have demonstrated the effectiveness of air-liquid hybrid configurations in maintaining battery temperatures within optimal ranges while minimizing energy consumption [489]. A novel air-liquid coupled cooling system developed for electric bus applications achieved comparable heat dissipation performance to pure liquid cooling systems while consuming only one-third of the energy [491]. This remarkable efficiency improvement was attributed to the intelligent load distribution between air and liquid cooling components, where air cooling handled baseline thermal loads while liquid cooling provided supplementary heat removal during peak demand periods.

The thermal performance characteristics of air-liquid hybrid systems are particularly advantageous under transient loading conditions commonly encountered in electric vehicle operations [493]. During acceleration phases or rapid charging scenarios, the liquid cooling component can rapidly respond to increased thermal loads while the air cooling system provides continuous background thermal management. This dual-mode operation ensures temperature stability across the entire operational envelope while preventing thermal excursions that could compromise battery performance or safety [492].

Advanced control strategies have been developed to optimize the operation of air-liquid hybrid systems, incorporating predictive algorithms that anticipate thermal loads based on vehicle operating patterns and environmental conditions [154]. These intelligent control systems can proactively adjust cooling capacity allocation between air and liquid components, minimizing energy consumption while maintaining optimal thermal performance. Neural network-based pre-

diction models have demonstrated the ability to reduce coolant energy consumption by 17.6% while maintaining temperature differences below 0.75 °C across battery modules [496].

B.5.2 Phase Change Material Integration in Hybrid Systems

PCMs into hybrid battery thermal management systems represents a significant advancement in passive thermal control technology, offering exceptional heat absorption capabilities during the phase transition process while providing thermal buffering effects that enhance overall system stability. PCM-based hybrid systems leverage the latent heat absorption characteristics of PCMs to manage thermal transients and peak heat generation events, effectively smoothing temperature fluctuations and reducing the burden on active cooling components [490].

Contemporary PCM formulations for battery thermal management applications have evolved to incorporate enhanced thermal conductivity additives, including expanded graphite (EG), metal foams, and nanoparticle dispersions that address the inherent low thermal conductivity limitations of pure PCMs [156]. Advanced composite PCM materials, such as graphene-coated nickel foam saturated with paraffin, have achieved thermal conductivity enhancements of up to 23 times compared to pure paraffin while maintaining excellent heat storage capabilities [157]. These material advancements have significantly improved the responsiveness and effectiveness of PCM-based thermal management systems.

Hybrid configurations combining PCMs with active cooling methods have demonstrated superior thermal performance compared to single-mode systems, particularly under high discharge rate conditions [493]. A hybrid system integrating expanded graphite-paraffin composite PCM with liquid cooling achieved maximum temperature reductions of $\sim$3°C compared to conventional liquid cooling while increasing battery cycle life by 6-15% [492]. The PCM component provided thermal buffering during peak heat generation periods, while the liquid cooling system ensured continuous heat removal to prevent PCM saturation and maintain long-term thermal stability.

The design optimization of PCM-hybrid systems requires careful consideration of material properties, geometric configurations, and thermal management strategies to maximize performance benefits [497]. Critical design parameters include PCM melting temperature selection, thermal conductivity enhancement methods, PCM volume fraction, and integration geometry with active cooling components [498]. Multi-objective optimization studies have identified optimal combinations of these parameters that minimize maximum temperature while maximizing temperature uniformity across battery modules.

Advanced PCM-hybrid configurations have incorporated novel architectural designs, including multi-layer PCM arrangements with varying melting temperatures, micro-encapsulated PCM dispersions, and PCM-integrated heat pipes that enhance heat distribution capabilities [464]. These sophisticated designs enable tailored thermal responses that can accommodate diverse operational scenarios while maintaining compact system geometries suitable for automotive applications. The thermal storage capacity of these advanced PCM systems has proven particularly valuable for managing TR propagation, providing critical heat absorption during emergency scenarios to prevent cascading failures across battery modules [185].

The optimization of hybrid battery thermal management systems requires a comprehensive approach that considers multiple performance metrics, design constraints, and operational requirements to achieve optimal thermal performance while maintaining practical feasibility. Contemporary optimization methodologies employ advanced computational techniques, including multi-objective genetic algorithms, response surface methodology, and machine learning approaches to identify optimal design configurations that balance competing objectives such as thermal performance, energy efficiency, weight, and cost [195].

The thermal-hydraulic design of hybrid cooling systems involves complex interactions between heat transfer mechanisms, fluid flow dynamics, and thermal energy storage that require sophisticated modelling approaches for accurate performance prediction [496]. Computational fluid

dynamics simulations coupled with thermal models provide detailed insights into temperature distributions, flow patterns, and heat transfer rates that inform design optimization decisions. These modelling capabilities have enabled the development of advanced cooling plate geometries, including micro-channel configurations, serpentine flow paths, and novel heat exchanger designs that maximize heat transfer while minimizing pressure losses.

Energy efficiency optimization has emerged as a critical consideration in hybrid BTMS design, driven by the need to minimize the impact of thermal management on vehicle range and performance [491]. Advanced energy management strategies incorporate predictive control algorithms that optimize cooling system operation based on anticipated thermal loads and operational patterns [154]. These intelligent control systems have demonstrated significant energy savings while maintaining thermal performance, with reported reductions in cooling energy consumption of up to 22% through optimized control strategies.

The development of next-generation PCMs with tailored thermal properties represents another critical research direction, focusing on the creation of composite materials with enhanced thermal conductivity, optimized melting temperatures, and improved long-term stability [499]. Advanced PCM formulations incorporating shape-stabilized composites, micro-encapsulated materials, and multi-functional additives promise to overcome current limitations while providing additional functionalities such as thermal conductivity switching and self-healing capabilities [159]. These material advancements will enable more effective thermal energy storage and management in hybrid systems.

Emerging cooling technologies, including thermoelectric cooling, magnetocaloric cooling, and advanced vapour chamber systems, offer new possibilities for hybrid thermal management system development. The integration of these technologies with conventional cooling methods could provide unprecedented thermal control capabilities while addressing specific challenges such as precise temperature control, rapid thermal response, and operation in extreme environments. Research into solid-state cooling technologies and their integration with traditional thermal management approaches represents a particularly promising avenue for future hybrid system development, offering the potential for highly efficient, reliable, and compact thermal management solutions that can meet the evolving demands of next-generation electric vehicle applications.

Appendix C

Additional datasets

Following chapter contains additional datasets and figures from the experiments and calculations made in Chapter 6: Battery Fire Resistance Testing Methodology.

C.1 Extra data to Empirical Evaluation of Open Flame Fire Resistance Testing Procedure

See Section 6.3 for further details.

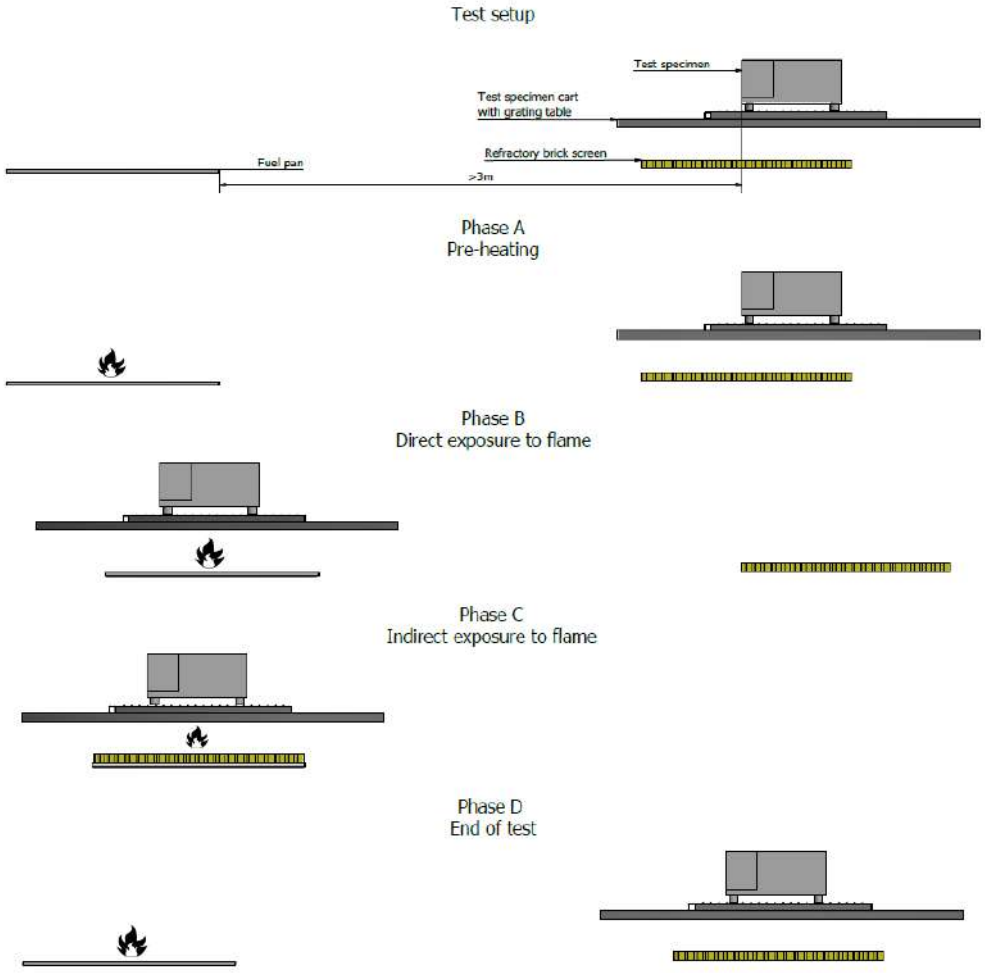

Figure C.1: UNECE R100.03 fire test set-up.

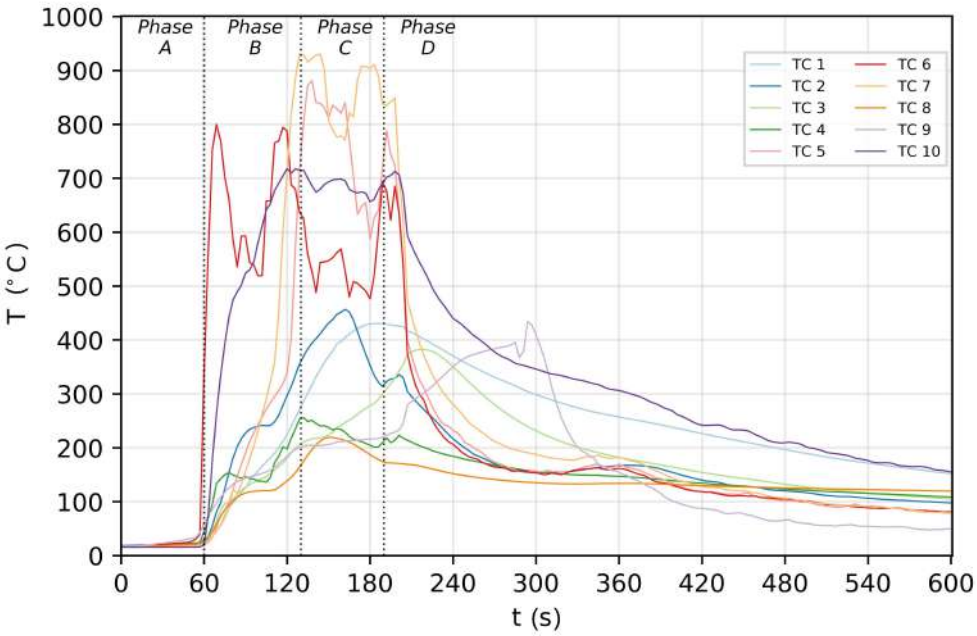

Figure C.2: Temperature graph of the UNECE R100.03 fire test.

C.2 Statistical analysis of Open Flame Fire Resistance Testing Procedure

See Section 6.4 for further details.

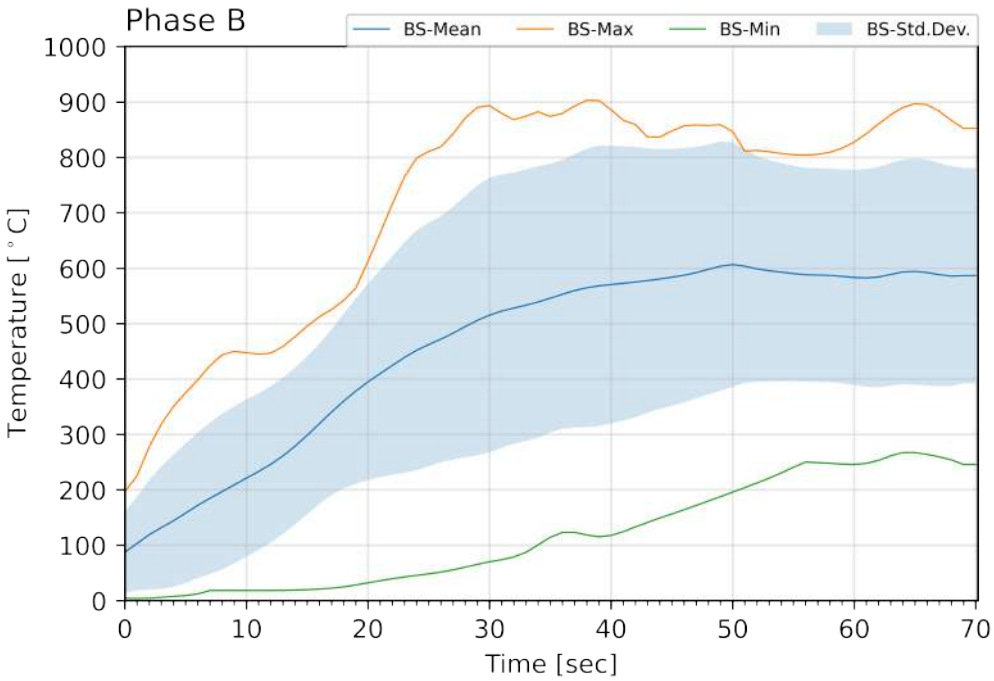

Figure C.3: Temperature graph of the thermocouple BS in Phase B.

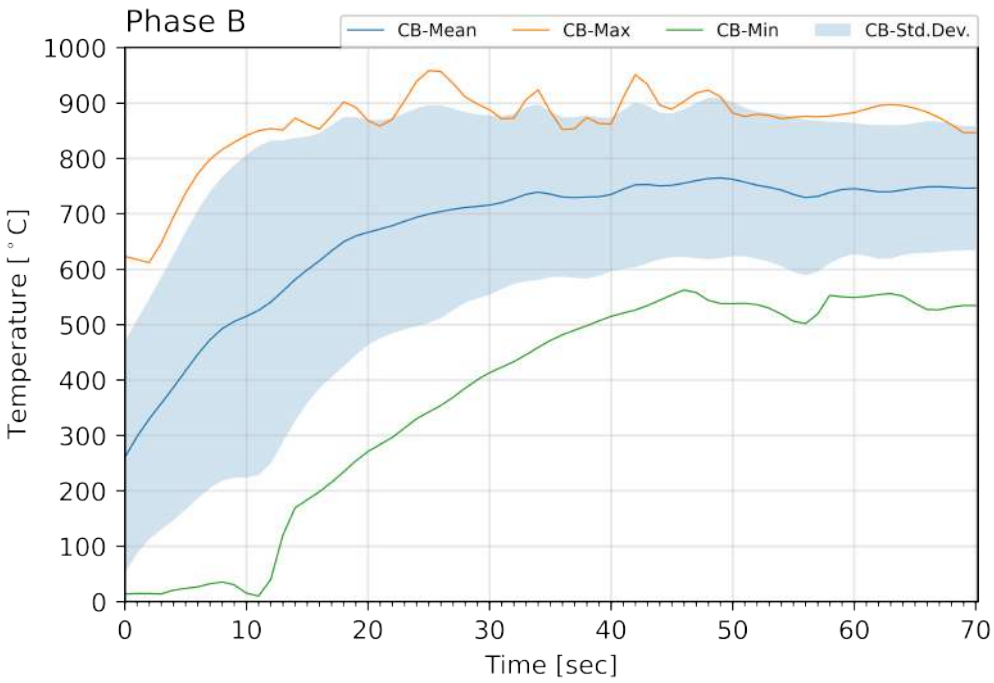

Figure C.4: Temperature graph of the thermocouple CB in Phase B.

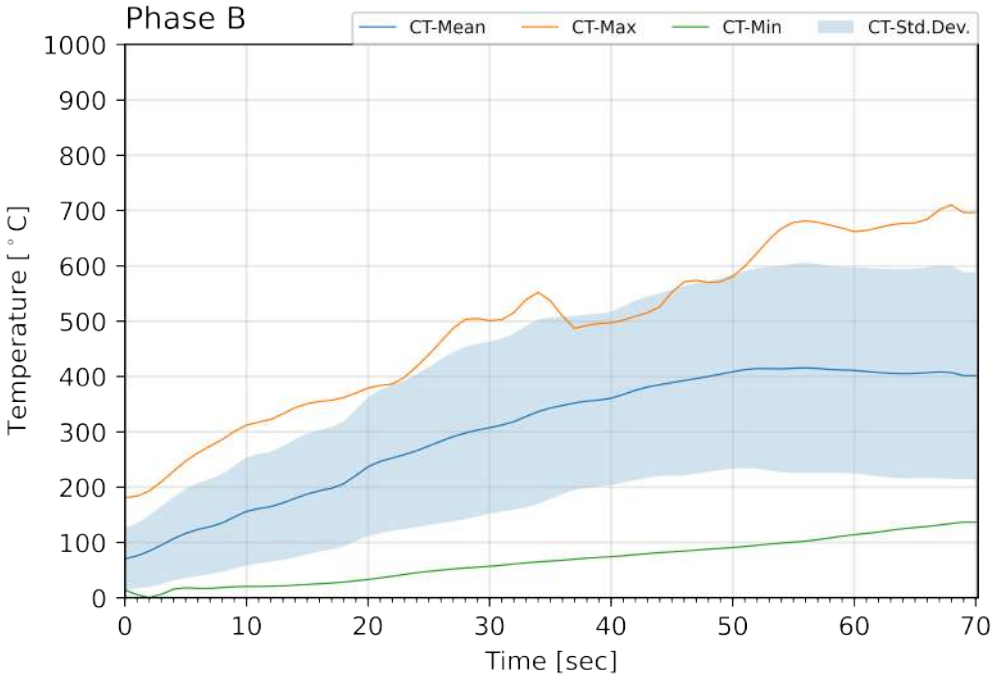

Figure C.5: Temperature graph of the thermocouple CT in Phase B.

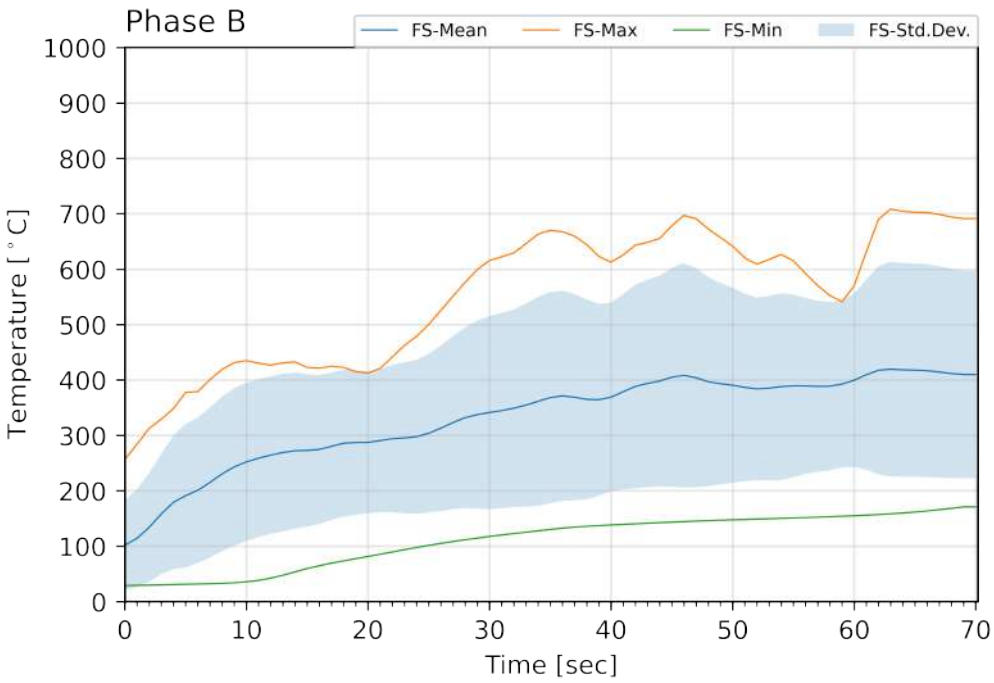

Figure C.6: Temperature graph of the thermocouple FS in Phase B.

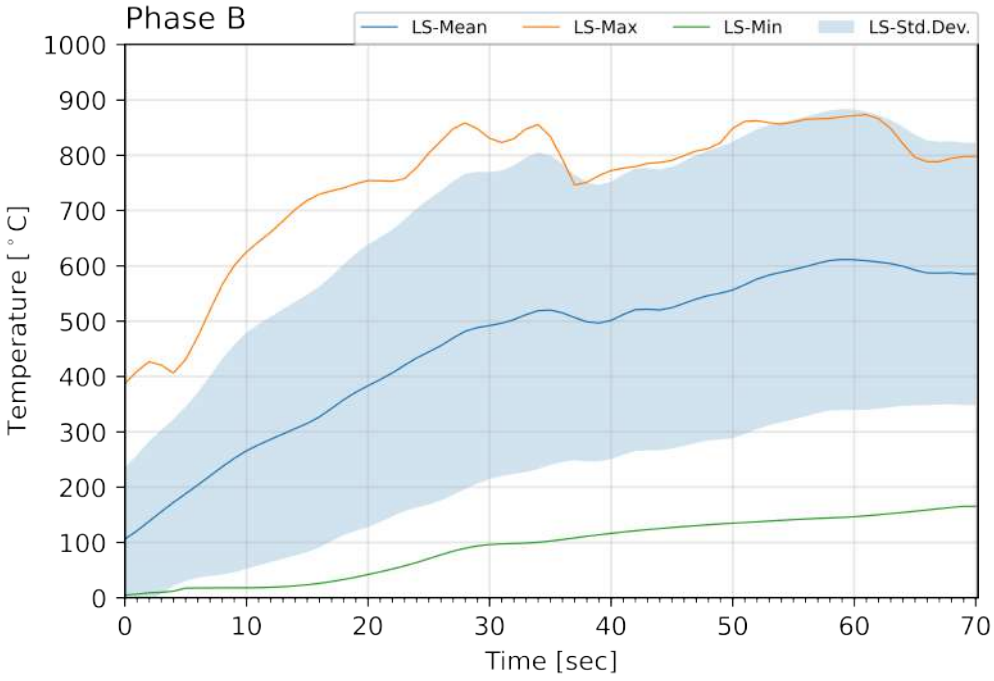

Figure C.7: Temperature graph of the thermocouple LS in Phase B.

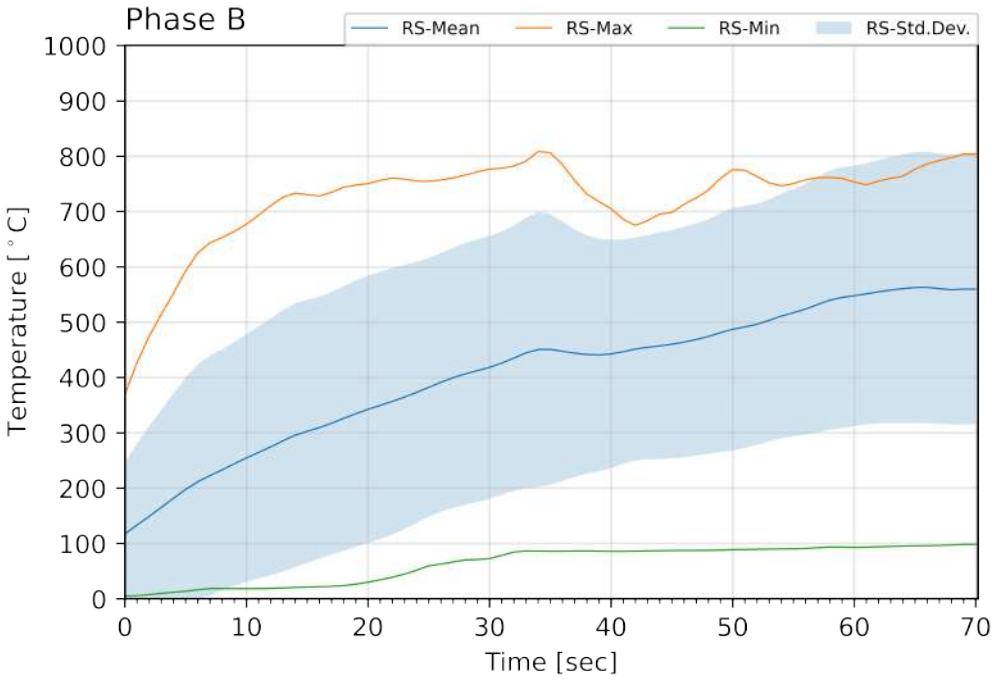

Figure C.8: Temperature graph of the thermocouple RS in Phase B.

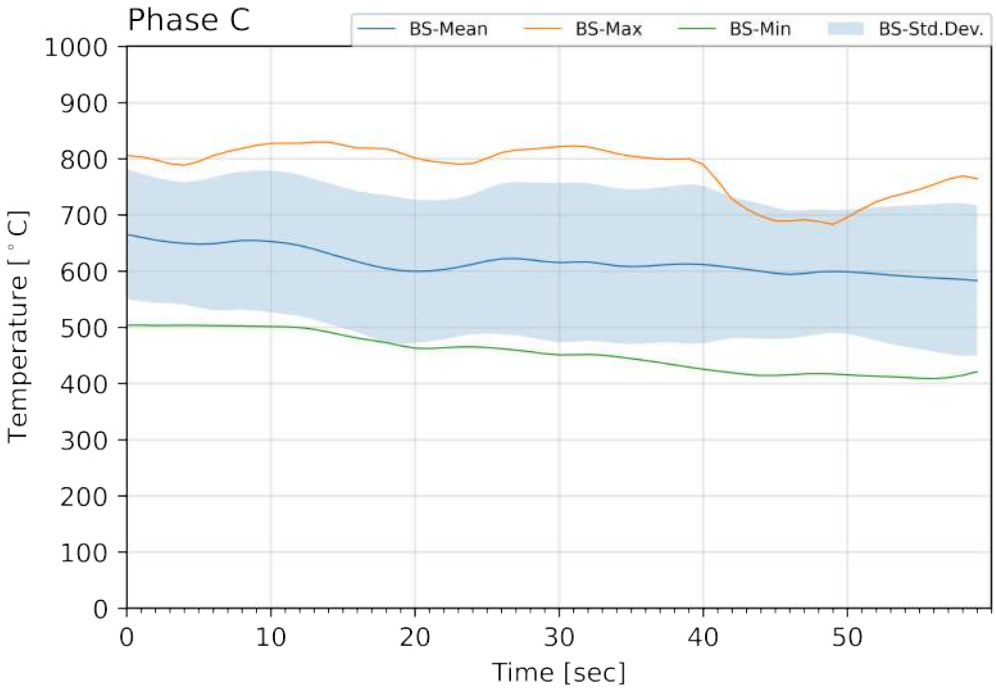

Figure C.9: Temperature graph of the thermocouple BS in Phase C.

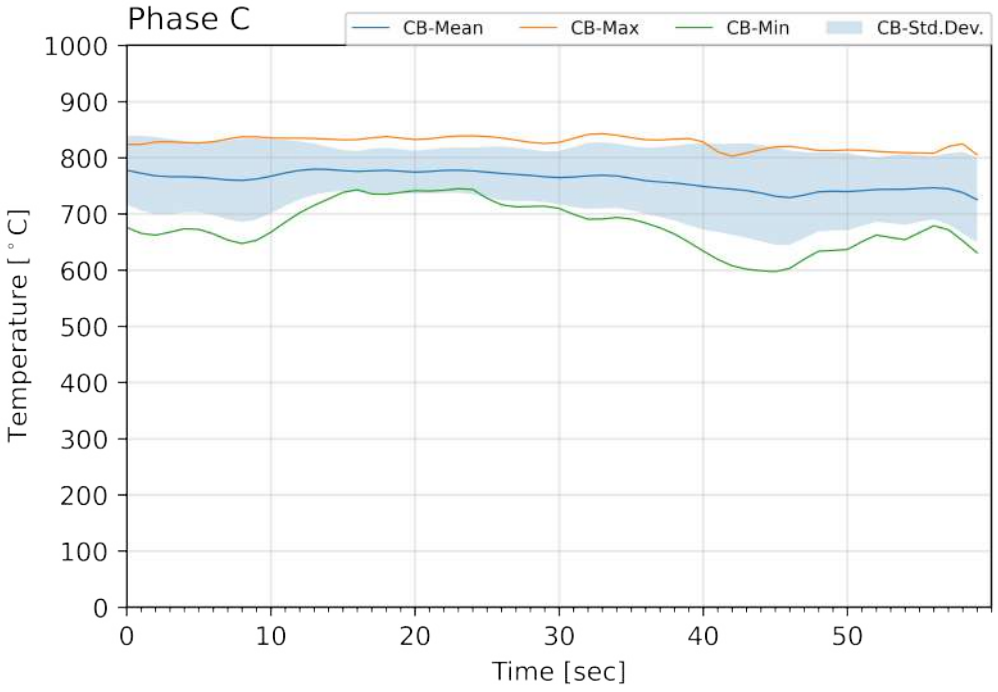

Figure C.10: Temperature graph of the thermocouple CB in Phase C.

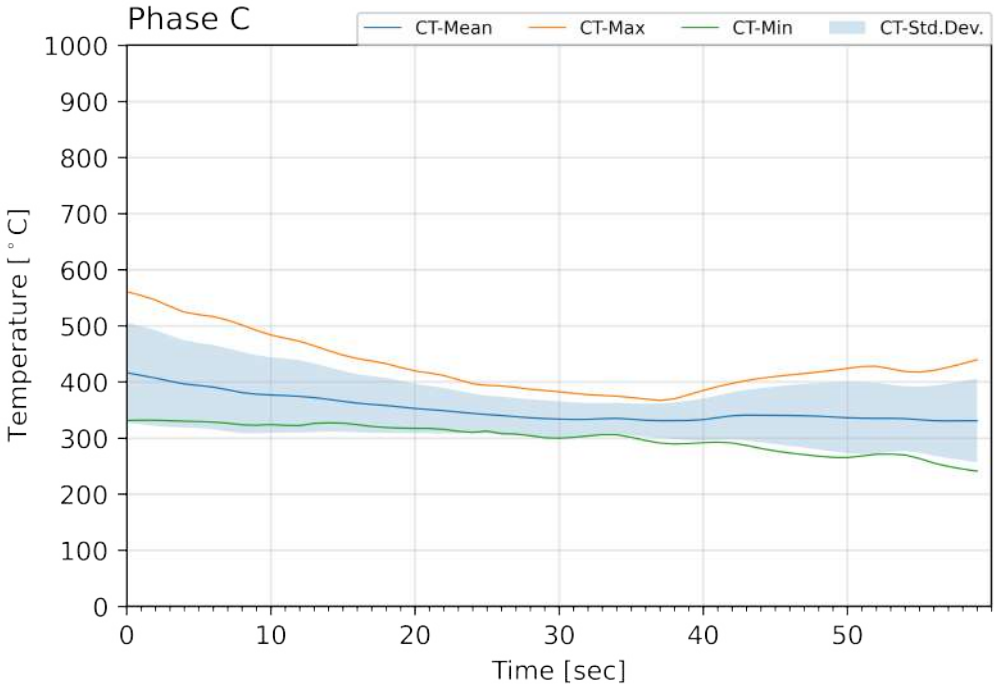

Figure C.11: Temperature graph of the thermocouple CT in Phase C.

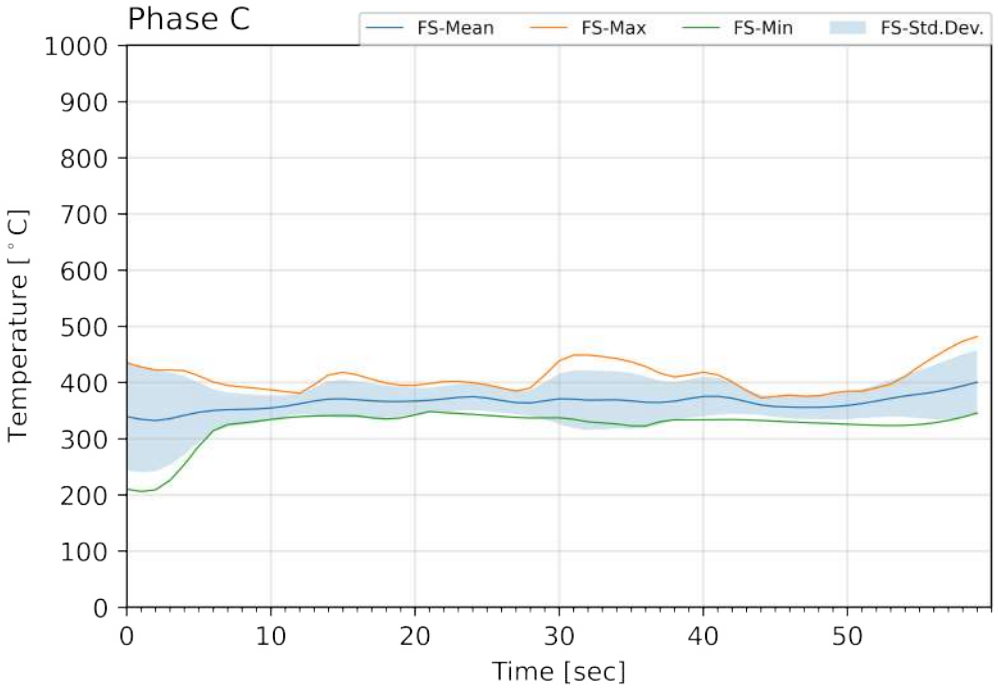

Figure C.12: Temperature graph of the thermocouple FS in Phase C.

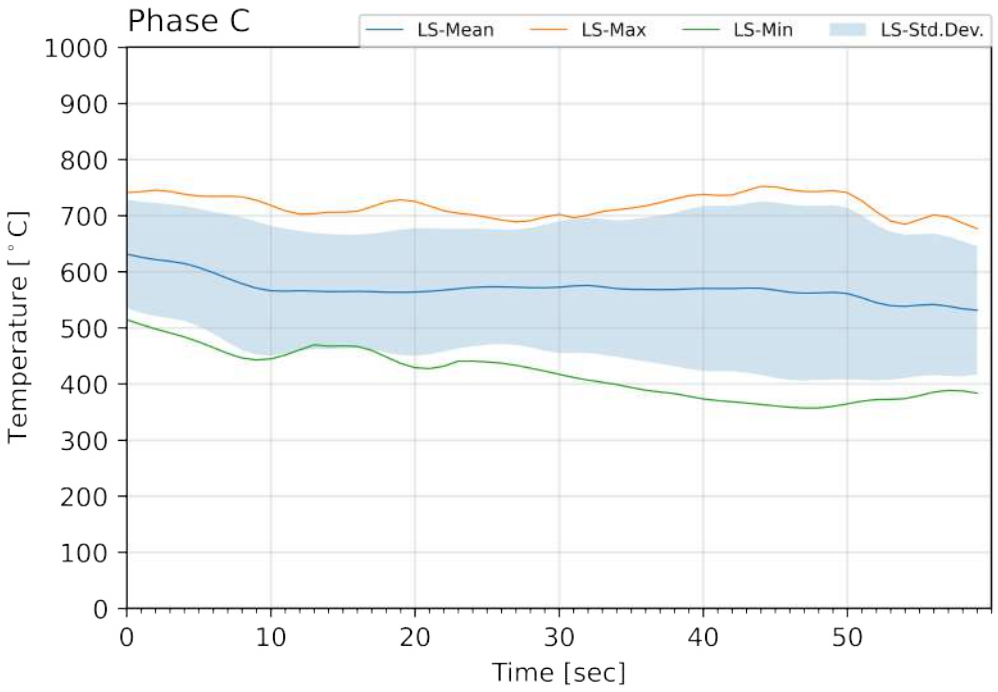

Figure C.13: Temperature graph of the thermocouple LS in Phase C.

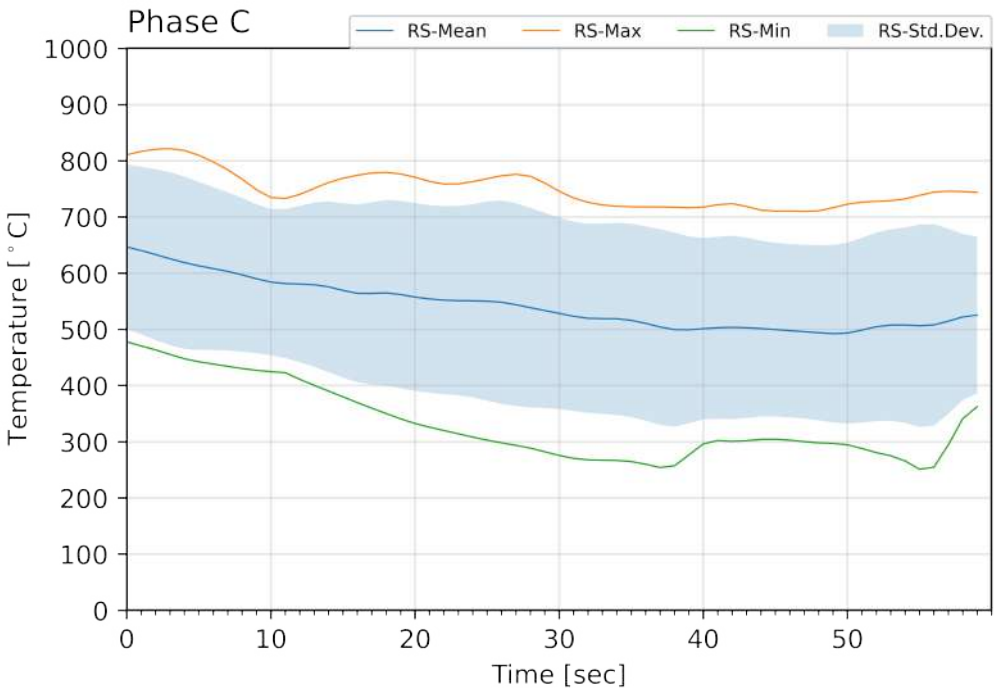

Figure C.14: Temperature graph of the thermocouple RS in Phase C.

Appendix D

Background for TREAS development

This appendix contains background works for the TREAS development leading to the construction of the prototype of the filtration system used for lithium-ion batteries under thermal runaway.

D.1 Thermal runaway emissions of lithium-ion batteries

Thermal runaway is preceded by the increase of temperature of the lithium-ion cell. First step is a breakdown of SEI layer (solid electrolyte interphase layer), layered on the anode. SEI layer purpose is to protect the anode from further reacting with the electrolyte [500]. The breakdown of the thin SEI layer occurs at 90–120 $°C$, producing primarily CO_2 [501]:

$$(CH_2OCO_2Li)_2 \longrightarrow Li_2CO_3 + C_2H_4 + CO_2 + \tfrac{1}{2}\,O_2$$

Subsequently, due to SEI layer decomposition anode and electrolyte start to interact. Typical electrolytes found in lithium-ion batteries and their reaction with anode form flammable hydrocarbons are shown below [502]:

$$2\,Li + C_3H_4O_3\,(EC) \longrightarrow Li_2CO_3 + C_2H_4$$
$$2\,Li + C_4H_6O_3\,(PC) \longrightarrow Li_2CO_3 + C_3H_6$$
$$2\,Li + C_3H_6O_3\,(DMC) \longrightarrow Li_2CO_3 + C_2H_6$$

Subsequently, polyethylene or polypropylene separator melts at 135 $°C$ and 166 $°C$ respectively, and ceramic coated separator is found to maintain integrity even over 200 $°C$ [503]. As the temperature increase the separator shrinks until cathode and anode come into contact with each other to induce ISC. ISC is a precursor for a thermal runaway, electric energy stored in the cell is further released in the approximately same amount [504].

Further reactions depend on the type of cathode used in the cell. These reaction mainly produce metallic oxides such as Co_3O_4 for LCO [505], $Li_xCO_yAl_zO_pforNCA$, $(Mn, Ni)O$ and $Li_x(Ni_{1/3}Co_{1/3}Mn_{1/3})O_2$ for NCM [406, 506] and other. Additionally, other by-products include oxygen and solid state metals.

Together with the cathode decomposition, electrolyte used in battery cell emits particular amount and type of toxic compounds. It is flammable and usually contains lithium hexafluorophosphate ($LiPF_6$) or other Li-based salts containing fluorine [323]. Promoted by the presence of water and humidity following reactions constitute to electrolyte decomposition [34]:

$$LiPF_6 \longrightarrow LiF + PF_6$$
$$PF_5 + H_2O \longrightarrow POF_3 + 2\,HF$$
$$LiPF_6 + H_2O \longrightarrow LiF + POF_3 + 2\,HF$$

The data has shown the production of HF and PO_3 per Wh at 100% SOC can be up to 193.3 mg and 22 mg respectively [34]. The production of other gaseous substances is dependent on the state of charge as well as type of chemistry used in the cell [507] and Figure D.1. Total gas generation is largely varying on used cathode material, state of charge of the cell and its shape. For the LCO/NCM 18650 type cell, it was found to be 265 mmol [508].

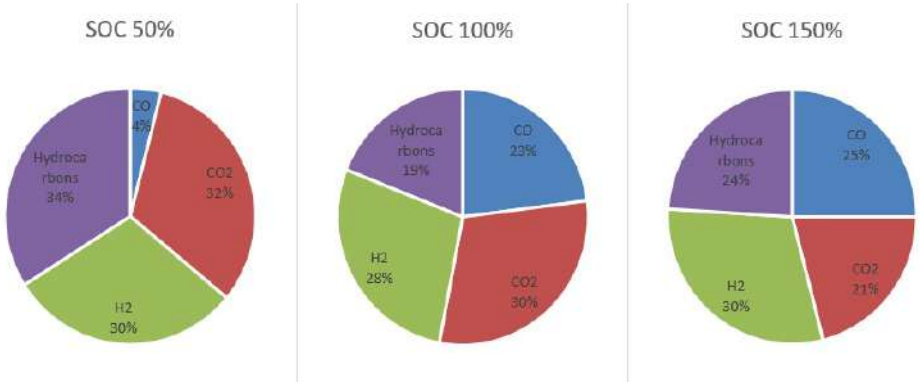

Figure D.1: Composition of gases generated from thermal runaway of commercial LIBs. Somendepalli et al. [507] results of gas generated from 7.7 Wh LCO cell at different SOC.

D.2 Cleaning methods of the gas emissions

Toxic and acid gases, such as $HCl, SO2, CO2, CO$ and HF can be neutralized by the designed agents, either supplied by the wet scrubbing equipment in absorbent solutions or by dry injection systems such as powdered alkaline sorbents [509]. Dry sorbent injection (DSI) systems characterise with low installed capital costs, relatively easy to retrofit to a majority of facilities, the system ensures good flexibility for various sorbents and low consumable requirements as well as parasitic power requirements to operate [510]. The two compounds have been predominantly used in the DSI - sodium or calcium-based [511, 509] - with the latter emerging as more accessible due to general availability of the limestone (calcium hydroxide) [512]. As such, calcium hydroxide was chosen for the TREAS to primarily clean hydrogen fluoride emissions.

After the calcium hydroxide is injected into gas emissions containing HF and CO_2 the following reactions can occur:

$$\mathrm{Ca(OH)_2 + 2\,HF \longrightarrow CaF_2 + H_2O}$$
$$\mathrm{Ca(OH)_2 + CO_2 \longrightarrow CaCO_3 + H_2O}$$

Thermodynamic calculations show the $CaCO_3$ and CaF_2 can only be formed at the temperatures below 600–800 °C [513]. The products of reaction of the dry sorbent injection are then removed with mechanical filters (bag filters) and transposed to waste. The filter is intermittently cleaned with the jet pulse of air aimed. The schematics for the Thermal Runaway Emissions Aftertreatment System using dry sorbent injection are shown in Figure D.2. From right to left: flue gas is collected by the use of extraction hood, transported through the ventilation pipes to the baghouse. In midway the calcium hydroxide hopper supplies a dry sorbent in form of powder; dryer is optional. The bag house consists of mechanical filter (bag filter), air pulse jet (a nozzle to release compressed air for bag filter cleaning) and waste funnel (cone-shaped to limit the air leakage), below the baghouse a bin collects used dry sorbent agent. Other devices were air compressor for the pulse jet and fan for air flow with extraction of gases.

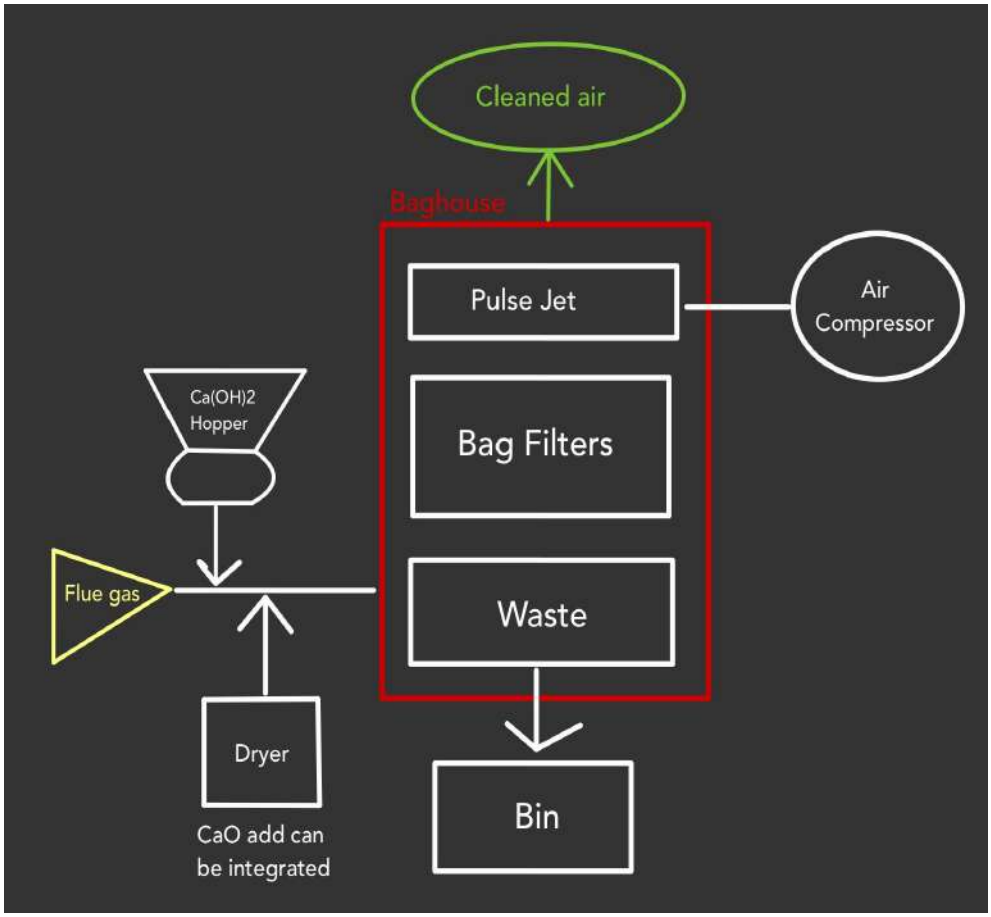

Figure D.2: TREAS schematics using dry sorbent injection and calcium hydroxide.

Appendix E

List of Standards and Regulations Referenced in the Thesis

ISO 12405-1:2011 *Electrically propelled road vehicles — Test specification for lithium-ion traction battery packs and systems — Part 1: Performance testing.*
Edition: 1

ISO 12405-2:2012 *Electrically propelled road vehicles — Test specification for lithium-ion traction battery packs and systems — Part 2: High-energy applications.*
Edition: 1

ISO 12405-3:2014 *Electrically propelled road vehicles — Test specification for lithium-ion traction battery packs and systems — Part 3: Safety performance requirements.*
Edition: 1

ISO 12405-4:2018 *Electrically propelled road vehicles — Test specification for lithium-ion traction battery packs and systems — Part 4: Performance testing.*
Edition: 1

ISO 6469-1:2019 *Electrically propelled road vehicles — Safety specifications — Part 1: On-board rechargeable energy storage system (RESS).*
Edition: 2

ISO 18243:2017 *Electrically propelled mopeds and motorcycles — Test specifications and safety requirements for lithium-ion battery systems.*
Edition: 1

ISO 834-1:2025 *Fire-resistance tests — Elements of building construction — Part 1: General requirements.*
Edition: 2

EN 1363-1:2020 *Fire resistance tests — Part 1: General requirements.*
Edition: 4

EN 45545-3:2013 *Railway applications — Fire protection on railway vehicles — Part 3: Fire resistance requirements for fire barriers.*
Edition: 1

IEC 62660-1:2018 *Secondary lithium-ion cells for the propulsion of electric road vehicles — Part 1: Performance testing.*
Edition: 2

IEC 62660-2:2018 *Secondary lithium-ion cells for the propulsion of electric road vehicles — Part 2: Reliability and abuse testing.*
Edition: 2

IEC 62660-3:2022 *Secondary lithium-ion cells for the propulsion of electric road vehicles — Part 3: Safety requirements.*
Edition: 1

UL 1973:2022 *Batteries for use in stationary, vehicle auxiliary power, and light electric rail applications.*
Edition: 2

UL 2580:2022 *Batteries for use in electric vehicles.*
Edition: 3

UL 9540A:2025 *Test method for evaluating thermal runaway fire propagation in battery energy storage systems.*
Edition: 5

UL 9540:2025 *Standard for energy storage systems and equipment.*
Edition: 3

UL 1642:2020 *Standard for lithium batteries.*
Edition: 6

UL 263:2023 *Standard for Fire Tests of Building Construction and Materials.*
Edition: 14

NFPA 68:2023 *Standard on Explosion Protection by Deflagration Venting.*
Edition: 2023

NFPA 69:2024 *Standard on Explosion Prevention Systems.*
Edition: 2024

SAE J2464:2009 *Electric and Hybrid Electric Vehicle Rechargeable Energy Storage System (RESS) Safety and Abuse Testing.*
Edition: 2009

SAE J2929:2013 *Safety standard for electric and hybrid vehicle propulsion battery systems utilizing lithium-based rechargeable cells.*
Edition: 2013

GB/T 31467.3-2015 *Safety requirements and test methods for traction battery of electric vehicle.*
Edition: 1

GB/T 31484-2015 *Lithium-ion batteries for electric vehicles — Cycle life requirements and test methods.*
Edition: 1

UNECE R100.03 (2021) *Uniform provisions concerning the approval of vehicles with regard to specific requirements for the electric power train.*
Revision: 3

UNECE Regulation No. 94 (2022) *Uniform provisions concerning the approval of vehicles with regard to the protection of the occupants in the event of a frontal collision.*
Revision: 4

UNECE Regulation No. 95 (2023) *Uniform provisions concerning the approval of vehicles with regard to the protection of the occupants in the event of a lateral collision.*
Revision: 4

UNECE Regulation No. 34 (2011) *Uniform provisions concerning the approval of vehicles with regard to the prevention of fire risks.*
Edition: 2011

UN GTR No. 20 (2018) *Global Technical Regulation on electric vehicle safety (battery safety including thermal propagation).*
Edition: 1

UN Manual of Tests and Criteria, Rev. 8 (2023) *Recommendations on the Transport of Dangerous Goods — Lithium battery testing, Part III, Sub-section 38.3.*
Edition: 8

FreedomCAR Battery Test Manual (2003) *Standardized test procedures for automotive battery systems in hybrid EVs.*
Edition: 2003

FreedomCAR EESS Abuse Test Manual (2006) *Abuse test manual for EV and hybrid vehicle applications.*
Edition: 2006

List of Figures

1.1 Holtzer-Cabot's 1895 model electric brake [5]. 4
1.2 Evolution of LIB energy density (Wh/kg) from 2010 to 2023 (based on [10, 11, 12]). 5
1.3 Global electric car stock trends over the years 2010 to 2023 [12]. 6
1.4 Electric car registrations and sales share percentage in selected countries and regions, 2015-2023 [12]. 7
1.5 Bar chart of the market share (%) of major electric vehicle types—Battery Electric Vehicles (BEV), Plug-in Hybrid Electric Vehicles (PHEV), Hybrid Electric Vehicles (HEV, other than plug-in), and Fuel Cell Electric Vehicles (FCEV), based on [12]. 8
1.6 New York City Fire Department LIB fire incidents increased track (based on [28, 29]). 10
1.7 Selected set of fire incidents involving LIBs. (a) Aftermath inside the APS McMicken battery container; (b) car carrier Felicity Ace ablaze in the Atlantic Ocean; (c) public bus depot fire in Stuttgart, (d) Tesla Megapack unit fire. 12

2.1 Schematic of the LIB design. 18
2.2 Comparison on LIB system level - cell, module or pack. 20
2.3 Comparison of the cell types: (a) cylindrical, (b) pouch and (c) prismatic. 22
2.4 Schematic chart of TR initiation. 23
2.5 Stages of the TR. 25
2.6 Abuse types for LIB assembly. 29
2.7 Visual representation of the overcharge process with increasing SOC. 30
2.8 Unwanted reactions of the LIB. 33

3.1 Heat propagation from cell to cell (denoted as C2C) example. 37
3.2 Cross-sectional diagram of a cylindrical cell's built-in safety vent (burst disk). . . 38
3.3 (a) The PCM-based cooling EV module. (b) Three different fin cases and corresponding experimental images [148]. (c) PCM/finned-HP integrated thermal management module. (d) the PCM integrated shell and tube battery pack [175]. 39
3.4 Comparison on the insulation materials - price vs. thermal conductivity (based on [158, 176, 177]). 40
3.5 Examples of segmentation and firebreak features to prevent a single cell failure in battery packs in electric vehicles (EVs): (a) Tesla's structural battery pack (Model Y with 4680 cells) [196]; (b) close-up of the Tesla structural pack's internal connections [197]. 45
3.6 Examples of segmentation and firebreak features to prevent a single cell failure in battery packs in BESS: (a) cross-sectional schematic of an EVLO stationary energy storage system enclosure (side view) [200]; (b) segmentation layout of a containerized stationary energy storage system (BESS) [201]. 46
3.7 (a) Optimization of cooling plate serpentine flow channels with splitter blades; (b) schematic of channel connections; (c) mini-channel cold plate designs [215]. . . . 51
3.8 Industrial water mist fire suppression system with overhead nozzles actively discharging a fine mist over a battery module area [237]. 54

3.9 Examples of segmentation and firebreak features. (a) Eaton's 3-in-1 battery pack vent valve for EVs [242]; (b) Example of vent path for the cylinder battery cell; (c) Deflagration vent panels on a BESS container [244]; (d) Example of a roof-mounted explosion vent panel (product image by REMBE) [243]. 56

5.1 Crushing fixtures; (a) IEC 62660-3:2022 cylindrical cell crush fixture; (b) IEC 62660-3:2022 prismatic cell crush fixture; (b) IEC 62660-3:2022 prismatic cell crush fixture [269]; (c) GB 38031-2020 crushing fixture [73]; (d) SAE J2464 and UNECE R100.03 crushing plate [254, 279]. 76
5.2 Testing set-up and procedure. 92
5.3 Testing setup and procedure according to UNECE R100.03 - KATRI testing rig [67]. 93
5.4 SAND2017-6925:2017 [275] and SAE J2464:2009 [279] testing set up - top view. . 94

6.1 Features of a turbulent fire plume, including axial variations on the centreline of mean excess temperature, δT_0, and mean velocity, u_0. 102
6.2 Calculation of the centreline temperature vs flame height based on Heskestad formulas' for pool values of 0.58, 1.64 and 2.10 m^2. 103
6.3 (a) Representation of non-tilted flame vortices (red), tilted flame partial engulfment of the DUT (orange), and cold air areas with eddy currents (blue). (b) DUT surface area relative to the required pool fire coverage. 109
6.4 (a) Radiative heat flux as a function of surface emissivity; (b) total thermal dose of SAE J2464 radiant panel test conditions. 112
6.5 Thermocouple positioning scheme and description. 115
6.6 Photograph with sample and test rig during the UNECE R100.03 test (Phase B). 116
6.7 Temperature (T) and RTC (v) over time (t) of thermocouples TC1 and TC10 in the first 600 s of the test. Phases A, B, C, and D according to Table 6.3 and Figure 6.5. 119
6.8 Temperature (T) and RTC (v) over time (t) of thermocouples TC2, TC4, and TC8 during the first 600 s of the test. Phases A, B, C, and D according to Table 6.2 and Figure 5.2. 119
6.9 Temperature (T) and RTC (v) over time (t) of TC3, TC5, TC7, and TC9 in the first 600 s of the test. Phases A, B, C, and D according to Table 6.2 and Figure 5.2.120
6.10 Model of the internal battery temperature calculation. See Section 6.3.3. 121
6.11 Calculated temperature inside the battery in comparison to TC1, TC6, and TC10. 122
6.12 Thermocouple positioning scheme for the dataset. 126
6.13 Test results charts. Temperature readings from the thermocouples located at the bottom centre of the DUT during Phase B (**a**) and C (**b**). Wind velocity in relation to average temperature (**c**) and average standard deviation (**d**) from each test (represented as points). Subsequent figures show pan coverage in relation to the average temperature (**e**) and average standard deviation (**f**). 127
6.14 Firebrick specification taken from UNECE R100.03 [254]. 130
6.15 ISO 834-1 Standard Time-Temperature Fire Curve. 133
6.16 ISO 834 furnace temperature (logarithmic profile) and corresponding heat flux variants. 136
6.17 ISO 834-1 / EN 1363-1 fire resistance test set-up (fire from inside the battery). . 138
6.18 ISO 834-1 / EN 1363-1 fire resistance test set-up (fire from inside the battery) - exploded view. 139
6.19 ISO 834-1 / EN 1363-1 fire resistance test - example photo from unexposed side. 140
6.20 ISO 834-1 / EN 1363-1 fire resistance test - example photo from exposed side. . . 141
6.21 ISO 834-1 Standard Time-Temperature Fire Curve - average (blue line) from the dataset with tolerances and standard deviation. 142

6.22 ISO 834-1 Standard Deviation of Fire Curve (from Figure 6.21) - T_{avg}, T_{avg} with standard deviation and T_{stan} standard curve. 143
6.23 κ factor (C to C_{crit} ratio; Y-axis) over time (X-axis) during the fire resistance test. 143
6.24 Fire inside test model representation. 145
6.25 Fire resistance test - fire from outside - example of a test set-up. 146
6.26 Thermal conductivity of cells depending on geometry - (a) cylindrical and (b) prismatic/pouch cell. 146

7.1 TREAS prototype testing site. P1, P2 and P3 probing points of the air flow. T1, T2, T3 temperature measurement points. 151
7.2 TREAS final model simulation at 50°C and 1500 m^3/h. 152
7.3 Flow measurements of the TREAS prototype at an ambient temperature and two fan performances. P1, P2 and P3 probing points of the air flow, see Figure 7.1. . 153

A.1 Comparison of the cathode types. 169

B.1 Air cooled battery assembly representation. 174
B.2 Liquid cooling of the battery module representation. 176

C.1 UNECE R100.03 fire test set-up. 182
C.2 Temperature graph of the UNECE R100.03 fire test. 183
C.3 Temperature graph of the thermocouple BS in Phase B. 183
C.4 Temperature graph of the thermocouple CB in Phase B. 184
C.5 Temperature graph of the thermocouple CT in Phase B. 184
C.6 Temperature graph of the thermocouple FS in Phase B. 185
C.7 Temperature graph of the thermocouple LS in Phase B. 185
C.8 Temperature graph of the thermocouple RS in Phase B. 186
C.9 Temperature graph of the thermocouple BS in Phase C. 186
C.10 Temperature graph of the thermocouple CB in Phase C. 187
C.11 Temperature graph of the thermocouple CT in Phase C. 187
C.12 Temperature graph of the thermocouple FS in Phase C. 188
C.13 Temperature graph of the thermocouple LS in Phase C. 188
C.14 Temperature graph of the thermocouple RS in Phase C. 189

D.1 Composition of gases generated from thermal runaway of commercial LIBs. Somendepalli et al. [507] results of gas generated from 7.7 Wh LCO cell at different SOC. 191
D.2 TREAS schematics using dry sorbent injection and calcium hydroxide. 192

List of Tables

1.1 List of recent incidents involving various LIBs. 11

2.1 Overview of selected LIB cell configurations, detailing variations in anode and cathode materials, electrolyte compositions, separator types, and cell formats, based on [87, 88, 89, 90, 91, 92, 93]. 21

3.1 Summary of major findings on TR prevention strategies in LIBs (based on [87, 94, 154, 155, 156, 157, 158, 159]). 35
3.2 Comparative overview of common insulation materials for high-temperature applications, including their thermal conductivity, approximate cost, and qualitative assessment of mechanical strength properties (based on [146, 179, 180, 181, 182]). 41

5.1 Comparative overview of international standards, regulations, and test methods for LIB safety and performance in electric vehicle (EV), battery energy storage system (BESS), and cell applications. 64
5.2 Comparison of Mechanical Shock Test Requirements Across Global EV Battery Safety Standards [73, 286, 254, 263, 279, 283, 276]. 68
5.3 Comparison of Drop Test Requirements in EV Battery Safety Standards [73, 254, 263, 286, 276, 279, 280, 283]. 70
5.4 Comparison of Nail Penetration Test Requirements in EV Battery Safety Standards [73, 268, 286, 254, 263, 276, 279, 280, 283]. 73
5.5 Comparative Analysis of International Standards Governing Mechanical Crush Testing Protocols for LIB Safety Assessment based on [73, 286, 254, 276, 279, 283, 285]. 75
5.6 Comparative overview of standardized vibration test procedures for BESS across international regulations and norms, based on [73, 286, 254, 263, 276, 279, 280, 283, 285, 304, 305, 306]. 79
5.7 Comparison of selected international safety testing standards for LIBs with respect to overcharge, overdischarge, and short-circuit scenarios, based on [69, 73, 260, 261, 279, 297, 285, 283, 304]. 84
5.8 Summary of environmental and thermal stress endurance parameters [73, 254, 260, 269, 279, 283, 285, 297]. 88
5.9 Comparison of the EV safety standards and regulations based on [73, 254, 259, 263, 276, 279, 283, 285]. 91
5.10 Overview of Battery Immersion Test Standards and Conditions based on [73, 263, 276, 279, 283, 321]. 98
5.11 Comparison of the protection levels IPx7 and IPx8 [321, 322]. 99

6.1 Heat flux and thermal dose numerical analysis theoretical results for the R100.03, UL 1973 and SAE J264 tests. 106
6.2 Fire-resistance testing procedure outline [254]. 107
6.3 Thermocouples locations on the RESS. 115

6.4 Maximal recorded temperature (°C) of thermocouples TC1–TC10 and the average temperature in a given phase. Phases A, B, C, and D according to Table 6.2 and Figure 5.2. 117
6.5 Maximal and average RTC v_{TC} (°C/s) for thermocouples. Phases A, B, C, and D according to Table 6.2 and Figure 5.2. 118
6.6 Information on the dataset: test method, ambient temperature, humidity, average wind velocity, initial fuel temperature, DUT length and width, pool fire length and width, and DUT coverage. 125
6.7 Summary of the exposure temperatures for Phases B and C - average temperature ($\overline{\overline{T}_i^p}$), repeatability standard deviation (σ_{Ri}^B) and κ factor for thermocouples CT, CB, RS, LS, FS, BS. 128

7.1 Testing configurations of number of cells, fan and jet pulse preset and dosage. . . 154
7.2 Mean values of the emitted gases. 154
7.3 Maximum temperature rises recorded in testing set-up 1-3 for thermocouple T1-3. 154

Bibliography

[1] A Arfwedson. Untersuchung einiger bei der eisen-grube von uto vorkommenden fossilien und von einem darin gefundenen neuen feuerfesten alkali. *J. Chem. Phys*, 22:93–117, 1818.

[2] Jons Jakob Berzelius. Ein neues mineralisches alkali und ein neues metall. *J. Chem. Phys*, 21:44–48, 1817.

[3] William Thomas Brande. *A Manual of chemistry*, volume 2. JW Parker, 1848.

[4] Gilbert N. Lewis and Frederick G. Keyes. The potential of the lithium electrode. *Journal of the American Chemical Society*, 35(4):340–344, 1913.

[5] Ernest Henry Wakefield. *History of the electric automobile: battery-only powered cars*. SAE International, 1993.

[6] William Sidney Harris. *Electrochemical studies in cyclic esters*, volume 8381. University of California Radiation Laboratory, 1958.

[7] Elena Dănilă and Dorin Dumitru Lucache. History of the first energy storage systems. In *Paper delivered at the 3rd International Symposium on the History of Electrical Engineering and of Tertiary-Level Engineering Education*, pages 27–29, 2010.

[8] Michel Armand and Philippe Touzain. Graphite intercalation compounds as cathode materials. *Materials Science and Engineering*, 31:319–329, 1977.

[9] Alain Mauger, Christian M Julien, John B Goodenough, and Karim Zaghib. Tribute to michel armand: from rocking chair–li-ion to solid-state lithium batteries. *Journal of The Electrochemical Society*, 167(7):070507, 2019.

[10] Borui Wang and Mingyin Yan. Research on the improvement of lithium-ion battery performance at low temperatures based on electromagnetic induction heating technology. *Energies*, 16(23):7780, 2023.

[11] Bernardo Faustino, Nuno Vieira Lopes, Diogo Costa, Helder Santos, Joel Vasco, Carlos Capela, Carlos Rabadão, and Carlos Ferreira. Modular lithium-ion cell battery management system with high current balancing. In *2023 3rd International Conference on Electrical, Computer, Communications and Mechatronics Engineering (ICECCME)*, pages 1–5. IEEE, 2023.

[12] International Energy Agency. Batteries and secure energy transitions. `https://www.iea.org/reports/batteries-and-secure-energy-transitions`, 2024. [Online; accessed: 2025-07-28].

[13] Oliver Smith, Oliver Cattell, Etienne Farcot, Reuben D. O'Dea, and Keith I. Hopcraft. The effect of renewable energy incorporation on power grid stability and resilience. *Science Advances*, 8(9):eabj6734, 2022.

[14] Zhenyu Liu, Jianguo Zhu, Xuebing Han, Yonghua Zheng, and Qingzhu Zhai. Energy storage in high variable renewable energy penetration systems. *CSEE Journal of Power and Energy Systems*, 6(3):586–595, 2020.

[15] European Environment Agency. New registrations of electric vehicles in europe, 10 2024.

[16] Platform for Electromobility. Platform's comments the EU Renewable Energy Directive in light of the EU Green Deal. Policy paper, Platform for Electromobility, Brussels, Belgium, February 2021. Platform for Electromobility – Policy papers.

[17] International Energy Agency. Global ev outlook 2024. Report, International Energy Agency, 2024. [Online; accessed: 2025-04-25].

[18] Daniel S. Cardoso, Paulo O. Fael, and António Espírito-Santo. A review of micro and mild hybrid systems. *Energy Reports*, 6:385–390, 2020.

[19] Samson Obu Showers and Atanda Kamoru Raji. State-of-the-art review of fuel cell hybrid electric vehicle energy management systems. *AIMS Energy*, 10(3):458–485, 2022.

[20] European Parliament and Council of the European Union. of the European Parliament and of the Council of 30 May 2018 on the approval and market surveillance of motor vehicles and their trailers, and of systems, components and separate technical units intended for such vehicles, amending Regulations (EC) No 715/2007 and (EC) No 595/2009 and repealing Directive 2007/46/EC. `https://eur-lex.europa.eu/legal-content/EN/TXT/?uri=CELEX:32018R0858`, May 2018. [Online; accessed: 2025-07-05].

[21] Seok Kang, KyuJin Shim, and Jiyoun Kim. Social media posts on the samsung galaxy note 7 explosion: A comparative analysis of crisis framing and sentiment in three nations. *Journal of International Crisis and Risk Communication Research*, 2(2):259–289, 2019.

[22] Nicholas Mohammad. Analyzing the samsung galaxy note 7 using care ethics. *STS Research Paper, University of Virginia*, pages 1–42, 2020. Academic thesis examining the Samsung Galaxy Note 7 recall and its impact on consumer trust.

[23] Ruiqing Shen, Yufeng Quan, James D McIntosh, Asad Salem, and Qingsheng Wang. Fire safety of battery electric vehicles: hazard identification, detection, and mitigation. *SAE International Journal of Electrified Vehicles*, 13(14-13-03-0024), 2024.

[24] Ulf Bergholm. Sammanställning av bränder i elfordon och eltransportmedel år 2018–2023. Technical Report MSB1647, Myndigheten för samhällsskydd och beredskap (MSB), Karlstad, Sweden, 2023. PM, Ärende nr 2020–02136.

[25] Xuning Feng, Minggao Ouyang, Xiang Liu, Languang Lu, Yong Xia, and Xiangming He. Thermal runaway mechanism of lithium ion battery for electric vehicles: A review. *Energy storage materials*, 10:246–267, 2018.

[26] Amandine Lecocq, Marie Bertana, Benjamin Truchot, and Guy Marlair. Comparison of the fire consequences of an electric vehicle and an internal combustion engine vehicle. In *2. International Conference on Fires in Vehicles-FIVE 2012*, pages 183–194. SP Technical Research Institute of Sweden. Boras, 2012.

[27] Tucker McGree. Vehicle fires: Supporting tables. Technical report, National Fire Protection Association (NFPA), Quincy, MA, November 2024. Based on data from NFIRS and NFPA fire experience survey.

[28] Robert S. Tucker New York City Fire Department. Fdny commissioner robert s. tucker announces significant progress in the battle against lithium-ion battery fires. https://www.nyc.gov/site/fdny/news/03-25/fdny-commissioner-robert-s-tucker-significant-progress-the-battle-against-lithium-ion, January 2025. [Online; accessed: 2025-07-30].

[29] Charles Fleischmann, Craig Weinschenk, Daniel Madrzykowski, Alexandra Schraiber, and Benjamin Gaudet. Quantifying the fire hazard from li-ion battery fires caused by thermal runaway in e-scooters. *Fire Technology*, 2024.

[30] Shi-Lin Wang, Xu Gong, Li-Na Liu, Yi-Tong Li, Chen-Yu Zhang, Le-Jun Xu, Xu-Ning Feng, and Huai-Bin Wang. Numerical analysis of explosion characteristics of vent gas from 18650 lifepo4 batteries with different states of charge. *Journal of The Electrochemical Society*, 171(3):030542, 2024.

[31] Gavin DJ Harper, Emma Kendrick, Paul A Anderson, Wojciech Mrozik, Paul Christensen, Simon Lambert, David Greenwood, Prodip K Das, Mohamed Ahmeid, Zoran Milojevic, et al. Roadmap for a sustainable circular economy in lithium-ion and future battery technologies. *Journal of Physics: Energy*, 5(2):021501, 2023.

[32] Gavin Harper, Roberto Sommerville, Emma Kendrick, Laura Driscoll, Peter Slater, Rustam Stolkin, Allan Walton, Paul Christensen, Oliver Heidrich, Simon Lambert, et al. Recycling lithium-ion batteries from electric vehicles. *nature*, 575(7781):75–86, 2019.

[33] Julian Mark. A tesla was in a junkyard for three weeks. then it burst into flames. https://www.washingtonpost.com/nation/2022/06/22/tesla-fire-sacramento/, 2022. [Online; accessed 28 July 2024].

[34] Fredrik Larsson, Petra Andersson, Per Blomqvist, and Bengt-Erik Mellander. Toxic fluoride gas emissions from lithium-ion battery fires. *Scientific Reports*, 7(1):10018, 2017.

[35] Adam Dorsz and Mirosław Lewandowski. Analysis of fire hazards associated with the operation of electric vehicles in enclosed structures. *Energies*, 15(1), 2022.

[36] Dorota Brzezinska and Paul Bryant. Performance-based analysis in evaluation of safety in car parks under electric vehicle fire conditions. *Energies*, 15(2), 2022.

[37] Mohammadmahdi Ghiji, Vasily Novozhilov, Khalid Moinuddin, Paul Joseph, Ian Burch, Brigitta Suendermann, and Grant Gamble. A review of lithium-ion battery fire suppression. *Energies*, 13(19), 2020.

[38] Juliette Michel. Us firefighters adapt to 'new hazards' in electric car blazes. https://techxplore.com/news/2022-06-firefighters-hazards-electric-car-blazes.html, 2022. [Online; accessed: 2025-06-20].

[39] Lucien Mathieu. Electric surge: Carmakers' electric car plans across europe 2019-2025. Report, European Federation for Transport and Environment AISBL.

[40] Ttc electric bus - caught fire; fleet grounded temporarily. https://www.bbc.com/news/uk-england-york-north-yorkshire-33273548, 2015. [Online; accessed 2025-04-18].

[41] Electric ferry (mf ytterøyningen) - fire suspected from battery compartment. https://vestbrannregion.no/wp-content/uploads/2019/11/Evalueringsrapport-Brann-i-MF-Ytter%C3%B8yningen.pdf, 2019. [Online; accessed 2025-04-18].

[42] Fred Lambert. Tesla model s plaid - spontaneously caught fire in pennsylvania; driver escaped. https://electrek.co/2021/06/30/tesla-model-s-plaid-caught-fire-strange-circumstances/, 2021. [Online; accessed 2025-04-18].

[43] InsideEVs Staff. Volkswagen id.3 - fire during charging at home. https://insideevs.com/news/527874/volkswagen-id3-netherlands-fire-charging/, 2021. [Online; accessed 2025-04-18].

[44] Thanos Pappas. Wuling mini ev - spontaneous combustion while parked. https://www.carscoops.com/2022/01/dongfengs-fengguang-mini-ev-is-the-alter-ego-of-wulings-hongguang-mini-ev/, 2022. [Online; accessed 2025-04-18].

[45] Reuters Staff. Bolloré bluebus - two paris buses caught fire; fleet suspended. https://www.reuters.com/business/autos-transportation/, 2022. [Online; accessed 2025-04-18].

[46] Sean. Li auto l9 - caught fire while charging. https://www.gizmochina.com/2023/01/30/li-auto-l9-catch-fire-china/, 2023. [Online; accessed 2025-04-18].

[47] Stephen Rivers. Mv fremantle highway - cargo ship fire; 500 evs onboard. https://www.carscoops.com/, 2023. [Online; accessed 2025-04-18].

[48] Associated Press and Tom Krisher. Tesla model s - crash into tree in oregon; fatal. https://www.kktv.com/, 2023. [Online; accessed 2025-04-18].

[49] Norafiqin Hairoman. Tesla model 3 - crash in south lake tahoe; 1 infant dead. https://www.cbsnews.com/sacramento/news/, 2023. [Online; accessed 2025-04-18].

[50] Stephen Rivers. Rivian r1t - came to fire at a repair facility. https://www.carscoops.com/2025/03/, 2024. [Online; accessed 2025-04-18].

[51] Joshua Bawor. Jaguar i-pace - several spontaneous fire reports; nhtsa investigation. https://www.facebook.com/InsideeVs/posts/, 2024. [Online; accessed 2025-04-18].

[52] WSFA 12 News Staff and Sally Pitts. Tesla model s - caught fire on i-65; 36,000 gallons to extinguish. https://www.wsfa.com/2023/12/26/driver-custody-after-tesla-crashes-burns-interstate-65/, 2024. [Online; accessed 2025-04-18].

[53] Ev dealership - electric car dealership burned down in lauffen am neckar. https://www.reddit.com/r/CatastrophicFailure/, 2024. [Online; accessed 2025-04-18].

[54] Latricia Thomas. Kia ev9 - caught fire in chattanooga, damaging vehicles and prompting evacuation. https://m.facebook.com/LatriciaThomasWTVC/, 2024. [Online; accessed 2025-04-18].

[55] WBTV. Tesla (unspecified model) - caught fire in charlotte neighborhood. https://www.wbtv.com/2025/04/14/, 2024. [Online; accessed 2025-04-18].

[56] People. Tesla (unspecified model) - crash and fire in toronto; four fatalities. https://people.com/4-killed-after-tesla-crash-sparks-fire-in-toronto-8743464, 2024. [Online; accessed 2025-04-18].

[57] Associated Press. Tesla cybertruck - crash and fire in las vegas; one fatality. https://www.pbs.org/newshour/nation/, 2025. [Online; accessed 2025-04-18].

[58] Andrew J. Hawkins. Rivian (unspecified model) - fire at rivian factory parking lot, vehicle damage. https://www.theverge.com/2024/8/26/24228982/rivian-factory-ev-fire-damage-battery, 2024. [Online; accessed 2025-04-18].

[59] Newsflare Staff. Deepal sl03 - fire incident in mainland china. https://www.newsflare.com/video/673305/, 2024. [Online; accessed 2025-04-18].

[60] Jack Aylmer. Xiaomi su7 - crash into guardrail in anhui; fire and three fatalities. https://san.com/cc/fatal-accident-in-china-involving-xiaomi-ev-leaves-3-dead/, 2025. [Online; accessed 2025-04-18].

[61] Sebastien Bell. Byd dealership - fire at byd dealership in fuzhou. https://www.carscoops.com/, 2024. [Online; accessed 2025-04-18].

[62] South China Morning Post Staff. Electric bicycles - fire in residential building in nanjing from e-bikes; 15 dead, 44 injured. https://www.scmp.com/news/china/politics/article/3253086/, 2024. [Online; accessed 2025-04-18].

[63] Wikipedia Contributors. Aricell battery factory - battery explosions at factory in hwaseong; 23 dead, 8 injured. https://en.wikipedia.org/wiki/Hwaseong_battery_factory_fire, 2024. [Online; accessed 2025-04-18].

[64] ABC News Australia Staff. Residential (battery fire) - lithium-ion battery fire killed one in sydney. https://www.abc.net.au/news/2025-02-18/nsw-fatal-house-guildford-fire-ebike-battery/104948908, 2025. [Online; accessed 2025-04-18].

[65] People Magazine Staff. Tesla cybertruck - crash and fire in piedmont, california; 3 fatalities. https://people.com/witness-recounts-cybertruck-crash-that-killed-3-college-students-in-november-2024-11714 2024. [Online; accessed 2025-04-18].

[66] Daniel Darnikowski, Magdalena Mieloszyk, and Mateusz Weryk. Fire resistance of construction elements. In *Sensors and Smart Structures Technologies for Civil, Mechanical, and Aerospace Systems 2022*, volume 12046, pages 203–218. SPIE, 2022.

[67] Economic Commission for Europe of the United Nations. Global technical regulation on the electric vehicle safety (evs). Regulation, March 2016.

[68] Electrically propelled road vehicles — Safety specifications — Part 1: Rechargeable energy storage system (RESS). Standard, International Organization for Standardization, Geneva, CH, April 2019.

[69] Secondary lithium-ion cells for the propulsion of electric road vehicles - Part 3: Safety requirements. Standard, The International Electrotechnical Commission, Geneva, CH, August 2016.

[70] Bhavya Kotak, Yash Kotak, Katja Brade, Tibor Kubjatko, and Hans-Georg Schweiger. Battery crush test procedures in standards and regulation: Need for augmentation and harmonisation. *Batteries*, 7(3), 2021.

[71] National Highway Traffic Safety Administration. Federal motor vehicle safety standards; fmvss no. 305a electric-powered vehicles: Electric powertrain integrity. https://www.federalregister.gov/, April 2024. Federal Register, Vol. 89, No. 73, pp. 26704–26754.

[72] Lithium-ion traction battery pack and system for electric vehicles—Part 3:Safety requirements and test methods. Standard, Standardization Administration of the People's Republic of China, Shenzhen, CN, May 2015.

[73] Electric vehicles traction battery safety requirement. Standard, Standardization Administration of the People's Republic of China, Shenzhen, CN, December 2020.

[74] David Wagman. Dispute erupts over what sparked an explosive li-ion energy storage accident. *IEEE Spectrum*. [Online; accessed: 2025-07-31].

[75] Reuters News Agency. Ship carrying porsches and bentleys ablaze near azores, towing boats en route. *Reuters*. [Online; accessed: 2025-07-31].

[76] Deutsche Welle News. Germany: Large fire at stuttgart bus depot. DW.com (English Service). [Online; accessed: 2025-07-31].

[77] Natalie Filatoff. Fire at victorian big battery now under control. *PV Magazine Australia*. [Online; accessed: 2025-07-31].

[78] Wei Shen, Ning Wang, Jun Zhang, Feng Wang, and Guangxu Zhang. Heat generation and degradation mechanism of lithium-ion batteries during high-temperature aging. *ACS Omega*, 7:4567–4578, 2022.

[79] Feng Gao, Wei Zhang, Yi Cui, and Dawei Wang. Development and challenges of $lifepo_4$ cathode material for lithium-ion batteries. *Energy & Environmental Science*, 4(4):1079–1093, 2011.

[80] Ahmet Koç, Denis Danilov, Michael Kohns, and Andreas Helwig. Review—recent advances and remaining challenges for lithium ion battery cathodes: I. nickel-rich, $lini_xco_ymn_zo_2$. *Journal of The Electrochemical Society*, 167(2):020502, 2020.

[81] Jiaxing Yang, Hengyun Zhang, Yidong Xu, and Peichao Li. Analysis of heat generation in lithium-ion battery components and voltage rebound based on electrochemical and thermal coupled model. *Journal of Energy Storage*, 72:108554, 2023.

[82] Kang Xu. Nonaqueous liquid electrolytes for lithium-based rechargeable batteries. *Chemical Reviews*, 104(10):4303–4418, 2004.

[83] Lijie Zhang, Xian Wang, and Jian Chen. A review of functional separators for lithium metal batteries: polyolefin membranes and modifications. *Frontiers in Energy Research*, 8:243, 2020.

[84] Seham Shahid and Martin Agelin-Chaab. A review of thermal runaway prevention and mitigation strategies for lithium-ion batteries. *Energy Conversion and Management: X*, 16:100310, 2022.

[85] Donald Bernardi, Edmund Pawlikowski, and John Newman. A general energy balance for battery systems. *Journal of the Electrochemical Society*, 132(1):5–12, 1985.

[86] Jian Wang, Zhenyu Niu, Zhaoxu Li, and Chengqiang Wang. Analysis of heat generation in lithium-ion batteries: reversible, irreversible and mixing contributions. *Journal of Power Sources*, 525:231120, 2023.

[87] Yixin Dai and Aidin Panahi. Thermal runaway process in lithium-ion batteries: A review. *Next Energy*, 6:100186, 2025.

[88] MJ Loveridge, Michael J Lain, ID Johnson, Alexander Roberts, Shane D Beattie, Richard Dashwood, JA Darr, and Rohit Bhagat. Towards high capacity li-ion batteries based on silicon-graphene composite anodes and sub-micron v-doped lifepo4 cathodes. *Scientific reports*, 6(1):37787, 2016.

[89] Francois Larouche, Frederic Voisard, Kamyab Amouzegar, Georges Houlachi, Patrick Bouchard, Ashok Vijh, and George P Demopoulos. Kinetics, mechanism, and optimization modeling of a green lfp delithiation process developed for direct recycling of lithium-ion batteries. *Industrial & Engineering Chemistry Research*, 62(2):903–915, 2023.

[90] Montse Casas-Cabanas, Alexandre Ponrouch, and M Rosa Palacín. Blended positive electrodes for li-ion batteries: From empiricism to rational design. *Israel Journal of Chemistry*, 61(1-2):26–37, 2021.

[91] Jean-Marie Tarascon and Michel Armand. Issues and challenges facing rechargeable lithium batteries. *Nature*, 414(6861):359–367, 2001.

[92] Yinyu Xiang, Junsheng Li, Jiaheng Lei, Dan Liu, Zhizhong Xie, Deyu Qu, Ke Li, Tengfei Deng, and Haolin Tang. Advanced separators for lithium-ion and lithium–sulfur batteries: a review of recent progress. *ChemSusChem*, 9(21):3023–3039, 2016.

[93] Satish Bolloju, Naresh Vangapally, Yuval Elias, Shalom Luski, Nae-Lih Wu, and Doron Aurbach. Electrolyte additives for li-ion batteries: classification by elements. *Progress in Materials Science*, 147:101349, 2025.

[94] Ming He, Xue Yang, Yifan Shen, Bo Li, and Jie Chen. Thermal runaway process in lithium-ion batteries: A comprehensive review. *Renewable and Sustainable Energy Reviews*, 203:112456, 2024.

[95] Yadyra Ortiz, Paul Arévalo, Diego Peña, and Francisco Jurado. Recent advances in thermal management strategies for lithium-ion batteries: a comprehensive review. *Batteries*, 10(3):83, 2024.

[96] Yuqing Chen, Yuqiong Kang, Yun Zhao, Li Wang, Jilei Liu, Yanxi Li, Zheng Liang, Xiangming He, Xing Li, Naser Tavajohi, et al. A review of lithium-ion battery safety concerns: The issues, strategies, and testing standards. *Journal of Energy Chemistry*, 59:83–99, 2021.

[97] Li Wang, Yuqing Chen, and Xiangming He. Thermal runaway process in lithium-ion batteries: A review. *Energy Storage Materials*, 62:102949, 2024.

[98] Xinlei Zhang, Shichun Chen, Jinhua Zhang, and Yifan Gao. A critical review of thermal runaway prediction and early-warning methods for lithium-ion batteries. *Energy Material Advances*, 4:0008, 2023.

[99] Xuning Feng, Dongsheng Ren, Xiangming He, and Minggao Ouyang. Time sequence map for interpreting the thermal runaway mechanism of lithium-ion batteries with $lini_xco_ymn_zo_2$ cathode. *Frontiers in Energy Research*, 6:126, 2018.

[100] Zhilong Liu, Hewu Wang, Kai Yang, Wei Huang, Chengshan Xu, and Yalun Li. Experimental study of thermal runaway process of 256ah prismatic nickel-rich battery. *Frontiers in Energy Research*, 11:1230429, 2023.

[101] Yang Yang, David Raymand, and Daniel Brandell. A cost-effective alternative to accelerating rate calorimetry: Analyzing thermal runaways of lithium-ion batteries through thermocouples. *Journal of Power Sources*, 612:234807, 2024.

[102] Taeho Yoon, Mickdy S Milien, Bharathy S Parimalam, and Brett L Lucht. Thermal decomposition of the solid electrolyte interphase (sei) on silicon electrodes for lithium ion batteries. *Chemistry of Materials*, 29(7):3237–3245, 2017.

[103] NE Galushkin, NN Yazvinskaya, and DN Galushkin. Mechanism of thermal runaway in lithium-ion cells. *Journal of The Electrochemical Society*, 165(7):A1303, 2018.

[104] Xiang Liu, Liang Yin, Dongsheng Ren, Li Wang, Yang Ren, Wenqian Xu, Saul Lapidus, Hewu Wang, Xiangming He, Zonghai Chen, et al. In situ observation of thermal-driven degradation and safety concerns of lithiated graphite anode. *Nature Communications*, 12(1):4235, 2021.

[105] Junxian Hou, Languang Lu, Li Wang, Atsushi Ohma, Dongsheng Ren, Xuning Feng, Yan Li, Yalun Li, Issei Ootani, Xuebing Han, et al. Thermal runaway of lithium-ion batteries employing lin(so2f)2-based concentrated electrolytes. *Nature communications*, 11(1):5100, 2020.

[106] Lei Ma, Shuping Wang, Xinyu Liu, Siqi Chen, Xuning Feng, Languang Lu, Xiangming He, and Minggao Ouyang. A fitting method to characterize the gaseous venting behavior of lithium–ion batteries in a sealed chamber during thermal runaway. *Energies*, 16(23):7874, 2023.

[107] Li Wang and Yuqing Chen. Gas venting techniques in ev battery during thermal runaway. *GreyB Research*, 2023.

[108] Federal Aviation Administration. Evaluation of lithium battery thermal runaway vent gas combustion hazard, 2022.

[109] Haoyu Fang, Ruixu Wang, Tongzhao Yan, and Yiyang Yan. The high-performance separators in the power lithium-ion batteries, 2021.

[110] ENTEK. Technology - lithium battery separators. https://entek.com/lithium/technology/, 2021. [Online; accessed: 2025-08-13].

[111] Bakhshish Preet Singh, Yashraj Gurumukhi, Engin Tekinalp, Hao Wu, Myung Ki Sung, and Nenad Miljkovic. Improved internal short circuit models for thermal runaway simulations in lithium-ion batteries, 2025.

[112] Soroosh Sharifi-Asl, Jun Lu, Khalil Amine, et al. Oxygen release degradation in li–ion battery cathode materials. OSTI Technical Report OSTI ID: 1526722, U.S. Department of Energy, Office of Scientific and Technical Information, 2019.

[113] Wei Zhang, Jian Liu, Qingsong Wang, and Shriram Santhanagopalan. Unveiling a critical exothermic reaction in the thermal runaway of lithium-ion batteries. *ChemRxiv*, 2025.

[114] Qingsong Wang, Binbin Mao, Stanislav I Stoliarov, and Jinhua Sun. A review of lithium ion battery failure mechanisms and fire prevention strategies. *Progress in Energy and Combustion Science*, 73:95–131, 2019.

[115] Wei Yan, Zhirong Wang, and Shichen Chen. Quantitative analysis on the heat transfer modes in the process of thermal runaway propagation in lithium-ion battery pack under confined and semi-confined space. *International Journal of Heat and Mass Transfer*, 176:121483, 2021.

[116] Binghe Liu, Yikai Jia, Chunhao Yuan, Lubing Wang, Xiang Gao, Sha Yin, and Jun Xu. Safety issues and mechanisms of lithium-ion battery cell upon mechanical abusive loading: A review. *Energy Storage Materials*, 22:1–27, 2019.

[117] Binghe Liu, Jinjie Zhang, Chao Zhang, and Jun Xu. Mechanical integrity of 18650 lithium-ion battery module: packing density and packing mode. *Engineering Failure Analysis*, 91:315–326, 2018.

[118] Hsin Wang, Thomas R. Watkins, Srdjan Simunovic, Philip R. Bingham, Srikanth Allu, and John A. Turner. Fragmentation of copper current collectors in li-ion batteries during spherical indentation. *Journal of Power Sources*, 364:432–436, 2017.

[119] Yikai Jia, Xiang Gao, Lin Ma, and Jun Xu. Comprehensive battery safety risk evaluation: aged cells versus fresh cells upon mechanical abusive loadings. *Advanced Energy Materials*, 13(24):2300368, 2023.

[120] J. Zhang, Q. Wang, J. Sun, and et al. Internal short circuit and failure mechanisms of lithium-ion pouch cells under mechanical indentation abuse conditions: An experimental study. *Journal of Power Sources*, 455:227–239, 2020.

[121] L. Zhao, Q. Wang, Y. Li, and et al. Failure mechanism of cylindrical lithium-ion batteries under large deformation. *SSRN Electronic Journal*, 2024.

[122] Zhixiong Chai, Junqiu Li, Ziming Liu, Zhengnan Liu, and Xin Jin. Experimental analysis and safety assessment of thermal runaway behavior in lithium iron phosphate batteries under mechanical abuse. *Scientific Reports*, 14(1):8673, 2024.

[123] F. Wenduo, S. Shiqi, and W. Bo. An overview of lithium-ion battery safety: Existing problems and potential solutions. *E3S Web of Conferences*, 606:02010, 2025.

[124] M. Chen, Q. Ye, C. Shi, Q. Cheng, B. Qie, X. Liao, H. Zhai, Y. He, and Y. Yang. New insights into nail penetration of li-ion batteries: Effects of heterogeneous contact resistance. *ChemSusChem*, 12:1–14, 2019.

[125] Mehmet Rona, YooEup Hyung, Brian Barnett, and Suresh Sriramulu. The relationship of the nail penetration test to safety of li-ion cells. In *2012 DOE Vehicle Technologies Program, Annual Merit Review and Peer Evaluation Meeting*, DOE SBIR Phase II Project, ES142, May 13–17, 2012, 2012. U.S. Department of Energy.

[126] Xi Zhang, Shun Chen, Jingzhe Zhu, and Yizhao Gao. A critical review of thermal runaway prediction and early-warning methods for lithium-ion batteries. *Energy Material Advances*, 4:0008, 2023.

[127] Rui Zhao, Jichao Liu, and Jinqiu Gu. A critical review on diagnosis and prognosis of battery short circuit. *Energies*, 13(6):1395, 2020.

[128] Battery Swap Cabinet. How to handle lithium battery overcharge: A complete safety guide, jun 2025. [Online; accessed: 2025-07-06].

[129] Xiaoping Yi, Guoqing Qi, Xunliang Liu, Christopher Depcik, and Lin Liu. Decomposition reactions of anode solid electrolyte interphase (sei) components with $lipf_6$-based electrolyte. *The Journal of Physical Chemistry C*, 128(32):13395–13401, 2024.

[130] Fredrik Larsson, Petra Andersson, Per Blomqvist, and Bengt-Erik Mellander. Gas generation in lithium-ion batteries: Mechanisms, failure pathways, and thermal safety implications. *Batteries*, 11(4):152, 2024.

[131] Ruslan R Samigullin, Zoya V Bobyleva, Maxim V Zakharkin, Emiliya V Zharikova, Marina G Rozova, Oleg A Drozhzhin, and Evgeny V Antipov. On the thermal stability of selected electrode materials and electrolytes for na-ion batteries. *Energies (19961073)*, 17(16), 2024.

[132] Yafei Huang, Haotian Yang, Yan Gao, Guorong Chen, Yan Li, Liyi Shi, and Dengsong Zhang. Mechanism and solutions of lithium dendrite growth in lithium metal batteries. *Materials Chemistry Frontiers*, 8(5):1282–1299, 2024.

[133] Separator testing for lithium-ion batteries. *TA Instruments*, April 2023.

[134] Evan Walter Clark Spotte-Smith, Thea Bee Petrocelli, Hetal D Patel, Samuel M Blau, and Kristin A Persson. Elementary decomposition mechanisms of lithium hexafluorophosphate in battery electrolytes and interphases. *ACS Energy Letters*, 8(1):347–355, 2022.

[135] Carla Menale, Francesco Vitiello, Antonio Nicolò Mancino, Vincenzo Sglavo, Francesco Vellucci, and Antonio Scotini. Analysis of the effects of overcharging lithium ion cells with graphite anode: Efficiency of protection devices integrated into the cells. *Chemical Engineering Transactions*, 111:523–528, 2024.

[136] Tianye Zheng, Madithedu Muneeswara, Haihong Bao, Jiaqiang Huang, Leiting Zhang, David S. Hall, Steven T. Boles, and Wei Jin. Gas evolution in li-ion rechargeable batteries: A review on operando sensing technologies, gassing mechanisms, and emerging trends. *ChemElectroChem*, 11(15):e202400065, 2024.

[137] Power Sonic. What is lead acid battery thermal runaway?, 2022. https://www.power-sonic.com/blog/sla-thermal-runaway/; [Online; accessed: 2025-06-27].

[138] C Hendricks, A Mansour, D Fuentevilla, J Ko, and G Waller. Copper dissolution investigations in large-format lithium-ion cells. In *48th Power Sources Conf.* Denver, CO, 2018.

[139] Jia Guo, Pengwei Li, Francesco Piccolo, Yulin Jie, Haojun Jia, Ruiguo Cao, Shuhong Jiao, Philipp Adelhelm, and Yaolin Xu. Degradation and failure mechanisms of lithium/lini$_x$co$_y$mn$_{1-x-y}$o$_2$ batteries using liquid electrolytes. *ACS Energy Letters*, 10(5):2318–2340, 2025.

[140] Taehoon Kim, Luis K. Ono, and Yabing Qi. Understanding the active formation of a cathode–electrolyte interphase (cei) layer with energy level band bending for lithium-ion batteries. *Journal of Materials Chemistry A*, 11(1):221–231, 2023.

[141] Siyan Chen, Zhenhai Gao, and Tianjun Sun. Safety challenges and safety measures of li-ion batteries. *Energy Science & Engineering*, 9(9):1647–1672, 2021.

[142] Tao Zhang, Kaixiang Xu, Yongyao Xia, Zhaosen Guo, Tsunghsuan Chen, and Khalil Amine. Oxygen release and its effect on the cycling stability of linixmnycozo2 (nmc) cathode materials for li-ion batteries. *Journal of the Electrochemical Society*, 164(7):A1361–A1369, 2017.

[143] Xin Gu, Yunlong Shang, Jinglun Li, Yuhao Zhu, Xuewen Tao, Hao Geng, Zhen Zhang, and Chenghui Zhang. Early warning of thermal runaway based on state of safety for lithium-ion batteries. *Communications Engineering*, 4(1):1–9, 2025.

[144] Jun Deng, Zhen Hu, Jian Chen, Jingyu Zhao, and Bai Zujin. Safety methods for mitigating thermal runaway of lithium-ion batteries—a review. *Fire*, 8(6):223, 2025.

[145] Pyrophobic Systems Limited. A guide to thermal runaway mitigation and containment. `https://pyrophobic.com/blog/thermal-runaway-mitigation-and-containment/`, April 2024. [Online; accessed: 2025-07-06].

[146] Fen Liu, Jianfeng Wang, Na Yang, Fuqiang Wang, Yaping Chen, Dongchen Lu, Hui Liu, Qian Du, Xutong Ren, and Mengyu Shi. Experimental study on the alleviation of thermal runaway propagation from an overcharged lithium-ion battery module using different thermal insulation layers. *Energy*, 257:124768, 2022.

[147] Wenxin Mei, Zhi Liu, Chengdong Wang, Chuang Wu, Yubin Liu, Pengjie Liu, Xudong Xia, Xiaobin Xue, Xile Han, Jinhua Sun, et al. Operando monitoring of thermal runaway in commercial lithium-ion cells via advanced lab-on-fiber technologies. *Nature communications*, 14(1):5251, 2023.

[148] Donal P Finegan, Mario Scheel, James B Robinson, Bernhard Tjaden, Ian Hunt, Thomas J Mason, Jason Millichamp, Marco Di Michiel, Gregory J Offer, Gareth Hinds, et al. In-operando high-speed tomography of lithium-ion batteries during thermal runaway. *Nature communications*, 6(1):6924, 2015.

[149] Evan Walter Clark Spotte-Smith, Samuel M Blau, Xiaowei Xie, Hetal D Patel, Mingjian Wen, Brandon Wood, Shyam Dwaraknath, and Kristin Aslaug Persson. Quantum chemical calculations of lithium-ion battery electrolyte and interphase species. *Scientific Data*, 8(1):203, 2021.

[150] Alexander Quinn, Jacob Darst, Matthew Keyser, Paul T Coman, Thomas P Barrera, Paul R Shearing, David Petrushenko, Donal P Finegan, and Eric Darcy. Achieving passive thermal runaway propagation resistance in li-ion battery packs. *The Electrochemical Society Interface*, 33(3):55, 2024.

[151] Avijit Karmakar, Hanwei Zhou, Bairav S. Vishnugopi, and Partha P. Mukherjee. Thermal runaway propagation analytics and crosstalk in lithium-ion battery modules. *Energy Technology*, 11(12):2300707, 2023.

[152] Niklas Weber, Christian Michel, Sebastian Schuhmann, Jens Tübke, and Hermann Nirschl. Simulation-based investigation on thermal propagation in li-ion battery modules with regard to the thermal management system. *Journal of The Electrochemical Society*, 171(11):110516, 2024.

[153] Andreas Pfrang and Vanesa Ruiz. Safer li-ion batteries by preventing thermal propagation. *JRC Science for Policy Report*, (EUR 29384 EN), 2018.

[154] Seham Shahid and Martin Agelin-Chaab. Development of hybrid thermal management techniques for battery packs. *Applied Thermal Engineering*, 186:116542, 2021.

[155] Seham Shahid and Martin Agelin-Chaab. Investigation of thermal properties of phase change materials for novel hybrid thermal management strategies for cylindrical li-ion cells. *Applied Thermal Engineering*, 242:122471, 2024.

[156] Fengqi He, Xinxi Li, Guoqing Zhang, Guanjin Zhong, and Jieshan He. Experimental investigation of thermal management system for lithium ion batteries module with coupling effect by heat sheets and phase change materials. *International Journal of Energy Research*, 42(10):3279–3288, 2018.

[157] Abid Hussain, Irfan H Abidi, C Yan Tso, K Chung Chan, Zhengtang Luo, and Christopher YH Chao. Thermal management of lithium ion batteries using graphene coated nickel foam saturated with phase change materials. *International journal of thermal sciences*, 124:23–35, 2018.

[158] Fumiaki Takahashi. Fire blanket and intumescent coating materials for failure resistance. *MRS Bulletin*, 46(5):429–434, 2021.

[159] Wencan Zhang, Zhicheng Liang, Xiuxing Yin, and Guozhi Ling. Avoiding thermal runaway propagation of lithium-ion battery modules by using hybrid phase change material and liquid cooling. *Applied Thermal Engineering*, 184:116380, 2021.

[160] A. K. Padhi, K. S. Nanjundaswamy, and J. B. Goodenough. Phospho-olivines as positive-electrode materials for rechargeable lithium batteries. *Journal of The Electrochemical Society*, 144(4):1188–1194, 1997.

[161] Weixiao Ji, Bolun Jiang, Fangxing Ai, Hanxi Yang, and Xinping Ai. Temperature-responsive microspheres-coated separator for thermal shutdown protection of lithium ion batteries. *RSC Advances*, 5:30611–30618, 2015.

[162] Weisi Li, KR Crompton, Christopher Hacker, and Jason K Ostanek. Comparison of current interrupt device and vent design for 18650 format lithium-ion battery caps. *Energy Storage Materials*, 25:101890, 2020.

[163] Beomsu Lee and Cheolsoo Jung. A corporate approach to enhancing lithium-ion battery safety through flame-retardant electrolyte development. *Frontiers in Energy Research*, 12:1508471, 2024.

[164] Keith Woodford, John Newman, and Yet-Ming Chiang. Li-ion battery separators, mechanical integrity and failure characteristics. *Scientific Reports*, 6:32578, 2016.

[165] B. Xu, D. Qian, Z. Wang, and Y. S. Meng. Recent progress in cathode materials research for advanced lithium ion batteries. *Materials Science and Engineering: R: Reports*, 73(5–6):51–65, 2012.

[166] Carlos Antônio Rufino Júnior, Eleonora Riva Sanseverino, Pierluigi Gallo, Murilo Machado Amaral, Daniel Koch, Yash Kotak, Sergej Diel, Gero Walter, Hans-Georg Schweiger, and Hudson Zanin. Unraveling the degradation mechanisms of lithium-ion batteries. *Energies*, 17(14):3372, 2024.

[167] Arunabh Ghosh and Fouad Ghamouss. Role of electrolytes in the stability and safety of lithium titanate-based batteries. *Frontiers in Materials*, 7:186, 2020.

[168] Caiyun Jin, Zexuan Wu, Guopeng Li, Zhan Luo, and Nian-Wu Li. Phosphazene-based flame-retardant artificial interphase layer for lithium metal batteries. *Acta Physico-Chimica Sinica*, page 100094, 2025.

[169] Yishu Qiu and Fangming Jiang. A review on passive and active strategies of enhancing the safety of lithium-ion batteries. *International Journal of Heat and Mass Transfer*, 184:122288, 2022.

[170] Kailin Chen, Yingxin Li, and Haoxiang Zhan. Advanced separators for lithium-ion batteries. In *IOP Conference Series: Earth and Environmental Science*, volume 1011, page 012009. IOP Publishing, 2022.

[171] Yan Yu, Guosheng Jia, Liang Zhao, Hengxue Xiang, Zexu Hu, Guiyin Xu, and Meifang Zhu. Flexible and heat-resistant polyphenylene sulfide ultrafine fiber hybrid separators for high-safety lithium-ion batteries. *Chemical Engineering Journal*, 452:139112, 2023.

[172] Xing-Yan Yao, Lingxi Kong, and Michael G Pecht. Reliability of cylindrical li-ion battery safety vents. *Ieee Access*, 8:101859–101866, 2020.

[173] Hang Li, Li Wang, Youzhi Song, Zhiguo Zhang, Hao Zhang, Aimin Du, and Xiangming He. Significance of current collectors for high performance conventional lithium-ion batteries: a review. *Advanced Functional Materials*, 33(49):2305515, 2023.

[174] Yitong Peng, Tao Meng, Pingan Li, Rongxin Li, and Xianluo Hu. Self-thermoregulating current collectors: built-in thermal protection for safe lithium-ion batteries. *Energy & Environmental Science*, 18(7):3177–3185, 2025.

[175] Sahin Gungor, Sinan Gocmen, and Erdal Cetkın. A review on battery thermal management strategies in lithium-ion and post-lithium batteries for electric vehicles. *Journal of Thermal Engineering*, 9(4):1078–1099, 2023.

[176] Christopher Lee, Ahmed O Said, and Stanislav I Stoliarov. Passive mitigation of thermal runaway propagation in dense 18650 lithium ion cell assemblies. *Journal of The Electrochemical Society*, 167(9):090524, 2020.

[177] International Energy Agency. Beyond nmc batteries: Supply chain issues for emerging battery technologies. `https://www.iea.org/reports/global-critical-minerals-outlook-2025/beyond-nmc-batteries-supply-chain-issues-for-emerging-battery-technologies`, 2025. [Online; accessed: 2025-07-28].

[178] Jin Tang, Xinyuan Wu, Jian Ren, Huihua Min, Xiaomin Liu, Yong Kong, Peipei Che, Wei Zhai, Hui Yang, and Xiaodong Shen. Suppressing thermal runaway propagation of nickel-rich lithium-ion battery modules using silica aerogel sheets. *Process Safety and Environmental Protection*, 179:199–207, 2023.

[179] Mingyi Chen, Minghao Zhu, Luyao Zhao, and Yin Chen. Study on thermal runaway propagation inhibition of battery module by flame-retardant phase change material combined with aerogel felt. *Applied Energy*, 367:123394, 2024.

[180] Danfeng Du, Zhisong Han, Fengmei Zhang, Zexin Liu, Liyun Sun, Chaowei Sun, and Xiurong Guo. Flame-retardant phase-change aerogel: Experimental characterization and battery thermal management simulation. *Applied Thermal Engineering*, page 127295, 2025.

[181] Ting Quan, Qi Xia, Xiaoyu Wei, and Yanli Zhu. Recent development of thermal insulating materials for li-ion batteries. *Energies*, 17(17):4412, 2024.

[182] Zhaorui Huo, Xiaobo Hong, Yanyan Li, Zihan Chen, and Dianbo Ruan. Numerical study of paraffin and glass fiber composites for thermal management of lithium-ion battery packs. *Asia-Pacific Journal of Chemical Engineering*, 19(1):e2989, 2024.

[183] Kai Shen, Jieyu Sun, Chengshan Xu, Shaw Kang Wong, Yuejiu Zheng, Changyong Jin, Huaibin Wang, Siqi Chen, and Xuning Feng. Experimental investigation for the phase change material barrier area effect on the thermal runaway propagation prevention of cell-to-pack batteries. *Batteries*, 9(4):206, 2023.

[184] Yin Chen, Minghao Zhu, and Mingyi Chen. Comprehensive experimental research on wrapping materials influences on the thermal runaway of lithium-ion batteries. *Emergency Management Science and Technology*, 5(1), 2025.

[185] Jingwen Weng, Dongxu Ouyang, Xiaoqing Yang, and et al. Alleviation of thermal runaway propagation in thermal management modules using aerogel felt coupled with flame-retarded phase change material. *Energy Conversion and Management*, 200:112071, 2019.

[186] Yikai Mao, Yaoyu Chen, Yanglin Ye, Yin Chen, and Mingyi Chen. Comparative study of thermal runaway propagation and material barrier effect of lithium-ion batteries. *Batteries*, 11(6):214, 2025.

[187] B Rajasekaran, G Kumaresan, M Arulprakasajothi, and Suresh Vellaiyan. Latent heat energy storage using nanomaterials as a heat sink for the prevention of thermal runaway: A study in conjugate heat dissipation. *International Communications in Heat and Mass Transfer*, 151:107225, 2024.

[188] Rojo Kurian Daniels and Aneesh Prabhakar. Experimental and numerical investigation on the effect of cell arrangement on thermal runaway propagation in air cooled cylindrical li-ion battery modules. *Journal of Energy Storage*, 72:108619, 2023.

[189] Zhirong Wang, Ning Mao, and Fengwei Jiang. Study on the effect of spacing on thermal runaway propagation for lithium-ion batteries. *Journal of Thermal Analysis and Calorimetry*, 140:2849–2863, 2020.

[190] Ana Olona and Luis Castejón. Influence of the layout of cells in a traction battery on the evolution of a fire in the event of a failure. Technical report, 2025.

[191] Alexander Quinn, Jacob Darst, Matthew Keyser, Paul T Coman, Thomas P Barrera, Paul R Shearing, David Petrushenko, Donal P Finegan, and Eric Darcy. Achieving passive thermal runaway propagation resistance in li-ion battery packs. *The Electrochemical Society Interface*, 33(3):55, 2024.

[192] Huichang Niu, Caixing Chen, Yanhui Liu, Lei Li, Zhao Li, Dan Ji, and Xinyan Huang. Mitigating thermal runaway propagation of ncm 811 prismatic batteries via hollow glass microspheres plates. *Process Safety and Environmental Protection*, 162:672–683, 2022.

[193] Canbing Li, Yuhang Wu, Xinxi Li, Wensheng Yang, Yunjun Luo, Juxiong Tian, Shuyao Li, Jian Deng, Minjie Shi, Ya Mao, et al. Flame-retardant composite phase change material with silicone resin and melamine phosphate for battery thermal safety. *The Innovation Energy*, 1(2):100021–1, 2024.

[194] Yuqian Fan, Yun Bao, Chen Ling, Yanyan Chu, Xiaojun Tan, and Shuting Yang. Experimental study on the thermal management performance of air cooling for high energy density cylindrical lithium-ion batteries. *Applied Thermal Engineering*, 155:96–109, 2019.

[195] Huang Li, Haodong Chen, Guobin Zhong, Yu Wang, and Qingsong Wang. Experimental study on thermal runaway risk of 18650 lithium ion battery under side-heating condition. *Journal of Loss Prevention in the Process Industries*, 61:122–129, 2019.

[196] Munro & Associates. Tesla model y 4680 structural battery pack teardown. `https://www.youtube.com/watch?v=yGZWoU9cDLg`, 2023. [Online; accessed: 2025-07-31].

[197] Munro & Associates. Structural battery pack teardown part 3: Internal link fuse strategy. `https://www.youtube.com/watch?v=3tD5DYZQYzI`, 2023. [Online; accessed: 2025-07-31].

[198] Nfpa 855: Standard for the installation of stationary energy storage systems. `https://www.nfpa.org/codes-and-standards/all-codes-and-standards/list-of-codes-and-standards/detail?code=855`, 2023. Approved as an American National Standard on September 1, 2022.

[199] Ul 9540a: Test method for evaluating thermal runaway fire propagation in battery energy storage systems. `https://www.ul.com/services/ul-9540a-test-method`, 2019. ANSI/CAN/UL 9540A:2019.

[200] EVLO Energy Storage Inc. Fire propagation prevention in modular bess enclosures. `https://evloenergy.com/blog/thermal-barrier-design-in-bess`, 2023. [Online; accessed: 2025-07-31].

[201] NPP Renewable Energy Solutions. Battery energy storage system (bess) design overview. https://npplithium.com/battery-energy-storage-system-bess/, 2023. [Online; accessed: 2025-07-31].

[202] Biao Ma, Jie Liu, and Ruiguang Yu. Study on the flammability limits of lithium-ion battery vent gas under different initial conditions. *ACS omega*, 5(43):28096–28107, 2020.

[203] Sascha Koch, Alexander Fill, and Kai Peter Birke. Comprehensive gas analysis on large scale automotive lithium-ion cells in thermal runaway. *Journal of Power Sources*, 398:106–112, 2018.

[204] Maria L. Guerra. Understanding ev battery vents. *Battery Tech Online*, June 26 2024. Senior Editor - Battery Technology, Informa Markets Engineering.

[205] Xingyan Yao, Lingxi Kong, and Michael Pecht. Reliability of cylindrical li-ion battery safety vents. *IEEE Access*, PP:1–1, 05 2020.

[206] Peiyi Sun, Roeland Bisschop, Huichang Niu, and Xinyan Huang. A review of battery fires in electric vehicles. *Fire technology*, 56(4):1361–1410, 2020.

[207] Weisi Li, KR Crompton, and Jason K Ostanek. Comparison of current interrupt device and vent design for 18650 format lithium-ion battery caps: New findings. *Journal of Energy Storage*, 46:103841, 2022.

[208] Sumiao Yin, Jianghong Liu, and Beihua Cong. Review of thermal runaway monitoring, warning and protection technologies for lithium-ion batteries. *Processes*, 11(8):2345, 2023.

[209] Hai-Zu Jin, Xiao-Feng Han, Petar M Radjenovic, Jing-Hua Tian, and Jian-Feng Li. Facile and effective positive temperature coefficient (ptc) layer for safer lithium-ion batteries. *The Journal of Physical Chemistry C*, 125(3):1761–1766, 2021.

[210] Daniel Williams, Royce Copley, Peter Bugryniec, Rob Dwyer-Joyce, and Solomon Brown. A review of ultrasonic monitoring: Assessing current approaches to li-ion battery monitoring and their relevance to thermal runaway. *Journal of Power Sources*, 590:233777, 2024.

[211] Rhodri E Owen, Ewelina Wiśniewska, Michele Braglia, Richard Stocker, Paul R Shearing, Dan JL Brett, and James B Robinson. Operando ultrasonic monitoring of the internal temperature of lithium-ion batteries for the detection and prevention of thermal runaway. *Journal of The Electrochemical Society*, 171(4):040525, 2024.

[212] JY Kim, ZL Wang, SM Lee, and JW Byeon. Failure analysis of thermally abused lithium-ion battery cell by microscopy, electrochemical impedance spectroscopy, and acoustic emission. *Microelectronics reliability*, 100:113363, 2019.

[213] Sascha Koch, Kai Peter Birke, and Robert Kuhn. Fast thermal runaway detection for lithium-ion cells in large scale traction batteries. *Batteries*, 4(2):16, 2018.

[214] Krishnadash S Kshetrimayum, Young-Gak Yoon, Hye-Ri Gye, and Chul-Jin Lee. Preventing heat propagation and thermal runaway in electric vehicle battery modules using integrated pcm and micro-channel plate cooling system. *Applied Thermal Engineering*, 159:113797, 2019.

[215] Thomas Imre Cyrille Buidin and Florin Mariasiu. Battery thermal management systems: Current status and design approach of cooling technologies. *Energies*, 14(16):4879, 2021.

[216] Inventor Name. Encapsulated fire-retardant materials to improve battery safety, Feb 2009.

[217] Lip Huat Saw, Hiew Mun Poon, Hui San Thiam, Zuansi Cai, Wen Tong Chong, Nugroho Agung Pambudi, and Yeong Jin King. Novel thermal management system using mist cooling for lithium-ion battery packs. *Applied Thermal Engineering*, 2023.

[218] S. Hemavathi and D.A. Antopaul. Design of dielectric fluid immersion cooling system for efficient thermal management of lithium-ion battery packs. *Energy Technology*, 2025.

[219] Marcus Runefors. On the effectiveness of aerosol extinguishing agents for battery vent gases and hydrogen. 2025.

[220] Meenakshi Rohilla, Amit Saxena, Yogesh Kumar Tyagi, Inderpal Singh, Rajesh Kumar Tanwar, and Rajiv Narang. Condensed aerosol based fire extinguishing system covering versatile applications: a review. *Fire Technology*, 58(1):327–351, 2022.

[221] Robert G. C. Reijns and Others. Firepro® condensed aerosol suppression of lithium-ion battery fires. *KIWA Report on Fire Tests*, 2017.

[222] DNV GL. Testing of aerosol fire extinguishing agent for li-ion battery fires, 2021.

[223] Danielson Forssberg & Co. (DAFO Vehicle Fire Protection). Thermal management and automatic fire-extinguishing system of automobile battery, Dec 2014.

[224] Chaohang Xu, Yajun Li, Xiankai Zhang, Ying Zhang, Gaopeng Shen, Jinquan Shi, and Bowen Mi. Preparation and characterization of fire-extinguishing efficiency of novel gel foam for lithium-ion battery fires. *Process Safety and Environmental Protection*, 197:106999, 2025.

[225] Wei Tang, Liming Yuan, Richard Thomas, and John Soles. Comparison of fire suppression techniques on lithium-ion battery pack fires. *Mining, Metallurgy & Exploration*, 40(4):1081–1087, 2023.

[226] Patrick Kiley. Reverse engineering the tesla battery management system to increase power available. *Proc. BLACK HAT*, pages 1–27, 2020.

[227] Sakari Palokangas. Battery cell fire detection and suppression system. 2022.

[228] Manjunatha H. Sun, Praveen Kumar Nambisan T. M., Pavan R., Hari Prasad Reddy P., Bharath G. M., Mukund Aravind Kulkarni, and Saravanan Sundaram. A review on fire prevention and suppression solutions for ev battery packs. SAE Technical Paper 2024-26-0012, SAE International, January 2024.

[229] Firetrace International. FM-200™ Fire Suppression Systems. `https://www.firetrace.com/en/fm-200`, 2025. Accessed: 2025-07-07.

[230] PT FM200 Indonesia. Specification Sheet: NOVEC 1230 Fluid. `https://fm200.co.id/documentation/clean-agent-gas/spesification-sheet/spesification-sheet_gas-novec-1230.pdf`, 2025. [Online; accessed: 2025-07-07].

[231] Civil Aviation Authority of Singapore (CAAS). AC 91-6-2(Rev 1) Halon Replacement for Fire Extinguishing Agents. `https://www.caas.gov.sg/docs/default-source/docs---srg/ac-91-6-2(rev-1)-halon-replacement-for-fire-extinguishing-agents.pdf`, 2023. [Online; accessed: 2025-07-07].

[232] Kuo Wang, Dongxu Ouyang, Shuai Yuan, Dejian Wu, Jianqi Zhang, Chongye Chang, Ke Yan, Haoshi Sun, and Xinming Qian. Experimental study on inhibition effect of novec-1230 on thermal runaway fire of lithium-ion battery packs induced by overcharging. *Journal of Energy Storage*, 120:116451, 2025.

[233] Mark B McKinnon, Sean DeCrane, Stephen Kerber, et al. *Four firefighters injured in lithium-ion battery energy storage system explosion-Arizona*. Underwriters Laboratory, Firefighter Safety Research Institute, 2020.

[234] Qichang Dong, Jiacheng Qi, Song Lu, and Long Shi. Synergistic effects of typical clean gaseous fire-extinguishing agents. *Fire Safety Journal*, 128:104206, 2024. Gas–liquid synergy (e.g., Novec 1230–water mist) provides rapid flame knockdown by Novec 1230 followed by cooling and re-flash prevention via water mist.

[235] Yan Cui, Jianghong Liu, Xin Han, Shaohua Sun, and Beihua Cong. Full-scale experimental study on suppressing lithium-ion battery fires with water-based deluge systems. *Fire Safety Journal*, 142:103040, 2022.

[236] Mark McKinnon, Adam Barowy, Alexandra Schraiber, and Jack Regan. Full-scale walk-in containerized lithium-ion battery energy storage system fire test data. *Data in Brief*, 45:108712, 2022.

[237] Kurtarır Fire Systems. Water mist fire suppression system – industrial nozzle discharge. `https://www.kurtarir.com.tr/en/water-mist-fire-suppression-system`, 2024. [Online; accessed: 2025-07-31].

[238] Wei Peng, Yan Zhang, Shaojie Zhang, and Xiaoyong Liu. Experimental study on the inhibition effect of water mist containing additives on the thermal runaway of lithium battery. *Fire and Materials*, 48(1):123–137, 2024.

[239] Hazard Control Technologies, Inc. F-500 encapsulator agent: Introduction to firefighting. Technical report, Hazard Control Technologies, 2022. [Online; accessed: 2025-07-28].

[240] Wei-Tao Luo et al. Research and development of fire extinguishing technology for lithium-ion battery fires. In *Procedia Engineering*, volume 211, page 531–537, 2018.

[241] Roeland Bisschop, Ola Willstrand, and Max Rosengren. Handling lithium-ion batteries in electric vehicles: preventing and recovering from hazardous events. *Fire technology*, 56(6):2671–2694, 2020.

[242] Eaton Corporation. 3-in-1 battery pack vent valve for evs, 2023. Product datasheet.

[243] REMBE GmbH Safety + Control. Explosion venting for bess applications, 2025. Product brochure.

[244] Anonymous. Protecting bess from fire and explosion hazards. *POWER Magazine*, July 2021. [Online; accessed: 2025-07-31].

[245] Metal.com. Lfp growth continues: Lithium carbonate remains key ... `https://www.metal.com/en/newscontent/103286548`, 2025. [Online; accessed: 2025-07-28].

[246] IF Monteiro, MM Silva, A Fidalgo-Marijuan, R Gonçalves, CM Costa, and S Lanceros-Mendez. Improving lithium-ion battery safety through separators with thermal shutdown characteristics induced by thermal expansion microspheres. *Journal of Power Sources*, 631:236311, 2025.

[247] Orhan Topal. Assessing risks of electric vehicles in underground parking facilities: Strategies for enhancing urban sustainability. *Isı Bilimi ve Tekniği Dergisi*, 45(1):84–96, 2025.

[248] International Organization for Standardization (ISO). Iso strategy 2030: Vision, goals and priorities. `https://www.iso.org/strategy2030.html`, 2021. Accessed 10 July 2025.

[249] Knut Blind et al. The impact of standardisation and standards on innovation. *Handbook of innovation policy impact*, pages 423–449, 2013.

[250] Tongxin Shan, Puchen Zhang, Zhenpo Wang, and Xiaoqing Zhu. Insights into extreme thermal runaway scenarios of lithium-ion batteries fire and explosion: A critical review. *Journal of Energy Storage*, 88:111532, 2024.

[251] United Nations. Ecosoc - about us. `https://www.un.org/ecosoc/en/content/about-us`. [Online; accessed: 2025-02-17].

[252] United Nations. Ecosoc subsidiary bodies. `https://www.un.org/ecosoc/en/content/ecosoc-subsidiary-bodies`. [Online; accessed: 2025-02-17].

[253] The United Nations Economic Commission for Europe. About unece - mission. `https://unece.org/mission`, 2022.

[254] Uniform provisions concerning the approval of vehicles with regard to specific requirements for the electric power train. Regulation, European Union, August 2021.

[255] European Free Trade Association European Union. Agreement on the european economic area (eea). `https://eur-lex.europa.eu/legal-content/EN/TXT/?uri=legissum:eea`, 1994. Official Journal L 1, 03/01/1994, pp. 3-522. [Online; accessed: 2025-07-28].

[256] International Organisation for Standardization. What we do - international organisation for standardization. `https://www.iso.org/what-we-do.html`, 2022. [Online; accessed: 2025-02-17].

[257] International Organisation for Standardization. Developing standards - international organisation for standardization. `https://www.iso.org/developing-standards.html`. [Online; accessed: 2025-02-17].

[258] ISO CEN. Agreement on technical co-operation between iso and cen (vienna agreement). `https://boss.cen.eu/media/CEN/ref/vienna_agreement.pdf`, 2021.

[259] International Organization for Standardization. Electrically propelled road vehicles — test specification for lithium-ion traction battery packs and systems — part 3: Safety performance requirements, 2014. [Online; accessed: 2025-07-10].

[260] International Organization for Standardization. Electrically propelled road vehicles — test specification for lithium-ion traction battery packs and systems — part 1: Performance testing, 2011. [Online; accessed: 2025-07-10].

[261] International Organization for Standardization. Electrically propelled road vehicles — test specification for lithium-ion traction battery packs and systems — part 2: High-energy applications, 2012. [Online; accessed: 2025-07-10].

[262] International Organization for Standardization. Electrically propelled road vehicles — test specification for lithium-ion traction battery packs and systems — part 4: Performance testing, 2018. [Online; accessed: 2025-07-10].

[263] International Organization for Standardization. Electrically propelled road vehicles — safety specifications — part 1: On-board rechargeable energy storage system (ress), 2019. [Online; accessed: 2025-07-10].

[264] Electrically propelled mopeds and motorcycles — Test specifications and safety requirements for lithium-ion battery systems. Standard, International Organization for Standardization, Geneva, CH, April 2017.

[265] International Electrotechnical Commission. History - international electrotechnical commission. https://iec.ch/history. [Online; accessed: 2025-02-17].

[266] International Electrotechnical Commission. What we do - international electrotechnical commission. https://iec.ch/what-we-do. [Online; accessed: 2025-02-17].

[267] International Electrotechnical Commission. Secondary lithium-ion cells for the propulsion of electric road vehicles - part 1: Performance testing, 2018. [Online; accessed: 2025-07-10].

[268] International Electrotechnical Commission. Secondary lithium-ion cells for the propulsion of electric road vehicles - part 2: Reliability and abuse testing, 2018. [Online; accessed: 2025-07-10].

[269] International Electrotechnical Commission. Secondary lithium-ion cells for the propulsion of electric road vehicles - part 3: Safety requirements, 2022. [Online; accessed: 2025-07-10].

[270] Regulation (eu) no 1025/2012 of the european parliament and of the council of 25 october 2012 on european standardisation, amending council directives 89/686/eec and 93/15/eec and directives 94/9/ec, 94/25/ec, 95/16/ec, 97/23/ec, 98/34/ec, 2004/22/ec, 2007/23/ec, 2009/23/ec and 2009/105/ec of the european parliament and of the council and repealing council decision 87/95/eec and decision no 1673/2006/ec of the european parliament and of the council text with eea relevance. Regulation, European Parliament, October.

[271] CEN. List of cen members. https://standards.cencenelec.eu/dyn/www/f?p=CEN:5, 2022. [Online; accessed: 2025-02-16].

[272] CENELEC. About cenelec. https://www.cencenelec.eu/about-cenelec/, 2022. [Online; accessed: 2025-02-16].

[273] IEC CENELEC. Iec - cenelec agreement on common planning of new work and parallel voting.

[274] National Highway Traffic Safety Administration. About nhtsa. https://www.nhtsa.gov/about-nhtsa. [Online; accessed: 2025-02-17].

[275] Recommended Practices for Abuse Testing Rechargeable Energy Storage Systems (RESSs). Standard, Sandia National Laboratories, Albuquerque, US, July 2017.

[276] United States Advanced Battery Consortium (USABC) and FreedomCAR, USA. *FreedomCAR Battery Test Manual for Power-Assist Hybrid Electric Vehicles*, 2003. Standardized test procedures for automotive battery systems.

[277] SAE International. About sae international. https://www.sae.org/about. [Online; accessed: 2025-02-17].

[278] SAE International. History - sae international. https://www.sae.org/about/history. [Online; accessed: 2025-02-17].

[279] Electric and Hybrid Electric Vehicle Rechargeable Energy Storage System (RESS) Safety and Abuse Testing. Standard, Society of Automotive Engineers, Warrendale, US, April 2009.

[280] Safety standard for electric and hybrid vehicle propulsion battery systems utilizing lithium-based rechargeable cells, 2013. Surface Vehicle Standard.

[281] Underwriters Laboratories. Standard for energy storage systems and equipment, 2025. [Online; accessed: 2025-07-10].

[282] Underwriters Laboratories. Test method for evaluating thermal runaway fire propagation in battery energy storage systems, 2025. [Online; accessed: 2025-07-10].

[283] Standard for batteries for use in electric vehicles, 2022. Edition 3: June 28, 2022.

[284] Underwriters Laboratories. Standard for lithium batteries, 2020. [Online; accessed: 2025-07-10].

[285] Underwriters Laboratories. Standard for batteries for use in stationary, vehicle auxiliary power, and light electric rail applications, 2022. [Online; accessed: 2025-07-10].

[286] United Nations Economic Commission for Europe. *United Nations Manual of Tests and Criteria, Part III, Sub-section 38.3: Recommendations on the Transport of Dangerous Goods*, eighth revised edition (rev. 8) edition, 2023. Adopted 27 November 2023. [Online; accessed: 2025-07-11].

[287] National Fire Protection Association. *NFPA 68: Standard on Explosion Protection by Deflagration Venting*. National Fire Protection Association, Quincy, MA, 2023 edition, 2023. NFPA 68-2023.

[288] National Fire Protection Association. *NFPA 69: Standard on Explosion Prevention Systems*. National Fire Protection Association, Quincy, MA, 2024 edition, 2024. NFPA 69-2024.

[289] What we do sac. `http://www.sac.gov.cn/sacen/aboutsac/who_we_are/201411/t20141118_169916.htm`, author = Standardization Administration of China. [Online; accessed: 2025-02-17].

[290] Xin Lai, Jian Yao, Changyong Jin, Xuning Feng, Huaibin Wang, Chengshan Xu, and Yuejiu Zheng. A review of lithium-ion battery failure hazards: Test standards, accident analysis, and safety suggestions. *Batteries*, 8(11):248, 2022.

[291] Håkan Stigson, Maria Krafft, and Anders Lie. Frontal impact patterns for realistic crash pulses–insights from the swedish crash pulse recorder system. *Accident Analysis & Prevention*, 39(6):1237–1245, 2007. CPR data on frontal impacts showing typical 14-27 g deceleration peaks.

[292] EU FP7 EVERSAFE Consortium. Eversafe final report: Real-world crash pulse analysis for injury prevention. Technical report, European Commission, FP7, 2013. Meta-study combining CPR and EDR data from Europe and North America.

[293] Carl Hirsch, Rolf Muller, and Thomas Schneider. Occupant compartment acceleration response in 50 km/h full-width rigid barrier tests of european small cars. *International Journal of Crashworthiness*, 20(3):219–228, 2015. Data on VW Up! and Seat Ibiza crash tests achieving occupant peaks of 46–55 g.

[294] National Highway Traffic Safety Administration (NHTSA) and Transport Canada. Full-width rigid barrier crash tests: Analysis of occupant-compartment peak accelerations (2000–2010 model years), 2011. Review of 56 km/h rigid barrier crash tests with peaks up to 50–55 g.

[295] Uniform provisions concerning the approval of vehicles with regard to the protection of the occupants in the event of a frontal collision, 2022. UNECE Regulation No. 94, Revision 4.

[296] Uniform provisions concerning the approval of vehicles with regard to the protection of the occupants in the event of a lateral collision, 2023. UNECE Regulation No. 95, Revision 4.

[297] Daniel H. Doughty and Chris C. Crafts. Freedomcar electrical energy storage system abuse test manual for electric and hybrid electric vehicle applications. Technical Report SAND2005-3123, Sandia National Laboratories, August 2006. Date of issue: August 2006. Accessed: 2025-07-29.

[298] Lithium-ion batteries for electric vehicles, 2006. Automotive Industry Standard of the People's Republic of China.

[299] Safety requirements and test methods for traction battery of electric vehicle, 2015. National Standard of the People's Republic of China.

[300] Tokihiko Yokoshima, Daikichi Mukoyama, Fujio Maeda, Tetsuya Osaka, Koji Takazawa, Shun Egusa, Satomi Naoi, Satoru Ishikura, and Koichi Yamamoto. Direct observation of internal state of thermal runaway in lithium ion battery during nail-penetration test. *Journal of Power Sources*, 393:67–74, 2018.

[301] Elham Sahraei, C.M. Locey, A. Eshraghi, and K. Digges. Homogenization of vehicle fleet frontal crash pulses from 2000–2010 model year frontal rigid-barrier crash tests. *Traffic Injury Prevention*, 13(2):156–163, 2012.

[302] Krystoffer Mroz, Martin Östling, and Nils Lubbe. Passenger cars in head-on crashes with heavy goods vehicles: For what severity should future car restraint systems be designed? In *Proceedings of the 24th Enhanced Safety of Vehicles (ESV) Conference*, 2015.

[303] Bhavya Kotak, Yash Kotak, Katja Brade, Tibor Kubjatko, and Hans-Georg Schweiger. Battery crush test procedures in standards and regulation: Need for augmentation and harmonisation. *Batteries*, 7(3):63, 2021.

[304] International Electrotechnical Commission. Iec 62619:2022 - secondary cells and batteries containing alkaline or other non-acid electrolytes - safety requirements for secondary lithium cells and batteries, for use in industrial applications, 2022.

[305] Iec 61373:2010 – railway applications – rolling stock equipment – shock and vibration tests, May 2010. [Online; accessed: 2025-07-11].

[306] SAE International. Sae j2380 - vibration testing of electric vehicle batteries, 2021.

[307] U.S. Department of Defense. Mil-std-810h: Department of defense test method standard - environmental engineering considerations and laboratory tests, method 514.8 vibration, 2019. [Online; accessed: 2025-07-13].

[308] Road vehicles — environmental conditions and testing for electrical and electronic equipment — part 3: Mechanical loads, 2023. Accessed: 2025-07-29.

[309] Battery operated vehicles - safety requirements of traction batteries, 2009. Automotive Industry Standard.

[310] Zhoujian An, Yabing Zhao, Xiaoze Du, Tianlu Shi, and Dong Zhang. Experimental research on thermal-electrical behavior and mechanism during external short circuit for lifepo4 li-ion battery. *Applied Energy*, 332:120519, 2023.

[311] Hossam A Gabbar, Ahmed M Othman, and Muhammad R Abdussami. Review of battery management systems (bms) development and industrial standards. *Technologies*, 9(2):28, 2021.

[312] Takahisa Ohsaki, Takashi Kishi, Takashi Kuboki, Norio Takami, Nao Shimura, Yuichi Sato, Masahiro Sekino, and Asako Satoh. Overcharge reaction of lithium-ion batteries. *Journal of power sources*, 146(1-2):97–100, 2005.

[313] Xin Lai, Yuejiu Zheng, Long Zhou, and Wenkai Gao. Electrical behavior of overdischarge-induced internal short circuit in lithium-ion cells. *Electrochimica Acta*, 278:245–254, 2018.

[314] Heather M Barkholtz, Yuliya Preger, Sergei Ivanov, Jill Langendorf, Loraine Torres-Castro, Joshua Lamb, Babu Chalamala, and Summer R Ferreira. Multi-scale thermal stability study of commercial lithium-ion batteries as a function of cathode chemistry and state-of-charge. *Journal of Power Sources*, 435:226777, 2019.

[315] Ul 2054 standard for household and commercial batteries, 2021. Accessed: 2025-07-16.

[316] Q. Wang, P. Ping, X. Zhao, G. Chu, J. Sun, and C. Chen. Temperature effect and thermal impact in lithium-ion batteries: A review. *Journal of Power Sources*, 364:258–273, 2017.

[317] Byoung-Hoon Kim, Hong-Jong Lee, Jin-Beom Jeong, Baek-Haeng Lee, Dong-Hyun Shin, Hyun-Sik Song, Tae-Hoon Kim, and Ji-Yoon Yoo. A study on effective thermal-shock test improvement of battery packs for phevs. In *Proceedings of the FISITA 2012 World Automotive Congress: Volume 3: Future Automotive Powertrains (I)*, pages 667–674. Springer, 2012.

[318] Nan Zhang, Tao Deng, Shuoqing Zhang, Changhong Wang, Lixin Chen, Chunsheng Wang, and Xiulin Fan. Critical review on low-temperature li-ion/metal batteries. *Advanced Materials*, 34(15):2107899, 2022.

[319] Electrically propelled road vehicles — Test specification for lithium-ion traction battery packs and systems — Part 3: Safety performance requirements. Standard, International Organization for Standardization, Geneva, CH, May 2014.

[320] Uniform provisions concerning the approval of vehicles with regard to specific requirements for the electric power train. Regulation, Economic Commission for Europe of the United Nations, August 2013.

[321] Road vehicles — degrees of protection (ip code) — protection of electrical equipment against foreign objects, water and access, August 2023.

[322] Iec 60529: Degrees of protection provided by enclosures (ip code) – ipx7 specification. `https://www.iec.ch/ip-ratings`, 2013. Accessed: 2025-07-13.

[323] Antonio Nedjalkov, Jan Meyer, Michael Köhring, Alexander Doering, Martin Angelmahr, Sebastian Dahle, Andreas Sander, Axel Fischer, and Wolfgang Schade. Toxic gas emissions from damaged lithium ion batteries—analysis and safety enhancement solution. *Batteries*, 2(1):5, 2016.

[324] A. Atreya. Convection heat transfer. In P. DiNenno and D Drysdale, editors, *SFPE Handbook of Fire Protection Engineering*, pages 1–44–1–72. NFPA, 2002.

[325] R.F. Simmons. Premixed burning. In P. DiNenno and D Drysdale, editors, *SFPE Handbook of Fire Protection Engineering*, pages 1–144–1–154. NFPA, 2002.

[326] G Heskestad. Fire plumes, flame height, and air entrainment. In Morgan J Hurley, Daniel T Gottuk, John R Hall Jr, Kazunori Harada, Erica D Kuligowski, Milosh Puchovsky, John M Watts Jr, Christopher J Wieczorek, et al., editors, *SFPE handbook of fire protection engineering*. Springer, 2015.

[327] Yan Cui, Jianghong Liu, Beihua Cong, Xin Han, and Sumiao Yin. Characterization and assessment of fire evolution process of electric vehicles placed in parallel. *Process Safety and Environmental Protection*, 166:524–534, 2022.

[328] Rosa E. Padilla, Daniel L. Dietrich, Gary A. Ruff, David L. Urban, Kelly C. Lynch, Alfredo Juarez, Susana A. Harper, and Christopher R. Nagel. Characterization of battery fires. In *Proceedings of the 49th International Conference on Environmental Systems (ICES)*, Boston, Massachusetts, July 2019. Presented at ICES-2019, NASA White Sands Test Facility; quantitative data on maximum heat release rate, total heat release, flame height/diameter, toxic gas emissions.

[329] Craig L Beyler. Fire hazard calculations for large, open hydrocarbon fires. In Morgan J Hurley, Daniel T Gottuk, John R Hall Jr, Kazunori Harada, Erica D Kuligowski, Milosh Puchovsky, John M Watts Jr, Christopher J Wieczorek, et al., editors, *SFPE handbook of fire protection engineering*. Springer, 2015.

[330] BM Cetegen, EE Zukoski, and Toshi Kubota. Entrainment in the near and far field of fire plumes. *Combustion Science and Technology*, 39(1-6):305–331, 1984.

[331] Sizuo Yokoi. On the heights of flames from burning cribs. *Bulletin of Japan Association for Fire Science and Engineering*, 13(1):22–27, 1963.

[332] G Heskestad. Dynamics of the fire plume. *Philosophical Transactions of the Royal Society of London. Series A: Mathematical, Physical and Engineering Sciences*, 356(1748):2815–2833, 1998.

[333] Kevin B McGrattan, Howard R Baum, and Anthony Hamins. Thermal radiation from large pool fires. *National Institute of Standards and Technology. US Department of Commerce. USA*, 2000.

[334] Carl-Christoph Höhne, Volker Gettwert, Fabian Frank, Sascha Kilian, and Andreas Menrath. Bench-scale fuel fire test for materials of rechargeable energy storage system housings. *Journal of Thermal Analysis and Calorimetry*, 148(2):305–313, 2023.

[335] Regulation No 34 of the Economic Commission for Europe of the United Nations (UNECE) — Uniform provisions concerning the approval of vehicles with regard to the prevention of fire risks. Regulation, Economic Commission for Europe of the United Nations, Geneva, CH, July 2011.

[336] Ping Jiang and Shou-xiang Lu. Pool fire mass burning rate and flame tilt angle under crosswind in open space. *Procedia Engineering*, 135:261–274, 2016.

[337] JM Chatris, J Quintela, J Folch, E Planas, J Arnaldos, and J Casal. Experimental study of burning rate in hydrocarbon pool fires. *Combustion and flame*, 126(1-2):1373–1383, 2001.

[338] Nikolaos Wassiliadis, Matthias Steinsträter, Markus Schreiber, Philipp Rosner, Lorenzo Nicoletti, Florian Schmid, Manuel Ank, Olaf Teichert, Leo Wildfeuer, Jakob Schneider, Alexander Koch, Adrian König, Andreas Glatz, Josef Gandlgruber, Thomas Kröger, Xue Lin, and Markus Lienkamp. Quantifying the state of the art of electric powertrains in battery electric vehicles: Range, efficiency, and lifetime from component to system level of the volkswagen id.3. *eTransportation*, 12:100167, 2022.

[339] Bing Chen, Shou-Xiang Lu, Chang-Hai Li, Quan-Sheng Kang, and Vivien Lecoustre. Initial fuel temperature effects on burning rate of pool fire. *Journal of hazardous materials*, 188(1-3):369–374, 2011.

[340] S Sudheer and SV Prabhu. Heat transfer in vertical casks engulfed in open pool fires. *Journal of fire sciences*, 31(6):541–562, 2013.

[341] Sudheer Siddapureddy, Klaus-Dieter Wehrstedt, and SV Prabhu. Heat transfer to bodies engulfed in di-tert-butyl peroxide pool fires-numerical simulations. *Journal of Loss Prevention in the Process Industries*, 44:204–211, 2016.

[342] Madhusoodan Ojha, Amit K Dhiman, and KC Guha. Simulation of thermally protected cylindrical container engulfed in fire. *Journal of loss Prevention in the Process Industries*, 25(2):391–399, 2012.

[343] Underwriters Laboratories. UL 263: Standard for Fire Tests of Building Construction and Materials, 2023. UL Standard.

[344] B. Lattimer. Heat fluxes from fires to surfaces. In P. DiNenno, editor, *SFPE Handbook of Fire Protection Engineering*, chapter 2-14. Society of Fire Protection Engineers, Boston, MA, 3rd edition, 2001.

[345] European Committee for Standardization. En 1363-1:2020. fire resistance tests – part 1: General requirements. `https://standards.iteh.ai/catalog/standards/cen/243adbdc-e0e0-43ac-a801-22c8e91e7f3c/en-1363-1-2020`, 2020.

[346] James T. Nakos. Uncertainty analysis of thermocouple measurements used in normal and abnormal thermal environment experiments at sandia's radiant heat facility and lurance canyon burn site. Technical Report SAND2004-1023, Sandia National Laboratories, 2004.

[347] B. Karlsson and J.G. Quintiere. *Enclosure Fire Dynamics*. CRC Press, Boca Raton, 1994.

[348] H. Jung, K. Kim, K. Lee, and H. Kwon. A study on fire resistance test procedure for traction battery. In *23rd International Technical Conference on the Enhanced Safety Vehicles*, Republic of Korea, 2003. KATRI.

[349] Fuels - Identification of vehicle compatibility - Graphical expression for consumer information. Standard, European Commitee for Standardization, Brussels, May 2021.

[350] International Organization for Standardization. *ISO 5725-1: 2023: Accuracy (Trueness and Precision) of Measurement Methods and Results-Part 1: General Principles and Definitions*. International Organization for Standardization, 2023.

[351] International Organization for Standardization. *ISO 5725-2: 2019: Accuracy (Trueness and Precision) of Measurement Methods and Results-Part 2: Basic method for the determination of repeatability and reproducibility of a standard measurement method*. International Organization for Standardization, 2019.

[352] International Organization for Standardization. *ISO 5725-4: 2020: Accuracy (Trueness and Precision) of Measurement Methods and Results-Part 4: Basic methods for the determination of the trueness of a standard measurement method*. International Organization for Standardization, 2020.

[353] Biserka Runje, A Horvatic Novak, and Zdenka Keran. Impact of the quality of measurement results on conformity assessment. In *Proceedings of the 29th DAAAM International Symposium, B. Katalinic (Ed.), Published by DAAAM International, ISBN*, pages 978–3, 2018.

[354] Fire-resistance tests — Elements of building construction. Standard, International Organization for Standardization, Geneva, CH, 2021.

[355] International Code for Application of Fire Test Procedures, 2010. Standard, International Maritime Organization, London, GB, 2010.

[356] Daniel Darnikowski and Magdalena Mieloszyk. Investigation into the lithium-ion battery fire resistance testing procedure for commercial use. *Batteries*, 7(3), 2021.

[357] Baki Mehmet Cetegen. *Entrainment and flame geometry of fire plumes*. PhD thesis, California Institute of technology, 1982.

[358] Sudheer Siddapureddy and SV Prabhu. Experimental and numerical simulation studies on heat transfer to calorimeters engulfed in diesel pool fires. *Journal of Fire Sciences*, 35(2):156–176, 2017.

[359] A. G. Asuero, A. Sayago, and A. G. González. The correlation coefficient: An overview. *Critical Reviews in Analytical Chemistry*, 36(1):41–59, 2006.

[360] Steven M Spivak and F Cecil Brenner. *Standardization essentials: Principles and practice*. CRC Press, 2018.

[361] Hyuk Jung, Bohyun Moon, Seulki Lee, and Joongho Bae. A study on thermal energy at fire resistance test for reess. In *25th International Technical Conference on the Enhanced Safety of Vehicles (ESV) National Highway Traffic Safety Administration*, 2017.

[362] Hyuk Jung, Bohyun Moon, and Gwang Goo Lee. Development of experimental apparatus for fire resistance test of rechargeable energy storage system in x ev. *Energies*, 13(2):465, 2020.

[363] Noshin Omar, Mohamed Daowd, Omar Hegazy, Grietus Mulder, Jean-Marc Timmermans, Thierry Coosemans, Peter Van den Bossche, and Joeri Van Mierlo. Standardization work for bev and hev applications: Critical appraisal of recent traction battery documents. *Energies*, 5(1):138–156, 2012.

[364] Jiao Lei, Wenyang Deng, Zhihui Liu, Shaohua Mao, Kozo Saito, Yang Tao, Hongmei Wu, and Chengli Xie. Experimental study on burning rates of large-scale hydrocarbon pool fires under controlled wind conditions. *Fire Safety Journal*, 127:103517, 2022.

[365] H Raza and S Li. The impact of battery electric bus fire on road tunnel. In *Expanding Underground-Knowledge and Passion to Make a Positive Impact on the World*, pages 3280–3288. CRC Press, 2023.

[366] European Committee for Standardization. EN 45545-3:2024: Railway applications – Fire protection on railway vehicles – Part 3: Fire resistance requirements for fire barriers. `https://www.en-standard.eu/en-45545-3-2024-railway-applications-fire-protection-on-railway-vehicles-part-3-fire-re` 2024. European Standard.

[367] Sebastian Ukleja, Marta Walk, Helena Modrzejewska, and Robert Kaźmierowski. Fire resistance testing of railway rolling stock–initial findings from the implementation of a standard en 45545-3: 2013. *Problemy Kolejnictwa*, 2014.

[368] George Thomson and RR Preston. Towards harmonized standard fire resistance testing. *Fire safety journal*, 27(2):91–112, 1996.

[369] EN 1364-2: Fire resistance tests for non-loadbearing elements – Part 2: Ceilings. `https://www.en-standard.eu/en-1364-2-fire-resistance-tests-for-non-loadbearing-elements-part-2-ceilings`, 2018. European Standard.

[370] Jiacheng He, Rekabra Youssef, Md Sazzad Hosen, Mohsen Akbarzadeh, Joeri Van Mierlo, and Maitane Berecibar. A novel methodology to determine the specific heat capacity of lithium-ion batteries. *Journal of Power Sources*, 520:230869, 2022.

[371] Ting Cai, Puneet Valecha, Vivian Tran, Brian Engle, Anna Stefanopoulou, and Jason Siegel. Detection of li-ion battery failure and venting with carbon dioxide sensors. *eTransportation*, 7:100100, 2021.

[372] Arumugam Manthiram. An outlook on lithium ion battery technology. *ACS Central Science*, 3(10):1063–1069, 2017.

[373] Seung-Taek Myung, Filippo Maglia, Kyung-Won Park, Cheolgi S. Yoon, Peter Lamp, Yong-Mook Kim, and Yang-Kook Sun. Nickel-rich layered cathode materials for automotive lithium-ion batteries: Achievements and perspectives. *ACS Energy Letters*, 2(1):196–223, 2011.

[374] Jürgen Vetter, Petr Novák, Rolf Wagner, Christoph Veit, Konrad-C Möller, Jürgen O. Besenhard, Martin Winter, Margret Wohlfahrt-Mehrens, Christoph Vogler, and Abdellatif Hammouche. Ageing mechanisms in lithium-ion batteries. *Journal of Power Sources*, 147(1-2):269–281, 2005.

[375] Yingchun Lyu, Xia Wu, Kai Wang, et al. An overview on the advances of $LiCoO_2$ cathodes for lithium-ion batteries. *Advanced Energy Materials*, 11(2):2000982, 2021.

[376] K. Mizushima, P. C. Jones, P. J. Wiseman, and J. B. Goodenough. Li_3CoO_2 ($0 < x \leq 1$): A new cathode material for batteries of high energy density. *Materials Research Bulletin*, 15(6):783–789, 1980.

[377] Zeqing Duan, Yunfan Wu, Jie Lin, Laisen Wang, and Dong-Liang Peng. Thin-film lithium cobalt oxide for lithium-ion batteries. *Energies*, 15(23):8980, 2022.

[378] Naoaki Nitta, Feixuan Wu, Jung Tae Lee, and Gleb Yushin. Li-ion battery materials: present and future. *Materials Today*, 18(5):252–264, 2015.

[379] ScottW.D. Gourley, TszChun Or, and Zonghai Chen. Breaking free from cobalt reliance in lithium-ion batteries. *iScience*, 23(9):101505, 2020.

[380] Amnesty International and Afrewatch. Democratic Republic of Congo: "This is what we die for": Human rights abuses in artisanal cobalt mines. Research report, Amnesty International, London, May 2016. [Online; accessed: 2025-07-05].

[381] Linda Gaines. The future of automotive lithium-ion battery recycling: Charting a sustainable course. *Sustainable Materials and Technologies*, 1-2:2–7, 2014.

[382] Geani Teodor Man, Andreea Maria Iordache, Ramona Zgavarogea, and Constantin Nechita. Recycling lithium-ion batteries—technologies, environmental, human health, and economic issues—mini-systematic literature review. *Membranes*, 14(12), 2024.

[383] Magnus Bekker. Battery Materials Market Report: Week Ending 19 February 2025. `https://www.linkedin.com/pulse/`, 2025. [Online; accessed: 2025-07-05].

[384] H.-J. Noh, S. Youn, C. S. Yoon, and Y.-K. Sun. Comparison of the structural and electrochemical properties of layered $Li[Ni_xCo_yMn_\zeta O_2$ ($x = 1/3 - 0.85$) cathode material for lithium-ion batteries. *Journal of Power Sources*, 233:121–130, 2013.

[385] Y. Zhang, W. Li, Y.-K. Sun, C. P. Grey, and J. Hong. Structural origin of the high-voltage instability of lithium cobalt oxide. *Nature Nanotechnology*, 16:115–121, 2021.

[386] Christopher L. Campion, Wen Li, and Brett L. Lucht. Thermal decomposition of lipf$_6$-based electrolytes for lithium-ion batteries. *Journal of The Electrochemical Society*, 152(12):A2327–A2337, 2005.

[387] D. P. Finegan, M. Scheel, J. B. Robinson, and P. R. Shearing. Investigating lithium-ion battery materials during overcharge-induced thermal runaway: an operando and multi-scale x-ray ct study. *Physical Chemistry Chemical Physics*, 18(38):30912–30919, 2016.

[388] Daniel Doughty and E.Peter Roth. A general discussion of Li ion battery safety. *The Electrochemical Society Interface*, 21(2):37–44, 2012.

[389] Violaine Sironval, Vittoria Scagliarini, Sivakumar Murugadoss, Maura Tomatis, Yousof Yakoub, Peter Hoet, Dominique Lison, and Sybille van den Brule. $LiCoO_2$ particles used in Li-ion batteries induce primary mutagenicity in lung cells via their capacity to generate hydroxyl radicals. *Particle and Fibre Toxicology*, 17(1):6, 2020.

[390] Soroosh Sharifi-Asl, Jun Lu, Khalil Amine, and Reza Shahbazian-Yassar. Oxygen release degradation in Li-ion battery cathode materials: Mechanisms and mitigating approaches. *Advanced Energy Materials*, 9(22):1900551, 2019.

[391] S. Ghosh et al. A review on high-capacity and high-voltage cathodes for next-generation lithium-ion batteries. *Journal of Energy Power Technology*, 4(1):1–31, 2022.

[392] J. M. Price et al. Optimising the synthesis of $LiNiO_2$: coprecipitation versus solid-state, and the effect of molybdenum doping. *Energy Advances*, 2(3):282–294, 2023.

[393] J. Cheng et al. Enhancing surface oxygen retention through theory-guided doping selection in $li_{1-x}nio_2$ for next-generation lithium-ion batteries. *Journal of Materials Chemistry A*, 8(44):23293–23303, 2020.

[394] J. H. Shim. Recycling cathode materials for lithium-ion batteries via hydro-to-cathode method. *Frontiers in Batteries and Electrochemistry*, 4:1397122, 2024.

[395] Xiaoyang Wang, Xiaoming Chen, and Jun Li. Techno-economic analysis of cathode material production using flame-assisted spray pyrolysis. *Applied Energy*, 278:115673, 2020. [Online; accessed: 2025-07-05].

[396] E. Mervine. Nickel mining a serious concern for climate action. *UQ News*, 2025. [Online; accessed: 2025-07-05].

[397] J. Kim et al. Thermal and safety characteristics of layered $linio_2$ cathode for lithium-ion batteries. *Journal of Power Sources*, 378:484–492, 2018.

[398] M. T. Wei et al. La doping $linio_2$ cathode to immobilize the lattice oxygen and enhance the cycling stability for lithium-ion batteries. *ACS Applied Materials & Interfaces*, 2025.

[399] S. K. Jung et al. Structural and thermal characteristics of $linio_2$ cathode materials for lithium-ion batteries. *Electrochimica Acta*, 137:1–10, 2014.

[400] Juyi Mu, Jinxing Wang, Jinghua Hao, Pin Cao, Shuoqing Zhao, Wen Zeng, Bin Miao, and Sibo Xu. Hydrothermal synthesis and electrochemical properties of v_2o_5 nanomaterials with different dimensions. *Ceramics International*, 41(12):16389–16397, 2015.

[401] Baohua Liang, Yung-Tse Sun, Jianhua Shi, Xiaolei He, Yu Meng, and Zhenyi Wu. Vanadium oxide: Phase diagrams, structures, synthesis, and applications. *Chemical Reviews*, 123(6):4581–4660, 2023.

[402] U.S. Geological Survey. Vanadium. *Mineral Commodity Summaries 2024*, pages 158–159, 2024.

[403] Shanghai Metals Market. Historical Price Charts of 99.5(V_2O_5). `https://www.metal.com/en/prices/202404120005`, 2025. [Online; accessed: 2025-07-05].

[404] Anindita Chakraborty, Arnab Dutta, Richard G. Haverkamp, and Michael K. Horne. Vanadium pentoxide inhalation: A mini-review. *Journal of Toxicology and Environmental Health, Part B*, 8(7):485–511, 2005.

[405] Huihui Yan, Cheng Yang, Liping Zhao, Jing Liu, Peng Zhang, and Lian Gao. A safe high-performance all-solid-state lithium–vanadium battery with a freestanding V_2O_5 nanowire composite paper cathode. *ACS Applied Materials & Interfaces*, 8(50):34309–34316, 2016.

[406] J Li, ZR Zhang, XJ Guo, and Y Yang. The studies on structural and thermal properties of delithiated $lixni_{1/3}co_{1/3}mn_{1/3}o_2$ ($0 < x \leq 1$) as a cathode material in lithium ion batteries. *Solid State Ionics*, 177(17-18):1509–1516, 2006.

[407] D. Lee, P. Oh, and J. Cho. Roles of surface chemistry on stability and performance of layered $LiCoO_2$ cathodes. *Scientific Reports*, 4:4355, 2014.

[408] Fang Zheng, Ming Li, and Rui Wang. Nickel manganese cobalt oxide (ncm) cathode materials. In Xiaodong Zhang and Wei Chen, editors, *Cathode Materials for Lithium-Ion Batteries*, pages 225–258. Royal Society of Chemistry, 2021.

[409] Tian Xu, Lei Zhang, and Yong Cui. Ni/li disordering in layered transition metal oxides and its impact on cathode performance. *Accounts of Chemical Research*, 52(6):1526–1535, 2019.

[410] Qi Xu, Jie Li, and Yufeng Sun. Improving $\mathrm{lini}_x\mathrm{co}_y\mathrm{mn}_{1-x-y}\mathrm{o}_2$ cathode–electrolyte interface under high voltage. *Advanced Energy Materials*, 10(14):1904061, 2020.

[411] Rocky Mountain Institute. Battery Circular Economy Initiative (BCEI) U.S. Supply Chain User Guide. User guide, Rocky Mountain Institute, April 2025. [Online; accessed: 2025-07-05].

[412] Argonne National Laboratory. Estimated Cost of EV Batteries 2019–2024 for GPRA Reporting (Benchmark EV Battery 2024-08-19). `https://www.anl.gov/sites/www/files/2024-08/EV%20Costs%202024%20for%20GPRA%20reporting%20(August%2019,%202024).pdf`, 2024. [Online; accessed: 2025-07-05].

[413] Muhammad Shafique, Muhammad Ateeq, Muhammad Rafiq, Anam Azam, and Xiaowei Luo. Prospects of recycling from end-of-life of li-ion batteries on alleviating materials demand-supply gap in new electric vehicles in asia. *Waste Management*, 171:207–217, 2023.

[414] Qingsong Wang, Ping Ping, Xuejuan Zhao, Guanquan Chu, Jinhua Sun, and Chunhua Chen. Thermal runaway caused fire and explosion of lithium ion battery. *Journal of Power Sources*, 208:210–224, 2012.

[415] Agus Purwanto, Cornelius Satria Yudha, U. Ubaidillah, Hendri Widiyandari, Takashi Ogi, and H. Haerudin. NCA cathode material: synthesis methods and performance enhancement efforts. *Mater. Res. Express*, 5:122001, 2018.

[416] Ayça Yiğitalp, Adnan Taşdemir, Selmiye Alkan Gürsel, and Alp Yürüm. Nafion-coated $LiNi_{0.80}Co_{0.15}Al_{0.05}O_2$ (NCA) cathode preparation and its influence on the Li-ion battery cycle performance. *Energy Storage*, 2:e154, 2020.

[417] Arumugam Manthiram. A reflection on lithium-ion battery cathode chemistry. *Nature Commun.*, 11:1550, 2020.

[418] Wojciech Mrozik, Mohammad Ali Rajaeifar, Oliver Heidrich, and Paul Christensen. Environmental impacts, pollution sources and pathways of spent lithium-ion batteries. *Energy & Environmental Science*, 14(12):6099–6121, 2021.

[419] Alessandro M. Ralls, Kaitlin Leong, Jennifer Clayton, Phillip Fuelling, Cody Mercer, Vincent Navarro, and Pradeep L. Menezes. The Role of Lithium-Ion Batteries in the Growing Trend of Electric Vehicles. *Materials*, 16(17):6063, 2023.

[420] Shanghai Metal Market. Historical Price Charts of NCA Ternary Cathode Material. `https://www.metal.com/en/prices/202411130001`, 2025. [Online; accessed: 2025-07-05].

[421] Yiqing Huang, Yuh-Chieh Lin, David M. Jenkins, and M. Stanley Whittingham. Thermal Stability and Reactivity of Cathode Materials for Li-Ion Batteries. *ACS Appl. Mater. Interfaces*, 8(11):7013–7021, 2016.

[422] Ying Luo, Taolin Lu, Yixiao Zhang, Liqin Yan, Jingying Xie, and Samuel S. Mao. Enhanced electrochemical performance of lini0.5mn1.5o4 cathode using an electrolyte with 3-(1,1,2,2-tetrafluoroethoxy)-1,1,2,2-tetrafluoropropane. *Journal of Power Sources*, 323:134–141, 2016.

[423] Seokyoung Choi, Wuliang Feng, and Yongyao Xia. Recent progress of high voltage spinel $limn_{1.5}ni_{0.5}o_4$ cathode material for Lithium-Ion Battery: Surface modification, doping, electrolyte, and oxygen deficiency. *ACS Omega*, 9(17):18688–18708, 2024.

[424] So Young Choi, Jong Hun Sung, Fuead Hasan, Sangram Keshari Mohanty, Madhusudana Koratikere Srinivasa, and Hyun Deog Yoo. Synthesis and electrochemical properties of the li3po4-coated lini0.5mn1.5o4 cathode materials for high-voltage lithium-ion batteries. *Energies*, 18(13), 2025.

[425] J. Zeng, X. F. Li, J. Liu, X. B. Meng, T. J. Tang, M. N. Banis, J. L. Yang, Y. H. Hu, R. Y. Li, M. Cai, and X. L. Sun. A novel coating onto $limn_2o_4$ cathode with increased lithium ion battery performance. *Applied Surface Science*, 317:884–891, 2014.

[426] Jennifer Dunn, Linda Gaines, and Y.-H. Shin. Estimating the cost and energy demand of producing lithium manganese oxide cathode material. `https://publications.anl.gov/anlpubs/2020/03/158938.pdf`, 2020. [Online; accessed: 2025-07-05].

[427] Hui Luo, Sheng Wang, and Xue Jin. Controlling cation ordering in $lini_{0.5}mn_{1.5}o_4$ spinel cathodes for enhanced electrochemical performance. *Advanced Energy Materials*, 6(13):1600134, 2016.

[428] Q. Xiao, X. Yu, Y. Meng, H. Li, J. Feng, and F. Pan. Oxygen-release-related thermal stability and decomposition pathways of $lini_{0.5}mn_{1.5}o_4$ cathode materials. *Chemistry of Materials*, 26(2):1108–1118, 2014.

[429] J. R. Dahn, E. W. Fuller, M. Obrovac, and U. von Sacken. Thermal stability of $lixcoo_2$, $lixnio_2$ and λMnO_2 and consequences for the safety of li-ion cells. *Journal of The Electrochemical Society*, 141(2):349–355, 1994.

[430] R. Spotnitz and J. Franklin. Abuse behavior of high-power, lithium-ion cells. *Journal of Power Sources*, 113(1):81–100, 2002.

[431] R. Dominko, M. Bele, M. Gaberscek, M. Remskar, and D. Hanzel. Porous olivine composites synthesized by sol–gel technique. *Journal of Power Sources*, 153(2):274–280, 2006.

[432] Jiangtao Hu, Yi Jiang, Suihan Cui, Yandong Duan, Tongchao Liu, Hua Guo, Lingpiao Lin, Yuan Lin, Jiaxin Zheng, Khalil Amine, et al. 3d-printed cathodes of limn1- xfexpo4 nanocrystals achieve both ultrahigh rate and high capacity for advanced lithium-ion battery. *Advanced Energy Materials*, 6(18):1600856, 2016.

[433] Atsuo Yamada, Sai-Cheong Chung, and Koichiro Hinokuma. Optimized lifepo4 for lithium battery cathodes. *Journal of the electrochemical society*, 148(3):A224, 2001.

[434] Li-Xia Yuan, Zhao-Hui Wang, Wu-Xing Zhang, Xian-Luo Hu, Ji-Tao Chen, Yun-Hui Huang, and John B Goodenough. Development and challenges of lifepo 4 cathode material for lithium-ion batteries. *Energy & Environmental Science*, 4(2):269–284, 2011.

[435] Dong-Han Kim and Jaekook Kim. Synthesis of lifepo4 nanoparticles and their electrochemical properties. *Journal of Physics and Chemistry of Solids*, 68(5-6):734–737, 2007.

[436] Elsa A Olivetti, Gerbrand Ceder, Gabrielle G Gaustad, and Xinkai Fu. Lithium-ion battery supply chain considerations: analysis of potential bottlenecks in critical metals. *Joule*, 1(2):229–243, 2017.

[437] AS Andersson and John Oswald Thomas. The source of first-cycle capacity loss in lifepo4. *Journal of Power Sources*, 97:498–502, 2001.

[438] Sung-Yoon Chung, Jason T Bloking, and Yet-Ming Chiang. Electronically conductive phospho-olivines as lithium storage electrodes. *Nature materials*, 1(2):123–128, 2002.

[439] Arumugam Manthiram. A reflection on lithium-ion battery cathode chemistry. *Nature communications*, 11(1):1550, 2020.

[440] Seongjae Ko, Hiromi Otsuka, Shin Kimura, Yuta Takagi, Shoji Yamaguchi, Takuya Masuda, and Atsuo Yamada. Rapid safety screening realized by accelerating rate calorimetry with lab-scale small batteries. *Nature Energy*, 10(6):707–714, 2025.

[441] Xiang Liu, Liang Yin, Dongsheng Ren, Li Wang, Yang Ren, Wenqian Xu, Saul Lapidus, Hewu Wang, Xiangming He, Zonghai Chen, Gui-Liang Xu, Minggao Ouyang, and Khalil Amine. In situ observation of thermal-driven degradation and safety concerns of lithiated graphite anode. *Nature Communications*, 12:4235, 2021.

[442] Sheng Yang, Wenwei Wang, Cheng Lin, Weixiang Shen, and Yiding Li. Investigation of internal short circuits of lithium-ion batteries under mechanical abusive conditions. *Energies*, 12(10):1885, 2019.

[443] Kangjia Hu, Xiaoyu Sang, Jiaxin Chen, Zetong Liu, Jiahui Zhang, and Xianluo Hu. High-safety lithium-ion batteries with silicon-based anodes enabled by electrolyte design. *Chemistry – An Asian Journal*, 18(24):e202300820, 2023.

[444] Qiang Liu, Tao Meng, Le Yu, Sheng Guo, Yu Hu, Zhaojun Liu, and Xianluo Hu. Interface engineering to boost thermal safety of microsized silicon anodes in lithium-ion batteries. *Small Methods*, 6(7):2200380, 2022.

[445] Guangyao Jin, Wanwei Zhao, Jianing Zhang, Wenyu Liang, Mingyang Chen, and Rui Xu. High-temperature stability of lifepo$_4$/carbon lithium-ion batteries: Challenges and strategies. *Sustainable Chemistry*, 6(1):7, 2025.

[446] Alok M. Tripathi, Wei-Nien Su, and Bing Joe Hwang. In situ analytical techniques for battery interface analysis. *Chemical Society Reviews*, 47(3):736–851, 2018.

[447] Jakob Asenbauer, Tobias Eisenmann, Matthias Kuenzel, Arefeh Kazzazi, Zhen Chen, and Dominic Bresser. The success story of graphite as a lithium-ion anode material – fundamentals, remaining challenges, and recent developments including silicon (oxide) composites. *Sustainable Energy & Fuels*, 4(11):5387–5416, 2020.

[448] Kai Liu, Jian Zhang, Yao Yang, Jun Li, Tao Wang, Ming Chen, Yongming Chen, and Guang Cui. Materials for lithium-ion battery safety. *Science Advances*, 4(6):eaas9820, 2018.

[449] Jürgen Janek and Wolfgang G. Zeier. A solid future for battery development. *Nature Energy*, 1(9):16141, 2016.

[450] Richard Schmuch, Ralf Wagner, Gudrun Hörpel, Tobias Placke, and Martin Winter. Performance and cost of materials for lithium-based rechargeable automotive batteries. *Nature Energy*, 3(4):267–278, 2018.

[451] Abniel Machín, Carmen Morant, and Francisco Márquez. Advancements and challenges in solid-state battery technology: An in-depth review of solid electrolytes and anode innovations. *Batteries*, 10(1):29, 2024.

[452] Jing Xie and Yi-Chun Lu. Designing nonflammable electrolytes for next-generation lithium-ion batteries. *Advanced Materials*, 37(2):e2312451, 2025.

[453] Byung-Wan Lee and Chan Jung. A corporate approach to enhancing lithium-ion battery safety through flame-retardant electrolyte development. *Frontiers in Energy Research*, 12:1508471, 2024.

[454] Roberto Sommerville, James Shaw-Stewart, Vannessa Goodship, Neil Rowson, and Emma Kendrick. A review of physical processes used in the safe recycling of lithium ion batteries. *Sustainable Materials and Technologies*, 25:e00197, 2020.

[455] John B. Goodenough and Youngsik Kim. Challenges for rechargeable li batteries. *Chemistry of Materials*, 22(3):587–603, 2010.

[456] Thomas A Yersak, Yubin Zhang, Fang Hao, and Mei Cai. Moisture stability of sulfide solid-state electrolytes. *Frontiers in Energy Research*, 10:882508, 2022.

[457] Changhong Wang, Jun Liu, J. T. K., and X. S. Prospects of halide-based all-solid-state batteries: From material design to practical application. *Science Advances*, 8(37):eadc9516, 2022.

[458] Dharini Shanmukaraj, Anna Tkacheva, Michel Armand, and Guoxiu Wang. Polymer electrolytes for lithium batteries: advances and prospects. *Chem*, 5(9):2326–2352, 2019.

[459] Jian Sun et al. Design of a multi-functional gel polymer electrolyte with a 3d compact stacked polymer micro-sphere matrix for high-performance lithium metal batteries. *Journal of Materials Chemistry A*, 10:12563–12573, 2022.

[460] Yongwei Yue et al. Effectively elevating ceramic fillers' dispersity in gel hybrid electrolyte through bridge–linked construction for high–performance lithium metal batteries. *Batteries*, 9(5):270, 2023.

[461] Jean-Marie Tarascon, Philippe Willmann, and Michel Armand. All-solid-state lithium–oxygen battery with high safety in wide temperature range. *Scientific Reports*, 5:13271, 2015.

[462] Justyna Minkiewicz, Gareth M Jones, Shaghayegh Ghanizadeh, Samira Bostanchi, Thomas J Wasely, Sima Aminorroaya Yamini, and Vahid Nekouie. Large-scale manufacturing of solid-state electrolytes: Challenges, progress, and prospects. *Open Ceramics*, 16:100497, 2023.

[463] Sung Cik Mun and Jong Ho Won. Manufacturing processes of microporous polyolefin separators for lithium-ion batteries and correlations between mechanical and physical properties. *Crystals*, 11(9):1013, 2021.

[464] Shijie Zhong, Botao Yuan, Zhaoxu Guang, Dongjiang Chen, Qun Li, Liwei Dong, Yuanpeng Ji, Yunfa Dong, Jiecai Han, and Weidong He. Recent progress in thin separators for upgraded lithium ion batteries. *Energy Storage Materials*, 41:805–841, 2021.

[465] Ali Akbar Heidari and Hossein Mahdavi. Recent development of polyolefin-based microporous separators for li-ion batteries: A review. *Chemistry & Biodiversity (Chem. Rec.)*, 20(6):570–595, 2020.

[466] Miaomiao Su, Guang Huang, Suqing Wang, Yanjie Wang, and Haihui Wang. High safety separators for rechargeable lithium batteries. *Science China Chemistry*, 64(7):1131–1156, 2021.

[467] Subramanian Natarajan, Krishnan Subramanyan, R. Baby Dhanalakshmi, A. Marian Stephan, and V. Aravindan. Regeneration of polyolefin separators from spent li-ion battery for second life. *Batteries and Supercaps*, 3(7):581–586, 2020.

[468] Xingyi Zhang, Qingwei Sun, Cheng Zhen, Yuliang Niu, Yuting Han, Guang Zeng, and et al. Recent progress in flame-retardant separators for safe lithium-ion batteries. *Energy Storage Materials*, 37:628–647, 2021.

[469] D. M. D. Babiker, Z. R. Usha, Chang Wan, M. M. E. Hassaan, Xiaojian Chen, and Likui Li. Recent progress of composite polyethylene separators for lithium/sodium batteries. *Journal of Power Sources*, 564:232853, 2023.

[470] Xue Sun, Yun Zhou, Dadi Li, Kun Zhao, Li Wang, Peng Tan, and et al. A review of electrospun separators for lithium-based batteries: Progress and application prospects. *Carbon Energy*, 6:e539, 2024.

[471] Yinyu Xiang, Junsheng Li, Jiaheng Lei, Dan Liu, Zhizhong Xie, Deyu Qu, Ke Li, Tengfei Deng, and Haolin Tang. Advanced separators for lithium-ion and lithium-sulfur batteries: A review of recent progress. *ChemSusChem*, 9(21):3023–3039, 2016.

[472] Tingrun Lai, Hong Zhao, and Youzhi et al. Song. Mechanism and control strategies of lithium-ion battery safety: A review. *Small Methods*, 9(1):e2400029, 2025.

[473] Li Zhao, Rui Wang, Shichun Chen, and Yifan Zhang. Review of thermal management techniques for prismatic li-ion batteries. *Energies*, 18(3):492, 2025.

[474] David Marcos, Maitane Garmendia, Jon Crego, and José Antonio Cortajarena. Functional safety bms design methodology for automotive lithium-based batteries. *Energies*, 14(21):6942, 2021.

[475] KW See, Guofa Wang, Yong Zhang, Yunpeng Wang, Lingyu Meng, Xinyu Gu, Neng Zhang, KC Lim, L Zhao, and Bin Xie. Critical review and functional safety of a battery management system for large-scale lithium-ion battery pack technologies. *International Journal of Coal Science & Technology*, 9(1):36, 2022.

[476] M Siva Ramkumar, C Subba Rami Reddy, Agenya Ramakrishnan, K Raja, S Pushpa, S Jose, and Mani Jayakumar. Review on li-ion battery with battery management system in electrical vehicle. *Advances in Materials Science and Engineering*, 2022(1):3379574, 2022.

[477] Guodong Xia, Lei Cao, and Guanglong Bi. A review on battery thermal management in electric vehicle application. *Journal of power sources*, 367:90–105, 2017.

[478] Noël Hallemans, David Howey, Alberto Battistel, Nessa Fereshteh Saniee, Federico Scarpioni, Benny Wouters, Fabio La Mantia, Annick Hubin, Widanalage Dhammika Widanage, and John Lataire. Electrochemical impedance spectroscopy beyond linearity and stationarity—a critical review. *Electrochimica Acta*, 466:142939, 2023.

[479] Yong Seok Choi and Dal Mo Kang. Prediction of thermal behaviors of an air-cooled lithium-ion battery system for hybrid electric vehicles. *Journal of Power Sources*, 270:273–280, 2014.

[480] Gang Zhao, Xiaolin Wang, Michael Negnevitsky, and Hengyun Zhang. A review of air-cooling battery thermal management systems for electric and hybrid electric vehicles. *Journal of Power Sources*, 501:230001, 2021.

[481] Foo Shen Hwang, Thomas Confrey, Colin Reidy, Dorel Picovici, Dean Callaghan, David Culliton, and Cathal Nolan. Review of battery thermal management systems in electric vehicles. *Renewable and Sustainable Energy Reviews*, 113:109245, 2019.

[482] K Muthukrishnan and C Ramesh Kumar. Study on the effect of tab cooling on the lithium-ion battery pack life cycle. *Archives of Thermodynamics*, 45(2), 2024.

[483] Le Duc Tai, Kunal Sandip Garud, Seong-Guk Hwang, and Moo-Yeon Lee. A review on advanced battery thermal management systems for fast charging in electric vehicles. *Batteries*, 10(10):372, 2024.

[484] Moustafa M Amer, Mahmoud A Shouman, Mohamed S Salem, Arunachala M Kannan, and Ahmed M Hamed. Advances in thermal management systems for li-ion batteries: A review. *Thermal Science and Engineering Progress*, page 102714, 2024.

[485] QL Yue, CX He, MC Wu, and TS Zhao. Advances in thermal management systems for next-generation power batteries. *International Journal of Heat and Mass Transfer*, 181:121853, 2021.

[486] Bin Xu, Jinwoo Lee, Daeil Kwon, Lingxi Kong, and Michael Pecht. Mitigation strategies for li-ion battery thermal runaway: A review. *Renewable and Sustainable Energy Reviews*, 150:111437, 2021.

[487] Lip Huat Saw, Yonghuang Ye, Ming Chian Yew, Wen Tong Chong, Ming Kun Yew, and Tan Ching Ng. Computational fluid dynamics simulation on open cell aluminium foams for li-ion battery cooling system. *Applied Energy*, 204:1489–1499, 2017.

[488] A Afass, B Lamrani, B Lebrouhi, MA Tankari, M Karkri, S Landini, and T Kousksou. Thermal assessment of li-ion batteries incorporating phase change materials using a new 2d model. *Energy Conversion and Management: X*, page 101051, 2025.

[489] Yuyang Wei and Martin Agelin-Chaab. Development and experimental analysis of a hybrid cooling concept for electric vehicle battery packs. *Journal of Energy Storage*, 25:100906, 2019.

[490] Ziye Ling, Fang Wang, Xiaoming Fang, Xuenong Gao, and Zhengguo Zhang. A hybrid thermal management system for lithium ion batteries combining phase change materials with forced-air cooling. *Applied Energy*, 148:403–409, 2015.

[491] Shengnan Wang, Yunhua Li, Yun-Ze Li, Yufeng Mao, Yanan Zhang, Wei Guo, and Mingliang Zhong. A forced gas cooling circle packaging with liquid cooling plate for the thermal management of li-ion batteries under space environment. *Applied Thermal Engineering*, 123:929–939, 2017.

[492] Siqi Chen, Xiongbin Peng, Nengsheng Bao, and Akhil Garg. A comprehensive analysis and optimization process for an integrated liquid cooling plate for a prismatic lithium-ion battery module. *Applied Thermal Engineering*, 156:324–339, 2019.

[493] Hengyun Zhang, Xiaoyu Wu, Qingyu Wu, and Shen Xu. Experimental investigation of thermal performance of large-sized battery module using hybrid pcm and bottom liquid cooling configuration. *Applied Thermal Engineering*, 159:113968, 2019.

[494] Maan Al-Zareer, Ibrahim Dincer, and Marc A Rosen. Novel thermal management system using boiling cooling for high-powered lithium-ion battery packs for hybrid electric vehicles. *Journal of power sources*, 363:291–303, 2017.

[495] Yuyang Wei and Martin Agelin-Chaab. Experimental investigation of a novel hybrid cooling method for lithium-ion batteries. *Applied Thermal Engineering*, 136:375–387, 2018.

[496] Chunrong Zhao, Antonio CM Sousa, and Fangming Jiang. Minimization of thermal non-uniformity in lithium-ion battery pack cooled by channeled liquid flow. *International journal of heat and mass transfer*, 129:660–670, 2019.

[497] Guiwen Jiang, Juhua Huang, Mingchun Liu, and Ming Cao. Experiment and simulation of thermal management for a tube-shell li-ion battery pack with composite phase change material. *Applied Thermal Engineering*, 120:1–9, 2017.

[498] Weixiong Wu, Wei Wu, and Shuangfeng Wang. Thermal optimization of composite pcm based large-format lithium-ion battery modules under extreme operating conditions. *Energy Conversion and Management*, 153:22–33, 2017.

[499] Jingwen Weng, Chengshan Xiao, Dongxu Ouyang, Xuning Yang, Mingyi Chen, Guangxu Zhang, et al. Mitigation effects on thermal runaway propagation of structure-enhanced phase change material modules with flame retardant additives. *Energy*, 239:122087, 2022.

[500] Liwei Zhao, Izumi Watanabe, Takayuki Doi, Shigeto Okada, and Jun ichi Yamaki. Tg-ms analysis of solid electrolyte interphase (sei) on graphite negative-electrode in lithium-ion batteries. *Journal of Power Sources*, 161(2):1275–1280, 2006.

[501] Hui Yang, Hyunjoo Bang, Khalil Amine, and Jai Prakash. Investigations of the exothermic reactions of natural graphite anode for li-ion batteries during thermal runaway. *Journal of the Electrochemical Society*, 152(1):A73, 2004.

[502] Grégory Gachot, Perrine Ribière, David Mathiron, Sylvie Grugeon, Michel Armand, Jean-Bernard Leriche, Serge Pilard, and Stéphane Laruelle. Gas chromatography/mass spectrometry as a suitable tool for the li-ion battery electrolyte degradation mechanisms study. *Analytical chemistry*, 83(2):478–485, 2011.

[503] Binbin Mao, Haodong Chen, Zhixian Cui, Tangqin Wu, and Qingsong Wang. Failure mechanism of the lithium ion battery during nail penetration. *International Journal of Heat and Mass Transfer*, 122:1103–1115, 2018.

[504] Xuning Feng, Xiangming He, Minggao Ouyang, Languang Lu, Peng Wu, Christian Kulp, and Stefan Prasser. Thermal runaway propagation model for designing a safer battery pack with 25 ah linixcoymnzo2 large format lithium ion battery. *Applied energy*, 154:74–91, 2015.

[505] Hajime Arai, Masayuki Tsuda, Keiichi Saito, Masahiko Hayashi, and Yoji Sakurai. Thermal reactions between delithiated lithium nickelate and electrolyte solutions. *Journal of The Electrochemical Society*, 149(4):A401, 2002.

[506] Ping Ping, Depeng Kong, Jiaqing Zhang, Ruoxi Wen, and Jennifer Wen. Characterization of behaviour and hazards of fire and deflagration for high-energy li-ion cells by over-heating. *Journal of Power Sources*, 398:55–66, 2018.

[507] Vijay Somandepalli, Kevin Marr, and Quinn Horn. Quantification of combustion hazards of thermal runaway failures in lithium-ion batteries. *SAE International Journal of Alternative Powertrains*, 3(1):98–104, 2014.

[508] Andrey W Golubkov, David Fuchs, Julian Wagner, Helmar Wiltsche, Christoph Stangl, Gisela Fauler, Gernot Voitic, Alexander Thaler, and Viktor Hacker. Thermal-runaway experiments on consumer li-ion batteries with metal-oxide and olivin-type cathodes. *Rsc Advances*, 4(7):3633–3642, 2014.

[509] Alessandro Dal Pozzo, Raffaela Moricone, Alessandro Tugnoli, and Valerio Cozzani. Experimental investigation of the reactivity of sodium bicarbonate toward hydrogen chloride and sulfur dioxide at low temperatures. *Industrial & Engineering Chemistry Research*, 58(16):6316–6324, 2019.

[510] Gerald Hunt and Melissa Sewell. Utilizing dry sorbent injection technology to improve acid gas control. In *Air and Waste Management Association - International Conference on Thermal Treatment Technologies and Hazardous Waste Combustors*, pages 144–156, 2015.

[511] Yougen Kong and Heidi Davidson. Dry sorbent injection of sodium sorbents for so2, hcl and mercury mitigation. In *North American Waste-to-Energy Conference*, volume 43932, pages 317–320, 2010.

[512] Ravi K Srivastava, Wojciech Jozewicz, and Carl Singer. So2 scrubbing technologies: a review. *Environmental Progress*, 20(4):219–228, 2001.

[513] D Schmal, ACP Ligtvoet, and A Brunia. Some physico-chemical aspects of dry sorbent injection for removal of hci and hf from waste incinerator flue gases. *JAPCA*, 39(1):55–57, 1989.